Campbell, Iain Innes (2024) *Induction melt thermoforming of multiaxial thermoplastic composites.* PhD thesis.

https://theses.gla.ac.uk/84186/

Induction Melt Thermoforming of Multiaxial Thermoplastic Composites

Submitted in fulfilment of the requirements for the degree of Doctor of Philosophy (PhD) in Mechanical Engineering

by Iain Innes Campbell

James Watt School of Engineering

College of Science and Engineering

University of Glasgow

November 2022

Abstract

Fibre reinforced thermoplastic composites are a widely used material with a growing global market share. This is partially driven by a need to improve energy efficiency through weight reduction. These composites offer high specific strength and stiffness thanks to their mix of a low-density polymer matrix and high-strength fibres. However, during the forming of complex geometries with multiple fibre reinforced plies, these plies must undergo significant deformation. This requires sliding between plies to relieve stress and avoid defects in the final part. Reducing friction coefficients between adjacent plies of fibre reinforcement could allow for more complex geometries to be formed with less wrinkling.

The principle aim of this study was to investigate the feasibility of a blue-sky concept: utilising molten metal as a lubricating interlayer in the thermoforming of thermoplastic composites. The low viscosity of the interlaminar tin is intended to reduce frictional stresses between adjacent sheets, thus reducing compressive stresses resultant wrinkling in the part. Induction heating is used to melt tin sheets in a hybrid composite tin layup and conduction leads to the melting of the matrix phase of adjacent nylon-carbon composites. A novel multi-step male tool is then used to form the part while simultaneously removing the majority of the interlaminar tin from the final part. Experiments showed layups with up to three interlayers of tin could be successfully heated and formed via induction heating. Another advantage of the method is the ability to use the metal layers to heat composite parts efficiently and uniformly from the inside.

Building on the development of the novel manufacturing process, mechanical testing, non-destructive testing and some numerical simulation was carried out to further explore the process. Microscope imaging, 2D x-rays and 3D CT scans are used to quantify residual tin. Residual tin volumes as low as 1.5 % were achievable when consolidating flat geometries. The interlaminar shear strength of manufactured components was tested. Despite reductions in yield and flexural stiffness, process refinements produced parts with interlaminar shear stiffness comparable to benchmark samples. Finally, simulation of the multistep forming process using a pantographic beam and membrane model allowed the influence of multi-step forming and friction variation to be studied.

Table of contents

Nomenclature

Latin Alphabet

A_i	Area
b	Part breadth
C_{th}	Combined thermal mass
C_i	Specific heat of part
E_b	Flexural modulus
F_p	Pull-out force
F_n	Normal force
f_c	Coefficient of friction
H	Hersey number
I	Intensity
ILSS	Interlaminar shear strength
ILSS_Y	Interlaminar shear stress at yield
j	Energy radiated
L	Part length
$n_{1,2}$	Refractive index
$\dot{Q}$	Heat transfer rate
R_s , R_p	Polarisation states
s	Test span
t	Part thickness
T	Temperature
T_d	Degradation temperature
T_g	Glass transition temperature
T_m	Melt temperature
U	Sliding velocity
V	Volume

Greek Alphabet

δ	Skin depth
ϵ	Emissivity
θ	Angle
η	Fluid viscosity
M	Magnetic permeability
μ	Linear attenuation coefficient
ξ	Wave speed in material
τ	Shear stress on interply interface
τ_0	Shear stress at zero velocity
P	Resistivity
ρ	Density of material
σ	Stefan Boltzmann constant
φ	Sliding angle
ω	Frequency

Acknowledgements

The author acknowledges support for this work from the Engineering and Physical Sciences Research Council provided in the form of a DTA PhD studentship funded by EP/N509668/1. The author would also like to acknowledge the support of funding provided by a feasibility study; part of EP/P006701/1.

List of Publications

1. Harrison P, **Campbell I**, Guliyev E, McLelland B, Gomes R, Curado-Correia N, et al. Induction melt thermoforming of advanced multi-axial thermoplastic composite laminates. Journal of Manufacturing Processes, 2020;60:673–83. https://doi.org/10.1016/j.jmapro.2020.10.026.

2. **Campbell I**, Mulvihill D.M., Harrison P. The influence of residual tin following induction melt thermoforming of composite parts. Composites Part A, 2023; 107286. https://doi.org/10.1016/j.compositesa.2022.107286.

Author’s Declaration

University of Glasgow

College Identity

Statement of Originality to Accompany Thesis Submission

Name: IAIN CAMPBELL

Registration Number:

I certify that the thesis presented here for examination for [a~~/an MPhil~~/PhD] degree of the University of Glasgow is solely my own work other than where I have clearly indicated that it is the work of others (in which case the extent of any work carried out jointly by me and any other person is clearly identified in it) and that the thesis has not been edited by a third party beyond what is permitted by the University’s PGR Code of Practice.

The copyright of this thesis rests with the author. No quotation from it is permitted without full acknowledgement.

I declare that the thesis does not include work forming part of a thesis presented successfully for another degree [unless explicitly identified and as noted below].

I declare that this thesis has been produced in accordance with the University of Glasgow’s Code of Good Practice in Research.

I acknowledge that if any issues are raised regarding good research practice based on review of the thesis, the examination may be postponed pending the outcome of any investigation of the issues.

Signature: ……………………………………………………….

Date: 28/10/2022 ………………………………………………………..

This completed statement must be bound into the submitted copies of the soft-bound thesis.

Chapter 1 Introduction

Fibre reinforced composites are a major global market worth ~$100 billion annually with predicted growth rates of 6 % annually [1]. Carbon fibre reinforcements offer high strength and weight savings, but can be more expensive than the more common glass fibre reinforcements. Thermoplastic composites are lightweight, offer high specific strengths, and unlike thermoset composites it is possible to reshape and recycle parts. These attributes make them well suited for many applications particularly in the automotive, aerospace, and wind energy industries [2]. Thermoplastics are however more energy intensive to form than thermosetting composites due to the higher temperatures and pressures required, but offer benefits in increased recyclability, good impact resistance and high toughness. A shared difficulty is the forming of complex geometries, such as in Fig 1.1a, where the draping mechanics of the fibre reinforcements restrict deformation. The key deformation mechanisms are intra-ply shear (fibres rotating) and inter-ply slip (adjacent sheets sliding relative to each other). These mechanisms help relieve compressive stresses during forming; however, if compressive stresses overcome the slight bending stiffness of the composite blank, then it can lead to buckling and wrinkling in the composite sheet as shown in Fig 1.1b. These wrinkles can then lead to lower strength and stiffness and increased risk of failure in the part [3], [4]. Thus, it is desirable to improve inter-ply slip mechanics to allow for thermoplastics to be thermoformed into more complex geometries with less defects.

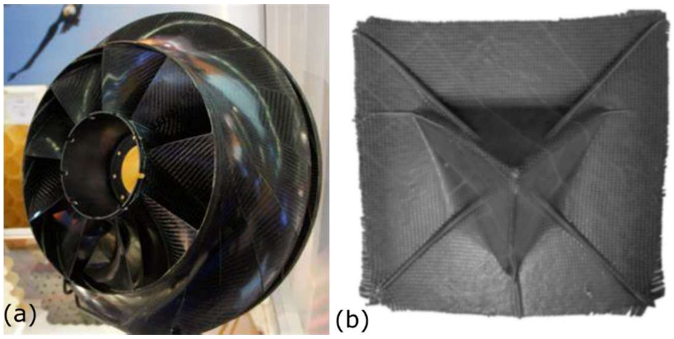

Figure 1.1. (a) Carbon fibre engine fan with complex geometry (image from [5]) (b) wrinkles when forming tetrahedron shape with twill weave carbon fibre fabric with +/-45 orientation (image from [6]).

Inter-ply slip in a fibre reinforced thermoplastic composite is influenced by pressure and the frictional behaviour of a viscous, resin rich interlayer between adjacent textile plies. Prior studies have shown that the frictional performance of this interlayer can be well described through a Stribeck curve [7]. Thus, for standard thermoforming conditions, decreasing matrix viscosity (i.e., by increasing temperature) and decreasing sliding velocity can both reduce friction coefficients. This thesis investigates a “Blue-Sky” idea to reduce interlayer viscosity and thus reduce inter-ply friction. The idea is to use a molten metal as a low viscosity lubricant. Specifically, tin is chosen to pair with a nylon matrix. Both have similar melt temperatures (232 °C vs ~220 °C respectively). Tin has a significantly lower viscosity than nylon (~.02 Pa.s vs ~200 Pa.s [8] [9]). Tin also has a high surface tension making it unlikely to mix with the molten nylon.

Several new techniques were explored in designing the process. Firstly, it was desired to have a multi-step forming tool capable of producing a pressure gradient from the centre of the blank towards the edges to remove molten tin during the forming process. Secondly, induction heating was explored as an option for heating a carbon-nylon / tin composite layup. This exploited the conductive properties of the tin enabling more targeted heat generation.

The main objectives of the thesis are as follows:

- Develop a novel process for thermoforming advanced thermoplastic composites while using a molten tin lubricating interlayer (iMelt).
- Identify methods of evaluating the quantity of residual tin in the part.
- Quantify any influence the presence of residual tin might have on mechanical properties.
- Numerically investigate the influence of changing friction coefficients and multistep tooling on the thermoforming of a complex geometry.

This project investigates a potential step change in the thermoforming of thermoplastic composites. The feasibility of utilising an extremely low viscosity interlayer (molten tin) to lubricate the forming blank is explored. To this end, an ‘Induction Melt Thermoforming’ process is created. The electromagnetic properties of the molten tin are exploited to heat a carbon-nylon composite /

tin hybrid layup and a multi-step tool is used to press form the composite while removing the interlayer. The idea for lubrication is inspired by Vanclooster who used layers of neat thermoplastic resin to lubricate the forming of glass reinforced polypropylene and found that increasing the interlayer thickness reduced the tendency to wrinkle [10]. The proposed method would likely be used for high volume, medium size components (up to approximately one meter in size) as there is a requirement for relatively expensive multistep tooling. The process also introduced small quantities of residual tin into the part which would likely pose regulatory challenges in industries such as aerospace, or in applications with high thermal cycling. Therefore the automative industry is a likely target for the technique. Chapter 2 will cover the relevant literature and motivations for the project in more depth.

Chapter 3 explores the development of the novel Induction Melt Thermoforming process. Several multilayer flat samples are consolidated, before progressing to multilayer forming of a ripple geometry. This Chapter also covers the development of an analogous thermoforming process using radiant heating, to act as a control to assess the quality of the induction melt thermoformed manufactured parts.

Chapter 4 develops processes for quantifying the amount of residual tin left in the formed parts. A mixture of microscope analysis of polished cross-sections, CT scans and X-ray scans are used to evaluate the quantity and distribution of residual tin, analysing both volume and projected surface area. CT scans offer high resolution detail on the residual tin quantity and allow for interpretation of the thickness and through thickness location of the residual tin. This is however time consuming and expensive, so conventional x-ray film is used to provide a faster, cheaper tool which could potentially be used for low-cost quality control in a manufacturing process. Algorithms are developed to quickly process CT and X-ray scans giving guidance as to part quality.

Chapter 5 assesses the influence that residual tin has on the mechanical performance of the part. The presence of residual tin between laminates raises questions about increased risk of delamination in the final part. This is assessed via interlaminar shear strength tests and results are compared with control samples without interlaminar tin. A sensitivity analysis is also carried out assessing the influence of tin on mechanical properties between test specimens.

In Chapter 6 simulation of a multistep forming process is carried out. Composite sheets representative of a glass fabric are modelled and the influence of varying friction, number of forming steps and geometry complexity are examined.

Chapter 7 presents the main conclusions of the work and indicates future avenues for exploration of the process and potential refinements which could be made to this prototype thermoforming process.

This thesis extends the state of the art by firstly showing that hybrid composite-tin layups can be heated via induction heating and formed using a novel incremental forming process to remove the vast majority of molten interlaminar tin. Secondly, it develops algorithms for the characterisation of residual tin within manufactured blanks and assesses the influence of the residual tin on the mechanical properties of the blanks. Finally, simulation of the forming process is carried out to assess the influence of multi-step forming on the stresses in the thermoformed blank.

Chapter 2 Literature Review

2.1 Introduction

Composites are materials composed of two or more constituent materials. A common form of composite involves combining fibres (high strength, high stiffness but low structural integrity) with a polymer matrix (low strength, low density) making the bulk of the material. Fibre reinforced thermoplastic composites commonly use reinforcements where the fibres are assembled in yarns before being combined to form flexible sheets. This reinforcement can then be embedded within a polymer matrix offering structural integrity to the composite. Combined, this can create high strength parts (due to the fibres) with low density (due to the low density of the polymer reinforcement). This combination makes it an attractive replacement for metal in structures where weight is a key concern. One driver of their adoption is a desire to reduce emissions in transport [11]. Dramatic weight reductions of ~50 % can be obtained by replacing steel or aluminium components with carbon fibre reinforced polymer composites due to their superior specific stiffness and strength, compared with conventional materials [12].

This thesis looks at a composite where a thermoplastic nylon matrix is reinforced with carbon fibres. In the rest of this Chapter an overview of common composite manufacturing methods, including key challenges involved in their forming, will be given. The general background is based on several reviews of composite processing [13], [14], [15], [16].

2.2 Fibre Reinforced Thermoplastic Composites

Fibre reinforced thermoplastic composites involve the use of a thermoplastic matrix material with reinforcing fibres adding stiffness and strength to the part. These can take the form of randomly arranged short fibres, or continuous fibres in the form of unidirectional tapes or woven textiles. In this thesis, layups consisting of multiple layers of unidirectional carbon fibres in a nylon matrix are formed into a complex geometry. These cross-ply laminates have continuous fibres with adjacent fibre layers in a [0/90/90/0] layup. This offers good formability and high strength in the two primary orientations. Fig. 2.1a shows a diagram of unidirectional fibres embedded in a matrix material. Fig. 2.1b shows a carbon fibre reinforced nylon car floor plate formed with press forming which is the technique explored in this thesis. Alternatively, Fig. 2.1c shows a carbon fibre reinforced nylon boat hull which was created via hand layup of fibres.

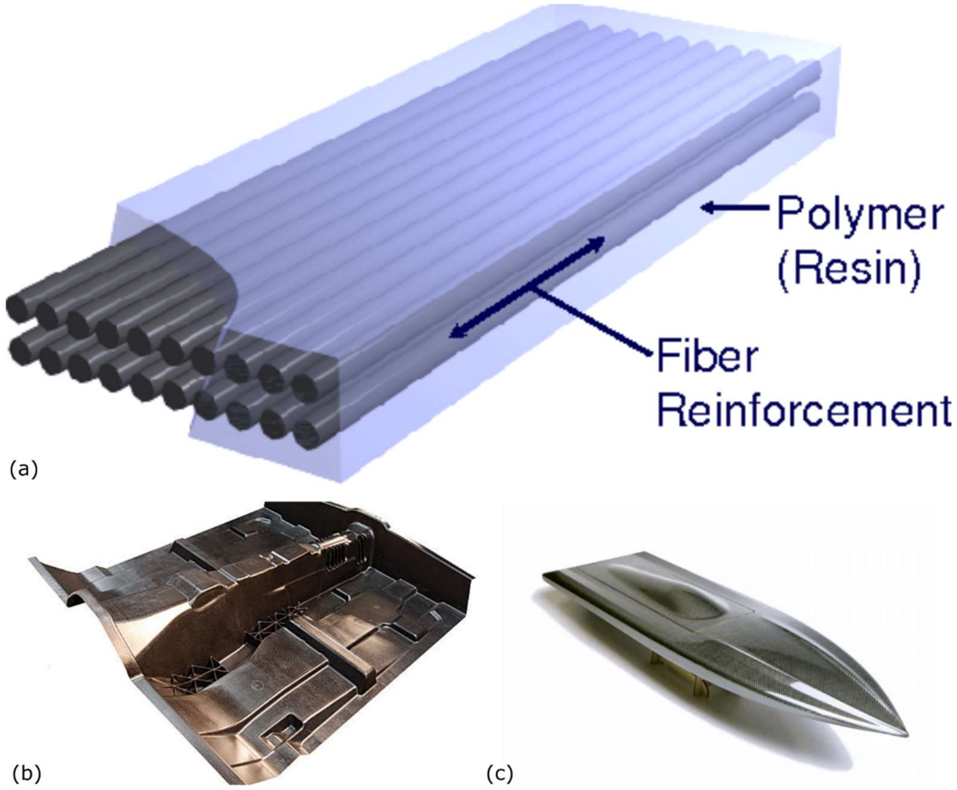

Figure 2.1: (a) Diagram of unidirectional fibres embedded in matrix material. Adapted from [17] (b) press formed nylon carbon fibre car floorplate (United States Council for Automotive Research LLC) (c) carbon fibre boat hull

2.2.1 Thermoplastic Matrix

In a composite material, the fibre reinforcement is embedded in a matrix material. The matrix has the primary aim of adding structural integrity to the fibres and preventing relative displacement. Doing so allows the fibre reinforcement's high stiffness and strength to be fully utilised. Polymers are a common matrix choice. These are made of small repeating units (known as monomers) which form long interwoven chains. Polymers are produced when monomers are exposed to some combination of high temperature, high pressure and a catalyst. For example, the nylon 6 used in this thesis is commonly produced by exposing the monomer caprolactam to temperatures of ~260 °C in an atmosphere of nitrogen gas. This formed epsilon-aminocaproic acid which can be condensed in a high temperature vacuum to produce nylon-6 [18]. Polymers can take the form of thermosetting and thermoplastic polymers. Thermosetting polymers such as epoxy undergo an irreversible curing process under exposure to heat, high pressure or a catalyst. This curing process creates strong chemical bonds between polymer chains creating a hard solid which cannot be easily reshaped; however, they can be degraded at very high temperatures (T_d) [19].

Thermoplastics consist of long polymer chains with high molecular weight. The polymer chains of thermoplastic polymers are joined by intermolecular forces (secondary or physical bonds) such as van der Waals interactions or hydrogen bonding [20]. High temperatures can weaken and eventually overcome the intermolecular bonds which transforms the thermoplastic from a semi-crystalline or amorphous solid at low temperatures, to a liquid at higher temperatures. Thermoplastics exhibit a glass transition temperature (T_g) above which the van der Waals interactions holding the amorphous phase together are overcome by increasing thermal energy and a melt temperature (T_m) where any crystalline structure begins to break down. During the cooling process, physical bonds are reset, and the crystal structure may reform. This enables repeated reforming through heat treatment. Typical variations in stiffness with temperature in both thermoplastic and thermosetting polymers are shown Fig. 2.2.

In the liquid state, the viscosity (a measure of resistance against flow) decreases with increasing temperature. Viscosity is a crucial factor in the quality of a final part as it determines the ease with which the matrix material can impregnate the fibres [14] as well as influencing the ease of forming complex shapes. Matrix materials need to fully wet the fibres during the forming process and a high viscosity makes this difficult. Thermoplastics have a high viscosity compared with uncured thermosets (e.g., PA6 has a viscosity of ~200 Pa.s at 250 °C [21] vs ~1 Pa.s for uncured Epoxy [22]). It is therefore common for thermoplastic composites to be pre-impregnated and pre-consolidated before forming to reduce void content. Methods include comingling thermoplastic and fibre yarns, use of film stacking (alternating polymer and fibre laminate sheets), or by infusing a low viscosity monomer which is then polymerised in situ. In situ polymerisation is promising as the lower viscosity monomers can aid the forming of complex geometries. However not all polymers are suited to in situ polymerisation due to the polymerisation process conditions required (temperature, pressure, catalysts). The process can also leave residual stresses (due to thermal gradients or crystallisation kinetics), high void content or unreacted monomers in the component all of which can have negative effects on the mechanical properties [23].

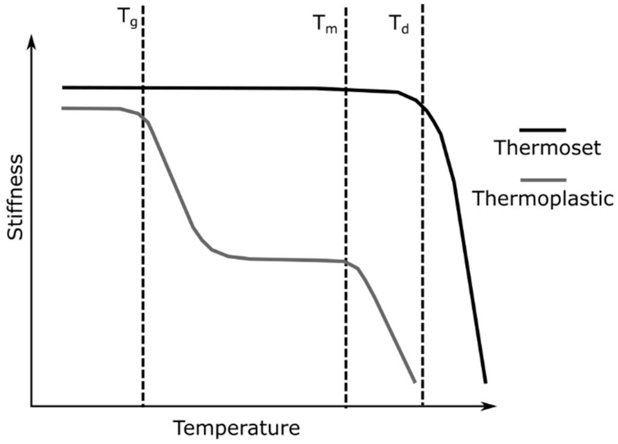

Figure 2.2: Example stiffness behaviour of thermoplastic and thermoset polymers. T_g = glass transition temperature, T_m=melt temperature, T_d=degradation temperature.

2.2.2 Fibre Reinforcement

Fibre reinforcements are made from individual fibres bound together into yarns or tows before being combined into individual sheets (plies), then multiple sheets can be combined to create laminates. Common fibre choices are glass or carbon fibres, but a variety of materials find use including aramid [24] or basalt [25] in addition to self-reinforced composites that use similar fibre and matrix materials [26]. Fibres offer high stiffness and strength axially along the fibre, but low strength and stiffness under transverse loading. This can be seen In Fig. 2.3 which shows the influence of loading angle on tensile strength for a unidirectional polypropylene fibre reinforced polypropylene composite. A strength drop-off of over 90 % can be seen when comparing specimens orientated parallel to the applied force compared with specimens orientated perpendicular to the applied force.

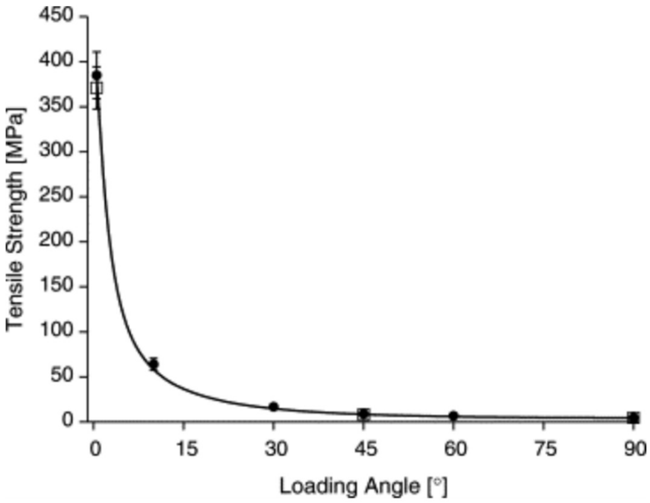

Figure 2.3. Plot showing tensile strength of unidirectional polypropylene matrix-fibre composite with varying loading angle. Figure adapted from [27].

This thesis examines the forming of thermoplastics reinforced with biaxial cross-ply carbon fibres, so a brief overview of the manufacturing process of carbon fibres will be given. A more general overview of fibre manufacturing and treatment can be found in [28]. Carbon fibres can be produced from several different precursor materials with the most common being polyacrylonitrile [29]. The specifics vary but the general process remains the same for all processes. First the polymer is spun into a multifilament fibre. This filament 'tow' is then oxidised at temperatures between 200-400 °C for approximately two hours. The fibre is then carbonised at temperatures of 1000-1700 °C in an inert atmosphere. This removes any hydrogen, nitrogen, or other impurities from the fibre, leaving it with a modulus of ~200 GPa. Exposure to heat leads to increased alignment of the carbon crystal structure which increases the stiffness of the fibre. Some fibres are then further heat treated at temperatures of ~3000 °C to increase their strength further [30].

Continuous fibre reinforcements in composite parts allow for high stiffness and strength in the directions of the fibres. The reinforcements are formed in a variety of ways, including weaving, and braiding of textile fabrics as well as tape laying of unidirectional reinforcements. Fig. 2.4 shows some examples of these, with Fig. 2.4a showing a unidirectional ply with white cross stitching to hold the fibres in place. Fig. 2.4b shows a biaxial [+/-45] non crimp fabric, and Fig 2.4c shows a biaxial [0/90] twill weave. Short fibre alternatives are easier to process however offer lower stiffness and strength than long fibre reinforced composites [31]. Unidirectional tapes can be formed into multiaxial composites by using automated tape laying machines to lay up multiple layers of unidirectional tape either before a separate consolidation process or as part of a single process whereby the tape layer also heats and locally bonds the parts [32]. This can be used to create simple flat sheets or used to precisely control fibre orientation in larger parts [32].

In general, there are trade-offs between the maximum strength or stiffness of the reinforcement and the ratio of strength in the major and minor axis. This can be seen in Fig. 2.5 where the tensile stiffness of several knitted (BSS, BT2, BD), woven and mat reinforced glass-epoxy composites is shown. The vertical axis refers to the warp direction and the horizontal axis to the weft direction. The woven textiles offer the highest performance in the axial directions, but the performance drops significantly at +/- 45 °. Knitted fabrics, on the other hand, offer lower but constant stiffnesses. As shown in Fig. 2.3, unidirectional fibres offer higher strength and stiffness in the primary orientation but have a much sharper drop off in the non-primary orientations.

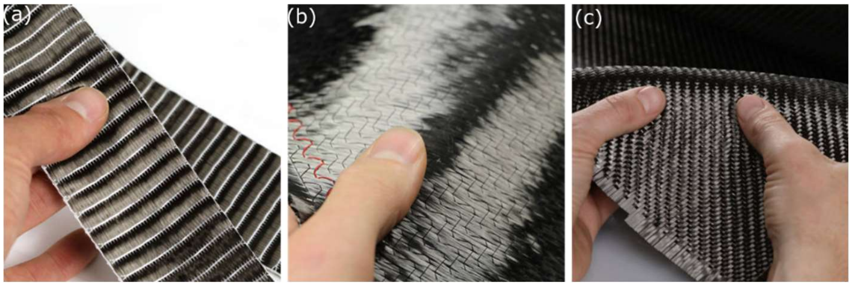

Figure 2.4: Diagram of different carbon fibre reinforcements (a) unidirectional tape with transverse stitching (b) biaxial non crimp fabric with +/- 45° layers (c) twill weave with 0/90 layup. Images sourced from Easy Composites [33].

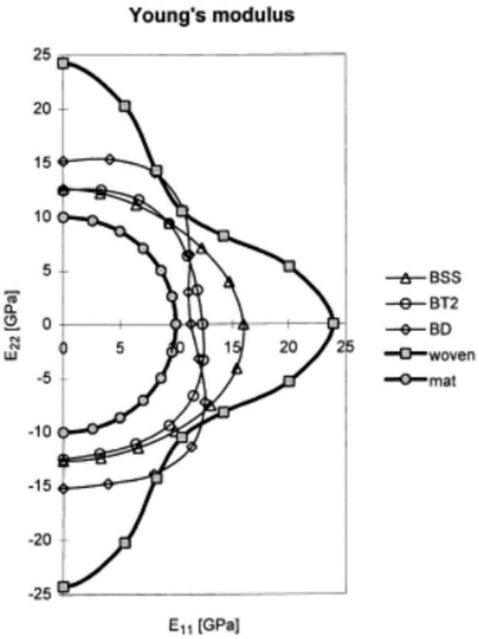

Figure 2.5: Polar plot showing stiffness of a variety of glass fibre reinforced epoxy composites from tensile tests with samples at varying orientations. BSS, BT2, BD are knitted fabric composites (Adapted from [34])

Another factor to note is the adhesion between the fibre and the matrix. This does not directly affect the forming properties but can affect the mechanical properties of the final part. Carbon-fibres often show low adhesion to the matrix material as the surface of a pristine carbon fibre is nonpolar and does not interact well with the (generally) polar molecular chains of polymer matrices [35]. This can lead to fibre pull-out and early delamination in the part and several avenues have been explored to improve this. Reducing the level of graphite in the fibre by extending the exposure to the gas feedstock in manufacturing the fibre, as well as partially oxidising the fibre to increase surface roughness has been successful [36]. However excessive oxidation damages the fibre negatively influencing the tensile properties of the composite. Other solutions include coating the fibre in a variety of polymer materials. Liu et al. used an epoxy emulsifier which coated the fibre surface and improved interfacial shear strength by 70% in an epoxy-carbon fibre composite [37]. Use of graphene oxide coatings have also shown good improvements in carbon-epoxy composites where interlaminar shear strength improved by 47%, and electrical conductivity improved by up to 127% [38]. Other techniques including metal coating of fibres (via electroplating), oxidation via exposure to ozone or plasma have been shown to have a positive influence on interfacial adhesion and improve fibre dispersion within a laminate. For nylon–carbon fibre interfaces, common surface treatments use nitric acid or involve oxidation at high temperatures. The oxidised graphite surface of a fibre can facilitate chemical bonding with nylon which enhances interfacial strength [39]. Appropriate surface treatments can also increase crystallisation rates and increase nucleation density in the nylon matrix [40]. A good summary of recent advances can be found in [35]. The experiments in this thesis introduce inclusions of tin into the final component and as such the bonding between the nylon matrix, carbon fibre reinforcement, and tin inclusions will be important to the final component. No literature on tin-nylon bonding was found, however some studies have identified that hygrothermal conditioning (removing moisture from the polymer) can reduce the interlaminar shear strength in an aluminium-epoxy glass fibre composite [41].

2.3 Thermoforming of Fibre Reinforced Thermoplastic Composites

Several methods exist for the manufacturing of composite parts. Factors such as reinforcement type, production volume, desired speed of production and required part quality all come into consideration when choosing a process. For short fibre reinforced composites, traditional thermoplastic processing methods such as injection moulding can be used. However, the nature of continuous fibre reinforcement introduces complexity as the fibres must conform to the desired shape. This often happens through draping mechanisms in thermoforming processes. There are two key factors that must be considered in the thermoforming process. First is the consolidation of the part, ensuring that there are no voids in the matrix, and the fibres are fully wetted by matrix material. Second is ensuring good conformation to the desired geometry.

Thermoplastic resins have a higher viscosity than uncured thermoset resins making them poorly suited to vacuum infusion processes however it is possible to infuse with monomers and polymerise in-situ [42]. In some cases, pliable commingled textiles are draped into shape before being heated to melt the polymer and consolidated under pressure to remove excess air. In other cases, pre-impregnated and pre-consolidated sheets can be heated under radiant or convection heaters before being shuttled to a press and stamped between male and female tooling. The cooled part can then be extracted for post processing or trimming.

Fig. 2.6 shows the general press forming process. A pre-consolidated or comingled composite is held by a blank holder and heated under an infrared or convection heater. It is then shuttled to a press where the part is consolidated between male and female tools. The male and female tooling can be a rigid body (i.e., steel) or a deformable body such as a high temperature rubber. Use of deformable bodies leads to a more homogenous pressure distribution but is more vulnerable to damage to the tool and increases cooling times.

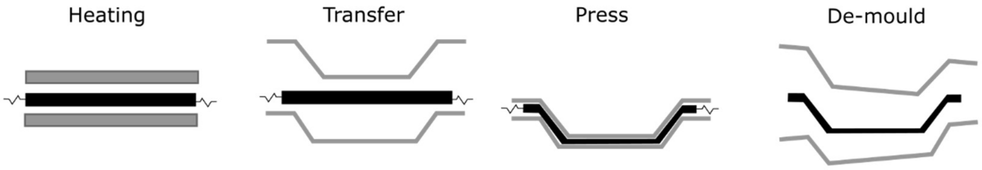

Figure 2.6: Press forming process. Part is first heated under infrared heater, then transferred to press, press formed into shape before being demoulded after cooling.

The blank holder supports the fibre-matrix layup (blank) during the heating and forming process. Blank holders often take the form of solid rings which apply pressure to the sheets as shown in Fig. 2.7a. They are designed to add tensile forces to the sheet via friction which counteract compressive forces which can trigger wrinkling in the part. The tensile forces must be balanced to allow some slippage otherwise rupture of the fibres may occur. The blank holder may use clamps to grip the blank or it may be held between two concentric rings or rollers. Careful design of a blank holder to apply membrane stresses can be used to reduce defects in the final part even when the draping requires high shear angles [43]. In some forming processes, the blank is supported by spring loaded clamps as shown in Fig. 2.7b. Use of springs can allow for greater control over applied tension than friction-based methods [44]. However, as the applied forces are anisotropic, it can lead to localised compressive forces and higher wrinkling relative to solid blank holders [45].

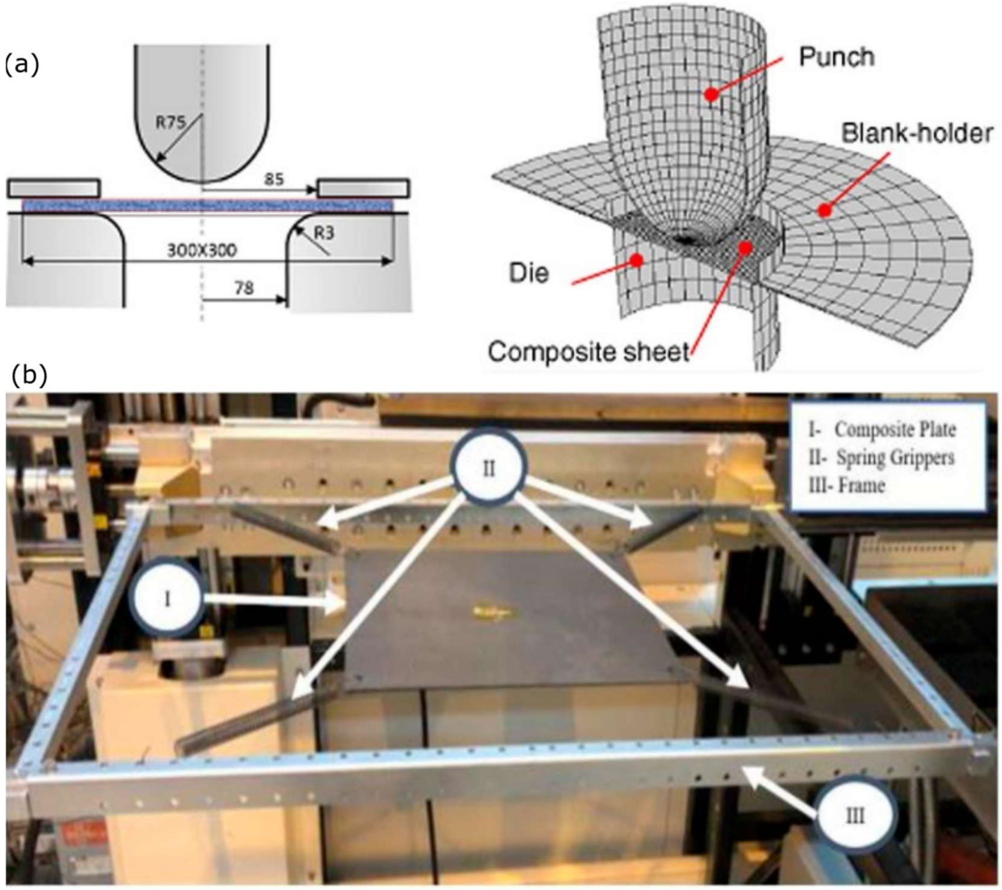

Figure 2.7: (a) Diagram of pressure based blank holder (Adapted from [46]). (b) Picture of composite plate with springs used to secure plate and add tension (Adapted from [47])

Diaphragm forming involves the addition of one or multiple diaphragm sheets to constrain the part and apply consolidation pressure via a vacuum. The application of external pressure through air, other fluid or rigid body tooling allows the blank to be deformed and adapt to the female tooling. Deformable diaphragm sheets can stretch during forming which improves consolidation quality by ensuring pressure is applied evenly. While the diaphragm itself can cause wrinkling at the contact points, overall, its presence ensures the full composite blank is kept under slight tension through friction with the diaphragm surface, reducing the chances of wrinkling by counteracting compressive stresses in the fibre [48].

More details on the mechanics of thermoforming are available in Section 2.5. In the experimental work for the present thesis, composites are formed between rigid die, male and female tooling. They are also secured by silicone rubber diaphragm sheets above and below the blank. Tension is applied to the diaphragm via a blank holder and a vacuum is applied to add consolidation pressure. This is discussed in more detail in Chapter 3.

2.4 Deformation Mechanics of Continuous Fibre Reinforced Composites

The thermoforming of complex shapes requires the fibre laminates to deform. The ability for fibre reinforcements to do this depends on various deformation mechanisms. The fibres themselves offer little potential for extension due to the high tensile stiffness and strength of the fibres, however, for woven fabrics, there may be a small amount of stretching due to fibre straightening (or woven fibres uncrimping) [49]. A key mechanism for intra-ply deformation is “trellis shear”. This occurs when fibres to rotate relative to each other. Fibres/tows can also experience in-plane bending, out of plane bending and torsion. Adjacent plies can also undergo inter-ply slip and rotation to relieve stresses. These mechanisms are shown in Fig. 2.8.

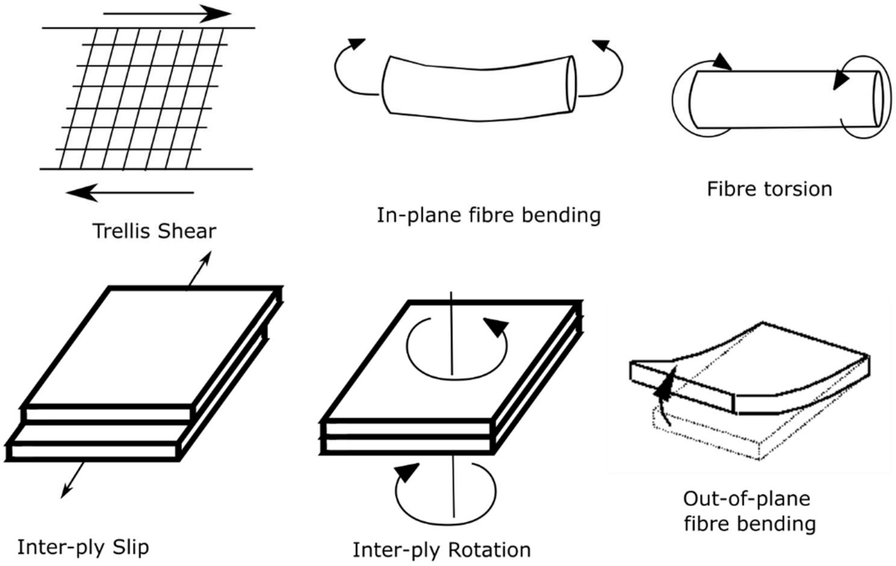

Figure 2.8: Deformation mechanisms for textile reinforcements

Experimental investigation and constitutive modelling of these deformation processes are an area of interest. Understanding of the limits around forming allows for part design to be optimised to avoid potential defects. Models have been developed which aim to identify areas of high stress (either tensile or compressive) or high trellis shear (which is a source of compressive stress). This literature review will have a brief discussion on intra-ply shear, before focusing on inter-ply slip which is the focus of the thesis. Numerical methods look to match the shear angle of fibres with resultant shear stress. These models are based on experimental characterisation, with Harrison et al. using uniaxial bias extension tests, cantilever bending tests, and picture frame tests to determine material properties [50]. Härtel et al. investigated methods for normalising the results of uniaxial bias extension tests to remove the influence of size on the relationship between shear force and shear angles [51].

2.4.1 Intra-ply Shear

Intra-ply shear occurs when adjacent tows rotate relative to each other, thus shearing the full sheet. At low shear, the resistance is dominated by frictional forces at the cross-over points between adjacent yarns [52]. However, at higher shear strains, the fibre yarns begin to compact laterally which restricts the ability for the fibres to continue rotating. As the rotation angle increases, the shear stress also increases. A common theory around this is the concept of a “locking angle” beyond which the shear stress rapidly increases. However, this point can be very subjective and the point at which shear stress rapidly increases depends on boundary and processing conditions [53], [54]. A typical stress-strain curve can be seen in Fig. 2.9.

Modelling of this has been carried out in Harrison et al. [55]. Experimental testing of this behaviour has been carried out using Picture Frame Tests [56] and Bias Extension Tests [57] both of which allow characterisation of the shear behaviour as in Fig. 2.9. Biaxial versions of the bias extension test have also been proposed [58]. Benchmarking of these tests has taken place showing that there is reasonable consistency between laboratories [59]. However, there are still potential sources of inconsistency, specifically the influence of clamping forces on the shear behaviour, the complications introduced by measurements at elevated temperatures and variability introduced by initial tensile preloading. Bias extension testing requires only a simple rectangular laminate with orthogonal plies and can be fast to set up. On the other hand Picture frame tests require a larger more complex test fixture, more complex specimen geometry and more involved test preparation. However well executed picture frame tests provide a more direct measurement of shear behaviour compared to the bias extension test which retains axial forces which must be considered in the interpretation [60]. As shear testing of thermoplastic composites can require elevated temperatures and the use of environmental chambers to melt the resin, the bias extension test is often preferred when analysing thermoplastic composites [61].

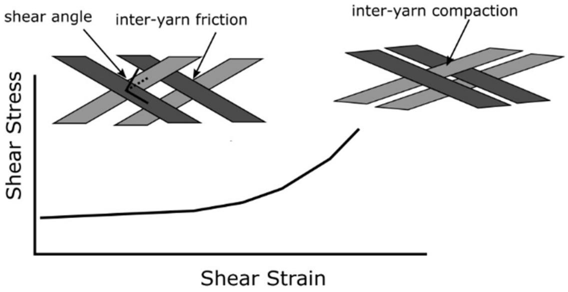

Figure 2.9: Representative shear stress as function of shear strain for inter-yarn shear. At low shear, resistance is due to inter-yarn friction, at higher shear angles the shear stress increases as yarns begin to compact. Adapted from [13]

2.4.2 Inter-ply Slip

Inter-ply slip is where adjacent reinforcing sheets move relative to each other. An example of where this is useful can be seen in Fig. 2.10, where the inner path of a concave shape is shorter than the outer path. This build up of stresses and strains at the end of a curved composite is referred to as bookending and can lead to failure. Slip then relieves compressive stresses on the inner plies. If the sheets cannot slide, then the plies on the inner surface are likely to buckle or wrinkle to relieve the stresses. This is referred to as ply-ply friction and is dominated by an interface of molten resin between the plies. Similar mechanics occur between the tool and the outer ply surfaces.

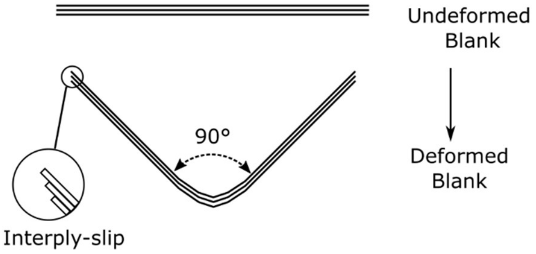

Figure 2.10: Inter-ply slip during deformation.

Constitutive equations are also able to accurately predict the locations and types of defects when thermoforming glass-polypropylene biaxial cross-ply composites [62]. Despite non-woven laminates being more likely to undergo slip, it was shown that inter-ply slip offers only a small contribution to the deformation mechanics. The modelling can also be further expanded by analysing factors such as the rheology of the matrix material, fibre volume fraction, and textile architecture [63]. This allows for temperature and rate dependency to be considered allowing development of a full understanding of the viscous behaviour which dominates thermoplastic forming.

When the intra-ply shear and inter-ply slip mechanics are not sufficient to allow enough deformation to form a geometry without creating large in-plane compressive stresses, composite sheets tend to continue deformation with out-of-plane buckling or wrinkling. This mechanism is undesirable as the wrinkles will firstly influence the aesthetic quality of the final part and, more crucially, they can reduce the mechanical performance of the part by introducing local stress concentrations and triggering premature delamination [64]. Evidence has shown that the presence of wrinkles frozen into a manufactured part can reduce strength by as much as 70% [65], [66]. Initial buckling occurs because of compressive stresses in the plane of the forming sheet [67]. The presence of the wrinkles also induces local stress concentrations when the formed part is under stress. These are influenced by factors such as the amplitude location and angle of wrinkles with several finite element models developed which can help predict this [64], [68]. It has been shown experimentally that the compressive forces peak at a low deflection before the buckling relieves the compressive stress in the fibre laminate [69]. Placing the part in a vacuum and applying atmospheric pressure through a diaphragm membrane can help reduce wrinkle initiation by creating tension, via friction, on the surface that resists buckling initiation [6].

Predicting and reducing wrinkling remains a topic of focus for researchers. This thesis looks to develop a solution for reducing inter-ply friction in cross-ply laminates and enhancing inter-ply slip with the hope of producing a step change in wrinkle reduction.

2.4.3 Stribeck Curve

Research by Gorczyca [7], [70] and Ten Thije [71], [72] have shown that the behaviour of the inter-ply region in composites can be characterised via a generalised Stribeck curve. The inter-ply region consists of two fibre layers separated by a molten thermoplastic boundary layer which acts to lubricate the sliding process. The generalised Stribeck curve describes friction coefficients between such lubricated surfaces and can be fundamentally broken into three regions. These are boundary lubrication, mixed lubrication and hydrodynamic lubrication. In boundary lubrication, asperities of the contact surfaces will touch. In hydrodynamic, the surfaces are fully separated by a lubricating fluid film. The mixed region acts as a transition between these two states. The Stribeck curve is a function of the Hersey number (H) which incorporates fluid viscosity (η), applied normal force (F_n) and sliding velocity (U) as:

$$H = \frac{\eta * U}{F_n} \tag{2.1}$$

The generalised shape of the Stribeck curve can be seen in Fig. 2.11. Friction coefficients are initially high due to contact between the surfaces in the boundary region. Friction coefficients then drop as the contact between surfaces reduces and the hydrodynamic boundary layer comes to dominate. The friction coefficient then tends to increase as the Hersey number increases further. Studies characterising the inter-ply and tool-ply behaviour in thermoplastic composites forming have shown that the friction can be characterised via a hydrodynamic boundary layer. An example can be seen in Fig. 2.12 (adapted from [70]) decreasing the Hersey number (in this case by decreasing velocity) also decreases friction coefficients (this can also be seen in Fig. 2.13). A similar effect can be seen when decreasing the Hersey number by decreasing viscosity or increasing normal pressure. This matches very well with the hydrodynamic region of the Hersey curve and (for most thermoplastic processing conditions) allows a linear relationship to be found between an approximated Hersey number and the friction coefficient.

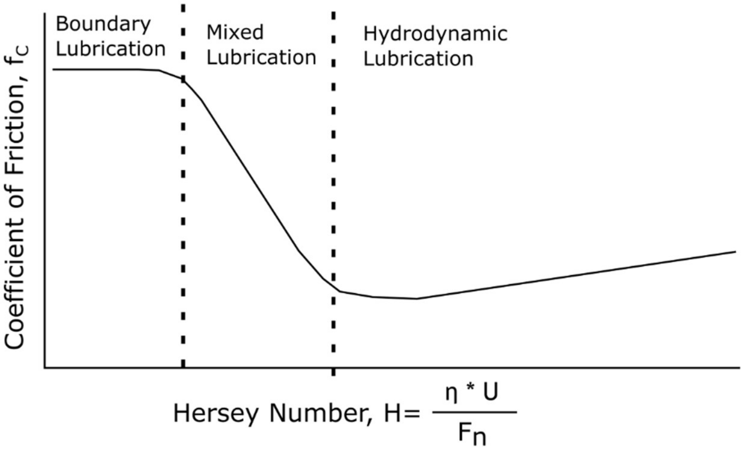

Figure 2.11: Theoretical Stribeck curve showing relationship between Hersey Number and friction coefficient for lubricated boundaries

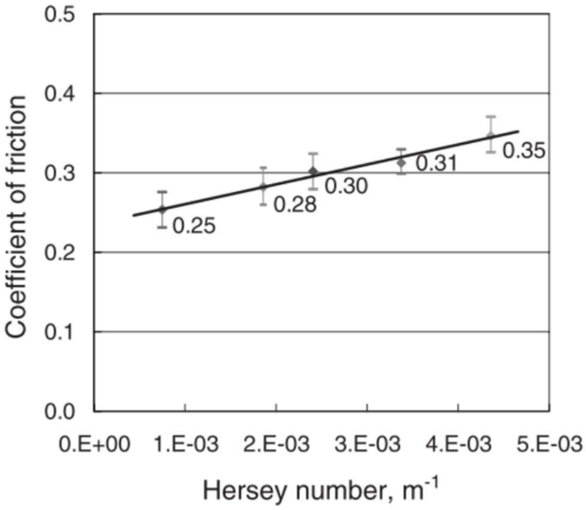

Figure 2.12: Coefficient of friction vs Hersey number for changing velocity in a commingled glass polypropylene woven fabric. Adapted from [70]

2.4.4 Dry Friction

Friction is a concern when forming dry fibre sheets (i.e., without a matrix material). This is useful in understanding the pre-forming of dry fibre reinforcements performed before vacuum infusion processes. Studying dry fibre friction also enables greater understanding of fibre-fibre and tool-fibre interactions. In the context of a Stribeck curve, this can be considered as unlubricated friction in the boundary region where contact between fibres dominates. These studies can be broken down into three scales: microscopic studies looking at behaviour within filaments, mesoscopic work looking at tow interactions and finally, macroscopic studies looking at interactions on a laminate scale. Investigation of contact between fibres and metallic tools has shown that the friction coefficients scale with pressure and physical contact area of the fibre [73], [74]. Analysis of the surface roughness in fibre tow-tool contact shows that the surface roughness has a strong influence [75]. Smoother surfaces can lead to a higher contact area and corresponding higher friction coefficients. However, this relationship does not hold at very high surface roughness as point contact between the fibre and the surface dominates. Analysis shows that real contact area can vary between different fibre architectures. The contact area is shown to increase as applied pressure increases. Comparison between unidirectional tows and non-crimp fibres shows that the tow-tool contact length for non-crimp fabric is ~67 % lower than a comparable unidirectional reinforcement [76]. For carbon fibre twill weaves, the real contact length can be as little as 4-8 % of the nominal length and resultant contact pressure 15,000 times higher than the nominal contact pressures [77]. Minimising contact between fibre reinforcements with interlayers is a good method for reducing the risk of high contact pressures which can damage tow structures and increase friction coefficients.

2.4.5 Viscous Friction

When thermoforming fibre reinforced thermoplastic composite sheets (i.e., with matrix material), inter-ply slip is driven by friction coefficients between neighbouring surfaces. This friction is dominated by the viscous behaviour of the molten thermoplastic matrix so fits in the hydrodynamic lubrication region of the Stribeck Curve. Testing these friction coefficients can be carried out through several methods. A simple method is the inclined plane method where a test specimen is placed on a horizontal surface. This horizontal surface is gradually inclined until the test specimen begins to slide. The friction coefficient (f_c) can then be calculated from the sliding angle (φ) from the equation:

$$f_c = \tan(\varphi) \tag{2.2}$$

To better model the processing conditions, a few similar test methods were developed. ASTM D 1894 [78] standard pull-out tests for determining friction coefficients for plastic films and sheets can be adapted for use with textile composite materials [79]. A schematic of a typical set up is shown in Fig. 2.13a. In simple terms, the pull-out force (F_p) required to move Specimen A from between two sheets of Specimen B when compressed under a normal load (F_n) is measured. The coulomb friction can then be calculated as follows

$$f_c = \frac{F_p}{F_n} \tag{2.3}$$

Representative results for this process for a steel-composite interface at a variety of pull-out rates can be seen in Fig. 2.13b (as adapted from [80]). An initial high peak force, representing the static friction coefficient, must be overcome before reaching a lower steady state dynamic friction coefficient. Static friction coefficients are generally higher than dynamic friction coefficients as there is a degree of microscopic interlocking between surfaces that must be overcome to initiate movement.

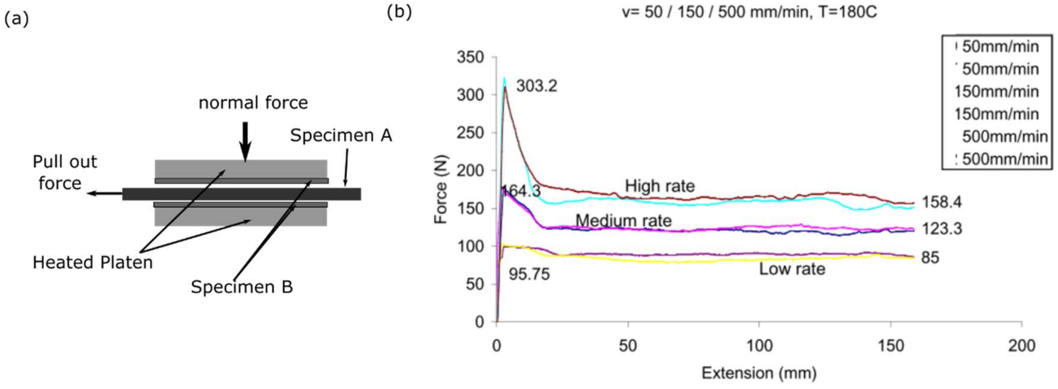

Figure 2.13: (a) example diagram of pull-out test. (b) representative force-extension curves for steel-composite interface at different pull-out speeds (adapted from [80])

Characterization by Murtagh et al [79], [81] suggested that the resistance to sliding at the interface of Carbon Fibre-PEEK composites varies based on normal pressure and viscous lubrication. It could then be represented via a power law of the following format.

$$\tau = \tau_0 + k * U^n \tag{2.4}$$

Where τ is the shear stress acting on the interface between plies and *U* is the velocity of sliding between adjacent Plies. τ_0 is the shear stress at zero velocity while *k* and *n* are process parameters which must be determined experimentally.

Work was then carried out which could relate *k* and *n* to process conditions such as temperature and pressure.

Friction coefficients in viscous composites (i.e., with a liquid matrix material) have been measured via pull-through and pull-out tests [7], [70], [71], [72]. Classic numerical models required the hydrodynamic interlayer thickness as an input to determine the viscosity terms. This is difficult to determine without experimental validation. Alternative methods by Harrison et al. assessed the friction coefficients via a custom test rig using a rheometer [82]. A model was developed which was able to predict the friction coefficients using temperature, pressure and sliding velocity. This removed the need for interlayer thickness as an input, simplifying the model.

To reduce defect formation and improve formability of thermoplastic composites, there is a desire to reduce inter-ply friction coefficients. One method of doing this is by lowering the Hersey number. Techniques such as increasing forming temperature (to lower interlayer viscosity), decreasing forming speed and increasing forming pressure can have positive influences on the ability to form wrinkle free geometries when forming composites with viscous interlayers that can be characterised as lubricated friction. As mentioned in the Introduction, the idea for lubrication is inspired by Vanclooster [10] who used layers of neat thermoplastic resin to lubricate the forming of glass reinforced polypropylene and found that increasing the interlayer thickness reduced the tendency to wrinkle[NO_PRINTED_FORM]. Other methods of lubrication include powders such as magnesium stearate which is used in the plastics industry to lubricate the motion of pellets (such as in plastics forming, or in drug manufacture[83]), aid in tool lubrication in moulding of plastics [84], and also used to reduce viscosity in the forming of polypropylene. Recent efforts have also included the use of liquid epoxy resin as a lubricant when forming non crimp fabrics [85], [86]. These have found a 64% reduction in fabric-fabric friction coefficient when comparing the sliding of the neat dry fabric and sliding with the lubricating epoxy interlayer, and evidenced that this reduced wrinkle formation. This agrees with the Stribeck curve described earlier in the chapter as the process moved from boundary to hydrodynamic lubrication. However this method would very likely leave residual epoxy resin within the composite which may be undesirable.

In this thesis liquid tin is used to lubricate the forming process of a carbon fibre reinforced nylon composite. Molten nylon has a viscosity of ~200 Pa.s at a temperature of 260 °C [9]. Molten Tin has a significantly lower viscosity at ~.02 Pa.s at 253 °C [8]. Both have similar melt temperatures (232 °C vs ~220 °C respectively) making them well suited. Molten tin also has a high surface tension (~550 mN/m at 230 °C [87]) making it unlikely to mix with the nylon matrix. This raises the possibility that tin could be used to lubricate the forming process and be removed from the laminate without leaving contaminating elements. The possibility of a lubricating interlayer while also removing contaminants motivated this choice.

2.5 Experimental Investigation of Thermoforming

Many studies and solutions have attempted to deal with the issue of unwanted wrinkling in fibre reinforced thermoplastic composites. This Section will cover some of them.

2.5.1 Matched Die Forming

Matched die forming was the subject of much early study [88]. Crucial factors identified were the need to maintain appropriate pressure and temperature throughout the consolidation period to ensure full consolidation and minimise void content. Uniform pressure distributions reduced squeeze flow and resultant fibre displacements. More recent work attempts to model and predict the way in which fibres reorientate during deformation and the influence that speed of forming can have on sheet temperatures [89]. Other factors to consider are lateral pressure on vertical walls to help to fully consolidate the matrix and remove void content and finally the influence cooling rate has on mechanical strength.

2.5.2 Diaphragm Forming

An example of an early diaphragm forming experiment can be seen in Fig. 2.14 as adapted from [90]. This forming experiment involved a stacked prepreg being placed between two rubber diaphragm sheets. The diaphragm sheets were secured by two clamping rings with a vacuum ring between the sheets ensuring a tight vacuum as seen in Fig. 2.14a. The bottom clamping ring was attached to a female mould base and pressure was applied to the upper surface by high pressure nitrogen as seen in Fig. 2.14b. This homogeneous consolidation pressure led to good quality parts however issues with the durability of the rubber diaphragm were noted. Numerous factors such as increasing diaphragm stiffness (to increase resistance to out of plane buckling), decreasing blank thickness (as the curving of thicker laminates leads to large differences in path length between inside and outside curvatures) and slowing the rate of forming (as the magnitude of compressive stresses depends on forming rate due to viscous effects) were shown to reduce wrinkling.

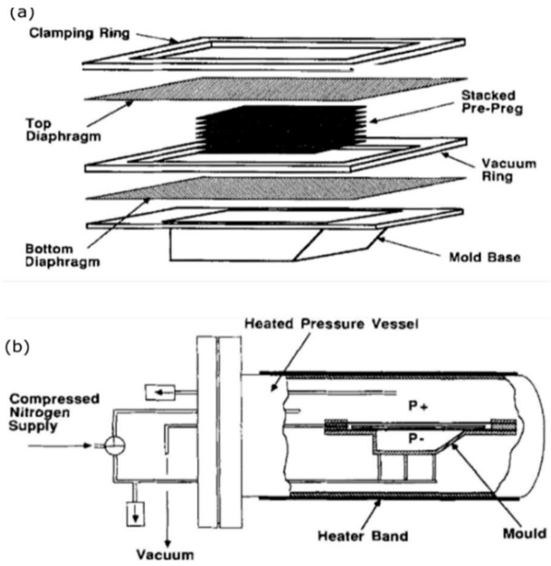

Figure 2.14: Example of diaphragm forming process. (a) exploded view of stacked prepreg, diaphragm sheet and mould (b) view of pressure chamber and heating apparatus. Adapted from [90].

Some experiments have shown that contact between the diaphragm and the matrix material can to be an issue [91]. Diaphragm material (Polyimide in this case) showed evidence of creep into gaps between fibres under high temperature and pressure, which was influenced by the stacking sequence [91]. Methods of automating and speeding up the diaphragm forming process via computer control were also successful in reducing the overall manufacturing time. Comparisons between diaphragm and matched die forming carried out by Krebs et al. [92] showed that, for the tested geometry, additional tensile stresses applied by the diaphragm helped limit the formation of wrinkling[92]. Nowacki et al. found that diaphragm forming allowed intra-ply rotation to occur more freely, which limiting wrinkle formation and that increasing diaphragm tension can counteract the compressive forces that initiate buckling was also shown in [93]. Other research has shown the potential benefits of different fabric styles, with knitted fabrics showing more ability to deform via loop stretching, and shown that while composites are likely to wrinkle at high shear angles, the shear angle is not the only consideration [94] as fibre slippage, interply slip and bending can alleviate stresses [111]. Other work by Prodromou et al. [95] has shown that, in multi-laminate layups, wrinkling initiated at lower deformation than in single laminate layups [95].

Studies have looked at using segmented blank-holders to vary the force applied to the blank in different segments, allowing for control over the fibre draw in rate which can reduce wrinkling. However, it is found that high normal forces applied by the blank holder, while suppressing wrinkling, can also lead to defects at the part edge [96], [97]. Further work has separated dry fibre multi-ply preforms with rigid aluminium interlayers [98]. These interlayer rings have large holes which allow forming around the central mould, but hold laminate layers apart at the edges, reducing friction coefficients and allowing more efficient draw-in of the laminate. However, while successful with dry fibre reinforcements this is less applicable to pre-impregnated composites with a viscous matrix material.

2.5.3 Bridging and Tearing

Another factor for consideration when drawing in fibres to curved geometries is the risk of fibre bridging or tearing. Recent work on diaphragm forming, has shown that the low pressure can lead to fibre bridging in more complex geometries as the fibres can resist being pulled into cavities or recesses [99]. One solution is the insertion of localised darts (cuts in the fibre reinforcement) to reduce tensile stresses. For a multi-ply and multi-axial sheet, localised openings in a single ply could be covered by other, differently orientated plies. However, this process would have a negative influence on the final strength of the part so should be used away from primary load paths. Finite element models were able to identify suitable locations for darts by looking at textile shear angle, textile compressive strain and tensile strength in fibres [99]. Conversely if forming pressures are too high, then they can tear due to high frictional forces preventing fibre sliding [100]. To avoid these issues, multi-cavity geometries are often manufactured by hand layup with sequential forming operations [101]. This thesis hopes to address some of these issues by reducing interlaminar friction and allowing greater ply-ply displacement.

2.5.4 Wrinkling

Some studies of curved laminates differentiate between global and local buckling. Global buckling often occurs because of the inside paths of curved shapes have a shorter path length, leading to excess material. If plies cannot easily slide relative to each other local buckling can then occur because of local compressive stresses [102]. This is shown in Fig. 2.15, which shows buckling in the plies on the internal face of the curved shape when deforming a stack of 10 carbon fabric plies. There is symmetrical bending in Fig. 2.15a, L-flange bending in Fig. 2.15b and bending after buckling in Fig. 2.15c.

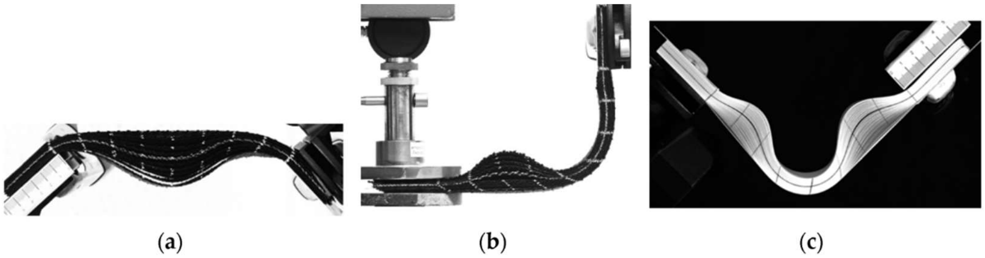

Figure 2.15: Laminate of 10 carbon fabric sheets bent in various configuration configurations, adapted from Huang et al. [103] (a) symmetrical bending (b) L-flange forming, (c) bending after buckling

Other studies have identified evidence of "micro buckling" where in-plane compaction allows tows to deform and conform to a 3D curvature [55]. Manipulating the order of forming using fibre steering techniques can also mitigate draw-in and reduce wrinkling [104]. Further studies showed some improvements to the wrinkling mechanics were found by lowering friction locally or reducing the number of challenging orientation interfaces, but complete avoidance of wrinkling was only possible by removing the challenging interfaces [105].

Challenging interfaces are generally non-orthogonal (I.e., 90/45 instead of 0/90). Intra-ply shear is a key deformation mechanism and relies on plies rotating relative to each other as discussed in Section 2.4. When adjacent plies are in non-orthogonal orientations at the start of the forming process, the ability to conform to the desired geometry is limited by interactions between laminates. As a result, non-orthogonal lay ups generate higher inter-ply shear and compressive stresses leading to earlier wrinkling [102], [106]. This process is exacerbated by additional plies in the laminate as shown with Prodromou et al. [95], and separation of the layers with active metal sheets away from regions experiencing deformation can reduce wrinkling as shown by Nezami et al. [98].

Vanclooster has shown that increasing the thickness of the viscous interlayer can reduce the tendency to wrinkle when forming glass fibre reinforced polypropylene [107]. As a result of the thicker interlayer, adjacent non orthogonal plies act more independent which reduces compressive stresses caused by intra-ply shear in neighbouring plies, reducing wrinkling. Vanclooster increased the interlayer thickness by inserting thin sheets of lower viscosity neat thermoplastic between pre-impregnated polypropylene-glass fibre laminates [10]. This lubricated the tangential slip, reduced the interaction between neighbouring plies and improved the formability of the setup. On the other hand, it also lowered the fibre volume fraction from ~35 % to ~14 % when comparing no interlayer and interlayers of 1.5 mm, respectively. This would have a negative influence on the specific properties of the final part so a solution which could lubricate the forming process while maintaining a high fibre volume fraction would be desirable. This idea of using low viscosity interlayers to separate adjacent plies acts as an inspiration for the present thesis.

Forming complex geometries with multiple non orthogonal plies remains a challenge despite many proposed solutions. Given the significant influence that fibre orientation has on the material properties of a resultant part, there is a strong need to explore other practical solutions to the problem. In Chapter 3, a multi-step thermoforming solution using a low viscosity metal interlayer is proposed and developed.

2.6 Numerical Investigation of Thermoforming

Experimental investigation of the thermoforming process is a crucial component of improving the process, however it can be expensive and time consuming to carry out tests and optimise the process through parametric studies. Numerical simulations then offer an ideal solution to allow for exploration of a variety of forming parameters and reduce costly experimental or manufacturing errors. Several predictive tools and simulation methods have been developed over the years to predict textile forming and wrinkle formation.

2.6.1 Kinematic Methods

Kinematic methods of analysing draped fabric were developed in the 1950's when studies into the differential equations of fitting a woven fibre reinforcement to a surface were developed by Mack and Taylor [108]. It acted as an early contribution to "cloth geometry" and concluded that general solutions would not be possible without arbitrary functions. These were built on by Heisey with mapping algorithms that treat the warp/weft intersections as pivot points with constant curvature between intersections [109]. The warp threads are modelled as straight lines between adjacent intersections (geodesic) and this extension allows non algorithmic surfaces to be described, providing they were continuously differentiable. Heisey hoped his work would act as a contribution towards Toffler's dream of computer automated perfectly fitted garments [110]. Sadly, much work remains to be done to achieve this dream, but the principle of the "fishnet" style modelling of textile deformation continues to be used.

Looking more specifically at modelling of composites, these basic kinematic models were built on in several ways. Long et al. developed an iterative procedure which used a geometric model for woven fibre preforms [111]. The model is used to calculate total shear strain energy for a given fibre architecture over a given mould and, by minimising the shear strain energy, can generate realistic drape patterns for hemispheric moulds. This was further built on to allow boundary conditions such as friction between laminate and blank holder to be considered allowing the press forming of fibre reinforced composites to be modelled [112].

Kinematic models can also be applied in reverse to generate formable geometries from formable drapes [101]. Such work uses a pin jointed net assumption and relies upon choosing two yarn paths across a surface. The work identified the useful curve glide geometries which are shapes which can be defined in 3D space when one curve glides along another curve to form a surface. Such curve glide patterns can be repeated to form tessellated structural core materials. While this is useful, reverse modelling drapable shapes is not always applicable as product needs are often driven by a desired shape. This method was expanded to allow the development of manufacturing instructions which could guide layup processes and increase the speed and accuracy of forming complex geometries [113].

Geometric drape analysis is fast and can be applied to complex geometries. They produce shear angles which can be compared with known fibre behaviour allowing for reasonable estimates of the formability of a geometry. However, the process does not consider the mechanical properties of the fibre reinforcement or process parameters such as friction or other constraints. It also requires defining a definite start point and initial vector directions and in real forming problems these are likely to vary. This makes them appropriate for simple problems, but they may struggle with asymmetric forming or boundary conditions mimicking more complex forming conditions.

2.6.2 Finite Element Methods

The alternative is to use finite element methods to simulate mechanical models which better represent the forces and boundary conditions involved in the forming process. Finite element models break large problems into small sub regions which are interconnected via appropriate boundary conditions. The complexity means these models are usually solved using explicit solution methods and they can be quite computationally expensive. A constitutive model for the material behaviour is required to accurately represent the anisotropic behaviour of the fibre reinforced composites. It is also necessary to track fibre orientations to predict stresses, help validate the simulation and allow for comparison with experimentally known fibre behaviour. Another method is to model the yarns with beams or truss elements and to place springs at the intersection points. This automatically tracks the fibre orientation and allows for accurate representation of several different textile properties. An alternative method is to use an anisotropic material with membrane or shell elements to represent the fibre behaviour. This method also requires tracking of the fibre orientation to ensure accurate modelling of the textile behaviour. Given the high computational requirements and relatively long (1-10 seconds) timeframe for thermoforming processes, mass, and velocity scaling are often used to speed up the simulation.

Examples of constitutive models for different fibre architectures can be found in the literature, with models being built for different forms of woven [114] or non-crimp fibres [115]. These models tend to approach the problem from a macro scale and use material properties gathered from experimental results of the chosen architecture. Non-orthogonal constitutive models allow the orientations of the fibres to be continuously updated and for the behaviour of the textile to be updated with the changing orientations. These models can be enhanced by combining them with beam or truss elements which help in modelling both out-of-plane and in-plane bending stiffness [116]. The beam or truss elements share nodes with the corners of the membrane or shell elements. By giving the beam or truss elements different properties from the membrane or shell elements, more parameters involved in composite forming behaviour can be independently controlled (such as of fibre bending and trellis shear). Representation of out-of-plane bending in composites remains an area of difficulty as the bending mechanisms do not result in matched compressive and tensile strains as would happen in a solid material. In practice, bending occurs because of slipping between fibres. A review of recent work on this phenomenon can be found in [117]. Another mechanism of concern is in-plane fibre bending. Observations show gradual changes in fibre directions which have been modelled to some success by looking at second gradient strain energies [118], [119].

Models can be extended to represent multi-ply laminates and can accurately model interactions between adjacent plies. For example, Ten Thije et al. modelled a multi-layer laminate simulated with shell elements which simulated the bending mechanics of the fibre laminate [120]. Friction is modelled via thin film lubrication and appropriate coefficients are obtained from tool-ply and ply-

ply friction experiments, and the inter-ply shear behaviour is based on bias extension test results. Other inter-ply slip models involving thermal and viscous effects have been developed and can be applied to finite element code [121]. Sjolander et al. [122] were able to model hot drape thermoforming with multiple plies and show that wrinkling often occurred because of interaction between adjacent plies. It was possible to match wrinkling in experiments with transverse strains on convex surfaces in the simulation. Changing the stacking order or cutting some layers helped relieve stress.

Another method used mutually constrained shell and membrane elements sharing the same nodes [6]. In this setup, the shell elements model the out of plane bending behaviour and the membrane elements model the in-plane behaviour. The membrane elements have no intrinsic bending stiffness and are assigned the tensile and nonlinear shear stiffnesses of the fibre reinforcement. The shell elements on the other hand are assigned zero shear rigidity and a young's modulus equivalent to the flexural stiffness. This decouples the high tensile stiffness and low flexural stiffness of the fibres. This method was able to model double diaphragm forming of a pyramid surface and capture the wrinkling effects caused by high bending strains in the fibre laminates which are then trapped by the normal applied pressure. More recent developments have attempted to address the high computational time required to accurately model the full part by using a simplified membrane model to identify potential problem areas. This is then followed by local sub models with shell elements and appropriate boundary conditions that can more accurately predict the behaviour and resulting wrinkles at these problem areas [123]. Potential risk areas can be identified by factors such as nodal distance between the meshes of the laminate and the tool as well as fibre shear angles. This method was able to reduce simulation times to 13 % compared with using the detailed model for the full part. Similar models have been used to model the draping process and therefore predict the crushing behaviour and fracture mechanics of the resulting deformed composite part [124].

Numerical models offer good approximations of the behaviour of composites under typical thermoforming conditions. Prediction of defects and optimisation of part design can be carried out without expensive experimental testing.

However, the full complexities of the anisotropic behaviour of the textile reinforcements remain difficult to model. Long computational times also remain an issue. In Chapter 6, a combined beam-membrane constitutive model [116] will be used to investigate a multi-step thermoforming process.

2.7 Heating methods in Thermoforming Processes

Several methods for the heating of thermoplastic composites have been developed and a brief overview of these methods can be found in [125]. The most common form of heating in the commercial thermoforming processes is thermal and radiant curing using radiant heaters and ovens [125]. These processes are mature and well understood, but still have limitations because of their surface heating mechanisms and the poor conductivity of polymers leading to long cycle times when forming thicker parts (I.e., Nylon has a thermal conductivity of ~0.24 W m^{-1} K^{-1} [126] and 304L Stainless Steel has a thermal conductivity of ~ 14 W m^{-1} K^{-1} [127], both at room temperature). A summary of these methods and other potential alternatives will be given in this Section.

Convective and conductive methods rely on heat transfer using hot gasses or liquids which pass over the surface of the composite. The simplest example of this uses an oven or autoclave to heat the surrounding air. This heats the surface of the composite layups and conduction through the thickness of the part transfers this heat through the full volume. Rapid, homogenous heating of larger parts is made difficult by the low thermal conductivity of thermoplastic polymers, so energy transfer rates are lower. Some advantages of autoclaves or ovens are that they are very well understood technology, easy to scale, relatively cheap to build and operate and as such they are used frequently [125]. Other methods can include the use of hot gas flames, lasers, or torches which allow heat to be applied to specific locations, thus can be suitable for welding or tow placement processes [128].

One alternative is the use of electromagnetic radiation (I.e., microwave or infrared). The energy in electromagnetic waves is converted into heat by inciting molecular vibrations in matter. Infrared radiation has strong resonance vibration with the polymer molecules and the energy is mostly transferred at the material surface. As a result of this, the intensity of the energy must be balanced with the ability for the heat to transfer through the thickness of the material and away from the surface. Microwave radiation has a lower energy and longer wavelength and penetrates deeper into the surface of the material. This allows for volumetric heating. The heating depends strongly on the properties of the fibre. It is effective for pure polymer materials, as well as glass fibre or aramid fibre reinforced composites [129]. However, carbon fibres have a high dielectric loss, making them effective reflectors of microwave radiation. This reduces the effectiveness of volumetric heating of carbon fibre composites using microwaves. Furthermore, the high conductivity can lead to localised areas of elevated temperature and electrical arcing between fibres [130]. Infrared heating is commonly used due to it's simplicity and low cost, however recent studies have shown that volumetric microwave heating can reduce cure time by 57.9% and energy use by 24.1% when compared with thermal curing in an oven [131] so it may see greater use as the technology matures.

Ultrasonic heating is sometimes used in thermoplastic welding. This method converts mechanical vibrations to heat via internal frictional and visco-elastic effects [132]. However, when applied to parts with high fibre volume content it can be damaging to fibre architecture. The process also requires a solid medium and strong surface to surface contact to transfer the energy meaning it is rarely used for consolidation and heating of full blanks but is instead used for spot heating or welding.

Resistive heating works by passing an electrical current through the part. Electrical current passed through a conductor will generate heat proportional to the square of current applied and the resistance of the conductor. This is attractive for use in spot welding or bonding by using a metal susceptor such as a metal plate or mesh which can be used to heat a part. Additionally, the conductivity of carbon fibres means the fibres themselves can be used to generate heat. This process can be used to heat composites with lower energy use relative to comparable autoclave or ovens [133]. On the other hand, the requirement for direct contact between fibres makes managing this process difficult especially for larger components, so it is not commonly used for preheating of blanks [125].

Another method of interest is the use of induction heating. Like resistive heating, it exploits the generation of heat via resistive losses when a current is passed through a conductor. However, induction heating uses an alternating magnetic field to induce eddy currents in the conductive material. Glass or Aramid fibre components can be heated using metallic susceptor materials. Carbon fibres are electrically conductive so eddy currents will form in the fibres themselves allowing for volumetric heating. Heat generation in these is caused by resistive loss along the length of the fibre and heating at the fibre junctions. If the fibres are not in contact at the junctions, then the dielectric properties of the matrix become significant, and the junction can be modelled as a resistor and a capacitor in parallel. If the fibres are in contact at the junctions, then the contact resistance is the predominate factor. These are shown diagrammatically in Fig. 2.16. Testing has shown that the interactions at the junctions are the key source of heat generation and that contact between fibres allows for more efficient heating [134].

Induction coils are sometimes used for localised heating of small areas in induction welding processes [135] or in local thermoforming of small sections of components [136]. Other methods suggest the use of induction heating of a steel mould to allow for greater control over mould temperature in thermoforming processes [137]. The process allows for volumetric heating, but this requires well distributed susceptors. Induction, ultrasonic and resistance heating is primarily restricted to welds rather than of full components. One study has shown that of the three, induction welding offers the lowest energy use due to it’s fast processing time, but induction heating also had the highest power requirements [138]. It also showed that resistance welding offered a weaker bond than induction or ultrasonic welding, with an approximately 15% drop in lap shear strength.

This thesis proposes placing a large susceptor (sheets of tin) within a thermoplastic composite and removing it during the forming process. Thus allowing an induction heating process to volumetrically heat a metal-composite hybrid layup in a prototype thermoforming process. This is also compared with a radiant heating process. The specific processes are discussed further in Chapter 3.

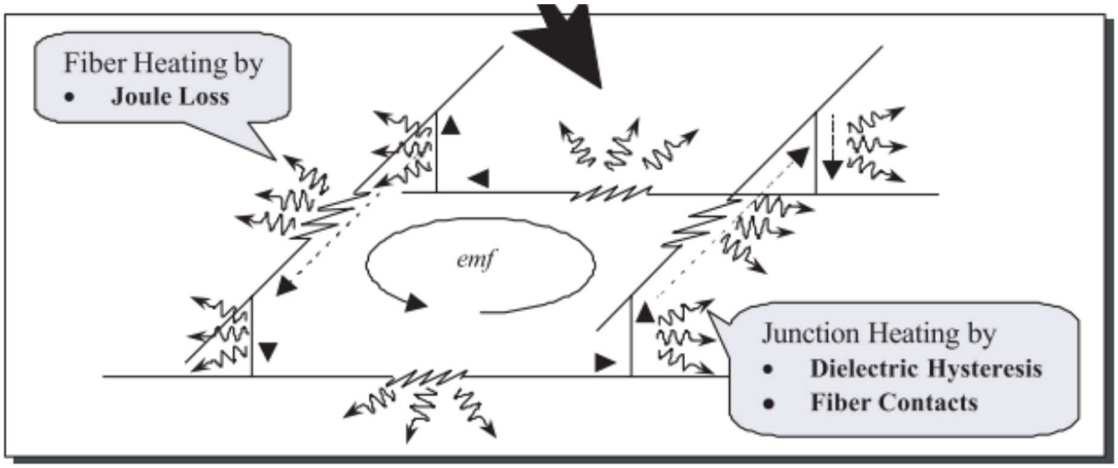

Figure 2.16. Potential mechanisms for heating during inductive heating of a carbon fibre composite. Adapted from [134]

2.8 Failure in Composites

Understanding failure mechanics is a key component of designing and manufacturing fibre reinforced thermoplastic parts. Defects such as wrinkles or unwanted voids or inclusions in the body of the part change the failure behaviour. The project undertaken in this thesis aims to reduce wrinkling, however the process may introduce unwanted defects between laminates. Understanding the influence this may have on failure is important.

Due to the anisotropic and heterogeneous qualities of fibre reinforced thermoplastic composites, their failure behaviour is complex and direction dependent. They also depend on the interaction of the matrix and the fibres. A recent review concluded that the anisotropic nature of composites leads to more complex failure mechanics than for metallic materials and that materials, structures, and failure modes are linked [139]. Several standardised tests have been developed which focus on three modes of loading: compression, tension, and shear. It is also possible to test for individual fibre and matrix properties. Preparation of the sample for specimens is crucial as specimens often experience stress concentrations at loading grips and the cut edges can generate raised stress levels. A discussion of these tests and references to relevant standards can be found in [13].

Several failure criteria have been developed over the years to help characterise behaviour under load. The simplest are the non-interactive theories which assume stress and strain states do not interact and simply states a maximum stress, or maximum strain which will lead to the laminate failing. While being simple to apply, these criteria do not address coupling effects between different stress and strain components, and so, are not particularly useful for multi-axial loading. Interactive failure models such as the Tsai-Wu failure criteria have been developed which take into effect the coupling between multi-axial loading and varying strengths in compression or tension [140]. However, these still primarily look at in-plane stresses and do not address out of plane stresses. Further developments have separated failure methods for fibres in tension and compression from matrix failure such as the Hashin and Sun failure criteria [141]. Other methods such as Puck's criterion have also been developed which consider out of plane forces acting at an angle and make attempts to predict the mode of failure [142].

Recent experimental work has looked to assess the influence that wrinkling has on the failure of composites. Hu et al. looked at wrinkles on the convex face of L-shaped laminates and showed that wrinkling triggered early inter-ply delamination and reduced strength by up to 30-40 % [64]. In other geometries this has been up to 70% [65], [66] . The amplitude and location of the wrinkles were also shown to be crucial factors. Nartey et al. looked at the influence of wrinkling caused by sheet overlap and found up to 37 % drop in strength while also being able to numerically model the influence of the severity of the wrinkle (via angle of deviation) to the resultant strength [4]. Other modelling work was able to more accurately predict both wrinkling and the influence wrinkling would have on part strength allowing for a more efficient design process and more efficient part design.

Interlaminar shear strength is another concern in the design of composites. This is the ability for adjacent layers to resist being pulled apart by shear forces. The existence of voids or defects between the fibre sheets that disrupt the matrix can have strong effects on the behaviour. Studies on carbon and glass fibre epoxy specimens used embedded PTFE tubes to create artificial, controllable voids [143]. These were then tested in a short beam shear setup to assess interlaminar shear strength. There was a strong tendency for failure to initiate at the voids (particularly in carbon/epoxy specimens). Further evidence showed that a reduction in effective cross sectional area caused by the presence of the voids also had a strong influence on reducing interlaminar shear strength by up to 11% when going from 0% to 8% porosity[144]. Other studies manufactured composite laminates with high, uncontrolled porosity showed that interlaminar shear strength decreased with increasing void content. There was also a high degree of scatter suggesting that shape and size of individual voids had an influence [144]. This shows that minimising and understanding the formation of defects is a key factor in designing efficient and safe composite components.

2.8.1 Modelling of failure in composites

No numerical modelling on the influence of tin inclusions on the strength and failure of nylon carbon composites was carried out in this thesis. However this Section will contain a brief investigation into potential methods that may be used to do so. The influence of the carbon fibres is discussed elsewhere in the literature, so this will focus on the tin inclusions.

The nylon-carbon fibre-tin component acts as a multiphase material. Modelling of failure in multiphase materials is often carried out at the meso-scale and is discussed in terms of a matrix material, an inclusion, and the interface between them [145]. Materials that have been modelled in this way include concrete [146], [147], fibre reinforced composites, and bones [148]. This concept allows the study of progressive failure conditions at interfaces, and enables the modelling of the different material properties which contribute to the overall properties of the multiphase material. It is suspected that the nylon-tin bonds will be weaker than nylon-nylon interlaminar bonds and that cracking may initiate at tin-nylon interfaces. It is suspected that the high ductility and lower yield strength of tin (tin has a tensile strength of ~ 220 MPa and a yield strength of ~12.5 MPa [149], whereas the composite used in the testing has a ~ 2000 MPa strength tensile strength and ~145 MPa in plane shear strength [150]) may facilitate higher levels of plastic deformation in the composite by absorbing energy that might otherwise cause crack growth. There is some evidence of both of these phenomena in the mechanical testing in Chapter 5.

Models used in concrete analysis offer a strong starting point for this analysis, as concrete is inherently multiphase with aggregate, mortar and pores all contributing to the bulk properties. There is also a requirement for modelling continuous beam reinforcements due to the wide use of steel rebar to provide tensile strength in concretes. A commonly used ABAQUS model (Concrete Damaged Plasticity) represents this on a continuum scale in shell and membrane elements [151]. However the behaviour of tin inclusions within nylon carbon fibre composites is not sufficiently well understood to be able to use a similar method.

Matrix and inclusion elements are modelled together and given their own properties. Additional elements (cohesive elements) are placed at the interfaces between the matrix and inclusion elements. These are then deleted at certain stress criteria to simulate interfacial cracking. The stress criteria are generally based on the concept of a fracture energy release rate (G_c) based on the Griffith energy balance [152]. This identifies a relationship between the stress at fracture initiation and the square root of the length of the defect which is constant for materials. Applied to the cohesive elements in ABAQUS this assumes that a linear elastic stiffness occurs along the element but there is no inherent limiting total stress. Therefore many models include a maximum stress to model plastic yielding which can blunt the crack tip [153]. Cohesive zone models extend this by assuming a cubic polynomial stress-displacement law, in which stress increases with displacement to a maximum stress value. Then the stress falls until a fracture distance is reached and the element is deleted. This process still imposes discrete steps between matrix and material, doesn’t always model complex fracture surfaces well, and requires remeshing to adapt to complex crack paths [145], [154].

Alternatives to this include the use of phase fields, where cracks are regularised by a continuous phase field facilitating the tracking of cracks [145]. This produces a phased transition between matrix, interface and inclusion material properties and allows easier identification of crack paths. The smooth transition can also improve numerical stability. Another method is known as Extended Finite Element method (XFEM) [155], [156]. This uses “enriched nodes” around a crack feature which introduces discontinuous basis functions to the standard polynomial functions in the nodes. The enriched elements contain additional degrees of freedom and this allows the behaviour and growth of cracks or discontinuities to be tracked without updating the finite element mesh.

In the context of the problem in this thesis, the tin inclusions are consistently located in between plies and, at least in the simple interlaminar shear stress tests performed in Chapter 5, the failure regularly occurred either between laminates or in tension opposite the loading nose. From this it is likely that cohesive elements placed between plies could be sufficient for this interlaminar failure.

Therefore the initial approach would involve a cohesive zone model. In this composite plies would be separated by a mixture of membrane or beam cohesive elements designed to model tin and nylon interlaminar bonds. Separate behaviour models would be required to separately model the Nylon, Tin and Composite layers. The composite and nylon models could likely be obtained from the literature, while the tin-nylon fracture model would require novel testing likely based on double cantilever beams. The lack of appropriate data or full knowledge suggests that building upon a simpler model would be appropriate. If this model proved insufficient or unstable then more computationally intensive models which require more input data such as phase field or XFEM could be incorporated. The basic Cohesive Zone Modelling proposed would also largely neglect shape effects of interlaminar tin and thus if required, CT scans or similar could be used to obtain mesh data as is often done in concrete analysis, where shape factors do prove significant in analysis [145].

2.9 Recycling of Thermoplastic composites

Recycling of composites is a growing concern. The proposed and the inclusion of residual metal may complicate the processes [157]. While partial energy recovery through incineration is possible, recycling the material is preferred [158]. While a variety of techniques are being explored the methods can be broadly grouped into the following three mechanisms.

- **Mechanical:** This method involves reducing the size of scrap composites by cutting or crushing into smaller granules or potentially milling them into a fine powder. Smaller particles are then often sorted using cyclones or sieves to separate fibre and matrix heavy particles [[159]. The smaller granules can then be reused as an input in manufacturing streams without changing the chemical makeup. This could take the form as pellets for injection moulding or filament for 3D printing [160]. Sorting and filtering could easily be tweaked to remove any residual metallic inclusions.

- **Thermal:** This method aims to recover the carbon fibres from the matrix material using heat. Pyrolysis is the most common method and involves heating the composite at temperatures of 500-750 °C to decompose the matrix material, allowing for recovery of full-length fibres. The process must balance desire to remove charred matrix material from the fibre with maintaining the material properties of the fibres, with carbon fibres showing more resilience to the high temperatures required [161]. A similar technique is the fluidised bed technique, which exposes a shredded composite to high temperatures in an oxygen rich environment. The shredded composite is placed in a bed of silica sand in a metallic mesh where the decomposition occurs [162], [163]. An airstream carries out lighter fibre and matrix particles for further treatment while heavier contaminants (such as residual tin) are retained in the bed. Fluidised beds are not used as commonly as pyrolysis as the resulting fibre properties are often worse when compared with pyrolysis [160].
- **Chemical:** This approach uses a reactive medium to chemically degrade the resin and allow recovery of the fibres. Breaking down the chemical bonds in the polymer leaves behind monomers and long fibres without any char residue [160]. Temperature, pressure, catalysts, and solvents are all variable depending on the chemistry of the matrix and fibres being treated. Tin is noncorrosive; however, corrosion still occurs when exposed to acids or alkali [164]. While detailed research or testing has not been carried out on this subject, the high temperatures and corrosive environment required to dissolve the polymer matrix is likely to either melt or oxidise residual tin allowing for it to be cleaned from the fibres.

Recycling of fibre reinforced thermoplastic composites is developing but is not yet ubiquitous. There are a variety of competing methods based around matrix and fibre style. Long term pressures to reuse materials seem likely to lead to standards and classification of composite parts to streamline recycling methods. Given the long lifespan of composites and the increasing complexity of inclusions and coatings that are being introduced, any commercial recycling process will need to be robust enough to deal with impurities. However this requirement is already widespread given the use of metallic fasteners in many composites. Mechanical recycling processes are promising in their ability to filter out residual metals via cyclones due to the difference in density between the materials. Thermal and chemical routes which can recover full-length fibres would need more detailed study on the chemistry of the tin to understand the behaviour and influence on recovery of clean fibres.

2.10 Conclusion

In this Chapter a brief overview of the properties and forming of textile reinforced thermoplastic composites is given. Fibre reinforced composites are a rapidly growing field however there are many issues which must be solved to fully unlock their potential. When forming thermoplastic composites, fibre reinforcements must undergo large deformations to conform to complex part geometry and this process requires extensive intra-ply and inter-ply deformation. Limits on these processes restrict the ability to form complex shapes and lead to unwanted defects in manufactured components.

Efforts to improve this include the development of numerical models which predict the draping and deformation mechanics of the fibre reinforcements [112]. This facilitates adjustments to the fibre layup such as adjusting the stacking order or adding cuts or extra layers to the design [99]. Further process improvements involve adjustment to supporting components such as blank holders and diaphragm sheets which enables improved control over the compressive forces which initiate wrinkling in the composite sheets [43], [99], [100]. Of interest to this thesis is the concept of reducing interlayer friction which can be obtained through higher forming temperatures. Of specific inspiration to this thesis is the idea to include a lower viscosity interlayer in the part which lubricates the forming and separates adjacent non-orthogonal layers [10], [107], [165]. While significant improvements have been made in composites forming processes, there are still desires to produce complex, multiaxial parts which are presently limited by wrinkle formation in forming [6], [106], [122]. Therefore, this thesis proposes a novel solution with the potential to act as a step changing in the thermoforming of thermoplastic composites. The feasibility of using a molten tin interlayer to reduce interlaminar friction coefficients, and therefore also reduce wrinkling formation, will be explored. Further Chapters include the development of the manufacturing technique, characterisation and testing of the manufactured parts and simulation work with the aim of furthering understanding of the process.

Chapter 3 Materials and Manufacturing

3.1 Introduction

Two thermoforming processes for carbon fibre reinforced nylon were developed during the project. First, an induction heated process intended to explore the feasibility of molten tin interlayers in the composite forming process, and their influence on the final part. The use of the induction heater was intended to exploit the paramagnetic properties of the tin interlayers and allow for heat generation in situ. Secondly, a radiant heated thermoforming process was developed to allow for the manufacture of control samples without the tin interlayer allowing the influence of tin on the wrinkling mechanics during forming and the mechanical properties of the manufactured part to be studied.

In this Chapter, the materials used in the experiments and the primary manufacturing and experimental techniques will be introduced. First, the thermoplastic composite materials will be discussed, before an exploration into the processes used to produce the interlaminar tin sheets. Finally, there is a detailed look at the two thermoforming techniques.

3.2 Materials

Pre-consolidated 400 x 400 mm sheets of carbon fibre – nylon composite consisting of four plies of TenCate Cetex® TC910 Nylon 6 UD tape [150] in a [0/90/90/0] layup were prepared by colleagues at the Institute of Science and Innovation in Mechanical and Industrial Engineering in Portugal (INEGI). These were initially bonded together using ultrasonic spot welding before being fully consolidated between heated platens using a pressure of 4 Bar at 270 °C for 30 seconds. It is then cooled in the press for 50 minutes (to 150°C) before being water cooled to room temperature. The average laminate thickness is 0.68mm with a standard deviation of 0.10 mm. The tape had a thickness of 0.16 mm, a fibre volume fraction of 49% and a polymer content by weight of 40%. The recommended processing temperature for the laminates is 249-271 °C. The matrix polymer is Ultramid B3W (PA6) which has a melt temperature of 223.4 °C. The forming behaviour of these composites is reported in Harrison et al. [166]. Limited rate and temperature dependent viscosity data for the matrix polymer are provided in the supplier's datasheet [150]. These four-layer pre-consolidated blanks are later reconsolidated and formed in a variety of processes which are outlined in the rest of this Chapter. In addition to this, a sixteen-ply laminate was prepared by INEGI from four of the [0/90/90/0] laminates discussed above for a combined layup of $[0/90/90/0/90/0/0/90]_S$. This was to act as a control mechanism for the manufacturing methods during the mechanical testing. This is discussed further in Section 5.2.1.

An additional point regarding the heated platens is that the sides of the laminate were unconstrained during the consolidation process. This led to a pressure-driven transverse squeeze flow which reduced the thickness of the laminates [167]. This is shown in Fig. 3.1 (a) where the border of the original sheet before the squeeze flow can be seen. Fig 3.1 (b) shows a diagrammatic representation of the pressure state during the press forming at INEGI.

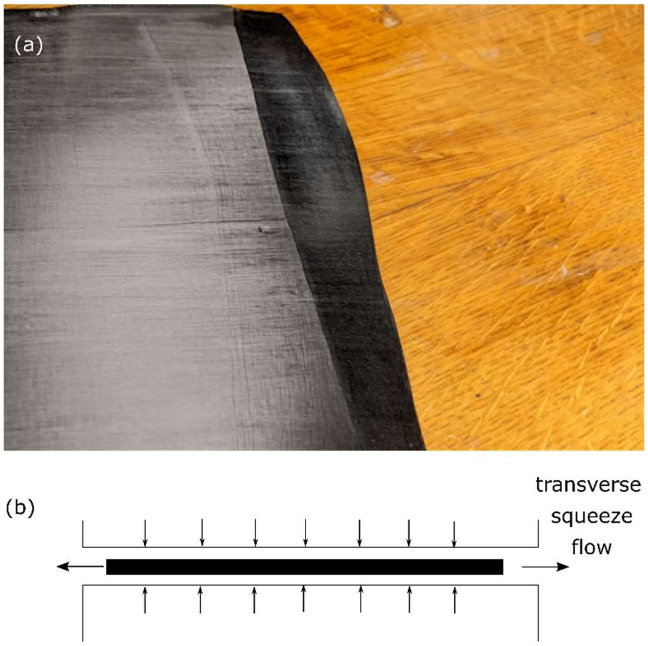

Figure 3.1. (a) shows the thinned edge of the consolidated laminates (b) diagrammatic representation of the process.

During the consolidation process, laminates were held in a 0.3 mm thick silicone rubber diaphragm bag under atmospheric pressure (Silex 60° Shore A Hardness High Temperature Silicone Rubber Sheet [168]). Additional 1 mm thick sheets of the same material were also used to help the forming process as discussed in Section 3.3.3.

3.2.1 Tin Sheet

A supply of tin sheets was required for the manufacturing process and a few considerations came into the decision making. Firstly, it had to produce consistent sheets of 150x150x1 mm at low cost. Secondly, given much of the tin was to be expelled, a method of recycling the tin was desired to help lower long-term costs. Therefore, a gravity fed aluminium mould was developed to produce the tin sheets. It consists of two aluminium parts bolted together as shown in Fig. 3.2a. Internally there is a short 40 mm wide and 100 mm long sprue to load the tin. This then leads into a 150 x 150 x 1 mm cavity as shown in Fig 3.2b. The total volume of the cavity was approximately 22.5 cm^3 while the volume of the sprue was approximately 120 cm^3. A few sources of tin and methods of producing the sheets were explored and are detailed below.

- **Pre-rolled Sheet:** Initially a small number of cold rolled tin sheets with 150 x 150 x 1mm dimensions were purchased from Advent Materials [169] at a cost of ~£60 per sheet. These were high quality however high costs prohibited continual purchase. As such, further research was carried out to provide a cheaper and recyclable source of tin.
- **Powder:** Tin powder was acquired from Gelest [170]. Despite a melt temperature of 231° C for pure tin, practically the tin powder required temperatures of more than 700° C to melt. Due to the small dimensions of the individual tin particles, a thin surface layer of tin oxide constituted a significant portion of the total volume of the powder. This tin oxide had a very high melt temperature so it is likely that the molten tin was trapped inside a tin oxide shell and high temperatures were required to overcome this. As there was no noble gas purge available this reduced the quantity of pure liquid tin that could be sourced from the powder as the high temperatures led to high oxidation (~50% by mass of the final product was

a tin oxide). This combination of high process temperature and reduced output meant that this method was a poor method of producing the tin sheets required for manufacture.

- **Solder:** Tin solder (commonly used on electronic circuits) is widely available in all hardware shops. A 99.3% Sn 0.7% Cu alloy was chosen. The alloy is eutectic with a melting point of 227° C which is similar to pure tin. Commonly available solders come with a rosin flux intended to clean and reduce oxidation in the solder during the soldering process. When the solder flowed into the mould, the rosin flux was left behind which fouled the cavity. Despite cleaning, residual flux remained and repeated exposure to high temperature, resulting in the decomposition of the flux, and the production of smoke. Avoiding this required time-consuming cleaning between cycles slowing the process down unnecessarily.
- **Shot:** 99.8% purity tin shot was purchased from Alfa Aesar at a cost of £227 for 2 kg [171]. This had an average particle size of 3.175 mm and, as such, the influence of oxidation on the surface of the shot was reduced. Not having rosin flux reduced issues with mould fouling and the protection offered by the mould itself reduced exposure to oxygen and thus only a small portion of the tin at the top surface of the flue experienced oxidation.

During the casting process, 250 g of tin shot was loaded into the sprue. This is sufficient to both fill the mould and apply sufficient pressure on the cavity to ensure a high-quality sheet with low porosity. The mould is then placed in an oven at 280° C for 180 minutes. The mould is then cooled by first quenching in a hot water bath at 95°C, then further quenched in room temperature water. There was no requirement for pouring of molten tin at any stage. It was also possible to use the mould to recycle used tin by cutting into small pieces and placing it in the sprue and cavity. Given the required mass of material for the casting process, the cost of the first sheet manufactured for tin shot came to ~£30 which is approximately half the price of the cold rolled tin. Tin remaining in the flue experienced oxidation during the casting process and was not recoverable. There was also evidence of surface oxidation in the bulk sheet when recycling material as can be seen in a cast sheet shown in Fig. 3.2c. The tin oxide forming in the flue can also be seen to the left of the image. There was no visible evidence of the tin oxidising during the thermoforming of the composites as the operation was carried out under a vacuum. Therefore, after forming the majority of the tin was recoverable allowing material costs to drop as material was recycled.

As a potential solution to the oxidation during casting, inert atmospheres (nitrogen or argon) have been used to reduce tin oxidation rates, and reducing atmospheres (i.e., containing hydrogen) have been used to remove oxygen (either in solution or in a tin oxide) [172], [173] so these could be explored to reduce oxidation rates and potentially recover oxidised tin. There is also evidence that use of phosphor as an alloying element may reduce oxide thickness [174]. These were not used during experimentation due to time and equipment issues.

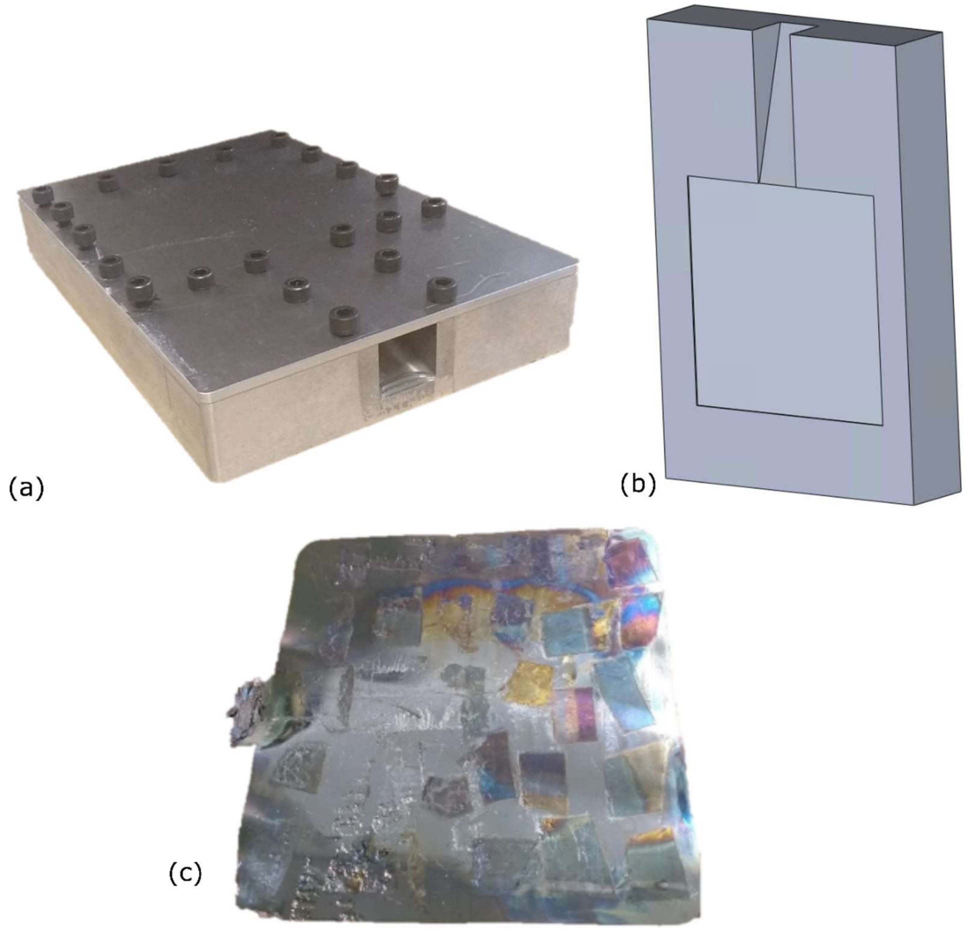

Figure 3.2. (a) image of aluminium mould (b) main part of mould showing sprue and cavity. (c) tin sheet partially formed from recycled tin

3.3 Experimental Method

3.3.1 Overview

Two thermoforming methods were developed during the project. These shared the aim of heating a composite layup within a vacuum diaphragm and forming into both flat and curved geometries, however the Induction Melt Thermoforming process included tin interlayers intended to lubricate the forming process. Due to the different heating methods employed (radiant vs Induction heating) the technical specifications for the components required different approaches. This Section will explore the resulting manufacturing methods. It is worth noting that the induction heating unit used in the process was rented from Induction Coil Solutions [175] and, as such, was only available for a short period of time. This limited the time available for optimising the induction thermoforming process (5 months).

A schematic of the basic induction heating setup is shown in Fig. 3.3a and Fig. 3.3b (i) shows the segmented male tooling. In (ii) there is a cross-section view of the Carbon-Nylon-Tin sample within the Silicone Diaphragm. In (iii) the vacuum pump is connected creating 1 Bar of consolidation pressure. At (iv), a blank holder secures a double-diaphragm arrangement consisting of silicone rubber sheets into which the composite and metal interlayers are placed. (v) shows a false base plate located in the bed of the universal test machine upon which, (vi) the segmented female tooling mounted on. (vii) An induction coil is placed just below the false base plate allowing in-situ heating. The distance, *d*1, is the gap between the coil and the laminate. *d*1 was 25 mm when forming flat geometries and 60 mm when forming ripple geometries. The increase in *d*1 was necessary to safely position the Female Tooling.

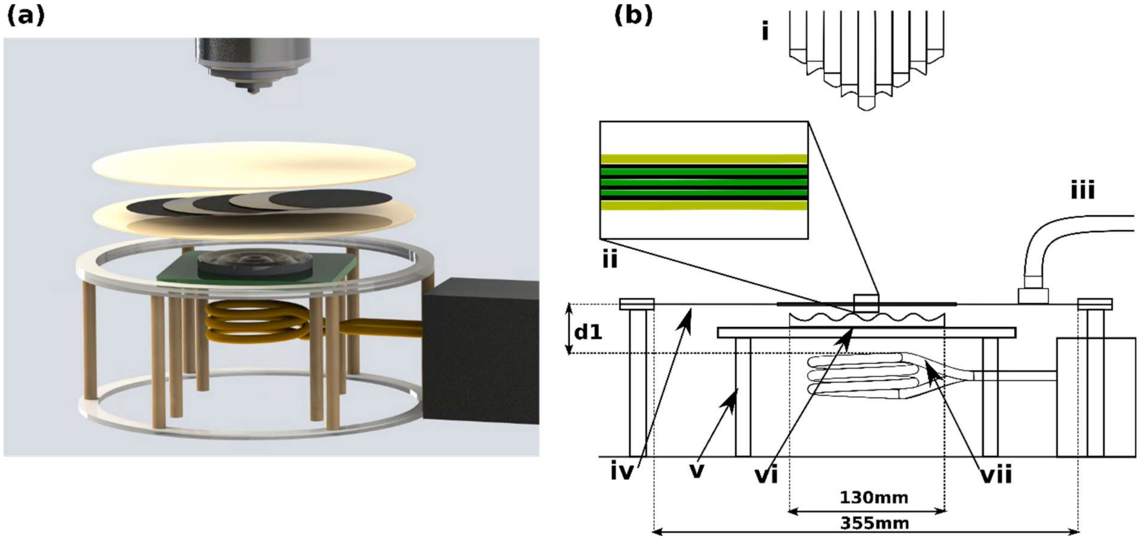

Figure 3.3: (a) 3D construction of thermoforming set up with diaphragm and samples exploded (b) Sectioned schematic of the induction thermoforming setup showing: (i) multistep male tooling with segmented ripple tooling attached, (ii) exploded view of tin and nylon layup (yellow represents the silicone diaphragm sheets, black is carbon-nylon composite and green is tin interlayer), (iii) vacuum pump connector, (iv) blank holder, (v) epoxy-glass fibre false base plate, (vi) female ripple tooling and (vii) solenoid induction coil. *d*1 refers to the distance between coil and Sample. *d*1 = 25 mm for forming of flat samples, and *d*1 = 60 mm when forming ripple specimens.

A diagrammatic overview of the radiant thermoforming setup is shown in Fig 3.4. Label (i) shows the multistep tool, label (ii) shows the radiant heater mounted on the shuttle system. In (iii), the aluminium blank holder is shown in the shuttle tray. (iv) shows the laminate within the silicone rubber diaphragm and (v) shows the forming base plate in the Zwick Z250 universal test machine. The distance *d*2 represents the distance between the radiant heater and the part which was a constant 110 mm.

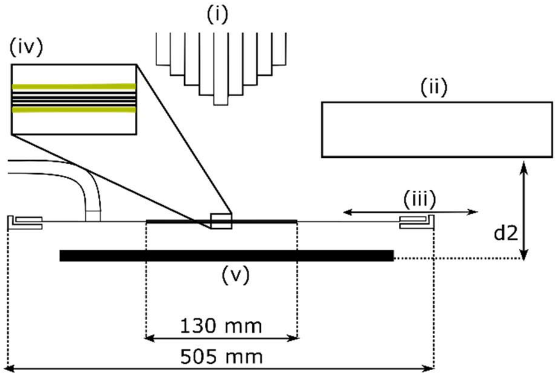

Figure 3.4: diagrammatic representation of radiant thermoforming set up: (i) multistep tool (ii) Watlow Raymax 2030 (iii) shuttle system (iv) sample (v) forming base plate. *d*2 refers to the distance between the heater and the sample. It was a constant 110 mm for all samples.

Both manufacturing set ups have several common components and some different components to address the different technical requirements imposed by the heating mechanisms. The induction heating requires non-conducting materials around the induction coil and has little requirements regarding resistance to high temperatures apart from the silicone rubber and the tooling. On the other hand, the radiant heating process has no requirements on electrical conductivity but does have a requirement that all components resist temperatures more than 250 °C due to exposure from the radiant heater. In the rest of this Section, the components and experimental parameters of the experimental setup will be explored in more detail. These are divided into the upper thermoforming set up, which consisted of:

- A multi-step forming tool fitted to a universal test machine,
- A lower thermoforming set up which used silicone diaphragm sheets to constrain the samples,
- A segmented tool head which allowed for the thermoforming of custom geometries,
- The heating apparatus.

3.3.2 Upper Thermoforming set up

A multi-step tool was designed by a final year project student, Emin Gulyilev [176], manufactured by an external contractor and was fitted into the universal test machine to carry out the experiments. The tool is designed to form from the centre of the part outwards, creating a pressure gradient and removing the tin interlayer during the forming process. It has four progressively longer annuli around a central cylinder. There is a cap at the top of the part which holds the annuli and attaches to the universal test machine as shown in Fig. 3.5a. A cross-section of the upper container is shown in Fig. 3.5b. Initially, the cylinder and annuli hang free with the central cylinder lower than the outer annuli (Fig. 3.5c) The tooling is initially actuated via its own self-weight (~63 kg). As the tool is lowered onto a surface, the central cylinder comes into contact with the part to be formed first, and the weight is transferred from the upper housing onto the part. When the central cylinder in (c) comes into contact with female tooling the cylinder will rise into hollow cavity as marked by the arrow in (b) untill reached the top surface. As each successive annuli comes into contact, additional pressure is applied to the surface from the centre outwards. Once all annuli come into contact with the surface, they also come into contact with the roof of the inner housing. This turns the multistep tool into a rigid body, allowing additional consolidation pressure to be applied. The total diameter of the tooling is 130 mm. The central cylinder is 14 mm diameter, and each annulus has a thickness of 14 mm. There is a 1 mm gap between each annulus. The pressure applied is a function of the height of the segment and the density of the steel, so is independent of area covered. This ranges from 47.2 kPa to 51.2 kPa (0.472-0.512 Bar) due to the variation in length of the segments. This steel tooling was used for both the radiant and induction heated thermoforming processes. A shorter prototype plastic version was also 3D printed from ABS plastic to prove the concept before final manufacture of the steel tooling. The cylinders were hollow and filled with lead shot to apply a pressure of ~10 kPa and an image can be seen in Fig. 3.5d.

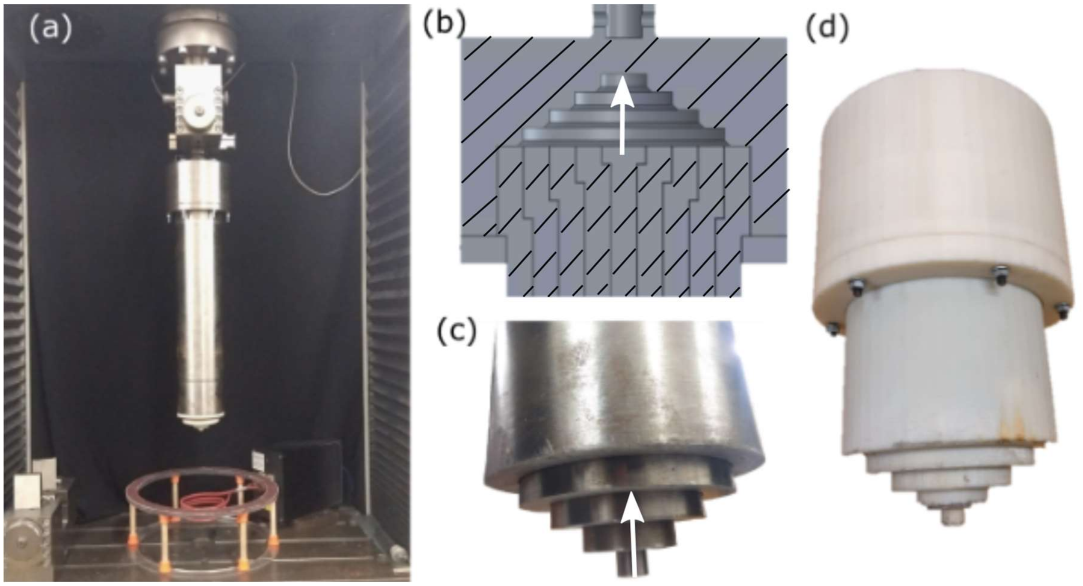

Figure 3.5: (a) Reconfigurable multi-step tool fitted inside a universal test machine. End of tooling fitted with 3D printed ABS ripple tooling, (b) internal geometry of the upper housing of the multistep tooling in free hanging position and (c) close-up showing the end of the steel tool, (d) plastic prototype of multistep tooling. When the central cylinder in (c) comes into contact with female tooling the cylinder will rise into hollow caviity as marked by arrow in (b)

3.3.3 Lower Thermoforming Set-up

The lower setup for both processes was slightly different. Fig 3.6 shows the setup for the induction heated thermoforming process. Fig 3.6a shows the lower setup prior to inserting the blank and diaphragm into the blank holder. Two perspex rings are supported by wooden dowels and secured using 3D printed ABS plastic supports. A non electrically-conductive glass fibre/kevlar/epoxy false base plate is positioned inside the blank holder and is supported by wooden dowels with white ABS printed supports. 24 sheets of glass fibre and 3 reinforcing sheets of kevlar were combined to ensure approprite stiffness to provide a reaction force for the upper tooling. Below the false base plate is a water cooled copper helical induction coil manufactured by Induction Coil Solutions, powered by a 12 kW 60 kHz induction heating unit from Ceia and controlled by a V6 control unit. This arrangement allows for in-situ heating of the composite/tin specimens without a shuttle system. The surface temperature of the upper diaphragm was monitored using both a FLIR One Pro thermal imaging camera and an Etekcity Lasergrip 1080 non-contact digital laser infrared thermometer (both use a wavelength range of 8-14 μm). A female tool (See Section 3.3.4) can be secured on the false base plate to allow for the forming of complex geometries. Both the baseplate and the female tool must be electrical insulators to allow the magnetic field to pass through them and into the specimen. A silicone diaphragm is then supported by the blank holder, above the false base plate. A silicone diaphragm was used for several reasons:

- **Safety**: the diaphragm constrains the molten tin during forming reducing the risk of burns and facilitating collection after forming process. The Silex Silicone sheet used had a long duration temperature rating of 300 °C [168].
- **Fixed position**: The diaphragm resists the force generated by the induction coil and imparts tensile stresses during the forming process, reducing tendency to wrinkle.
- **Consolidation**: The vacuum pressure adds 1 bar of pressure evenly over the sample. It was found that the isostatic pressure provided by the atmosphere did not force tin out of the sample. Whereas the localised pressure gradient provided by the tooling did force the tin out.

- **Oxidation**: By expelling air, the risk of the molten tin oxidising under high temperature is reduced
- **Air ingress**: The unconstrained molten tin tends to form a dendritic pattern (see Fig. 3.10) which would draw air into the part and disrupt the eddy currents resulting in heterogenous temeparture distribution over the sheet.

During the experiments, it was discovered that additional protective sheets of silicone rubber with 1 mm thickness and a diameter of 150 mm placed above and below the sample were helpful in aiding the forming. This is shown in Figure 3.6b: the nylon-composite sandwich (black) on top of the extra silicone rubber sheet (red) all set above the lower silicone diaphragm (white) along with the required breather cloth and vacuum connectors. The addition of the extra silicone rubber sheets helped for three primary reasons.

- **Insulation**: It lowered the heat transfer rate in the *z*-direction out of the sample reducing heat loss and improving the relative significance of conduction within the carbon nylon blank, improving temperature homogenieity
- **Stiffness**: It improved the structural integrity of the diaphragm, helping it support the molten tin and reduce the chance of it flowing away from the sample.
- **Pressure**: During the forming process, the rings led to sharp discontinuities in the pressure gradient. The addition of a thicker layer of silicone rubber appeared to smooth over these discontinuities, thus ensuring a continuous pressure gradient assisting with the removal of the tin.

Fig. 3.6c shows the upper ring fixed in postion with 12 g-clamps and shows vacuum connectors and a pressure gauge attached (to facilitate monitoring of pressure during forming). Emery cloth was applied to the bonded faces of the blank holder to ensure a tight vacuum seal. The experimental setup is key to achieving a homogenous temperature distribution with factors such as distance between coil, power applied by the heater and quality of the tin sheet influencing the outcome.

The radiant thermoforming process required materials with a high temperature resistance. As such, an aluminium blankholder of internal diameter 505 mm was manufactured. Due to the size and weight of the radiant heater, it was also required to shuttle the heated blank between the radiant heater and the tooling, a typical setup for the radiant heating process [44], [177], [178]. The radiant heater was mounted to a shuttle designed by Alexander Angelov (a final year project student [176] and adapted to fit the aluminium blank holder. This allowed the sample to be heated then quickly transferred to the multistep press for forming. Fig 3.7a shows the aluminium blank holder within the shuttle bed. The blankholder is secured by 4 G-clamps. Fig. 3.7b shows the blankholder within the shuttle and underneath the radiant heater. It is then ready to transfer to the multistep press for forming.

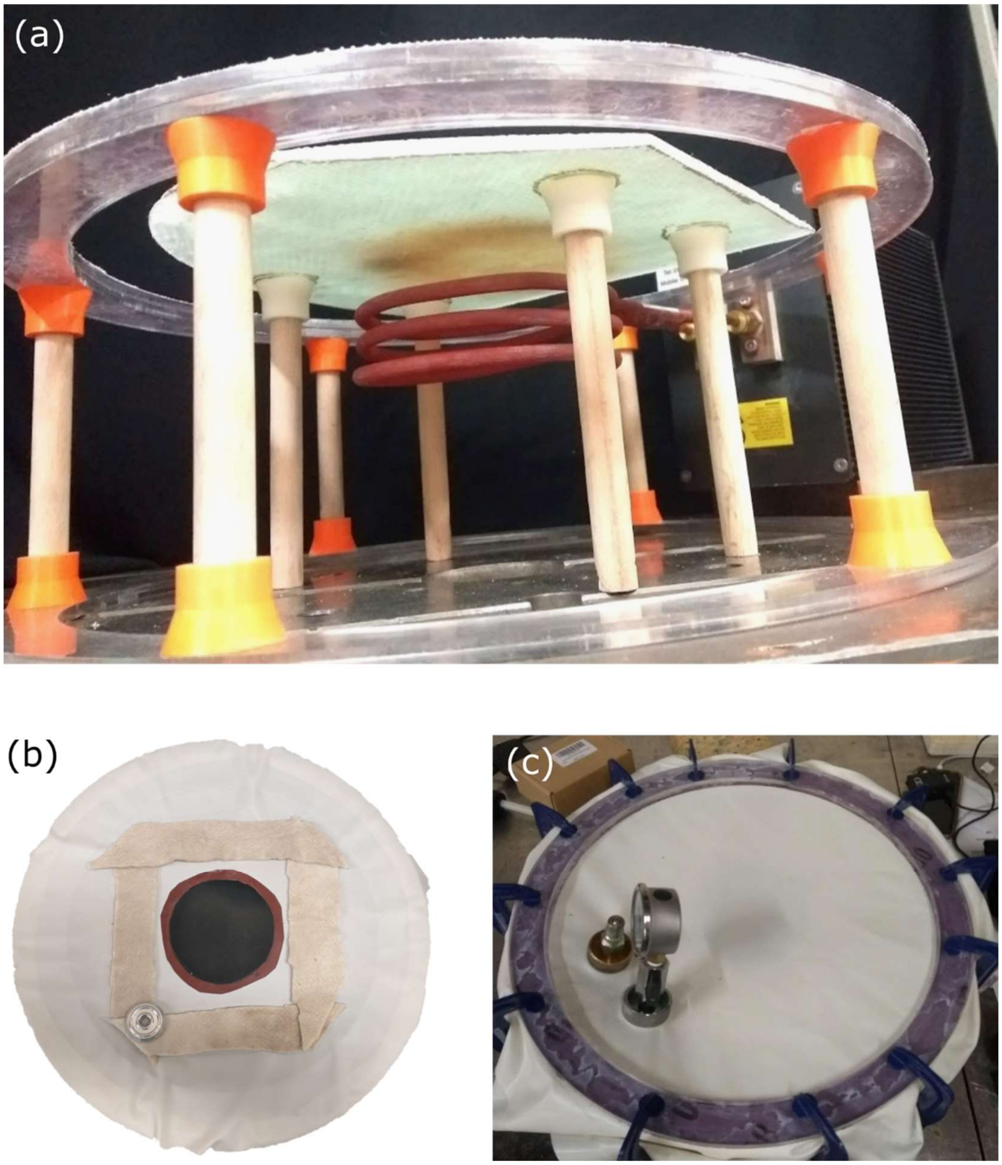

Figure 3.6: (a) Helical induction heating coil positioned below a 'false base-plate' positioned above induction coil and below silicone diaphragm, (b) internal setup of silicone diaphragm containing sample (black), extra silicone barrier (red) and vacuum connectors and (c) diaphragm back secured in place with clamps.

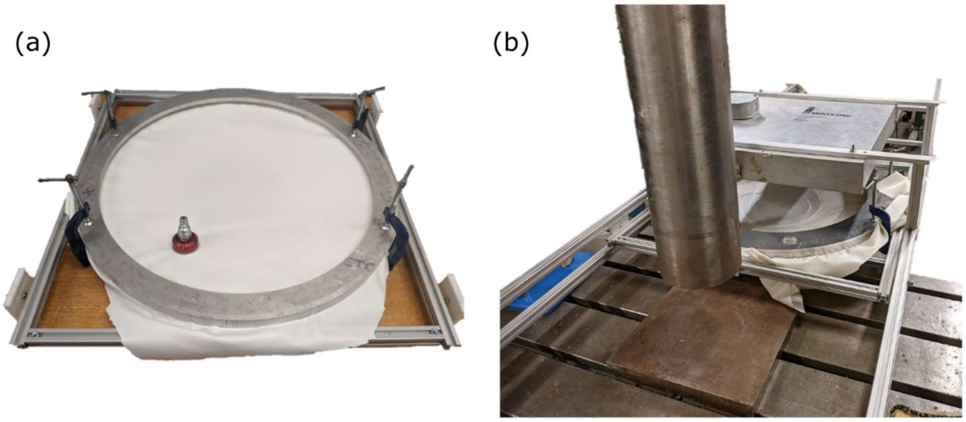

Fig 3.7 (a) Sample within silicone rubber diaphragm secured by aluminium blank holder within shuttle bed. (b) Image of the blank holder under radiant heater and prepared to shuttle to universal test machine.

3.3.4 Segmented Tooling

To analyse the influence on wrinkling mechanics, a ripple geometry was chosen for the segmented tooling. This was used as the recesses may trap the sheet if formed in a single step. The design could also be suited for future parametric study by tweaking the amplitude, wavelength and number of waves as will be carried out in the numerical simulations in chapter 6. In Fig. 3.8 a cross-section of the tool can be seen in the open (Fig. 3.8a) and closed (Fig. 3.8b) positions. The male tool follows a cosine curve with an amplitude of 6 mm and a wavelength of 26 mm. The female tool is offset with a constant cavity height gap of 1.74 mm to offset material thickness. Fig. 3.9a shows a cross-section of the segmented male tooling while Fig. 3.9b shows the segmented female tool. Fig 3.9c shows the segmented 3D printed ABS plastic male tooling while Fig. 3.9d shows the female tooling. The ABS female tooling was used in the induction thermoforming experiments as it is not magnetically conductive and, as such, will not interact with the inductive heating process. The ABS tooling was printed using a Stratasys F270 FDM machine with an accuracy of ± 0.2 mm. Aluminium versions of the male and female tooling were also manufactured for the radiant heating thermoforming.

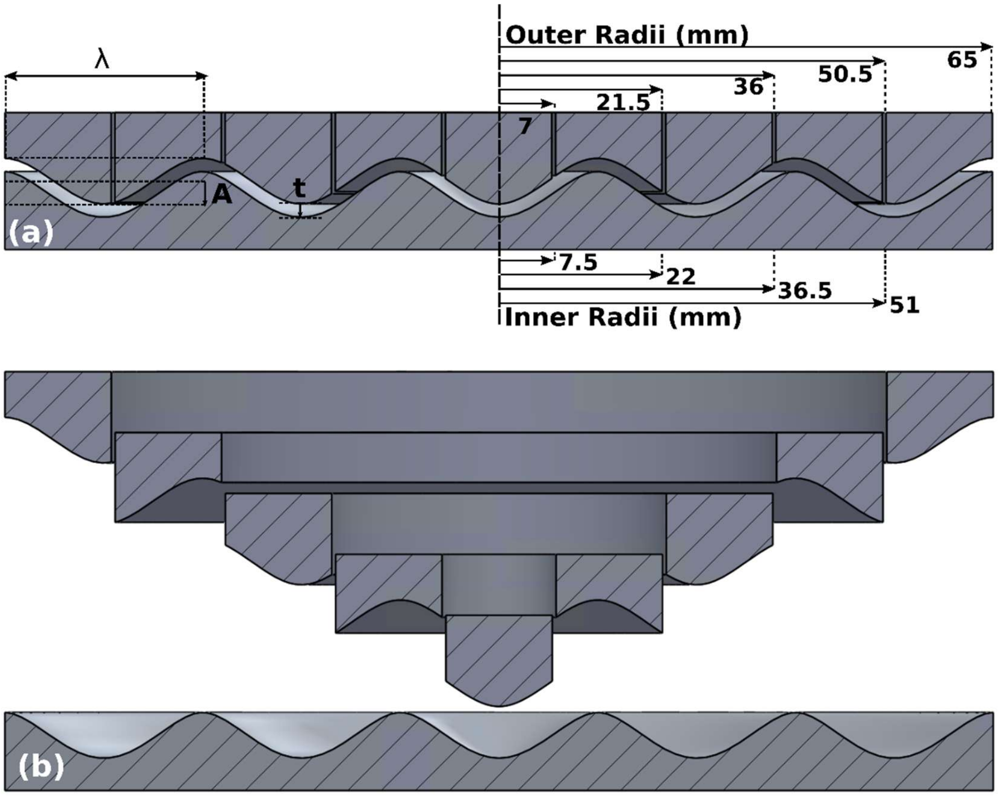

Figure 3.8: (a) Cross-section of male and female rippled tools in closed position. Wavelength, λ, is 26 mm, Amplitude, A, is 6 mm and tool gap, t, is 1.74 mm. The outer radii of the central cylinder and four annuli are marked along with the inner radii of the four annuli on the right side. (b) cross-section of female tooling and segmented tips for male tooling in open position.

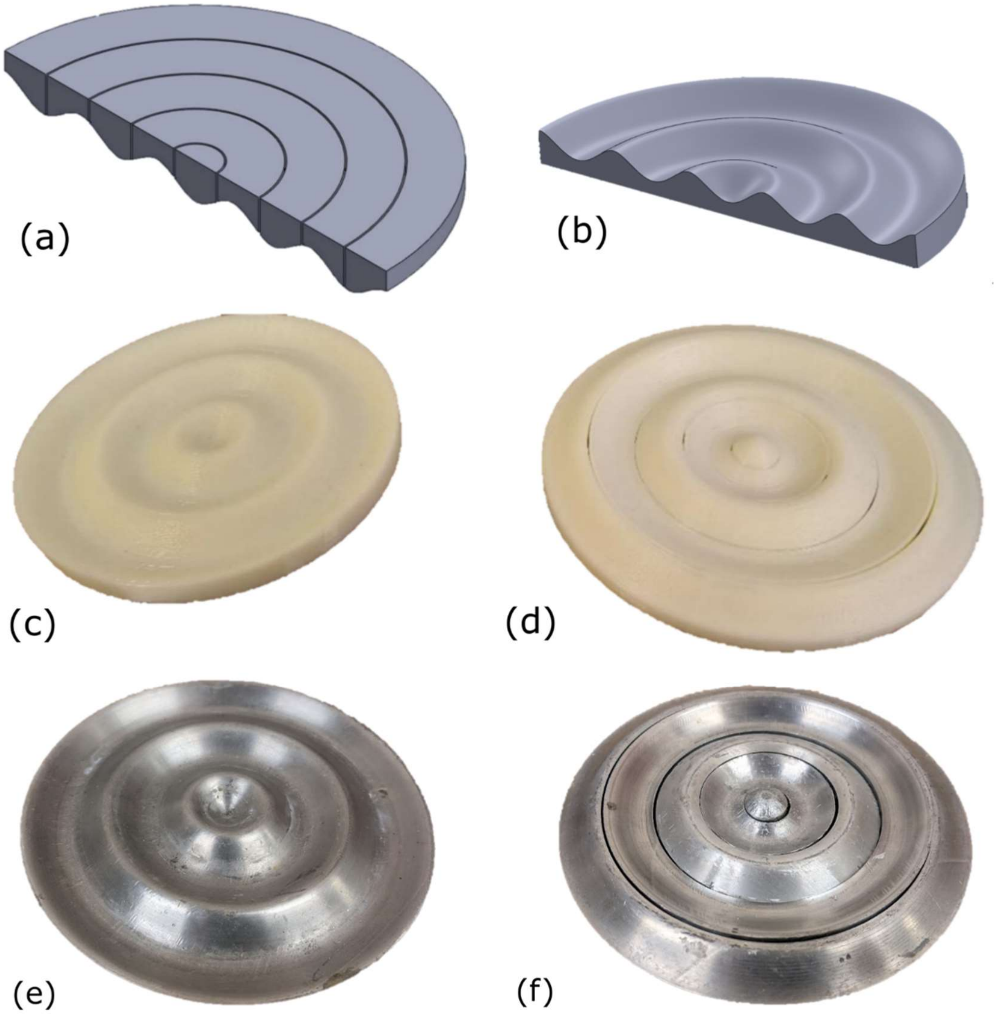

Figure 3.9: (a) CAD showing cross-section through segmented male ripple tool, (b) cross-section through female ripple tool, (c) 3D printed ABS single piece female ripple tool, (d) 3D printed ABS segmented male ripple tool, (e) single piece aluminium female tooling, (f) segmented aluminium male tooling.

3.3.5 Induction Heating

The primary metallic allotrope of tin, white ß tin, is a paramagnetic material which can be heated via induction heating. An induction heater involves a high frequency alternating current passing through an electromagnetic induction coil. This creates rapidly changing magnetic fields which then generate small eddy currents in the conductive material to be heated. A key factor in optimising induction heating is the ‘skin effect’. This is the tendency for the eddy currents to be concentrated near the surface of a body. The skin depth, δ, is defined as the depth in which 87 % of power is dissipated and can be calculated as,

$$\delta = \sqrt{\frac{2\mathrm{P}}{\mathrm{M}\omega}} \qquad (3.1)$$

where P is the resistivity of the material, M is the absolute magnetic permeability [179] and ω is the frequency (Hz) [180]. Note that, $\mu = 1.256 \times 10^{-6}$ Hm^{-1} and for tin, $\rho = 1.09 \times 10^{-7}$ Ωm. A skin depth of ~1.4 mm occurs at a frequency of ~80 kHz. This is appropriate for the 1 mm thick sheets used in these experiments as a significant portion of the energy in the coil can be captured. However the larger skin depth still allows for flexibility in heating multiple tin sheets. Heating solely the nylon-carbon laminates via conductive effects in the carbon fibres was attempted. However, this proved very inconsistent between laminates (likely due to small differences in fibre-fibre contact area) and struggled to get temperatures above ~60 °C.

For the induction heating process, a 12 kW, 80 kHz induction heating unit, manufactured by Ceia [181], was rented from Induction Coil Solutions. This was controlled by a V6 control unit. Initial experiments were carried out to establish the feasibility of melting the tin interlayers and heating the nylon via conduction. Fig. 3.10a and Fig. 3.10b show helical and pancake coils respectively. Helical coils provide a high level of magnetic flux (and thus energy transfer) through the centre of the coil while pancake coils provide the highest level of magnetic flux just above and below the surface of the coil. Fig. 3.10c shows an initial experiment where a single sheet of 40 x 40 x 1 mm tin is heated until molten in the centre of a helical coil. The tin sheet was completely molten in 10 seconds showing the potential power of the heating mechanism. A dendritic pattern is seen in the distribution of the molten tin. A similar pattern can be seen in Fig. 3.10d where a single sheet of 40 x 40 x 1 mm tin was heated until partially molten between 0.5 mm thick sheets of carbon-nylon composite. The frozen tin also shows a dendritic pattern. This brings in two risks, firstly this pattern could draw unwanted air into the laminate. Secondly, a non-continuous sheet would influence the eddy currents and resultant heat generation and transfer within the tin, making the heating process more unpredictable and difficult to control.

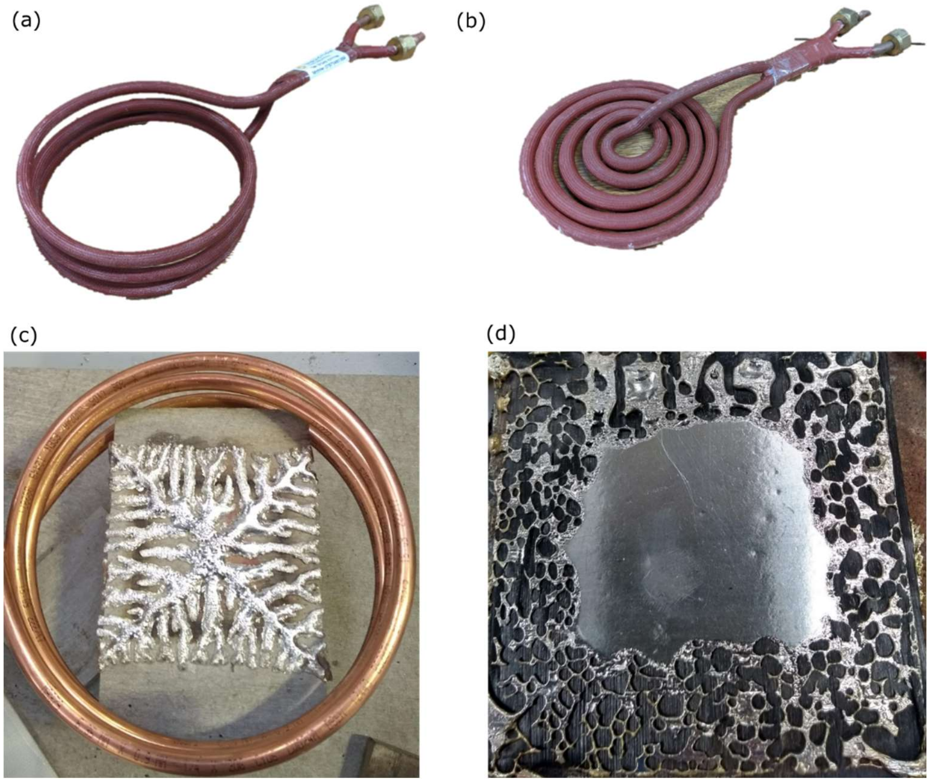

Figure 3.10: Images of the early induction heating experiments: (a) shows a helical induction coil, (b) shows a pancake induction coil, (c) shows single sheet of tin melted with helical coil and (d) shows sheet of interlaminar tin partially molten, then refrozen between nylon sheets.

Creating a uniform temperature across the tin sheet is a non-trivial process and was one of the greatest causes of variability within the investigation. The heating of the specimen is a function of numerous parameters including, for example: **(i)** heater power, **(ii)** distance between induction coil and specimen, **(iii)** relative position of coil and specimen in the (*x, y*) plane, **(iv)** specimen size and shape, **(v)** heat transfer between tin, composite, and rubber diaphragm, **(vi)** temperature measurement system and **(vii)** flow of tin within the specimen. As a result of these varied parameters, achieving accurate and reliable temperature control was challenging. Electromagnetic fields induce voltages in thermocouples making them poorly suited to temperature measurement. The temperature of the specimen was therefore measured on the upper surface of the silicone diaphragm with a thermal camera (Flir One) and a Etekcity laser thermometer as detailed in Section 3.3.3. Due to the small distances in the *z*-direction and the fact that heat is created in the centre of the part, it was assumed that temperature variation through the stack would be small. Furthermore, the fact that silicone is semi-transparent in the wavelengths used by the cameras [182] meant the measured temperature was close to the temperature of the laminate. There was temperature variation in the (x, y) plane due to the lower thermal conductivity of the nylon and flow of the molten tin, leading to non-uniform heat generation. Despite the tin's molten state and being subject to 1 Bar of normal pressure, due to the lack of pressure gradient inside the diaphragm, observations showed that there was no flow of tin out of the specimen prior to the forming process.

Temperature control was managed by manually adjusting the induction coil generator power with an on-off control unit (up to 6 kW, 50% of maximum power output) and by manually shifting the position of the induction coil during the heating process, based on real-time feedback from the two temperature measurement techniques (thermal camera & laser thermometer). The lower power output reduced high temperature hotspots. Fig. 3.11 shows images from the thermal camera, Fig. 3.11a shows the heating of a tin-carbon-nylon layup (with no rubber diaphragm) using a high power (10 kW) showing the localisation of hotspots. Fig. 3.11b and Fig. 3.11c show heating of a tin and carbon-nylon layup when placed within the diaphragm sheets and using lower power (6 kW). The images in Figure 3.11 demonstrates improved temperature homogeneity. The aim was to produce an evenly distributed temperature profile across the specimen, hot enough to melt the tin and composite matrix phase while avoiding localised hot spots that could lead to failure of the diaphragm. An overall surface temperature reading of 250°C was the criteria used to initiate forming tests. This took approximately five minutes when heating two-layer composite specimens, and approximately ten minutes when heating four-layer composite specimens using 6 kW of power.

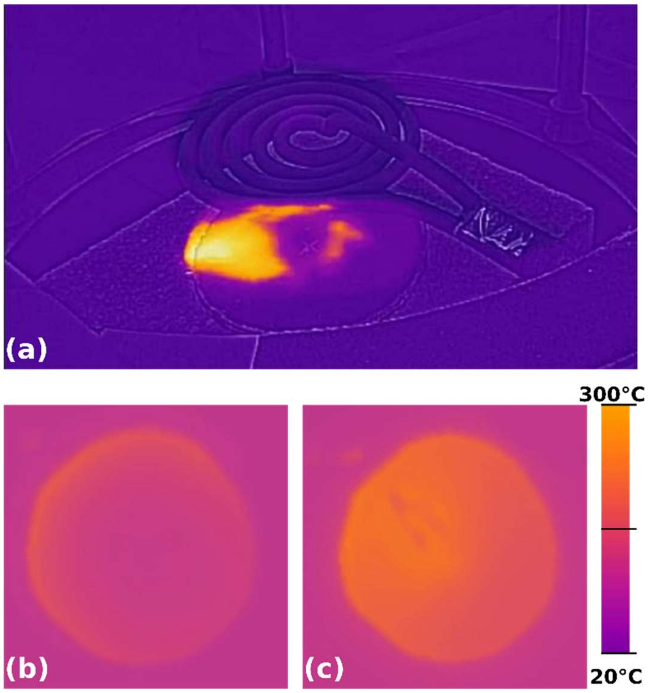

Figure 3.11: Captured Images from Flir One IR camera. (a) 10 kW heating of nylon-carbon tin layup with hotspots (no rubber diaphragm sheet), (b) 6 kW heating of tin and carbon-nylon layup within silicone diaphragm after 30s, (c) 6 kW heating of tin and carbon-nylon layup within silicone diaphragm after 300s. Scale bar refers to (b) and (c).

Inevitably, manual control led to variable results, with failure rates decreasing to around 20 % as familiarity with the process and skill in adjusting the setup in real-time improved. The behaviour of the tin was unpredictable once molten as the weight of the tin also deformed the silicone rubber diaphragm and often led to pooling in the middle of the sample. This was partially solved by adding additional layers of silicone rubber as discussed in Section 3.3.3; however, a longer term more robust solution is to be required. That could take the form of reducing the quantity of tin or improving the stiffness of the diaphragm sheet supporting the specimen, however solutions for this will have trade-offs. Furthermore, as heat generation occurred volumetrically in the tin, and the tin flowed unpredictably, managing heat distribution remained a challenge throughout. The most common outcome was that the liquid tin pooled to the centre of the laminates as the weight of the tin deformed the diaphragm. This meant that the tin was located at the centre of the laminate for the start of the forming process and could be pushed outwards from the centre. Improving the stiffness of the diaphragm with additional insulating layers helped improve the predictability of the pooling effect. Manually adjusting the position of the induction coil also aided in providing a homogenous temperature distribution. However, it was not possible to fully resolve the variability in the time available. An enhanced setup with more refined and automated feedback-based heating control, informed by greater understanding gained through process modelling, would likely further reduce failure rates.

Another major challenge in the induction melt thermoforming experiments was related to the polymeric nature of the male and female ripple tooling used in the investigation. It was desired to carry out the heating process in situ to explore the possibility of removing shuttle systems, this required that the tooling had to be non-conducting, the only option available within the timeframe of the initial project funding was 3D printed ABS tooling. ABS has a glass transition temperature of ~110 ^{o}C and is usually printed at ~230 ^{o}C. Consequently, it becomes soft below temperatures required to melt tin and nylon. As a result, and despite being thermally protected by the rubber diaphragm, the ABS tooling was inevitably exposed to high temperatures and therefore prone to distortion after multiple runs during thermoforming. Consequently, it had to be re-printed several times throughout the investigation. Future testing could potentially use higher temperature thermoplastics such as PEEK, or 3d printed ceramics which are a novel but promising area of development Despite these challenges, a large test matrix was conducted (20 experiments in total) and meaningful results were obtained. In Sections 3.4 and 3.5, a selection of results from the full investigation are presented and discussed.

3.3.6 Radiant Heating

Radiant heat uses infrared electromagnetic waves to transmit heat. These waves are generated by the thermal vibration of particles above absolute zero. This allows for non-contact transfer of heat from a hot object to a colder object. The wavelength and energy contained in these waves depends on the temperature of the source body and the Stefan-Boltzmann law describes this for a ‘black body’, as being proportional to the fourth power of the temperature of the emitting object. A black body is a body that perfectly emits and absorbs all radiation. Bodies that do not emit or absorb perfectly can be characterised by their emissivity which gives their energy absorbed and emitted as a proportion of the theoretical black body radiation. This can be written as:

$$j = \varsigma \sigma T^4 \tag{3.2}$$

Where j = energy radiated, ς = Stefan-Boltzmann constant ($5.67x10^{-8}\ \frac{j}{s\,m^2\,k^4}$), T = temperature and ϵ = emissivity (ranges from 0 for a perfect reflector and 1 for a perfect emitter). Further details on the use of radiant heating for heat transfer can be found in Thermal Radiation Heat Transfer [183]. Radiant heaters use this principle by heating the surface of the heater to a high temperature to emit infrared radiation which is then absorbed by the part being heated.

In these experiments, a Watlow RAYMAX 2030 heater was used to heat the parts. It has a power output of 5.7 kW and dimensions of 407 x 457 mm. This power output was similar to the 6 kW used in the induction coil. It was controlled using a Ez-Zone PM controller panel and the temperature on the surface of the heater was monitored by an insulated type K thermocouple. An on-off control cycle enabled through the Ez-Zone controller was used to control the heating element. Initial calculations were made to estimate the required heater surface temperature to obtain a part temperature of 260 °C. The procedure to do this is provided by the manufacturer's technical specifications [184].

It is desired to estimate the required power output to appropriately heat the composite parts to the desired temperature. This requires considering factors such as the heater dimensions, change in temperature, emissivity's, distances and desired time taken to heat the part. In addition to this, the thermal mass of the sample and the surrounding silicone diaphragms (C_{th}) can be calculated as outlined in the following equation.

$$C_{th} = A_i\ t_i\ \rho_i\ C_i \tag{3.3}$$

where A_i= Area of the part t_i = Thickness of the part ρ_i = density of the material and C_i = Specific heat of the part. The relevant properties required for calculations of the thermal mass of the component parts are outlined in Table 3.1.

Table 3.1 Parameters and results for calculations of thermal mass of heated parts.

Parameter	Nylon	0.3 mm silicone diaphragm	1 mm silicone sheet
Radius (r) (m)	0.065	0.265	0.075
Area (A) (m^2)	0.013	0.22	0.18
Thickness (d) (m)	0.002	0.0006	0.002
Density (ρ) (kg/m^3)	1280	1700	1700
Specific Heat (C) (J/(kg.K)	1700	1100	1100
Thermal Mass (C_{th}) (J/K)	57.8	218.4	58.3

From this, the heat flow necessary to raise the temperature of the part can be worked out from

$$\dot{Q} = \frac{C_{th}\ \Delta T}{time} \tag{3.4}$$

where $\dot{Q}$ = heat transfer rate and C_{th} = combined thermal mass. From the calculated heat transfer rate, it is then possible to approximate the required temperature of the radiant heater, T_h, by rearranging the following equation:

$$\dot{Q} = \frac{\sigma\,(T_h^4 - T_p^4)\epsilon\ F\ A_h}{SF} \tag{3.5}$$

as

$$T_h = \sqrt[4]{T_p^4 + \frac{\dot{Q}\ SF}{\sigma\ \epsilon\ F\ A_h}} \tag{3.6}$$

In this, T_p is the desired temperature of the part (523 K), σ is the Stefan-Boltzmann constant, SF= safety factor of two (to account for any cooling effects and the thermal mass of the aluminium blank holder close to the silicone rubber), *F* is the view factor which is a function of heater dimensions (406 mm x 457 mm) and distance to the part (130 mm) as detailed in the heater documentation [185]. Finally, ϵ is the effective emissivity and can be calculated from:

$$\epsilon = \frac{1}{\frac{1}{\epsilon_h}+\frac{1}{\epsilon_p}-1} \tag{3.7}$$

where ϵ_h= emissivity of the heater and ϵ_p= emissivity of the silicone rubber. The input parameters and results are summarised in Table 3.2. Based on the part parameters, heater parameters, and specified dimensions it was found that an approximate heater temperature of 415°C was required to heat the part to 260 °C.

Table 3.2 Initial parameters for radiant heater calculations. Calculated outputs in bold

Parameter	Value
Heater area (A_h)	0.185 m^2
Desired Temperature of Part (T_p)	533 k (250 °C)
Change in temperature (ΔT)	250 k
Time to heat	300 s
Product Emissivity (ϵ_p)	0.85
Heater Emissivity (ϵ_h)	0.85
Effective Emissivity (ϵ)	0.74
View Factor (F)	0.5
Safety Factor (SF)	2
Total Thermal Mass	**334.5 J/K**
Required Heat Transfer Rate ($\dot{Q}$)	**278.7 W**
Required Temperature of Heater (T_h) (K)	**688 K (415 °C)**

These calculations gave an approximation of the heating requirements needed for the radiant heater. It was then required to validate this in practice with calibration experiments. Several samples were heated, and temperature was recorded on the surface of the heater using the thermocouple built into the control loop. The temperature was recorded on the upper surface and lower surface of the silicone diaphragm using a Flir E8-XT infrared camera and an Etekcity infrared laser thermometer (Note- This infrared camera had improved resolution and temperature range compared to the Flir One used for the induction heating Section. Unfortunately, it was only acquired after the rented induction heater was returned). Fig. 3.12 shows this temperature calibration.

The heater is set to 425°C and the top and bottom of the diaphragm reach stable state temperatures of ~285 °C and ~230 °C respectively giving an estimate part temperature of 257 °C. The actual heater temperature is therefore slightly higher than the predicted required temperature of 415 °C suggesting that the influence of the aluminium blank holder or the cooling effects of the lab were slightly underestimated when choosing the safety factor. The radiant heater reaches the set temperature in approximately 180 seconds and the diaphragm reaches steady state temperature in approximately 600 seconds. In the experiments, a heating time of 900 seconds is used to ensure that the part is appropriately heated throughout. Temperatures higher than 425°C tended to damage the silicone rubber used in the diaphragm bag leading to the bag rupturing during press forming (see Fig. 3.20), showing the limitations of the radiant heating process in forming at higher temperatures. Fig. 3.13 shows IR images taken with the Flir E8-XT IR camera at the start of the heating process (Fig. 3.13a) and at the end of the heating process (Fig. 3.13b). The sample appears to heat evenly, and the high temperature of the radiant heater can be seen reflected in the aluminium blank holder.

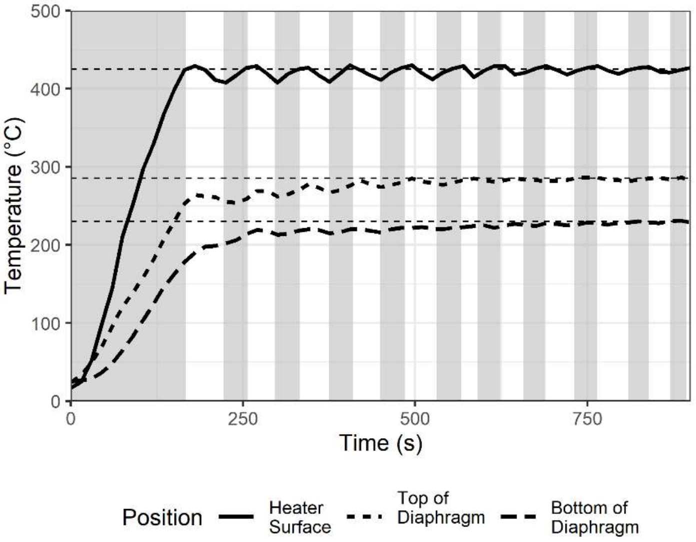

Figure 3.12 Temperature vs time at three measurement positions during calibration of radiant heater. Gray Shading shows active heating. Process approaches steady state temperatures of 425, 285 and 230 °C for heater surface, top of diaphragm and bottom of diaphragm respectively.

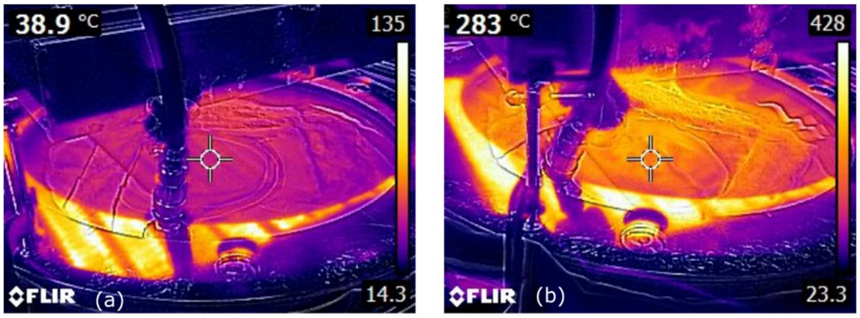

Fig 3.13 Captured images from Flir E8-XT IR camera: (a) showing heated sample shortly after heating begins and (b) showing sample at high temperature before forming.

This Section has introduced the basic setup of a novel induction melt thermoforming process that will aim to use molten tin to lubricate the forming of a nylon-carbon fibre composite (a lubricated blank). It also discusses the details of a radiant heater thermoforming process that will be used as a control to help evaluate the relative performance of the Imelt thermoforming process. Selected results from the induction melt and radiant heater thermoforming processes will be discussed in the rest of the Chapter.

3.4 Induction Melt Thermoforming Results

The Imelt thermoforming results progress from simple cases proving the experimental setup and progress to more complicated set ups as outlined below.

- Consolidation of two nylon-carbon fibre laminates while expelling a single layer of tin
- Consolidation of four nylon-carbon fibre laminates while expelling three layers of tin
- Thermoforming a ripple pattern using two nylon-carbon fibre laminates while expelling a single layer of tin
- Thermoforming a ripple pattern using three nylon-carbon fibre laminates while expelling two layers of tin

The objectives are to first prove that single layers can be heated and expelled, then multiple layers can be heated and expelled. From there the process was repeated while forming the sheets into complex ripple geometries. A further summary of the forming conditions can be seen in Table 3.3 at the end of the Chapter.

3.4.1 Heating and consolidation of a flat plate with one layer of tin

Initial experiments looked to heat and consolidate two [0/90/90/0] pre-consolidated carbon-nylon sheets and expel a single layer of molten tin. The objective of this was to test the feasibility of heating the laminates via induction heating and check that the molten tin would evacuate the sample. Therefore a layup of [0/90/90/0/$\bar{T}$]$_S$ was chosen. This has two pre-consolidated laminates of carbon-nylon composite and one sheet of tin, all sheets were circular with a diameter of 130 mm. This initial exploration used a hollow plastic 3D printed prototype of the multi-step forming tool (filled with lead shot to create a self-weight pressure of ~10 kPa). A picture of this can be seen in Fig. 3.5d. The specimen was held under vacuum pressure with the silicone rubber diaphragm. The specimen was heated until a diaphragm surface temperature of 250 °C was reached and the part was pressed at 500 mm/min against a flat false base plate. The pressure of the vacuum and the self-weight of the tooling was applied without any extra consolidation pressure. The result is shown in Fig. 3.14a (plan view) and in Fig 3.14b (internal cross-section). The tin flowed out the side of the specimen due to the squeeze flow and initial visual inspection of a cross-section (later reinforced with x-rays) suggests a low residual tin content. Therefore the objectives for this test was considered a success.

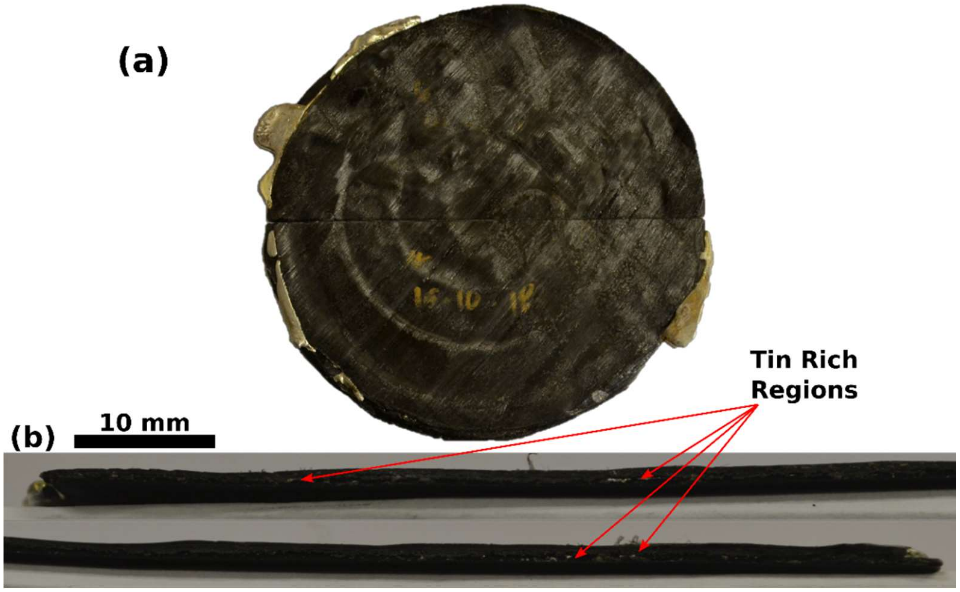

Figure 3.14. Single layer of tin expelled from two carbon-nylon laminates [0/90/90/0/$\bar{T}$]$_S$: (a) plan view showing cutting line, (b) cross-section along cutting line showing small traces of residual tin (above, from left edge to centre, below from centre to right edge).

3.4.2 Heating and consolidation of a flat plate with three layers of tin

For all tests going forward, the steel version of the multistep tooling was used as it had completed manufacture (See Fig 3.5a-c). The intentions were twofold. Firstly to prove the feasibility of heating and expelling multiple sheets of tin. Secondly to produce samples for later mechanical testing.

This test had three interlayers of tin separating four circular nylon sheets for an overall layup of $[0/90/90/0/T/90/0/0/90/\bar{T}]_S$. All sheets were 130 mm in diameter. The specimen was held under vacuum inside the silicone rubber diaphragm and heated until a diaphragm surface temperature of 250 °C was achieved before being pressed at 500 mm/min against the false base plate. The pressure of the vacuum and the self-weight of the steel multistep tool (50 kPa) was used to consolidate the part. A selected result is shown in Fig. 3.15a (plan view) and in Fig. 3.15b (internal cross-section). Initial visual inspection of the cross-section (Fig. 3.15b) again indicates a low residual tin content. A varying thickness is visible in Fig. 3.15 which is a result of manufacturing errors in the tooling annuli meaning there was ~0.2 mm difference in the level of the annuli when fully compressed.

A total of six similar tests were performed. In one of these, full melting of the interlaminar tin was not obtained (i.e., a small region of undeformed tin sheet with no bonding between nylon plies was left behind), deeming that test a failure. The other five were successful in both obtaining full melting and in removing the vast majority of the interlaminar tin (see Section 4.3). The last two of these tests used an additional 1 mm thick layer of silicone rubber above and below the specimen layup (see Section 3.3.3) which appeared to aid the heating of the part and the expulsion of the tin. A summary of the parameters can be seen in Table 3.3, under Tin-IA and Tin-IB (Referring to specimens without the additional 1 mm thick layer of silicone rubber, and with the additional layer respectively). These specimens are also discussed in more detail in Chapters 4 and 5 as the specimens are used to produce test coupons for exploration of the residual tin quantities and mechanical properties.

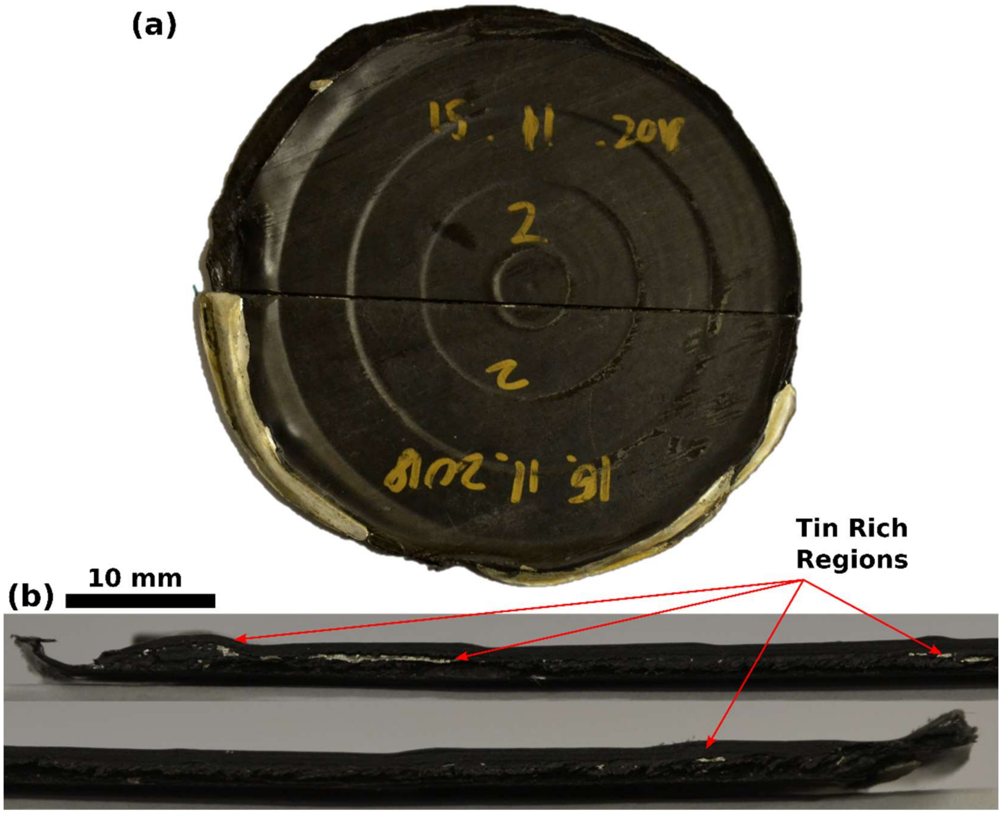

Figure 3.15: Three layers of tin expelled from four carbon-nylon laminates $[0/90/90/0/T/90/0/0/90/\bar{T}]_S$: (a) plan view showing cutting line, (b) cross-section along cutting line showing small traces of residual tin (above, from left edge to centre, below from centre to right edge).

3.4.3 Ripple forming using a single layer of tin I

This test used the steel multi-step tool to form a specimen containing a single tin layer and two carbon-nylon sheets with an overall layup of $[0/90/90/0/\bar{T}\ ]_S$. The objective is to test if tin can be removed when forming a complex geometry and identify trends in wrinkle formation.

The layup is held inside the silicone diaphragm under vacuum pressure with an extra 1 mm protective silicone sheet above and below the specimen as observation in previous trials indicated this increased temperature homogeneity and smoothed over pressure discontinuities . The 3D printed female tool (Fig. 3.9) was placed on the false base plate and the ABS segmented male tool was attached to the multi-step tool with a weak adhesive (See Fig. 3.9c and Fig. 3.9d for images of the male and female tooling, and Fig. 3.5a for an image of the multistep tool with ABS tooling attached). The specimen was heated to a surface temperature of 250 °C before being pressed at 500 mm/min (refer to Table 3.3, Ripple-I).

The outcome is shown in Fig. 3.16a (plan view) and in Fig. 3.16b (section view). The cross-section reveals good expulsion in some regions, but poor in others with significant amounts of residual tin. The surface of the formed ripple shape has minimal defects and the cross-sectional shape matches the original ripples. There were however areas of residual tin which formed thicker cross-sections. This tended to happen at the peaks and troughs in the ripple shape due to a mixture of gravity pooling the molten tin into the troughs and mismatches in the tool cavity height. The mismatches arose as a result of additional insulating diaphragm material being required to meet heating requirements. The multi-step forming process appears to successfully mitigate damage to the surface of the composite. By drawing the blanks into the dips sequentially the tensile stress in the fibres is lower than if the part was formed in a single step. A total of five specimens were carried out with this layup with 4 being deemed successes and 1 a failure.

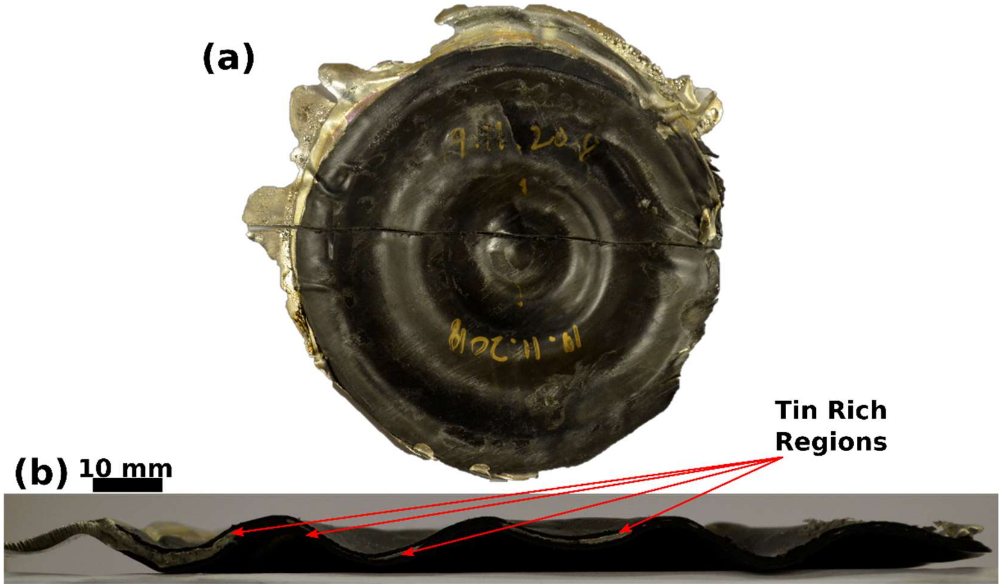

Figure 3.16: One layer of tin expelled from two carbon-nylon laminates [0/90/90/0/$\bar{T}$]$_s$: (a) plan view prior to cutting and (b) cross-section along cutting line showing very little residual tin along the right-hand section but significant amounts of residual tin in the left-hand section.

3.4.4 Ripple forming using a single layer of tin II

A similar test setup as used in Section 3.4.3 was used for this, except the fibre orientation was changed to [0/90/90/0/T/-45/45/45/-45]. This introduces greater translational displacement between adjacent plies increasing opportunity to investigate any lubrication provided by the tin interlayer and its ability to mitigate wrinkling (Refer to Table 3.3, Ripple-I). The result is shown in Fig. 3.17a (plan view), Fig. 3.17b (oblique view), and Fig. 3.17c (internal cross-section). Fig 3.17a shows a smooth wrinkle free appearance in the lower left section of the part and reveals wrinkling in the top right section of the part. These wrinkles are shown more clearly in Fig 3.17b. It was noted that the defect free side of the part tended to lie in the same side as the greatest flow of exiting tin. From internal cross-sections and later x-ray analysis it was noted that the wrinkled side had negligible tin content. It is therefore plausible that the tin is acting as a lubricant, however there are other potential explanations such as regions of high tin content correlating with higher temperatures. The cross-section in Fig. 3.17c shows a reasonable portion of residual tin.

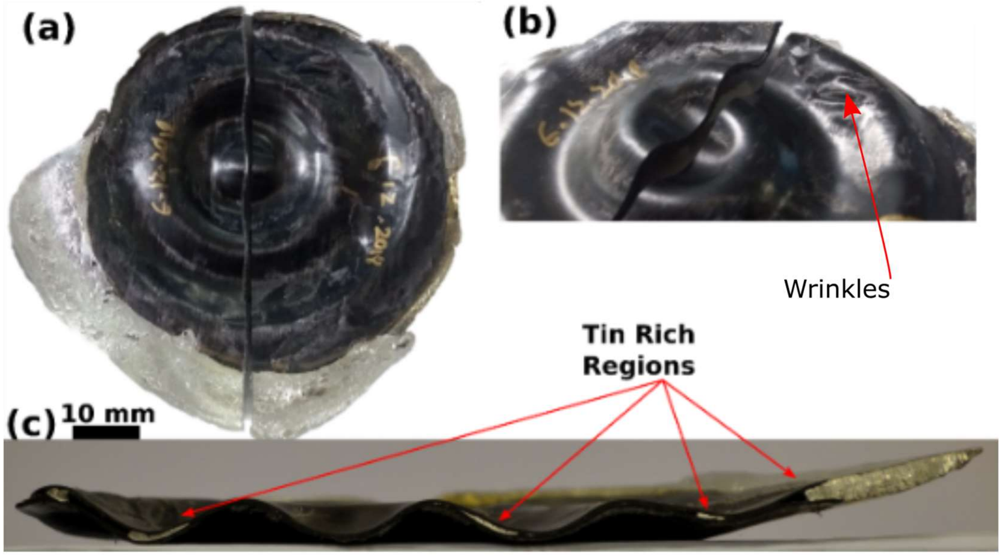

Figure 3.17: Second attempt with one layer of tin expelled from two carbon-nylon laminates [0/90/90/0/T/-45/45/45/-45]: (a) plan view and (b) cross-section along cutting line showing very little residual tin along most of the cross-section. Tin does however, tend to ‘stick’ at corners.

3.4.5 Ripple forming using two layers of tin

As a final experiment, specimens consisting of two tin interlayers and three pre-consolidated carbon/nylon laminates with a layup of $[0/90/90/0/T/-45/45]_s$ were tested. This reduced the heating requirements while still preserving the challenging non-orthogonal forming interfaces. The result is shown in Fig. 3.18a (plan view) and Fig. 3.18b (section view). It can be seen in Fig. 3.18a that there are no wrinkles and there is a high level of symmetry to the part and the tin expulsion. Due to softening of the female polymeric tooling (see Section 3.3.4), the laminate has not conformed to the ripple shape of the tooling and has flattened on the left side. Nevertheless, the internal cross-section in Fig. 3.18b shows good removal of the tin interlayer across the cross-section but with significant localised residual tin on the righthand side of the part.

The results show a lack of wrinkling, indicative of lubrication. It also suggest that it is possible to expel almost all the tin, given the right conditions, as evidenced by the low tin content in the left-hand side of the formed part. However, if the conditions are not suitable, then the tin is not expelled, as evidenced by the high tin content in the right-hand side of the specimen. Therefore the specimen is a partial success has not been a success it suggests that the process could be further optimised to enable effective lubrication, as shown in this example, and effective removal of residual tin, shown in one half of the sample.

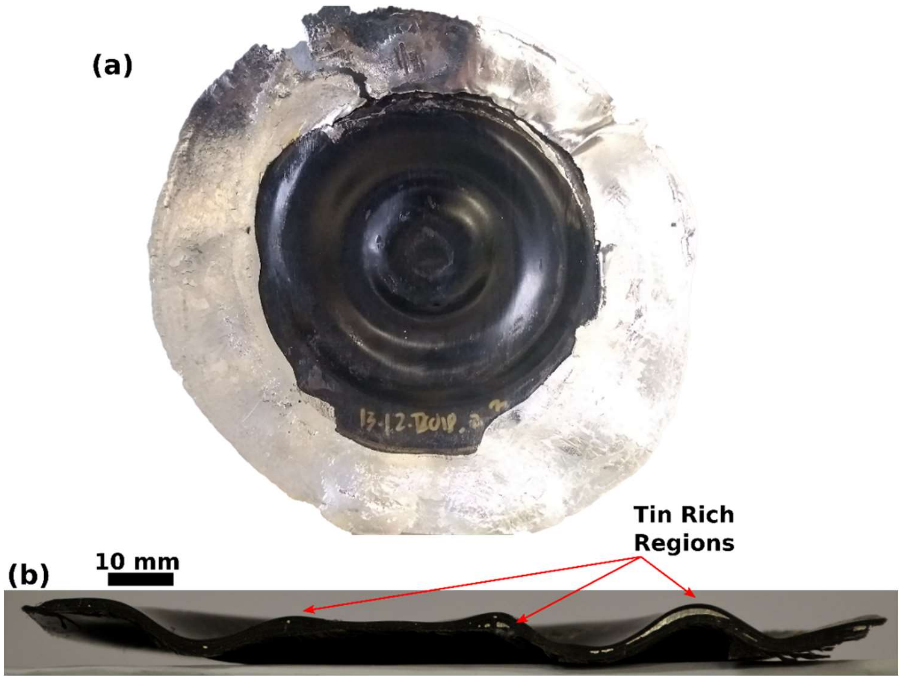

Figure 3.18: Attempt with two layers of tin expelled from three carbon-nylon [0/90/90/0/T/-45/45]$_S$: (a) plan view and (b) cross-section along cutting line showing little residual tin along most of the cross-section.

3.5 Radiant Thermoforming Results

In this Section, some results from the radiant thermoforming will be presented. These were intended to mimic the induction thermoforming and act as a control to assess the influence of the radiant heating process. First, several flat specimens with a layup of [0/90/90/0/90/0/0/90]$_S$ were manufactured for the purposes of later mechanical testing. These will not be discussed in detail in this Section, but they are referred to in Section 5.2 and in Table 3.3 (No Tin-R). Testing then progressed to the thermoforming of the ripple geometry and some results will be presented in the remainder of this Section. For details of the overall setup, refer to Section 3.3 and Fig. 3.4 and Fig. 3.7.

3.5.1 Rippled Thermoforming I

This test used the steel multi-step forming tool with three circular nylon sheets stacked together for an overall layup of [0/90/90/0/90/0]$_S$. The segmented aluminium male tooling (See Fig. 3.5f) was attached to the multistep tool with a light adhesive. The aluminium female tool (see Fig. 3.5e) was secured to the base of the universal press. All sheets were 130 mm in diameter and the specimen was held under vacuum with the silicone rubber diaphragm. The specimen was also covered by a 1 mm thick 150 mm diameter silicone rubber sheet above and below the specimen to mimic the forming conditions used in the induction thermoforming tests. The specimen was heated as outlined in Section 3.3.6 with a part temperature of 260 °C before being shuttled to the press and then formed at 500 mm/min between the multistep male tooling and aluminium female tooling. Fig. 3.19 shows the outcome of this test from a plan view. The specimen has successfully formed and has done so without obvious wrinkling on the surface.

Figure 3.19: Rippled specimen with layup of $[0/90/90/0/90/90/0]_s$.

3.5.2 Rippled Thermoforming II – High Temperature

This test thermoformed three circular nylon sheets with an overall layup of $[0/90/90/0/+45/-45]_s$. This layup introduces translational displacement between adjacent non orthogonal plies during the forming process, thus making it more challenging to form. The circular nylon sheets were 130 mm in diameter and were covered above and below by additional 1 mm thick 150 mm silicone rubber sheets. The specimen was formed with a radiant heater temperature of 475 °C (part temperature of ~280 °C). The specimen was held under vacuum and was formed at 500 mm/min using the steel multi-step tooling with the ripple toolheads. From Fig. 3.20a (plan view) the part has formed well without major wrinkles; however, there are some surface defects as highlighted in red. However, by forming at this higher temperature the upper diaphragm was exposed to high temperatures and was damaged during the forming process (as seen in Fig. 3.20b). This shows some limitations of heating radiantly and the potential benefits of generating heat from within the specimen itself as damaging the surface of the silicone rubber was not an issue when heating inductively. Due to the high costs of the high temperature silicone rubber (~£50/ m^2 [186]) used in the experiments, reuse is strongly desired.

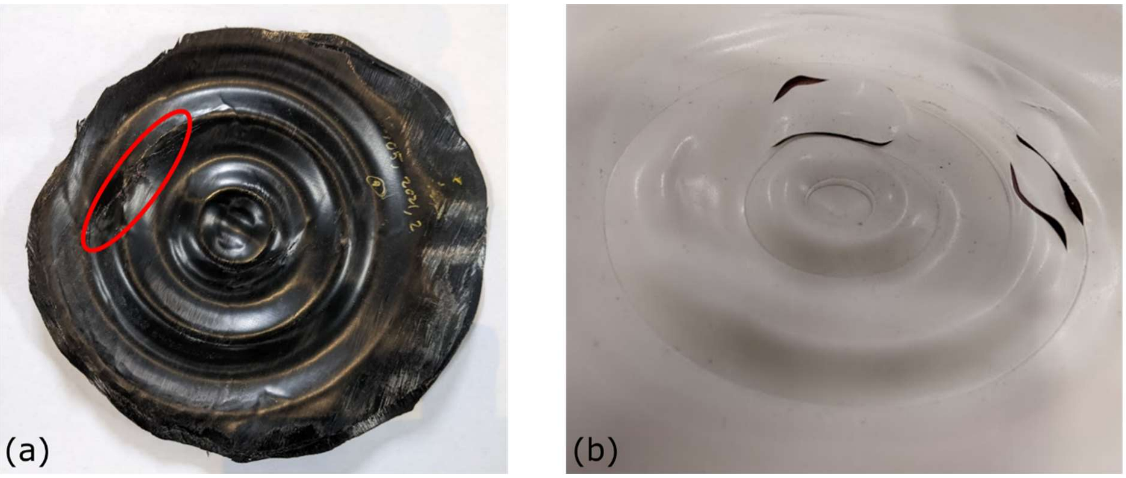

Figure 3.20: Rippled specimen formed with radiant heater temperature of 475 °C and with layup of $[0/90/90/0/+45/-45]_S$: (a) plan view of specimen (Red circle marks defects in part) and (b) Damage to silicone rubber due to high forming temperature.

3.5.3 Rippled Thermoforming III

This final experiment shows a specimen with the same layup and setup as the previous specimen except this specimen is formed at a lower temperature. The fibre layup is $[0/90/90/0/+45/-45]_S$. The part is heated to a temperature of 260 °C as outlined in Section 3.3.6 before being shuttled to the press and formed at a speed of 500 mm/min. The result is shown in Fig. 3.21 and there is wrinkling in the outer ring as highlighted by the red circles. The presence of similar wrinkles persisted in specimens formed at 425 °C. While it appears, these can be mitigated by increasing temperature, this damaged the high temperature silicone rubber. In previous results, the presence of the molten tin may have helped in two ways: (a) reducing damage to the silicone rubber diaphragm sheet by exposing it to a lower temperature and (b) lubricating the forming process allowing for wrinkle-free parts to be produced at lower temperatures.

Figure 3.21 Rippled specimen formed with radiant heater temperature of 425 °C and with layup of $[0/90/90/0/+45/-45]_s$. Red marks show wrinkles near edge of part.

3.6 Conclusions and further steps

In this Section the feasibility of heating and forming carbon-nylon laminates, which were lubricated with molten interlaminar tin, into multi-cavity geometries was explored. A multi-step tool was used to provide a mechanism for generating a pressure gradient that could expel molten tin from within the laminate during forming. The induction thermoforming process was compared with a more conventional radiant thermoforming process to assess the influence of the novel heating method and the influence of interlaminar tin. A summary of the different forming mechanisms can be found in Table 3.3.

Induction heating of the tin interlayers was shown to be an effective method of heating the laminate from within. It was possible to thermoform laminates with three interlayers of tin and remove large quantities of the residual tin (the precise amounts are measured in Chapter 4). It was also possible to form complex geometries, however there were clearly issues with retained molten tin. There is some weak evidence to suggest that the wrinkling defects are mitigated when forming into complex geometries. It is believed that the lubricating properties of the tin may contribute to this, however further work would be required to further confirm this. While the multi-axial radiant heated specimens experienced some wrinkling (Section 3.5.3), the fact that a biaxial non lubricated specimen (Section 3.5.1) can successfully form suggests that the geometry is perhaps not challenging enough for a full evaluation of the lubricating influence of the tin interlayer. Chapter 6 numerically investigates the influence of rippled tooling with a higher amplitude which would be more challenging to form. Future investigations should therefore focus on more challenging geometries to better evaluate positive influence on wrinkling coefficients. The induction heating process had a high failure rate of around 20% due to imprecise manual control (despite the operators' best efforts) indicating that the process requires automation and refinement going forward.

Given the high capital costs required for multistep tooling and heating capacity any commercial use for this technique would require large production volumes to amortise the fixed costs. Furthermore, even with future improvements it is likely that some quantity of residual tin inclusions would be left in the components. This is likely to rule out high performance sectors such as aerospace, and the differential thermal expansion coefficients of tin and nylon risks crack initiation if there is thermal cycling. Therefore a potential use case would be the automative industry where high volumes, complex geometries and low thermal cycling (away from the engine) could provide a viable business case. However proof of consistent tin removal and minimal impact on mechanical properties would be required and these are tested later in the thesis.

Some limitations and potential improvements to the induction thermoforming process have been identified such as

- **Female Tooling:** The use of ABS plastic with a low melt temperature hindered the process. It is believed that use of machined PEEK (or similar thermoplastic with a high melt temperature) or a 3D printed or machined ceramic for the female tooling are fruitful avenues for future exploration.
- **Male tooling:** Large gaps of 1 mm were left between annuli in the multistep tool to ensure that it moved freely. Smaller gaps would however allow for a smooth pressure gradient. It may also be possible to increase the number of steps in the forming process and better match the steps with the design of the tooling to improve flow of interlaminar tin out of the part.

- **Improve and automate the heating process:** These experiments used manual control of the heating process leaving a high level of uncertainty around the forming temperature. Automation and optimisation of the heating process would be required for commercial viability. (E.g., automated system of adjusting power and position of the heating system with a feedback loop based on the temperature distribution over the specimen)
- **Diaphragm**: The weight of the tin deformed the diaphragm. This was partially alleviated by adding thicker 1 mm layers above and below the specimen (see Section 3.3.3).
- **Parametric study:** better understanding of the various process parameters including, but not limited to, influence of tin interlayer thickness, and diaphragm thickness, and design and their influence on the heating process. Furthermore, looking at the influence of forming velocity, forming temperature, and design of the multi-step tooling on the wrinkling mechanics and removal of the metallic interlayer.

Given the time (5 months) and cost constraints of the induction heater rental, fully exploring these options was not possible. This Chapter was focused on proof of concept and producing some prototype results to gain an understanding of the influence of the molten tin. However, given the improvements possible by intuitive adjustments to the process, I believe that further improvements to remove higher quantities of tin and better control the heating process are possible. The rest of the thesis will cover the compositional characterisation and mechanical testing of the produced parts and numerically investigate the forming process of the ripple geometries.

Table 3.3: Details of the forming processes. Specimens produced are 130 mm diameter circular plates unless otherwise specified.

	1. No Tin-R	2. No Tin-P	3. Tin-IA	4. Tin-IB	5. Ripple-I	6. Ripple-R
Objective	Flat Control Specimens produced internally	Flat Control Specimens produced externally	Flat specimens with interlaminar tin for mechanical testing	Flat Specimens with interlaminar tin for mechanical testing - additional diaphragm material	Ripple specimens with interlaminar tin	Ripple specimens without interlaminar tin
No. Specimens Produced - Layup	**3** - [0/90/90/0/90/0/0/90]$_S$	**1** - [0/90/90/0/90/0/0/90]$_S$ 300 x 300 mm sheet	**3**- [0/90/90/0/T/90/0/0/90/$\bar{T}$]$_S$	**2** - [0/90/90/0/T/90/0/0/90/$\bar{T}$]$_S$	**4** of [0/90/90/0/]$_s$ **4** of [0/90/90/0/-45/+45/+45/-45] **3 of** [0/90/90/0/+45/-45]$_s$	**3** of [0/90/90/0/]$_s$ **3** of [0/90/90/0/-45/+45/+45/-45] **3 of** [0/90/90/0/+45/-45]$_s$
Consolidation Temp (°c)	270	270	250	250	250	270
Consolidation Pressure (Bar)	2	4	2	2	2	2
Heating Method	Radiant Heater	Heated Platens	Induction Heater	Induction Heater	Induction Heater	Radiant Heater
Cooling Method	15 min. consolidation in press	50 min. air cooling -> 10 min. water cooling	15 min. consolidation in press	15 min. consolidation in press	15 min. consolidation in press	15 min. consolidation in press
Consolidation Tool	Multi-Step Press + Steel Base	Heated Platens	Multi-Step Press + Epoxy-glass fibre base	Multi-Step Press + epoxy glass fibre base	Multi-Step Press + male/female Aluminium tooling	Multi-Step Press + male/female Aluminium tooling
Diaphragm	0.3 mm Silicone Rubber + 1.0 mm thick Silicone rubber around layup	n/a	0.3 mm Silicone Rubber	0.3 mm Silicone Rubber + 1.0 mm thick Silicone rubber around layup	0.3 mm Silicone Rubber + 1.0 mm thick Silicone rubber around layup	0.3 mm Silicone Rubber + 1.0 mm thick Silicone rubber around layup
Diagrammatic representation (Not to scale)	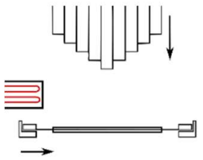	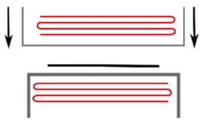	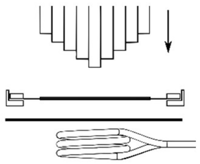	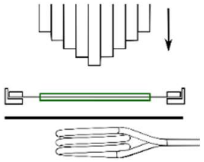	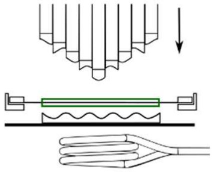	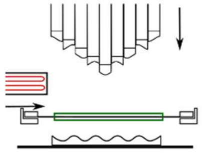

Chapter 4 Non-Destructive Testing and Tin Quantification

4.1 Introduction

The manufactured parts discussed in Chapter 3 contain quantities of residual tin. Being able to measure the location and quantity of residual tin is highly desirable for a few reasons. Firstly, quantification is required to assess any influence the tin has on part properties. Secondly, being able to swiftly and cheaply evaluate part quality is necessary if the iMelt thermoforming process is to be used in industry.

4.1.1 Non-Destructive Testing

One method of assessing the residual tin is optical microscopy. This requires cutting the part and polishing a surface to obtain a clean cross-section. This cross-section can then be analysed by either optical or scanning electron microscopes. This method has been used successfully to identify factors such as fibre volume fraction, porosity, fibre length and fibre orientation [187]. However, only exposed surfaces can be examined. Thus, full examination of the interior of a specimen effectively destroys the specimen. It is therefore desirable to also identify methods of examining specimens non-destructively. One such technique is x-ray radiography. As x-ray beams pass through a material, energy is lost via absorption or scattering [188]. By measuring the electromagnetic waves after they pass through an object, the differing intensities allow for evaluation of the internal structure. X-ray intensity along a path can be found using the Lambert-Beer's law as follows [189]:

$$I_x = I_0 e^{-\mu x} \tag{4.1}$$

where I_x is x-ray intensity at depth x, I_0 is initial x-ray intensity and μ is the linear attenuation coefficient. Strictly, this is only valid for x-rays of a single energy and wavelength. However, it provides a good approximation of the behaviour of even polychromatic beams [189]. The linear attenuation coefficient is influenced by several factors and depends on photo absorption effects, Rayleigh scattering and Compton scattering [190]. Contrast between materials requires those materials to have differing linear attenuation coefficients. In this investigation, the aim is to identify tin embedded in a nylon-carbon fibre laminate. The approximate linear attenuation coefficients of 6 cm^{-1} for tin, 0.4 cm^{-1} for pure carbon [191] and 0.2 cm^{-1} for nylon [192] mean that full depth penetration of the nylon-carbon fibre sample is possible, and there is good contrast between the tin and the carbon/nylon composite due to the difference in attenuation coefficients.

Conventional radiography involves passing high energy electromagnetic radiation (x-rays) through an object and on to a detector (e.g., film, phosphor plate or semiconductor for digital imaging), creating a 2D 'shadow’ of the internal structure of the object [193]. This process could be used to image the residual tin quickly; however, the technique does not give information on through-thickness location [194], [195]. In contrast, x-ray computed tomography (x-ray CT) can be used to construct a 3D image of an object. X-ray images are collected from multiple angles and reconstructive algorithms are used to create full 3D images [190]. While x-ray CT is primarily used in the medical field, it has also been used to image the internal structure of naturally occurring rocks [189], manufactured products [196] and in visualising the meso- and micro-structure of polymer composites, allowing imaging of internal fibre architecture and damage, with a potential resolution of around 5-7 microns [197], [198], [199], [200], [201].

As powerful as CT scans are, they do have drawbacks. High resolution scans can only be performed on small volumes, the scanning and reconstruction process can be time consuming, and the initial cost for the equipment is high [197]. Furthermore, care must be taken in the setup of the scans and the interpretation of the results to avoid artifacts in the images. X-ray beams consist of photons of varying energy. As these photons pass through an object, the lower energy photons are preferentially absorbed, increasing the mean energy of the beam as shown in Fig. 4.1 This is referred to as beam hardening and can lead to imaging artifacts when interpreting the scan results, such as dark streaks between optically dense objects. In order to manage this phenomenon, a tin prefilter was used to “pre-harden” the x-rays used in the CT scanning used in this chapter. Other artifacts can occur when dense objects are only partially captured by the x-rays, or when overly dense objects absorb large quantities of photons leading to “Photon starvation” and noisy projections. More details on artifacts and imaging issues can be found in Barrett et al [202].

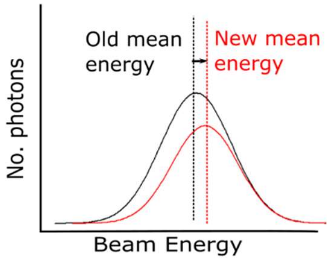

Figure 4.1: Influence of beam hardening on mean energy. The average energy of an x-ray beam increases after passing through an optically dense object. The increased average energy can then affects the interpretation of other objects.

Thresholding is an image processing method used to distinguish between objects and background. This is often based on grey-level histograms where the colour intensity of the object and background is used to differentiate between materials. For clearly defined images, a bimodal distribution will be seen allowing for the bottom of the valley to be chosen as the threshold. Many images are not bimodal and thus more complex algorithms are required. Examples of these include the Otsu Algorithm [203], iterative algorithms [204] and algorithms based on information entropy [205]. A survey of recent developments in the field can be found in [206]. The work presented in this Chapter later uses Renyi’s Entropy Algorithm [207] along with grey value segmentation to threshold x-ray images. Optical measurements are also used to verify and calibrate the thresholding.

4.1.2 Fresnel’s Equation’s

When electromagnetic waves (such as x-rays) move between mediums of differing optical density, the incident wave is split between a reflected portion and a refracted portion as shown in Fig. 4.2. The transmitted light is refracted in accordance with Snell's law [208]. The nomenclature is as follows. θ_i = angle of incident light, θ_r= angle of reflected light, θ_t= angle of transmitted light, n_1= refractive index of first medium n_2=refractive index of second medium.

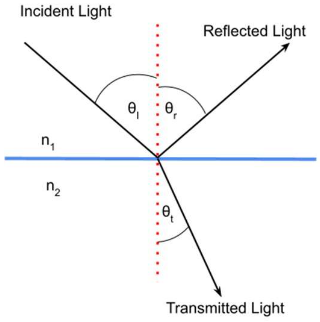

Figure 4.2 Diagrammatic representation of behaviour of electromagnetic wave incident on boundary between two media of differing optical density. θ_i = angle of incident light, θ_r= angle of reflected light, θ_t= angle of transmitted light, n_1= refractive index of first medium n_2=refractive index of second medium.

Fresnel equations describe the proportional split between the reflected and the transmitted waves at the boundary of optical media of differing densities. Incident light can be split into s-polarised (normal to plane of incidence) and p-polarised (perpendicular to plane of incidence). The intensity of light reflected for each polarisation state (R_s and R_p respectively) is defined by Eqs. 4.2 and 4.3. For unpolarised light, the effective reflectiveness (R) can then be taken as the average of the two values as shown in Eq. 4.4 [209].

The complex refractive index (n) for materials can be calculated as shown in Eq. 4.5 and is formed of two components ($Delta\ (d)$ and $Beta\ (\beta)$). At wave energies of 30 keV, these values are;

d= 1.34 x 10^{-6} and β= 9.64 x 10^{-8} for tin [210],

d= 5.56x 10^{-7} and β= 1.81x 10^{-10} for nylon [210].

The resulting refractive indexes can be seen in Table 4.1, along with the relative magnetic permeabilities (M) [211], [212]. The refractive index and magnetic permeability for air can both be assumed as being one [209].

$$R_s = \left(\frac{\left(\frac{n_1}{\mathrm{M}_1}\right) \cos(\theta_i) - \left(\frac{n_2}{\mathrm{M}_2}\right) \cos(\theta_t)}{\left(\frac{n_2}{\mathrm{M}_2}\right) \cos(\theta_i) + \left(\frac{n_2}{\mathrm{M}_2}\right) \cos(\theta_t)} \right)^2 \tag{4.2}$$

$$R_p = \left(\frac{\left(\frac{n_2}{\mathrm{M}_2}\right) \cos(\theta_i) - \left(\frac{n_1}{\mathrm{M}_1}\right) \cos(\theta_t)}{\left(\frac{n_2}{\mathrm{M}_2}\right) \cos(\theta_i) + \left(\frac{n_1}{\mathrm{M}_1}\right) \cos(\theta_t)} \right)^2 \tag{4.3}$$

$$R = \frac{R_s + R_p}{2} \tag{4.4}$$

$$n = 1 - d + i\,\beta \tag{4.5}$$

Table 4.1. Magnetic permeability and refractive indexes of air, tin, and nylon [23].

Material	Magnetic Permeability (M)	Refractive Index (n)
Air	1	1
Tin	0.999977	0.99999856
Nylon	0.999986	0.99999944

Given this information, the reflection coefficient for the air-nylon, air-tin, and tin-nylon interfaces can be calculated and is shown as a function of incidence angle in Fig. 4.3. This shows that a negligible portion of the incident light is reflected at the interfaces, and a marginal difference between the interfaces. As very little of the incident light is reflected, any drops in x-ray intensity can be primarily attributed to attenuation losses through the thickness of the material.

Note, the exact reflection coefficient depends on the energy of the incident waves, however δ and β tend to become smaller with higher energy, leading to smaller reflection coefficients [210]. Thus, given that the energies used in the x-ray analysis in this section were higher than 30 keV, the reflection coefficients will be smaller than calculated here.

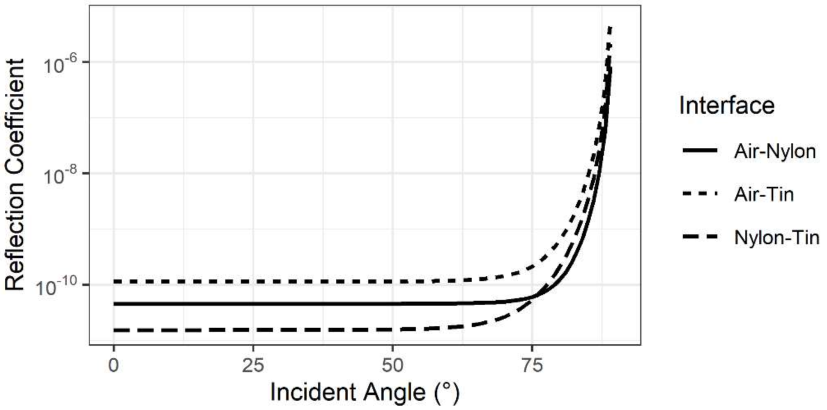

Figure 4.3 Reflection Coefficient for air-nylon, air-tin and nylon-tin interface at 30 keV as a function of incidence angle. A very small portion of incident waves are reflected.

4.1.3 Potential Influence of Residual Tin

High levels of residual tin are potentially detrimental for three main reasons. First, they will increase the mass of the final part as Tin is significantly denser than nylon. The percentage change in density ($\%_{\Delta\rho}$) when a volume of tin (V_t) replaces an equivalent volume of CFR nylon from a part with original volume (V_o) can be found as follows,

$$\%_{\Delta\rho} = \frac{[\rho_{CFRnylon}(V_o - V_t) + \rho_{tin}(V_t)] - (V_o) \times \rho_{CFRnylon}}{V_o \times \rho_{CFRnylon}}. \tag{4.6}$$

Taking $\rho_{CFRnylon} = 1.45\ \mathrm{g/cm^3}$ [131], and $\rho_{tin} = 7.28\ \mathrm{g/cm^3}$ [149]gives the following:

$$\%_{\Delta\rho} = \frac{\rho_{tin} - \rho_{nylon}}{\rho_{nylon}} \times \frac{V_t}{V_o} => \ 4.02\frac{V_t}{V_o} \tag{4.7}$$

[213]This shows that the density of a composite with one percent of tin by volume would be ~ 4 percent denser than without the tin, and five percent of tin by volume would be ~ 20 percent denser. This clearly necessitates minimising tin content for the process to be viable.

Secondly, the presence of tin replaces interlaminar nylon bonds with a nylon-tin-nylon interface. Strong hydrogen bonds form between nylon molecular chains and these are unlikely to form with a tin lattice resulting in a weaker interface. Testing on this is carried out in Chapter 5.

Thirdly, recycling of composites is a growing concern, and the inclusion of residual metal may complicate the processes [157]. While partial energy recovery through incineration is possible, recycling the material is preferred [158]. Given the common use of metallic fasteners in composites this is unlikely to be a unique blocker, however recycling was discussed in Section 2.9.

4.2 Methods

4.2.1 Imaging

The quantity and distribution of residual tin in the post-consolidated laminates was measured using three techniques: 2D x-rays, 3D x-ray CT and optical imaging of cross-sections. Both x-ray techniques were used to obtain information about the distribution of the residual tin. The x-ray CT scans give more information about the residual tin than the 2D x-rays but are significantly more expensive in processing time and capital investment. Both are compared to first validate the results, and secondly to see if the extra information provided by the x-ray CT is necessary for bulk observations which might be used in quality control processes. Optical imaging gives a high-resolution view of the residual tin which can be reliably interpreted and, as such, can be used to calibrate the thresholding of the x-ray results.

For the 2D x-ray analysis, samples were scanned at 130 kV and 5 mA for 2 seconds from 600 mm, using an x-ray generator as shown in Fig. 4.4 (a). The images were collected on D4 film [214] and digitised using a backlight and digital camera. For the 3D x-ray analysis, selected samples were scanned in a Nikon XT H 225/320 LC computed tomography device at 140 kV and 136 μA as shown in Fig. 4.4 (b). A 0.5 mm tin pre-filter was placed over the x-ray tube to reduce the influence of beam hardening effects [202] as discussed in Section 4.1.1. A voxel size of approximately 60 microns was achieved for all samples. The CT scan data was compared with polished cross-sections to ensure accurate thresholding values were chosen. For the sectioning, samples were bisected, mounted in resin, and polished using a Struers LaboForce-50. Images were then captured using a Thorlabs Cerna optical microscope with 8-megapixel digital camera and a x5 lens. The sample was mounted on a motorised stage and images were taken to cover the full sample. The images were then merged using Hugin Panorama photo stitching software.

CT scans were carried out on five flat multi-layer sheets (Tin-IA and Tin-IB, as discussed in Section 3.4.2). Film x-rays were carried out on the same flat samples and additionally on the ripple geometry specimens (Ripple-I) outlined in Sections 3.4.3-3.4.5. Readers can also refer to Table 3.3 which summarises the forming processes used for each of the experiments.

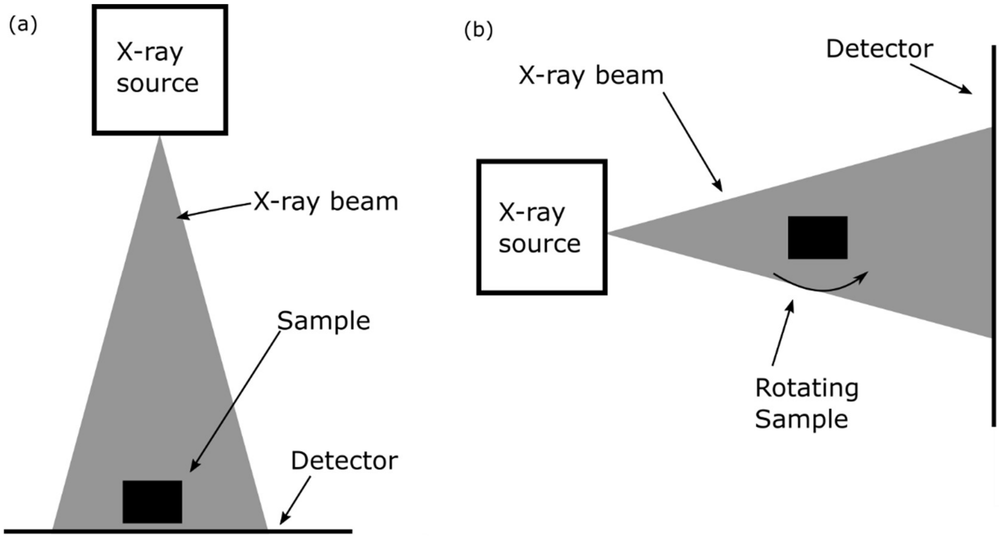

Figure 4.4: Schematic of x-ray set up: (a) conventional x-ray with beam landing on D4 film and (b) CT scan with rotating sample and digital detector.

It was hypothesised that the influence of the tin on final material properties might correlate with either: **(1)** the percentage projected surface area covered by residual tin, or **(2)** the percentage volume of residual tin in a part. The first metric gives an indication of the interrupted interlaminar bonding between plies. The second provides an estimate of the mass of residual tin within the laminate. Note that neither of these measures provides information on the distribution of the tin within the laminate.

4.2.2 Analysis

To quantify these metrics, the CT scan data was first segmented in Simpleware ScanIP (Synopsys, USA) to identify regions of tin. Scans were segmented by light intensity and the scans were cross referenced with microscope cross-sections to determine the appropriate values. The scan was then exported into a 3D image stack and analysed in MATLAB. Surface area characterisation was obtained by projecting the full image stack onto a single plane and then calculating the areal tin coverage using the known voxel dimensions. Volume characterisation used a similar method, however a count was kept to determine the “thickness” of each superimposed pixel. This approximated thickness was then used to calculate the total volume of residual tin [205].

The 2D X-rays were digitised, then converted to grayscale before being reorientated and rescaled to match the CT scans. The images were then segmented in ImageJ using a Renyi Entropy algorithm to differentiate between the tin and nylon-carbon [207]. The thresholded images were then imported into MATLAB, allowing the surface area covered by tin to be calculated using known part dimensions and pixel sizes. To approximate the volume of residual tin from film x-rays, data points corresponding to the same identifiable physical feature on both the film and CT scan results are compared. The thickness of residual tin (t) from the CT scans is compared with the grayscale (Ω) values from the film X-rays. From these data points an estimated thickness-greyscale correlation was obtained as follows

$$t = 0 \qquad if\ \Omega < 25 \tag{4.8}$$

$$t = p_1 * G + p_2 \qquad if\ \Omega \geq 25 \tag{4.9}$$

Where p_1 = 0.003645 (95% confidence range, 0.002828-0.004462) and p_2 = 0.1275 (95% confidence range, 0.04169- 0.2134). These datapoints are shown in Fig. 4.5 along with the correlation in red. This confidence range and equation applied to the digitised film x-rays is then used to calculate the tin volumes seen in Table 4.2.

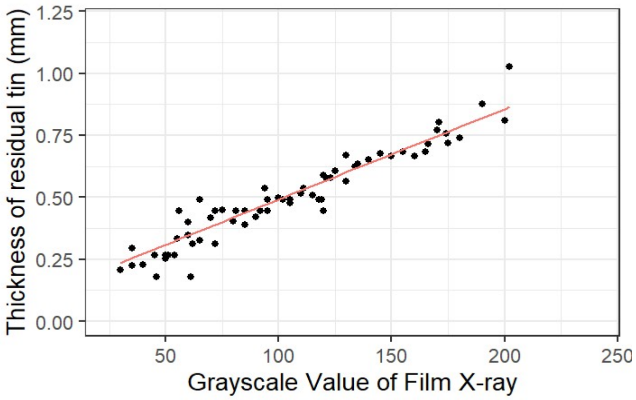

Figure 4.5: Plot of thickness of residual tin (Obtained from CT scans) compared with grayscale value obtained from film x-rays.

4.3 Results

4.3.1 Residual tin content

In this Section, an overview of the x-ray and optical analysis of the residual tin content is given. Table 4.2 shows the volume of residual tin (as a percentage of final part volume) for a selection of the flat consolidated discs. The scans were carried out using a Nikon XT H 225/320 LC Computer Tomography system as detailed in Section 4.2.1. Over the duration of the investigation, the iMelt process was steadily improved - this is apparent in the results presented chronologically from top to bottom in Table 4.2: i.e., residual tin quantities decreased as the process was improved over time. Results show tin volumes consistently below 5-10 % when heating and forming multilayer flat specimens, demonstrating the basic principle of the multistep tooling, i.e., generation of a squeeze flow capable of expelling most of the interlaminar tin. Tests Tin-IA1 to Tin-IA3 use a single 0.3 mm thick silicone diaphragm sheet above and below the part whereas tests Tin-IB4 and Tin-IB5 were constrained by an additional 1 mm thick silicone diaphragm sheet above and below the part as discussed in Section 3.3.3. Potential reasons for these improvements are (1) higher temperatures in the molten tin due to improved thermal insulation or (2) more continuous pressure profile caused by the thicker rubber layer smoothing over discontinuities caused by the step profile in the tooling or mismatches in the male and female tooling.

Table 4.2: Residual tin volume as a percentage of final part volume for [0/90/90/0/T/90/0/0/90/$\bar{T}$]S layup on flat plate, determined using CT scans. Tin-IA1-3 were constrained by a single 0.3 mm diaphragm sheet above and below while Tin-IB4-5 were additionally constrained by an additional 1 mm thick 150 mm diameter sheet above and below the sample. Uncertainties relate to the resolution of the CT scan (~50 µm)

Test	Residual Tin Volume (%)	Volume of Original Tin Interlayer Removed (%)
Tin-IA1	$5.7 \pm^{4.1}_{2.6}$	$97.0 \pm^{2.1}_{1.4}$
Tin-IA2	$4.2 \pm^{2.4}_{1.6}$	$97.8 \pm^{1.3}_{0.9}$
Tin-IA3	$1.5 \pm^{0.8}_{0.5}$	$99.4\pm^{0.2}_{0.4}$
Tin-IB4	$2.5 \pm^{2.2}_{1.3}$	$98.6\pm^{0.8}_{1.3}$
Tin-IB5	$1.6 \pm^{1.6}_{0.9}$	$99.0\pm^{0.5}_{0.9}$

Table 4.3 shows the volume of residual tin as a percentage of the volume for a selection of formed ripple geometry parts. This information comes from film x-rays as outlined in Section 4.2.2. The tin volume percentages in Table 4.3 are higher than for the flat discs, ranging from 8-32 %. In addition to the challenges discussed in Section 3.3.5, several factors increased the comparative difficulty in expelling tin for the ripple geometry. One was tooling misalignment and tooling tolerances: deviations in tool axis alignment, or inaccuracies in the coarse 3D printed male and female tool surface geometries could all alter the pressure gradient acting on the molten tin. The segmented male tooling was also manufactured with large tolerances, resulting in small gaps between annuli (up to 1 mm, see Fig. 3.8) potentially resulting in low pressure areas that could disrupt the outward pressure gradient. Furthermore, the ABS tooling experienced deformation due to exposure to high temperatures. The tooling was regularly replaced to minimise this, but the pressure distribution would be affected. The complex shape of the ripple geometry also caused shear deformation of the nylon/carbon fibre laminate leading to varying laminate thickness. Given that the designed gap between the tools is constant at 1.74 mm thickness, this would lead to regions of high and low pressure, again disrupting the squeeze flow out of the laminate.

Table 4.3: Residual tin volume as percentage of final part volume for ripple geometries. Determined from X ray scans of part. Uncertainties relate to the resolution of the X-ray (~0.2 mm)

Test number	Layup	Residual Tin Volume (%)	Volume of Original Interlayer Removed (%)
Tin-IC6	[0°/90°/90°/0°/$\bar{T}$]$_s$	$18.2\pm^{5.6}_{6.2}$	$82.4 \pm^{6.0}_{5.4}$
Tin-IC 7	[0°/90°/90°/0°/$\bar{T}$]$_s$	$11.4\pm^{3.7}_{4.5}$	$88.8\pm^{4.4}_{3.6}$
Tin-IC8	[0°/90°/90°/0°/$\bar{T}$]$_s$	$15.9\pm^{5.0}_{5.6}$	$86.4\pm^{4.8}_{4.3}$
Tin-IC9	[0°/90°/90°/0°/$\bar{T}$]$_s$	$15.2\pm^{5.0}_{4.5}$	$83.9\pm^{4.8}_{5.2}$
Tin-IC10	[0°/90°/90°/0°/T/-45°/45°/45°/-45°]	$20.2\pm^{7.5}_{6.4}$	$81.2\pm^{6.9}_{6.0}$
Tin-IC11	[0°/90°/90°/0°/T/-45°/45°/45°/-45°]	$12.3\pm^{4.1}_{5.0}$	$86.8\pm^{5.4}_{4.4}$
Tin-IC12	[0°/90°/90°/0°/T/-45°/45°/45°/-45°]	$32.4\pm^{9.7}_{10.6}$	$72.4\pm^{8.8}_{8.0}$
Tin-IC13	[0°/90°/90°/0°/T/-45°/45°/45°/-45°]	$11.1\pm^{3.5}_{4.2}$	$88.4\pm^{3.7}_{4.4}$
Tin-IC14	[0°/90°/90°/0°/T/-45°/45°]$_s$	$8.3\pm^{3.2}_{4.2}$	$96.4\pm^{1.9}_{1.4}$

4.3.2 Imaging and distribution

The microscope images of the polished cross-section in Fig. 4.6 show that the residual tin lies exclusively in the three interfaces corresponding to the original tin sheet locations and does not penetrate through the plies. It can also be seen from the images that the residual tin tends to form large fragments with the vast majority being above 100 microns in size. This indicates that the CT scans will detect most of the residual tin inside the sample and can be used to give an accurate representation of the level of residual tin.

Fig. 4.7 shows a comparison between a 3D CT scan and a 2D film X-ray of a bisected sample. Fig. 4.7a shows the raw segmented data from the CT scan with a significant number of residual tin fragments distributed around the specimen. In Fig. 4.7b this data has been transformed in MATLAB to produce a 2D projection with light intensity scaling with thickness of tin. Fig. 4.7b shows that most of the residual tin is, in fact, quite thin (<0.25mm). Finally, in Fig. 4.7c a digitised 2D film x-ray of the same sample is shown. In this instance, both methods capture similar physical phenomena, although the CT scan has higher resolution and can detect smaller fragments than the 2D x-ray. The importance of the 2D x-ray lies in the speed at which it can be deployed in the quality control of parts. Although less accurate in detecting smaller fragments, Fig. 4.7 (which contains a relatively high volume of tin) indicates that the 2D film x-ray may be sufficient to rapidly assess the quality of mass-produced parts.

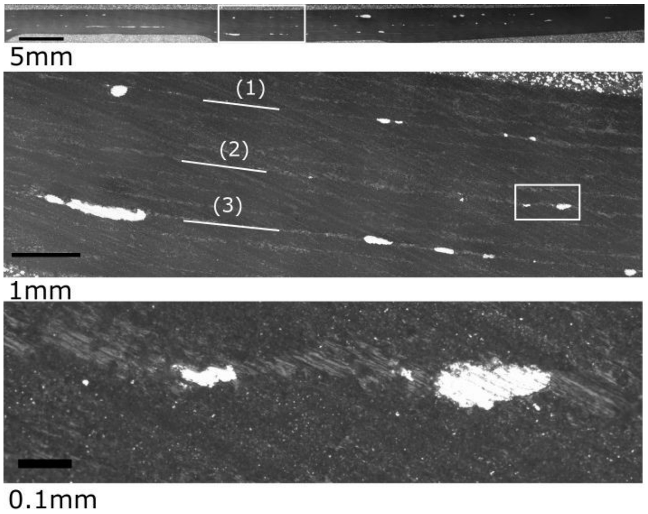

Figure 4.6: Microscope images of the polished cross-section. Images taken from sample Tin-IA3. Lines indicate the three interlaminar layers which originally contained interlaminar tin.

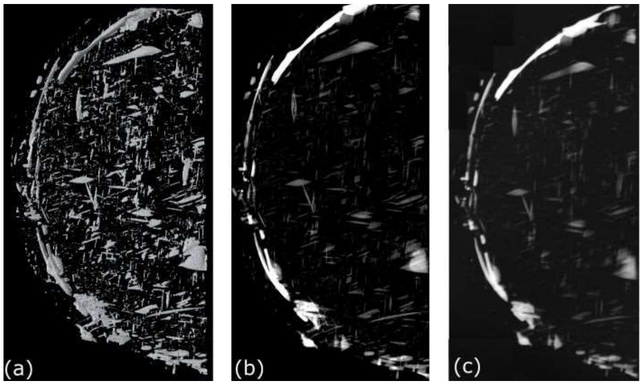

Figure 4.7: Comparison between (a) segmented 3D CT scan showing residual tin in a bisected circular sample, (b) 2D projection of same 3D scan with intensity adjusted for thickness and (c) 2D X-ray of same sample. Results are from the Tin -IA1 sample (containing ~5.7 % vol of tin).

Datasets regarding residual tin fragments of the flat CT scanned samples were extracted via Simpleware to explore the distribution and dimensions of the residual tin fragments. In Fig. 4.8 the orientation of the major axis is compared with the length along the major axis (90° = parallel to surface). The vast majority of the residual tin fragments lie parallel to the surface of the part with the median fragment orientation being 87.4 °. Furthermore, the likelihood of the fragment lying parallel to the surface increases as the fragments become larger. Fig. 4.9 shows that most of the tin fragments are long and thin, with an average minor to major axis ratio of 0.232. Given the high level of similarity in orientation and size (particularly of the larger fragments), it suggests that the presence of tin could be accurately predicted from a surface projection only. The fact that the tin fragments lie primarily in two orthogonal axis also suggests that the tin may be flowing in channels parallel to the filaments which would be of interest in further research.

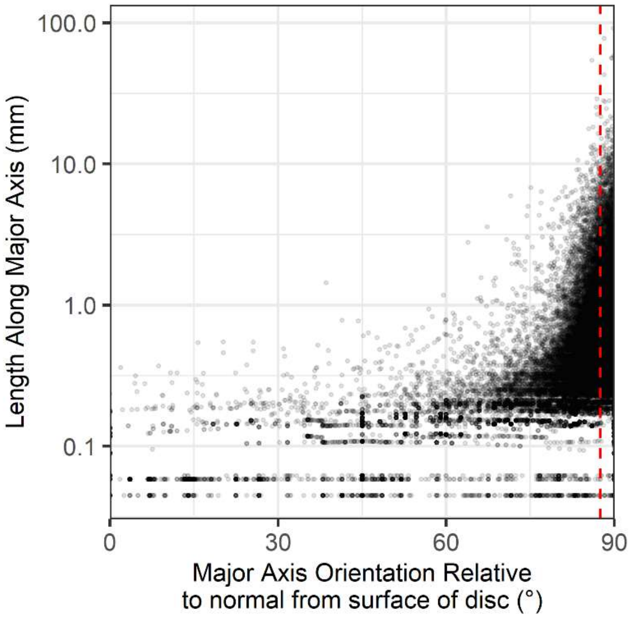

Figure 4.8: Orientation of residual tin fragment major axis compared with length of the fragment. 90 ° = parallel to surface. Median orientation (87.4°) is marked with red dashed line. Data extracted from flat consolidated CT scanned samples highlighted in Table 4.1

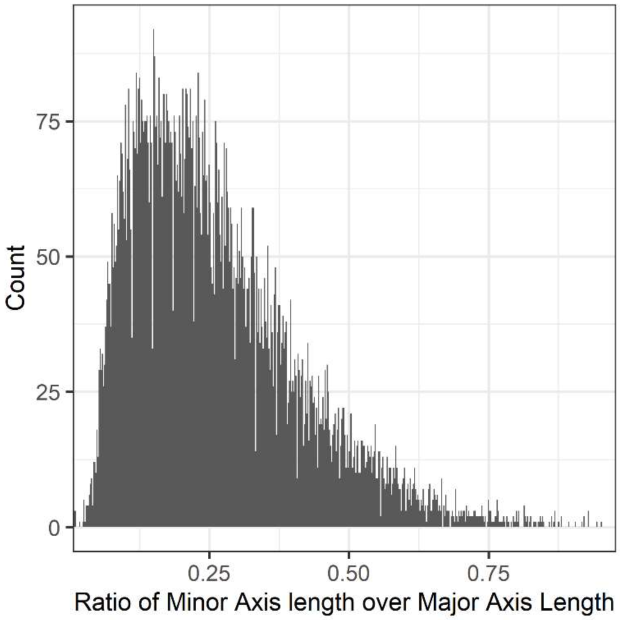

Figure 4.9: Histogram showing distribution of minor axis length over major axis length for tin fragments which are greater than 0.2% of the total volume in the disc.

4.3.3 Relationship between CT and X-ray

Further analysis of the CT scanned parts was carried out in MATLAB (see Section 4.2.2). A total of 64 small rectangular test specimens (dimensions 20 x 10 mm) were cut from the manufactured parts and later mechanically tested using the interlaminar shear test (See Chapter 5). The methods outlined in Section 4.2.2 are used to calculate the total tin volume and the total projected surface area covered by tin for these smaller test specimens. The larger CT scan results were matched with the known locations of the smaller cut test specimens to allow for cropping and analysis of the small areas. The volume versus projected surface area of residual tin within each test piece is plotted in Fig. 4.10. A high level of correlation is apparent ($r^2 = 0.92$), suggesting that the lateral projected surface area of residual tin is proportional to its volume.

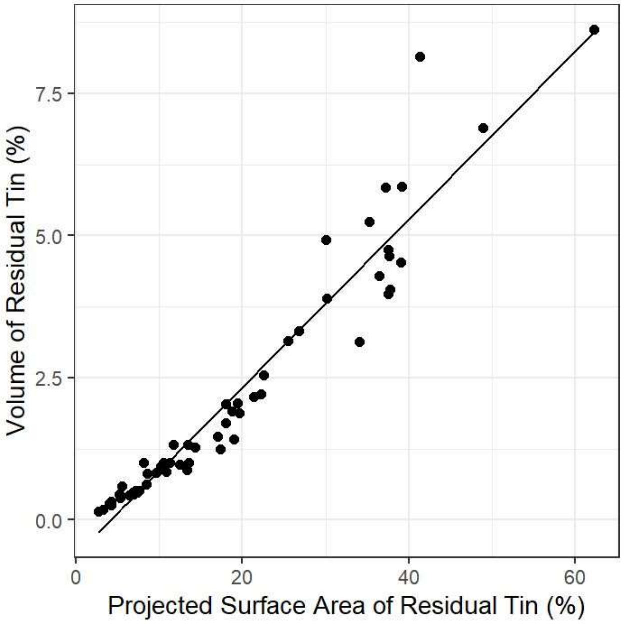

Figure 4.10: Volume of residual tin versus projected surface area, measured using 3D x-ray CT. $r^2 = 0.92$.

The strong correlation between projected surface area and volume of residual tin indicates again that the simpler 2D x-ray approach may be sufficient to make judgement calls on residual tin content. To test this possibility, a comparison between the projected surface area from the CT scan and the calculated surface area of tin from the 2D film x-rays was made. Film x-rays (captured and digitised as detailed in Section 4.2.1) were thresholded via the Renyi Entropy thresholding algorithm [205] in ImageJ. These thresholded images were then analysed via MATLAB to establish the projected surface area of residual tin in the samples (see Section 4.2.2). A comparison between the surface area percentage as calculated from the x-ray CT scans with that calculated from the film x-rays is shown in Fig. 4.11a, with the residual differences between the two shown in Fig. 4.11b. The dashed line represents a 1:1 relationship and r^2 of 0.83 is found. The plotted data suggest that the CT scans tend to give a higher value than the 2D film x-rays, however this tendency fades at higher quantities. It is therefore plausible that smaller fragments of residual tin are missed by the lower resolution 2D film x-rays and a higher resolution system may be required to fully match the x-ray CT scans.

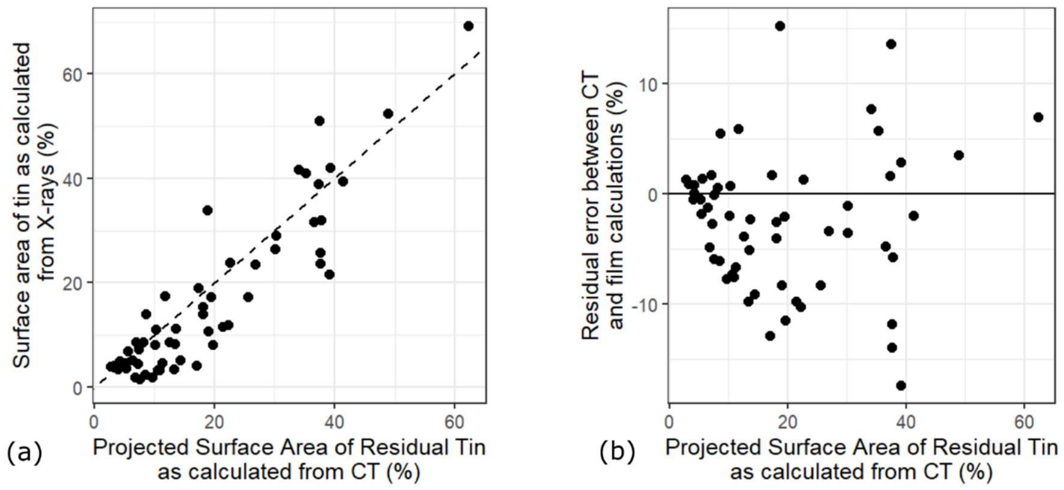

Figure 4.11: (a) Comparison between surface area calculated via film x-rays and projected surface area calculated via the 3D CT scans. Dashed line represents 1:1 relationship. The film x-rays underpredict the surface area of each analysed fragment. R^2 of 0.83, (b) residual differences between calculations via CT and film.

4.4 Conclusions

In this Chapter, the amount of residual tin in a series of manufactured parts was quantified using a mixture of microscope imaging, x-ray scans and CT scans. The quantity of residual tin in flat parts was found to range from 1.6% - 5.7% and the quantity showed a downward trend as the process was improved. However, when forming ripple geometries, the final part volume of residual tin ranged from 8-32% of the part volume. High levels of tin are likely to be detrimental to the material properties, mass and recyclability of the final part. Furthermore, comparison is made between both volume and projected surface area measurements to assess the quality of the parts. A strong linear correlation (r^2 = 0.92) is found between projected surface area and volume (as calculated from CT scans). Similar results (r^2 = 0.83) are found when assessing projected surface area results as calculated from CT scans and as calculated from film x-rays. Assessment of the data points suggests that the volume of tin is slightly underestimated compared to the CT scans and may be down to resolution limitations in the equipment used. The 2D approach would be suited to rapid quality control and assessment of mass-produced parts while the 3D approach is likely to be useful in further research into the influence on mechanical properties.

Chapter 5 Interlaminar Shear Strength

5.1 Introduction

Chapter 3 introduced iMelt thermoforming, a manufacturing process for composite parts which can leave unwanted residual tin in the parts. Chapter 4 quantified the amount of this residual tin. In Chapter 5 the influence of the residual tin on some mechanical properties of the manufactured part is investigated.

One concern is that the existence of residual tin at the ply interface could lower the inter-laminar shear strength (ILSS). Adhesion between solids occurs through a variety of mechanisms such as mechanical interlocking, physical bonding (e.g., Van Der Waals interactions) and chemical bonding [215]. Bonding in nylon structures relies primarily upon hydrogen bonds between adjacent polymer chains [20]. These bonds are strong, and as such, their interruption by the presence of residual tin may reduce the strength of the interlaminar interface, weakening the part and leading to failure via interlaminar shear. Another factor is the differing stiffness between tin and the as-manufactured Carbon Fibre reinforced Nylon sheets (~45 GPa [216] and ~100 GPa [150] respectively). Interlaminar shear strength can be characterised using test standards, e.g., ISO 14130 [217], and is a measure of resistance to shear-induced delamination failure in laminated composites [25], [218]. In this investigation, it is used to examine the effect of residual tin on the ILSS of parts manufactured as outlined in Chapter 3. Adhesive bond strength can be very sensitive to material composition at the surfaces of the bonded materials. For example, appropriate use of surface oxidation and coatings (such as phenoxy) on fibres can dramatically increase the interlaminar shear strength of nylon-carbon composites with increases in excess of 100% being possible [219], [220], [221]. The presence of voids and sharp changes in fibre density can also reduce the ILSS [222], [223]. Indeed, interlaminar failure at the metal/composite interfaces in epoxy-aluminium/carbon fibre laminates has been demonstrated previously [41],

[224], [225], [226]. Specific studies into bonding on tin/nylon surfaces were not found, however some research has shown that tin/polymer bond strength is sensitive to the type of polymer used (e.g., polyurethane vs polyurethane acrylic) [227]. Understanding the influence of the residual interlaminar tin on the ILSS of carbon/nylon composites is an important goal of this investigation. For simplicity, the current investigation is limited to the case of flat laminates (see Section 3.4.2) rather than thermoformed parts of complex geometry. This should be the easiest and simplest scenario to examine the influence of any residual tin following the iMelt process. The remainder of the Chapter explores the material testing methods and manufacturing processes before discussing the key results.

5.2 Experimental Methods

5.2.1 Materials and Manufacturing

This Chapter carries out tests on four distinct carbon fibre reinforced nylon sheets with a $[0°/90°/90°/0°/90°/0°/0°/90°]_S$ layup. Two varieties were formed with a lubricating interlaminar tin layer. **Tin IA** and **Tin IB** differ in that Tin IB was formed with an additional 1 mm thick silicone rubber sheet insert above and below the composite during the heating and forming. Three samples of Tin IA were formed (Tin IA1, TIN IA2, and TIN IA3) while 2 samples of Tin IB were formed (Tin IB4 and TINIB5). The details of these forming processes can be found in Chapter 3.

Two further varieties without interlaminar tin were tested and these acted as control samples. One was produced internally using the bespoke multistep tooling, and another was produced externally. Both are described below.

- **No Tin (Radiant):** Four $[0/90]_s$ carbon-nylon sub-laminates in a $[0°/90°/90°/0°/90°/0°/0°/90°]_S$ layup were heated under vacuum in a 0.3 mm thick silicone rubber diaphragm bag at 250 °C (without interlaminar tin) using a 5.7 kW radiant heater (Watlow Raymax 2030) before being shuttled across and further consolidated with the multistep tooling described in Section 3.3.2 [228], creating a total consolidation pressure of 2 Bar from the vacuum pressure and pressure from the forming tool. Temperature was monitored using a Flir E8-XT Infrared Camera at the upper diaphragm surface. The part was heated for 15 minutes and consolidated between the steel male and steel female tool, then allowed to cool for 15 mins. This laminate is used as a control to help assess the influence of residual interlaminar tin (see Section 3.5.1 for further details).

- **No Tin (Platens)**: Four carbon-nylon sub-laminates were consolidated (without interlaminar tin) between electrically heated platens at 4 Bar and 270°C for 30 seconds. The platens were air cooled for 50 mins to 150°C before being water cooled for 10 minutes to room temperature. The overall layup was again $[0/90/90/0/90/0/0/90]_S$. The two ‘No Tin’ laminates serve as examples of conventional consolidation methods. This was carried out by colleagues at INEGI in Porto. This was used as an external control to validate our manufacturing process.

Table 5.1 summarises the conditions used in each of the four consolidation methods and highlights the number of manufactured samples that are tested. A larger number of tin samples were analysed to provide a larger dataset allowing for more detailed exploration of the influence of residual tin. A final point to note is the variable cooling conditions, particularly between ‘No Tin-P’ and the other methods. ‘No Tin-P’ was cooled over 50 mins while the others were cooled over 15 mins in contact with the multistep tool. Slower cooling rates have been shown to lead to higher crystallinity [229] in finished samples, and as a result, may lead to higher interlaminar fracture strength [230], [231].

5.2.2 Mechanical Testing

Interlaminar shear strength tests were carried out using a three-point bending fixture in accordance with ISO 14130. The manufactured samples had thickness, t, ranging from 1.9 - 2.67 mm, and as such, test coupons of length L = 20 mm and breadth b = 10 mm were prepared by cutting from the larger sample using a diamond coated rod saw. The test was carried out in a Deben Microtester (Deben, UK) with a 5 KN loadcell. The test setup is shown in Fig. 5.1. A loading plunger (a) with radius 5 mm is used to apply force at the mid-span. The coupon (b) is mounted on two supporting bars (c) of radius 2 mm. The span, s, of the support was set to 12.5 mm. The flexural properties of the coupons may be influenced by the relative orientation of the layup to the long axis of the coupons and, as such, two types of test coupon were prepared: one with the outer fibres parallel to the long axis of the coupon (Orientation 1) and the other having the outer fibres perpendicular to the axis of the coupon (Orientation 2). The rectangular coupons were carefully cut out from the formed discs using a diamond coated rod saw before being filed to size. The location of each cut coupon was recorded to enable accurate cross referencing with the CT scans (See Chapter 4). This allowed for estimation of the residual tin content specific to each of the ILS coupons. Coupons from the four manufacturing processes described in Table 5.1 were tested. The key mechanical properties (ILSS and flexural modulus etc.) were then determined from the force-displacement curves.

Interlaminar shear stress was calculated via the following equation in accordance with ISO 14130.

$$\text{Interlaminar shear stress} = 0.75\frac{P}{bt} \tag{5.1}$$

where P is the applied plunger force, b is coupon width and t is coupon thickness. Both the maximum value (i.e., interlaminar shear strength, ILSS) and its yield value (ILSS_Y) were considered. Interlaminar shear strength was defined in accordance with ASTM D2344 via the maximum force reached when any one of the following conditions were met: (a) two-piece coupon failure, (b) a force drop-off of 20% or (c), 1.8 mm of plunger displacement was reached. 1.8 mm was chosen as, beyond this point, the coupon begins to be compressed between the plunger and the supporting bars, causing a rapid increase in the applied load. The limit on nominal plunger displacement is used in the ASTM standard to address the risk of compression in ductile samples. As there was considerable variation in the coupons and the force-displacement plots, yield was defined by either a 0.2% yield offset or by a drop in force (whichever occurs first). The yield stress was similarly calculated using Eq. 5.1.

The Flexural Modulus (E_b) of the coupons was defined, in accordance with ASTM D790, as:

$$E_b = \frac{L^3 m}{4bt^3}, \tag{5.2}$$

where, L is span length, b is coupon width, t is coupon thickness, and m is the slope of the initial straight-line portion of the load deflection curve. This measure is not strictly valid for the Interlaminar Shear Stress tests as the specimens fail in shear, not flexure. However, the gradient of the initial slope will be representative of a stiffness behaviour in the materials tested and it is felt that there is useful information contained in the measure. The Flexural Modulus calculation from ASTM D790 is used to help provide a correction for the variable thickness of the test coupons

Table 5.1 shows the breakdown of the tested coupons based by consolidation method, orientation, and part dimensions. A total of 96 coupons were tested. Orientation 1 has the outer fibre parallel to the long axis of the part, and Orientation 2 has the outer fibre perpendicular to the long axis.

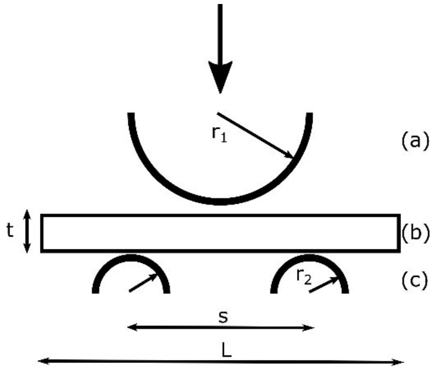

Figure 5.1: Schematic of ILS test setup: (a) loading cylinder with radius r_1= 5 mm, (b) coupon of approximate dimension 20 x 10 x 2 mm and (c) support cylinders of radius r_2 = 2 mm and span s = 12.5 mm.

Table 5.1: Detailed dimensions of interlaminar shear coupons by forming method and orientation.

Forming Method	Orient-ation	No. coupons Tested	Thickness (mm)	Length (mm)	Breadth (mm)
No Tin-R	1	6	2.08 ± 0.04	19.90 ± 0.25	10.08 ± 0.19
No Tin-R	2	6	2.06 ± 0.07	19.87 ± 0.13	9.94 ± 0.13
No Tin-P	1	6	2.30 ± 0.05	19.72 ± 0.39	9.98 ± 0.17
No Tin-P	2	6	2.32 ± 0.06	19.88 ± 0.25	9.90 ± 0.09
Tin-IA1	1	7	2.42 ± 0.08	20.18 ± 0.26	10.02 ± 0.12
Tin-IA1	2	9	2.42 ± 0.11	19.91 ± 0.41	10.03 ± 0.10
Tin-IA2	1	7	2.36 ± 0.07	20.09 ± 0.54	10.13 ± 0.09
Tin-IA2	2	8	2.35 ± 0.08	19.91 ± 0.53	10.10 ± 0.10
Tin-IA3	1	7	2.27 ± 0.13	19.78 ± 0.34	10.06 ± 0.20
Tin-IA3	2	8	2.28 ± 0.30	20.17 ± 0.36	9.96 ± 0.11
Tin-IB4	1	7	2.48 ± 0.17	20.12 ± 0.29	10.46 ± 0.37
Tin-IB4	2	7	2.37 ± 0.18	20.25 ± 0.48	10.49 ± 1.0
Tin-IB5	1	6	2.48 ± 0.15	20.27 ± 0.61	9.99 ± 0.32
Tin-IB5	2	6	2.34 ± 0.18	20.11 ± 0.31	10.18 ± 0.27

5.3 Results

5.3.1 Effect of Heating and Consolidation Method

The graphs in Fig. 5.2 show the running mean of the extension versus ILSS curves for each manufacturing method. This allows the reader to better appreciate the nature of the failure of the test coupons produced by the different production methods. Each graph shows average results, for both relative orientations, indicated by the continuous (Orientation 1) and dashed lines (Orientation 2). The range of results (highest and lowest measurement) is shown by the lighter shade colour, and all individual curves are plotted in the bottom right. Looking at the range (shaded region) in the plots of Fig. 5.2, the laminates without tin clearly show less scatter. Finally, all specimens, except for ‘No Tin-P’, exhibit gradual plastic failure. As the crosshead displacement increased, these ductile specimens were bent to such a degree that they were eventually compressed between the plunger and the two support bars, at which point the results become invalid. This occurs at a displacement ~1.8 mm: consequently, all results shown in Fig. 5.2 have been truncated accordingly. Note, samples which experience early, brittle failure are removed from the running average. Therefore the line slightly misrepresents behaviour at high extensions as only relatively ductile specimens are still included in the running average. This does limit the applicability of the results somewhat and use of the test setup in ASTM D2344 short beam strength test may help in future [232]. The ASTM D2344 uses a test rig with support pins of 3 mm diameter and a loading pin with 6 mm diameter. The smaller loading and support pins would allow for more deflection before compressing against the pin allowing specimens with higher ductility to be evaluated to failure.

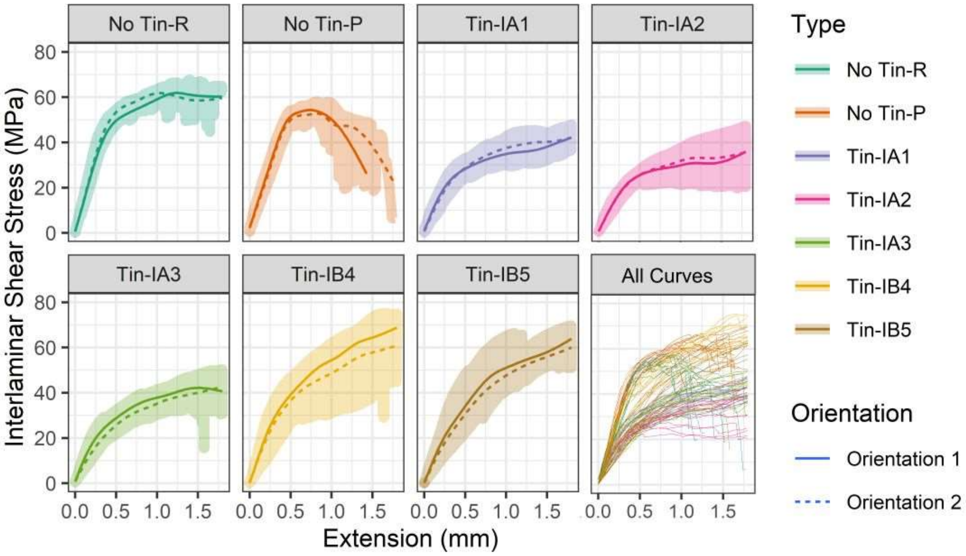

Figure 5.2: Mean interlaminar shear stress versus extension for each coupon type and orientation. The range of the results is indicated by the faded background. The bottom right plot shows all individual curves.

Table 5.2 shows the P-values of a Welch Two Sample T-test used to evaluate the influence that specimen orientation had on the results. The high P-values (>0.05) suggest that the influence of orientation on the measured material properties is not significant. For consistency, we will continue to show results for each orientation separately.

Table 5.2: Statistical impact of the orientation of the tested coupon on the mechanical properties of the specimen. Welch Two Sample T-test was used. P-values are shown. Orientation shows no statistically significant impact on mechanical properties.

	P-value ILSS	**P-value $ILSS_y$**	**P-value Flexural Modulus**
No Tin-R	0.73	0.06	0.53
No Tin-P	0.22	0.68	0.16
Tin-IA	0.79	0.28	0.20
Tin-IB	0.12	0.12	0.86

5.3.2 Failure Mechanics

Fig. 5.3 shows interlaminar shear stress versus crosshead displacement (extension) for one representative ‘No Tin-R’ coupon. Inset photos show the progression of deformation and failure corresponding to points (A to D) on the loading curve. The coupon initially begins to deform plastically (B) before visible delamination occurs in the midplane, half-way between the applied loading and the support cylinders - i.e., corresponding to the locations of maximum shear stress in three-point bending. In Fig. 5.4, results for a representative coupon having high residual tin content (~21% surface area, from ‘Tin-A2’) is shown. The coupon fails via delamination occurring close to an agglomeration of residual tin, as shown in (C). This is again close to the location of maximum shear stress, so the presence of tin appears to have weakened the coupon and eventually leads to tensile failure of the part in (D). In Fig. 5.5, results for another representative coupon containing less residual tin (~6.8% surface area, from ‘Tin-A3’) are shown. In this case, the initial visible delamination occurs between the loading cylinder and the support cylinder but appears in the bottom half of the laminate (highlighted in C). The propagation of this delamination is limited, and the coupon primarily experiences plastic deformation. For most examples, failure tended to initiate around the midpoint between the loading and supporting cylinder. This corresponds with the location of maximum shear stress in the three-point bending arrangement (Makeev et al. [233]).

In some cases, the presence of tin leads to weakening of the inter-ply interface and more rapid delamination. However, in many cases the tin leads to a more ductile response. In a number of samples the tin appears to improve the ability of the beam to absorb energy via accommodation of further bending rather than by propagation of cracks to sudden failure. One example is seen in Fig. 5.5. Interlaminar veils have been used with varied success to improve resistance to fracture and improve ductility within composites [234], [235], [236]. One of the mechanisms is the deflection of crack growth towards longer and harder paths, increasing energy required for crack propagation [237]. Residual tin fragments may mimic this behaviour by deflecting crack growth and absorbing energy through ductile deformation. This behaviour will require closer examination as factors such as size of inclusion, and coatings have a strong influence on the final behaviour in interlaminar veils and are likely to also influence the behaviour of interlaminar residual tin [236], [238]. The behaviour was seen in multiple cases, however accurate monitoring is challenging as interlaminar tin away from the exterior surfaces cannot be seen during testing. The random distribution also prohibited empirical exploration of correlations between tin volume or location with Interlaminar Shear Strength (I.e., does the interlaminar layer in which the tin resides affect the final strength). Crack growth around tin inclusions would merit more focused study and via techniques such as double cantilever beam which can better isolate crack growth.

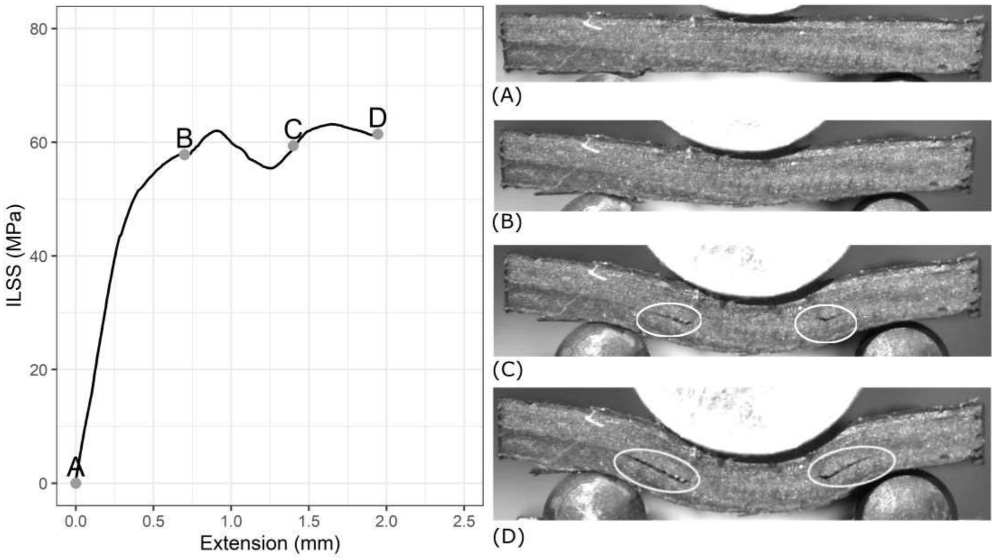

Figure 5.3: Interlaminar shear stress versus extension for a selected ‘No Tin-R’ radiant heated coupon. Inset photos show the progression of deformation and failure corresponding to points (A to D) on the loading curve. The circled areas indicate regions of shear-induced delamination corresponding to the locations of maximum shear stress.

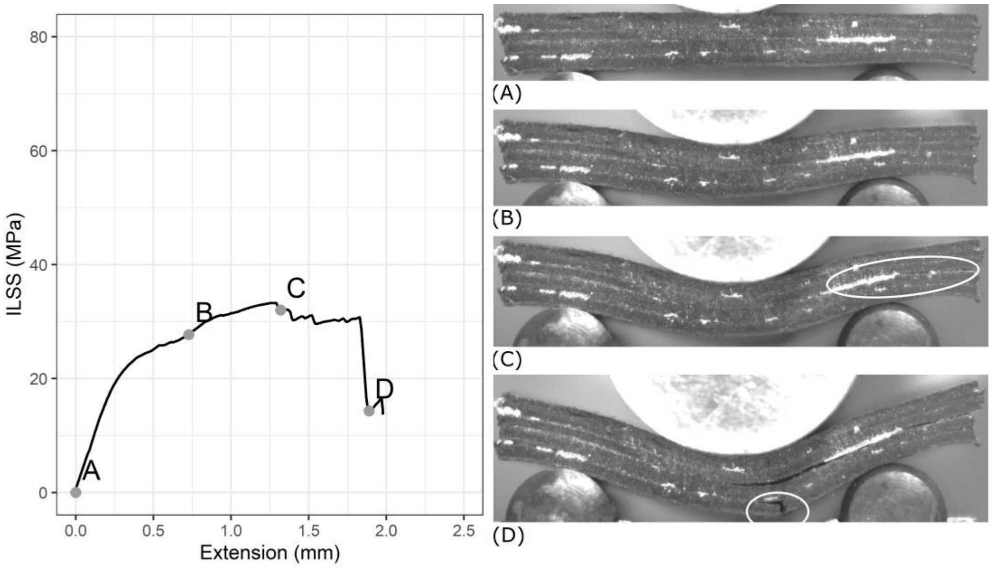

Figure 5.4: Interlaminar shear stress versus extension for a selected coupon containing high quantities of residual tin (from disc ‘Tin-IA2’). Inset photos show the progression of deformation and failure corresponding to points (A to D) on the loading curve. Failure initiates near the location of high tin content which also corresponds with the location of the maximum shear stress in (C). Further cracking is apparent later in (D) due to tensile bending stress. Stress-extension plot shows a sudden ‘brittle like’ failure.

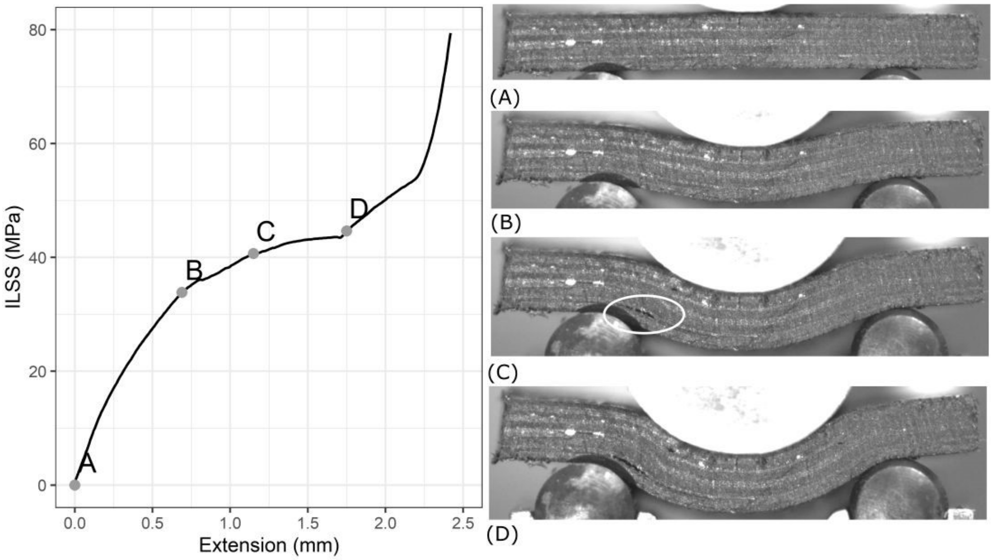

Figure 5.5: Interlaminar shear stress versus extension for a selected sample containing lower quantities of residual tin (from disc 'Tin-IA3'). Inset photos show the progression of deformation and failure corresponding to points (A to D) on the loading curve. In this sample, delamination has occurred near the cross-section of maximum shear stress. Stress-extension plot shows a 'ductile-like' response such that there is no sudden failure, and the sample deforms until it gets compressed between plunger and support bars after Point (D).

5.3.3 Mechanical Properties

Fig. 5.6 shows the mean interlaminar shear strength of the tested coupons. In the case of the samples without tin (i.e., 'No Tin-R' & 'No Tin-P'), platen heated and consolidated samples ('No Tin-P') show lower ILSS than those heated and consolidated with the radiant heater and multi-step tool ('No Tin-R'). As discussed in Section 5.2.1, slower cooling rate ('No Tin-P') has been shown to lead to high crystallinity and lower interlaminar shear strength [230], [231] which agrees with these results. For samples heated via induction heating and consolidated using the multi-step tool (with tin present), 'Tin-IA' samples show a significantly lower strength than the 'No Tin' cases, whereas 'Tin-IB' samples had comparable values. Some individual 'Tin-IB' specimens exhibited higher ILSS than the control specimens. These exhibited ductile behaviour after yield as tin inclusions deformed plastically as opposed to fracture occurring in the fibres. As mentioned, 'Tin-IA' & 'Tin-IB' samples are similar, except for an additional 1 mm thick silicone rubber sheet inserted between the sample and the diaphragm bag in 'Tin-IB' samples which is suspected to have improved the consolidation by smoothing over pressure discontinuities and reducing temperature variation during forming (see Section 3.3.3). The changes in resultant heating and cooling patterns appears to have led to improvements in mechanical performance of the resulting samples. This combined with the improved tin expulsion by smoothing over pressure discontinuities may have mitigated the formation of localised agglomerations of tin in the samples during consolidation (the tin content of individual specimens will be discussed in some detail in Section 5.3.4). The samples that used tin interlayers ('Tin-IA' & 'Tin-IB') show higher variability than the samples without tin interlayers, due to the stochastic nature of residual tin coverage within the consolidated samples. The fact that the ILSS of the 'Tin-IB' samples have statistically insignificant differences with the 'No Tin-R' & 'No Tin-P' samples is encouraging and shows that simple, and not always obvious, changes to the setup can significantly improve the process (though the exact mechanism for this improvement is not yet fully understood).

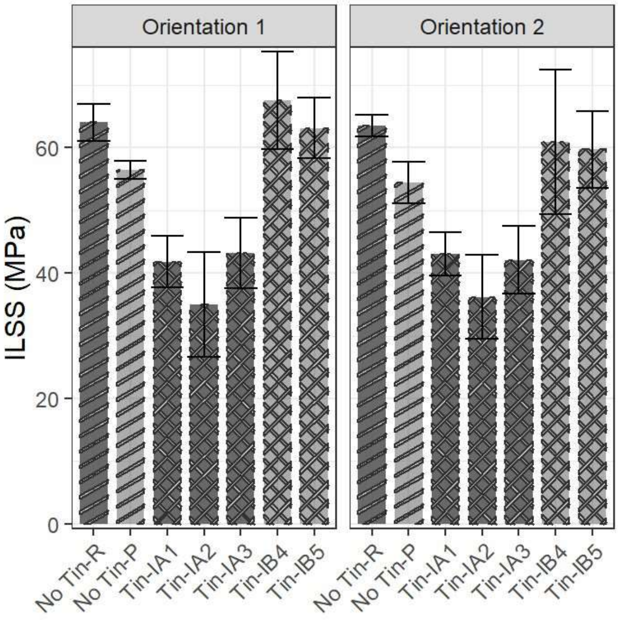

Figure 5.6: Mean Interlaminar Shear Strength (ILSS) by sample and orientation. Error bars show standard deviation of results.

The mean interlaminar shear stress at yield ($ILSS_y$) is shown in Fig. 5.7. The results here are less positive for the samples manufactured using the iMelt process. Coupons with a tin interlayer ('Tin-IA' & 'Tin-IB') both show significant reductions compared to the 'No Tin' samples, though the reduction for 'Tin-IB' is notably less than that of 'Tin-IA', again suggesting that changes to the process can lead to notable improvements, this time for the interlaminar shear yield stress. It is probable that the presence of interlayer tin initiates earlier onset of shear-induced delamination owing to a reduction in the adhesive bond strength of the inter-ply interface. Why this occurs for yield strength (Fig. 5.7) and not for the maximum strength (Fig. 5.6) is unclear.

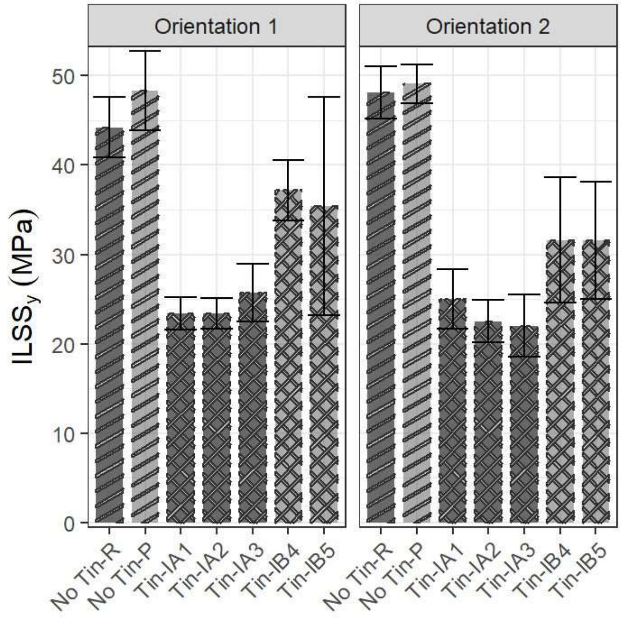

Figure 5.7: Mean interlaminar shear stress at yield (ILSS$_Y$) by sample and orientation. Error bars show standard deviation of results.

Fig. 5.8 shows the flexural modulus of the test coupons and is perhaps the mechanical property most adversely affected by use of tin interlayers during the heating and consolidation process. The 'No Tin (P)' coupons show a statistically insignificant difference compared with the 'No Tin (R)' coupons (p-value=0.63). However, there is a statistically significant drop off in the average flexural modulus of all coupons manufactured using tin interlayers, 'Tin-IA' & 'Tin-IB'. The variability of the flexural modulus also increases in the coupons with tin interlayer and the difference between the 'Tin-IA' and 'Tin-IB' results is not statistically significant (p-value=0.12). It is possible that the presence of residual interlayer tin weakens the interlaminar bonds between plies and facilitates earlier yield. That this doesn't then effect is less pronounced in maximum strength perhaps suggests that the higher ductility of the tin then enables further plastic deformation.

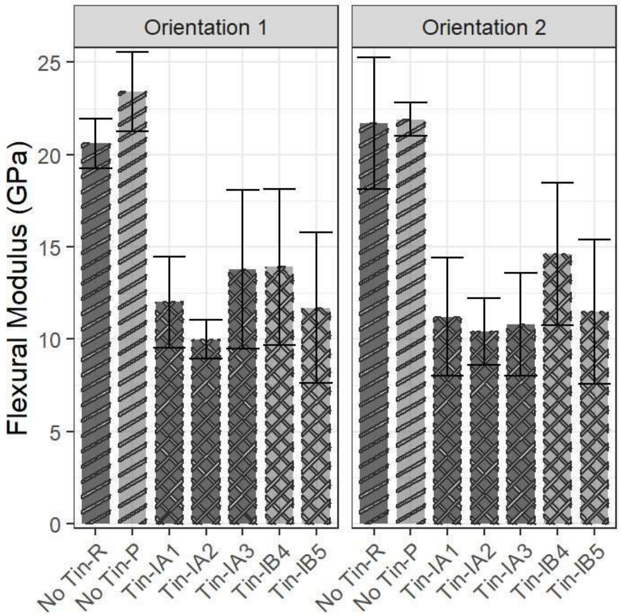

Figure 5.8: Flexural modulus of test coupons by sample and orientation. Error bars show standard deviation of results.

Fig. 5.9 shows the flexural work done on the beam before either failure or 1.8 mm plunger displacement is reached. This shows that the externally produced control samples offered greater ductility in failure than the internal control samples. This may be influenced by the varying cooling rates and the resultant impacts on interlaminar bonding and matrix crystallinity. The Tin samples all show higher work done than the internal control samples (No Tin-P) however in the case of Tin-IA this is within the margin of error. The Tin-IB samples show stronger performance than the Tin-IA samples which again may be related to the influence of the additional diaphragm sheets on temperature and pressure during forming. Care should be taken when interpreting these results as not all samples had reached failure before a plunger extension of 1.8 mm. Due to the limitations in the test this won't be included in further statistical examination. However, there is an indication that the inclusion of tin may improve ductility of samples.

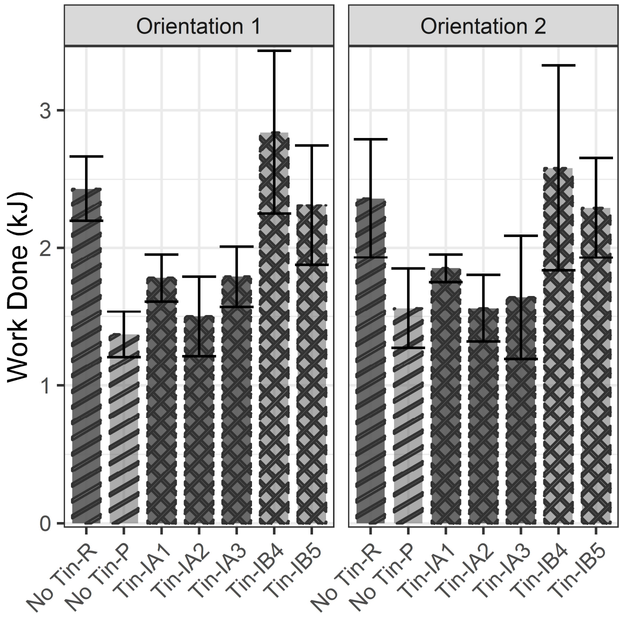

Figure 5.9: Flexural work done on beam before 1.8mm displacement. Test coupons segregated by sample and orientation. Error bars show standard deviation of results.

Table 5.3 summarises the average thicknesses and mechanical properties by sample type, with the percentage difference compared with the control 'No Tin-R' coupons marked in brackets. The coupons manufactured with the multistep tooling are 11.5 to 16.9 % thicker than those produced with the heated platens, 'No Tin-P'. This is primarily because the edges of the platen formed samples were unconstrained during consolidation, leading to some degree of transverse squeeze flow and mass-loss out the side of the sample during consolidation [167]. There are differences between the mechanical properties of the 'No Tin-R' and the 'No Tin-P' test coupons, but these differences are small suggesting that the impact of the varying thickness is not a major factor in the properties of the coupons.

Table 5.3: Overall mean thickness and mechanical properties for the interlaminar shear results. Percentage change from the radiant samples (as a reference) is shown in brackets

	thickness (mm)	ILSS (MPa)	Yield Strength (Mpa)	Flexural Modulus (GPa)
No Tin-R	2.31	63.7	46.1	21.2
No Tin-P	2.07 (-10.1 %)	55.4 (-13.1 %)	48.7 (+ 5.5 %)	22.7 (+ 7.2 %)
Tin-IA	2.35 (+ 1.9 %)	40.3 (- 36.7 %)	23.7 (- 48.7 %)	11.3 (- 46.5 %)
Tin-IB	2.42 (+ 4.9 %)	62.9 (- 1.3 %)	34.0 (- 26.4 %)	13.0 (- 38.4 %)

5.3.4 Influence of residual tin on Interlaminar Shear Strength

To better understand the sensitivity of various parameters on the mechanical properties of the consolidated samples, Fig. 5.10 shows a matrix of the full test results produced using ‘Tin-IA’ and ‘Tin-IB’. Viewing the data in this way allows a granular analysis of the entire dataset of results produced using the iMelt heating and consolidation process. The matrix allows direct comparison between each of the following parameters: tin surface area coverage (as calculated in Section 4.3), coupon thickness and the mechanical properties (ILSS, $ILSS_y$ & Flexural Modulus). The axes related to each plot can be found by referring to the end of the row and column occupied by the plot. The colours in the legend represent the various manufactured specimens, 'Tin-IA1’ to ‘Tin-IA3’ and ‘Tin-IB4’ to ‘Tin-IB5’) from which mechanical test coupons were cut. The sub-figures on the top right show linear regressions carried out on the full dataset, along with r^2 values. Table 5.4 shows p-values for the significance of the correlation between tin surface area cover and the mechanical properties for the overall dataset (all samples taken together) and for the datasets separated by sample. Correlations between tin surface area also hold for tin volume (as discussed in Section 4.3) but the results will focus on surface area for brevity.

There is a statistically significant (all p-values >0.05) negative correlation between tin surface area and the measured mechanical properties when looking at all results together (see Fig. 5.10a). This correlation is quite weak with r^2

values of 0.13, 0.09 and 0.10, respectively. The significance of this correlation disappears when the results are separated by sample as seen by the high p-values in Table 5.4 (see also, Fig. 5.10b). As might be expected, there is a correlation between the ILSS and the $ILLS_Y$ of the tested coupons ($r^2 = 0.55$). There is a weak correlation between flexural modulus and ILSS ($r^2 = 0.13$) and no significant correlation between the flexural modulus and $ILLS_Y$. It is also possible to see clustering of results by manufactured samples (Fig. 5.10c). Given the weak correlations found between tin content and mechanical properties, especially within single manufactured samples, it appears that variation in processing conditions had a significant influence on the final properties, complicating interpretation of the results. The difficulty in optimising the induction heating of the tin interlayer via manual control led to some variation in forming temperatures between samples. In addition to this, the addition of extra silicone rubber sheets for 'Tin-IB4' and 'Tin-IB5' smoothed over pressure discontinuities produced by the multistep tool during consolidation and lowered heat flow out of the part, thereby changing the heating and cooling profiles.

Table 5.4. Adjusted P-Values from linear regression on relationship between surface area of tin and selected mechanical properties. Significant results (<0.05) are shown in bold. A significant relationship appears when looking across all samples, but when data is segregated by sample this correlation disappears (Excluding $ILSS_y$ in Tin-IA2).

P-Values	ILSS	$ILSS_y$	Flexural Modulus
All Samples	**0.01**	**0.02**	**0.01**
Tin-IA1	0.27	0.18	0.18
Tin-IA2	0.54	**0.03**	0.44
Tin-IA3	0.32	0.89	0.21
Tin-IB4	0.96	0.80	0.87
Tin-IB5	0.21	0.34	0.82

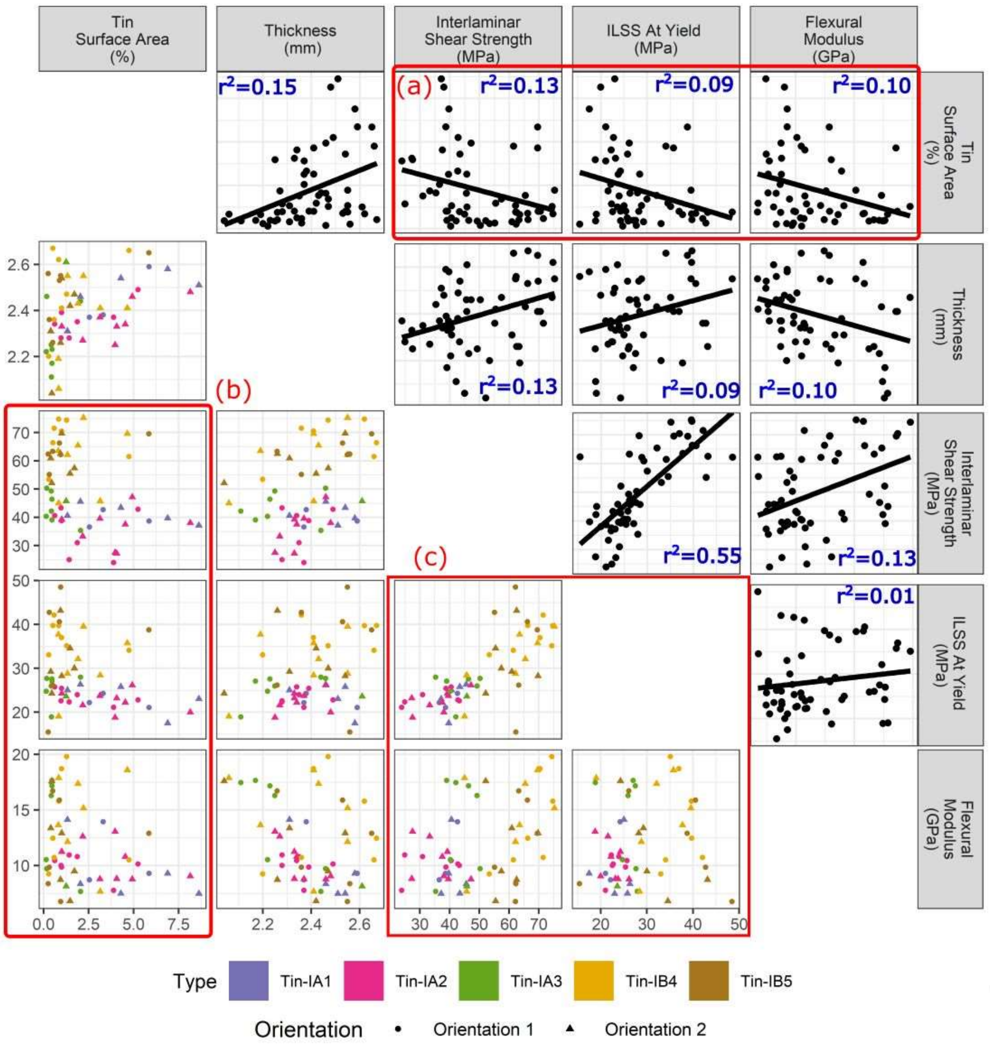

Figure 5.10: Pair plots of the full set of results obtained from the tested tin-based specimens: Top right shows linear regression + adjusted r^2 value over all results. Bottom left shows results segregated by sample type: (a) tin surface area vs mechanical properties, (b) tin surface area vs mechanical properties by sample and (c) relationship between mechanical properties.

5.3.5 Discussion

The experiments were designed to assess the influence of the residual tin on the mechanical properties of the produced part. The orientation of the tested coupons showed no significant impact (See Table 5.2). Referring to Table 5.3, the maximum measured ILSS (63.7 MPa) occurs in the radiant heated 'No Tin-R' control samples. 'Tin-IA' is significantly lower than this, at just 40.3 MPa, though 'Tin-IB' has a similar strength of 62.9 MPa. This difference in the performance of Tin-IA and Tin-IB samples has a few potential explanations: (1) improved temperature/pressure conditions as a result of improved operator control of the heating process (specifically, slowing down the heating rate and adjusting the induction coil to address cold spots) and the addition of extra silicone rubber layers around the sample, (2) the presence of a thin scattered layer of residual tin may act to distribute shear stresses away from the midplane location of maximum shear [233]. The yield Strength and flexural Modulus of the 'Tin-IA' test coupons are 48.7% and 46.5% lower than the No Tin-R coupons. The Yield Strength of the 'Tin B' coupons is also lower than the No Tin-R coupons by 26.4 % and is therefore an improvement in performance compared to the 'Tin-IA' coupons. However, the Flexural Modulus of the 'Tin B' coupons does not significantly recover and retains a 38.4 % reduction.

There was a statistically significant difference between manufactured samples with tin interlayers, and a weak negative correlation between tin quantity and mechanical properties when all results were considered together. However, there was little evidence of any direct correlation between mechanical properties and quantity of tin within individual manufactured parts (see Table 5.4). Some possible reasons for this are: **(1)** the distribution of residual tin within the specimen is likely to influence the behaviour and this may be more significant than simply the quantity, **(2)** the inclusion of any interlaminar tin may significantly weaken the part, with additional weakening beyond the first inclusion having less marginal influence on the strength of the part, **(3)** the variation in forming conditions between these samples (such as temperature, pressure and cooling rates) had more influence on final properties than the marginal change caused by an additional percentage of tin. These factors are known to be important in determining material properties following consolidation of thermoplastic composites [230]. It is also possible that the smaller sample size is not sufficient for any correlation to be seen.

The maturity of the induction heating process was very much in its infancy during the work and as such, there is likely to be significant scope to improve repeatability. For example, we have shown that the simple addition of the extra silicone rubber protection in the ‘Tin-IB’ samples led to significantly lower residual tin content (See Table 4.1) as well as higher ILSS and yield strength (See Table 5.4).

The results obtained from the ‘Tin-IB’ samples (i.e., after refinement of the process) are encouraging. Interlaminar shear strength for these specimens was comparable with the ‘no tin’ (platen heated) specimens. Although the tin-containing samples did experience a significant drop off in stiffness (≈ 38 to 47 %), they did appear to exhibit another possible advantage. Several tin-based specimens responded similarly to Fig. 5.5 where significant bending deformation occurred without any drop-off in loading. This suggests that the tin may play a role in increasing energy absorption by facilitating further deformation of the coupons as opposed to sudden failure by detrimental propagation of cracks. Unfortunately, work to failure could not be reliably evaluated in the experiments as many of the specimens were so ductile that they deformed in bending to such a degree that they were compressed between the loading plunger and the support pins before showing any drop-off in load (see Fig. 5.5). Not achieving full failure due to ductile behaviour is accommodated for in the ASTM standard so it was considered valid to use results from these tests. However, use of the ASTM short beam shear standard may have enabled testing of the more ductile specimens to failure due to the smaller diameter of the loading and support beams specified [232].

5.4 Conclusions

Mechanical properties were assessed via interlaminar shear testing in three-point bending on small rectangular test coupons cut from the formed sheets and having known tin content (i.e., measured from the x-ray analysis in Chapter 4). Results were compared to those from testing of coupons produced without interlaminar tin sheets ('No Tin-P’ and ‘No Tin-R’). With refinement of the process, interlaminar shear strengths of 62.9 MPa were achieved (from Tin-IB, where the samples contained a median tin content by volume of 2.03%), and this is comparable to the 63.4 MPa achieved with control specimens produced without interlaminar tin ('No Tin-R'). There was, however, a reduction of about 26% in the value of interlaminar shear stress at yield and about a 38% reduction in flexural modulus when the optimised tin-based samples were compared with the radiant heated control samples. However, several tests exhibited a more ductile failure in the samples containing tin. A statistically significant, but weak, negative correlation was found between tin content and ILSS (r^2=0.13), ILSS$_y$ (r^2=0.09) and the flexural modulus (r^2=0.10) when looking at the entire sample set. However, the finding was not statistically significant when looking within individual samples. There is also evidence of results clustering based on manufactured part. Given there were challenges in controlling the heating process and continuing variability between manufactured samples, this suggests that processing parameters such as temperature, pressure and cooling may also influence both tin removal and mechanical properties. Other aspects such as the spatial distribution of the residual tin may be more significant (at least in these results) than tin quantity alone. This suggests that the manufacturing process itself needs further refinement before firm conclusions on the influence of tin on material properties can be drawn. Due to time and financial limitations further refinement of the manufacturing could not be completed during the timeframe of this project.

Chapter 6 Numerical Simulation of Forming Process

6.1 Introduction

Further investigation of the influence of factors such as tooling geometry, number of forming steps used and interlayer friction is desired to further understand the forming process. Simulations are therefore a useful tool in this endeavour. In this Chapter, a blank (with the properties of a glass fabric) is modelled with the intention of gaining an understanding of general multi-step forming behaviour. Particularly compressive and tensile forces within the fibres, and shear angles due to fibre rotation during deformation. The rate and temperature independent material behaviour of the assessed glass fabric does not closely replicate the carbon fibre cross ply blank used in manufacture for reasons discussed in Section 6.2.6. However, it is believed that useful, if limited, conclusions about the influence of the multistep tooling can be drawn, even if the simulations do not fully capture the complexity of the lubricated, temperature and rate dependent thermoforming behaviour involved in the iMelt process.

6.1.1 Material Behaviour

Material properties in fibre reinforced composites are highly anisotropic and include multiple independent parameters. This includes tensile stiffness in the fibre direction, in-plane shear stiffness, in-plane and out-of-plane bending stiffness and torsional stiffness [116], and complex friction behaviour involving adhesion and lubrication between plies and tooling. The influence of boundary conditions such as applied pressure and clamping also plays a key role. Full characterization of these properties has been the focus of much research, and they are crucial to understanding the deformation of fibre reinforcements. Balancing computational time with accuracy is a challenge. Accurately measuring material properties is also highly time-consuming. Use of multi-scale predictive models can shorten the time required for material characterisation [239].

6.1.2 Finite Element Modelling

A common method of numerically assessing forming behaviour is to use mechanical modelling approaches such as the Finite Element method. Here, the materials are broken into discrete units (elements) connected via nodes [240]. Boundary conditions can be applied to the nodes and a mix of structural elements can be used to independently model appropriate material properties. Common element types such as membrane, shell, beam, or truss elements are often used to model the mechanical properties of prepregs and engineering fabrics, using commercial codes (such as ABAQUS, PAMFORM or LSDyna) during the forming process. A more detailed overview of past work was given in Section 2.6. A brief overview of different element types is discussed in the remainder of this Section.

6.1.2.1 Truss Elements

Truss elements are 1-D elements that support loading along their axis. Simple methods have used networks of truss elements to model shear and tensile resistance. One example by Sharma et al. consists of a unit cell containing four “Tow elements” forming a square, with a “Shear element” across one of the diagonals [241]. An example of the unit cell developed by Sharma is shown in Figure 6.1 (a). The elements are joined with pin joints. The tow elements are given a constant stiffness which accommodates for fibre decrimping or slippage during deformation. The diagonal shear elements are given a nonlinear stress-strain response. A similar model was developed in Skordos et al which retained the same tow elements but had shear trusses across both diagonals [242]. The diagonal shear elements allowed for a non-linear response where shear resistance increases at higher strains. The model developed by Skordos et al. also allowed for the modelling of buckling by deleting tow elements which experienced compressive stresses. Both models could be validated against bias extension tests and used to model thermoforming processes. However, models of these types could only simulate in plane shear resistance and did not model out of plane bending. This is because the truss elements only transmit load axially and cannot process loads perpendicular to the axis of the truss, or bending moments through the truss. Exclusive use of 1D elements also restricts the modelling of frictional behaviour. Limitations in the contact algorithms used within Abaqus prevent the use of Node based surfaces as “master surfaces”, and surfaces defined on truss or beam surfaces are restricted to the use under general contact algorithms [151] .

6.1.2.2 *Membrane Elements*

Membrane elements are 2-D elements that have stiffness in the plane of the element, but offer no bending stiffness. These 2-D elements can increase simulation times vs truss elements, but can be designed with constitutive equations which consider the tensile stress in the fibre direction and the shear resistance at the crossover points [243], [244], [245], [246]. Use of 2-D elements also allows for more control of friction measurements when compared with 1-D truss elements [247]. The constitutive equations in the membrane elements require careful consideration of the frame of reference and require the fibre orientations to be constantly updated to ensure accurate representation of the stresses as the fibre directions change.

6.1.2.3 *Truss + Membrane Elements*

Solutions which combine truss and membrane elements have also been developed. The membrane elements can represent in plane shear resistance while truss elements represent the tensile and bending stiffnesses of the fibres [248], [249], [250]. These elements are “mutually constrained” at shared joints which allow free rotation. This node matching requires custom mesh generators. This also means that adaptive meshing cannot be used during the simulation [251]. Free rotation at the nodes also means there is no resistance to out of plane bending. This can lead to early buckling of the simulated composite ply when compared to real ply, which can resist small compressive forces [116]. This early buckling can however be useful as it offers a margin of safety when designing parts, but at the same time prevents accurate completion of simulations.

6.1.2.4 Shell Elements

Shell elements are 2-D elements with additional degrees of freedom compared to membrane elements and model out of plane bending stiffness. These are often used to model thin sheets and can be used to model composite sheets [115], [252]. Stress resultant shell elements allow for separate specification of tensile and bending behaviour [253]. Other methods use combined shell and membrane elements, or multiple overlapping shell elements to decouple the tensile and bending behaviour of the sheets. An example of this can be found in Yu et al. [254] which uses a composite layup with differing stiffnesses to implement out of plane bending stiffnesses. The unit cell for this can be seen in Figure 6.1 (b). However, the additional computational power required for shell elements as a result of their three additional rotational degrees of freedom can be onerous, with some studies reporting up to a 3x increase in processing time compared with membrane element based simulations [114].This is further exacerbated by the need for elements smaller than expected wrinkle size to ensure accurate modelling of defects.

6.1.2.5 Beam and Membrane Elements

The method used in this Chapter is to pair beam elements with membrane elements using hinge connectors. Use of this so-called, ‘mutually constrained pantographic beam and membrane mesh’ allows independent control of fibre stiffness, flexural moduli of the sheet (both in and out of plane) in addition to the in-plane shear compliance. Beam elements model the axial stiffness, the in-plane flexural moduli, and the out-of-plane flexural moduli of the fibres. Membrane elements provide in-plane shear resistance of the sheet through a constitutive model implemented in VUMAT [115]. Vertical hinges are used to join beam elements (warp and weft) with membrane elements which are all vertically offset. Figure 6.1 (c) shows mutually constrained beam and membrane elements without the pantographic hinges, and Figure 6.1 (d) shows the unit cell used in this chapter with the pantographic hinge elements. This method was chosen as it provides a useful method of independently controlling in plane trellis shear stiffness and in/out of plane fibre bending stiffnesses. However this potentially comes with high computational costs due to the large number of elements, and small size and high degrees of freedom in the beam elements. The remainder of this Chapter will cover the numerical approach used in the simulations, and an overview of the results, before drawing conclusions.

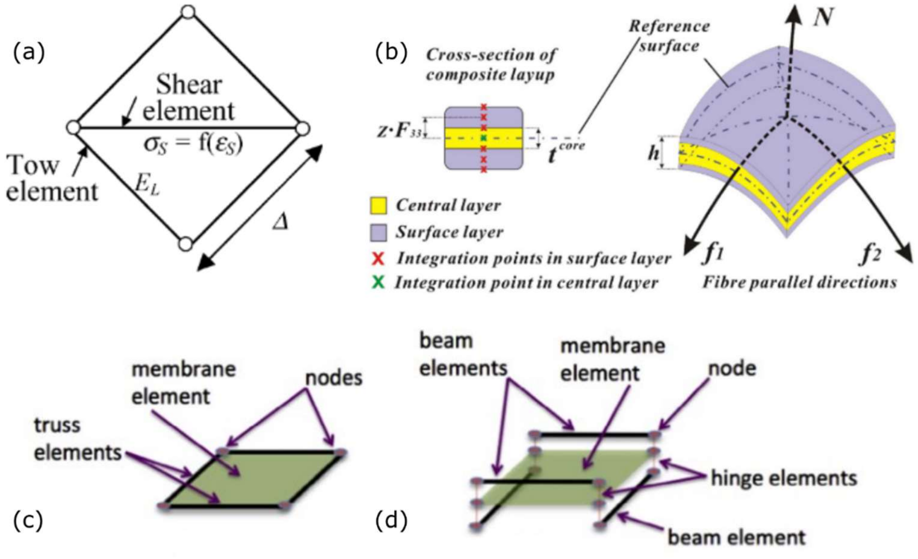

Figure 6.1 Diagram of repeated unit cells. (a) Example of truss based unit cell from Sharma et al.[241] (b) composite shell based unit cell adapted from Yu et al. [254] (c) mutually constrained truss-membrane elements and (d) mutually constrained pantographic beam and membrane elements. Warp and Weft beam elements are offset in z-direction and joined with membrane elements with zero-torque hinge elements. Adapted from [116]

6.2 Numerical approach

The numerical modelling was carried out in the explicit solver of the commercial finite element code Abaqus. The model consisted of three main components. First were circular sheets (the composite blank) consisting of a pantographic beam-membrane model with orthogonal beams with the unit cell as shown in Fig. 6.1d. Each of these sheets represents one of the [0/90/90/0] composite sheets used in the manufacturing process (Section 3.2). Second is a hyper elastic sheet modelling the silicone rubber diaphragm. Third is the rigid multistep male and female tooling. The overall assembly involved three composite sheets with [0/90], [+/-45] and [0/90] orientations. The sheets are held between top and bottom silicone rubber diaphragm sheets and then formed between the rigid body multistep tooling.

6.2.1 Composite Blank

The composite blank was modelled using a mutually constrained pantographic beam + membrane model which developed by Harrison [116]. Fig 6.1 shows a comparison between a truss-membrane mesh (Fig. 6.1c) and the mutually constrained pantographic beam (type B31) and membrane (type M3D4R) mesh used in this investigation (Fig. 6.1d). The beam elements model fibre tensile stiffness, out of plane and in-plane bending, and torsion. The use of beam elements rather than truss elements introduces bending moments during trellis shear. This is solved by the offset in the *z*-direction and connection by zero torque hinge elements constrains the relative position of the nodes and allows for free rotation.

The membrane elements have a thickness of 0.26 mm, and the material is modelled with a constitutive model implemented in the membrane elements using the VUMAT facility available in Abaqus. The presence of the membrane elements also facilitated the modelling of contact in the simulation. The model is adapted from [115] and a more detailed explanation of the mathematics behind the model can be found in that paper. The constitutive model has two primary functions. First is to model the fibre directional properties using a non-orthogonal stress-strain relationship. The constitutive equation is derived by considering the stresses in a conceptual structural net made of unit cells containing two sets of pin-jointed warp and weft fibres. The latter track the fibre orientations through the simulation and the fibre stress and strain are updated as they undergo both stretch and rotation. However, for this simulation, the stiffness of the fibres in the non-orthogonal constitutive model was set to be very low so that the contribution from the fibre stiffness in the membrane elements was very low. The fibre stiffness was instead represented by the beam elements. Despite this, the constitutive model is still able to track fibre orientation in the simulation. The second objective of the constitutive model is to represent the shear properties of the ply. The model defines unit vectors along the fibre orientations and from this, the stresses are represented in the non-orthogonal system. The non-orthogonal stress components can be used to define the instantaneous shear stress in the specimen, and the shear stress is incremented during the simulation based on the change in shear angle through the simulation. Details on the mathematics of the model can also be found in [115].

The Timoshenko beam elements are rectangular type B31 with a general section behaviour. These use a linear elastic material behaviour and have a Poisson's ratio of 0. The warp and weft elements are respectively placed slightly above and below the membrane elements as shown in Fig 6.1b. The weft and warp beam elements are connected to the corner nodes of the mesh with hinge connector elements. An Abaqus input file compatible mesh was generated using a pre-developed in-house Matlab code [255]. The material properties of the beams are calculated to provide realistic and independent values for the axial fibre stiffness, in-plane and out of plane bending stiffness, and torsional stiffness of a glass fabric blank.

The properties used in the membrane elements and beam elements were calculated from literature properties of the modelled fabric. The model uses the properties of a glass fabric (AllScot – ECK12) which is characterised via picture frame tests, uniaxial bias extension tests, and cantilever bend tests by various internal students at Glasgow University. The processes followed can be found in the various papers by Harison et al. [50], [116], [256]. Further details of the constitutive model in the membrane elements is available in the literature, specifically in Yu et al. [246] and Harrison et al. [256]. Calculations used to derive the beam and membrane parameters from the characterised properties can be found in Harrison et al. [116] and derivation of the torsional constants can be found in a further paper [50]. The parameters used in this model are detailed in Appendix A.

6.2.2 Silicone Rubber Diaphragm

The silicone rubber diaphragm sheets are meshed with S4R shell elements. The shell elements had a thickness of 0.3mm. The silicone rubber sheets are modelled with a diameter of 400 mm with an inner region of 200 mm with a higher density mesh. The outer region of the diaphragm has a mesh size of 0.01 mm, with the inner region having a mesh size of 0.001 mm. The varying mesh size is to reduce the total number of elements while maintaining high resolution in the central region which experiences significant deformation. The outer edge of the diaphragm is fixed in position with an encastre boundary condition. These shell elements have a hyper-elastic Ogden model applied to them. The parameters are laid out in Table 6.1. The parameters are obtained from [99] which modelled the room temperature behaviour of the silicone rubber sheets used in the experiments outlined in Chapter 3.

Table 6.1: Material parameters for the silicone rubber diaphragm. An Ogden model is applied in the Abaqus finite element code. Adapted from [99]

Material	**Mu$_1$ (Pa)**	**Alpha$_1$**	**Mu$_2$ (Pa)**	**Alpha$_2$**
Silicone	150,904	3.0918	813,392	0.18451

6.2.3 Rigid Body Tooling

The male and female tooling is modelled by a rigid body part with R3D4 elements. Two versions of this were produced: one with an amplitude of 6 mm (refer to the experimental version in Fig. 3.8 and 3.9) and another with an amplitude of 9 mm. The 9 mm amplitude was chosen as it will be a more challenging geometry to form and should lead to higher shear angles and higher stresses in the fibres.

Both versions of the tooling were divided into 15 segments instead of 5 to enable simulations with an increased number of forming steps. Segments are moved simultaneously to mimic single step forming, in groups of 3 to simulate five step forming as done in testing, and individual to model 15 forming steps. This segmentation involved a central cylinder with a diameter of 4 mm, and 14 concentric annuli with thickness of 4.25 mm. Each annuli had a separation of 0.25 mm. Both 6 mm and 9 mm amplitude versions of the tooling simulated have a radius of 65 mm and consist of five sin waves of 26 mm wavelength. A cross-section of the 15 step 9 mm amplitude male and female multistep tooling is shown in Fig. 6.2a, an image of the meshed male tooling in Abaqus CAE is shown in Fi.g 6.2b, and plan views of both the 5 and 15 segment tooling are shown in Fig. 6.2c and Fig. 6.2d respectively.

6.2.4 Boundary and Interface Conditions

The simulations were set up to mimic the forming conditions experienced in the experimental part. A representative diagram (not to scale) of the geometry of the set-up is shown in Fig. 6.3. The segmented 15 step male tooling begins 1.59 mm (d1) above the upper silicone diaphragm as seen in Fig. 6.3a. The diagram shows the 6 mm amplitude tooling. The silicone rubber diaphragms are located 1 mm above and below the centre line and are fixed on their outer edges by an encastre boundary condition and can be seen in Fig 6.3b. Three composite sheets are located between the diaphragms. There are two sheets with a 0/90 orientation located 0.5 mm above and below the centre line, and a third sheet with a +/- 45 orientation on the centre line as seen in Fig 6.3c. The female rigid tooling is fixed with an encastre boundary condition, and the top of the tooling is 0.5 mm below the bottom silicone diaphragm as shown in Fig. 6.3d.

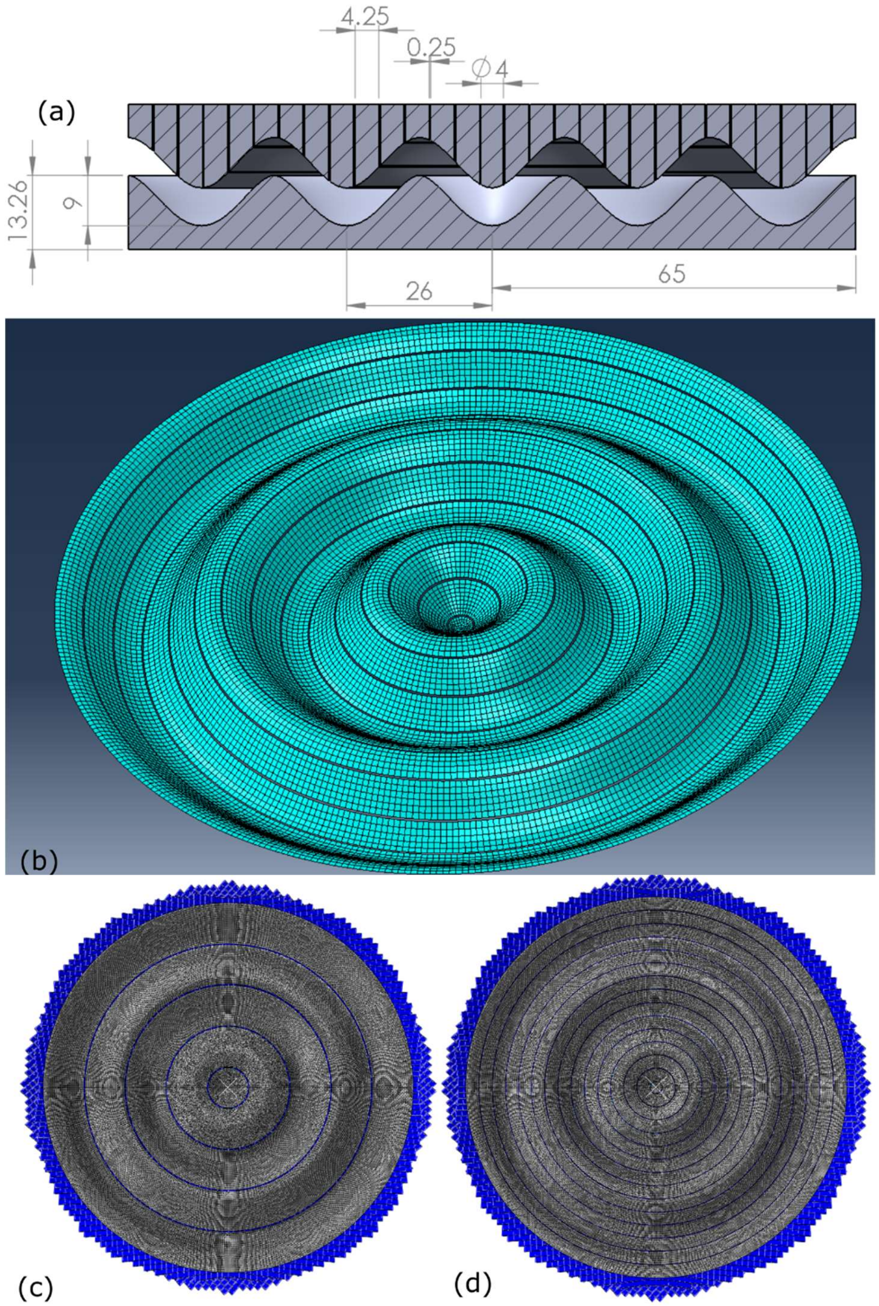

Figure 6.2: 15-step rigid body tooling with 9 mm amplitude. (a) Cross-section of male and female tooling with marked dimensions. Female tool has radius of 65 mm and pattern has five sin waves with 26 mm wavelength. Amplitude of sin wave is 9 mm. Male tooling has one central cylinder with a diameter of 4 mm and 14 annuli with 4.25 mm thickness. There is a gap of 0.25 mm between annuli. (b) segmented male tool mesh as displayed in Abaqus CAE. (c) Plan view of 5 segment tooling. (d) Plan view of 15 segment tooling.

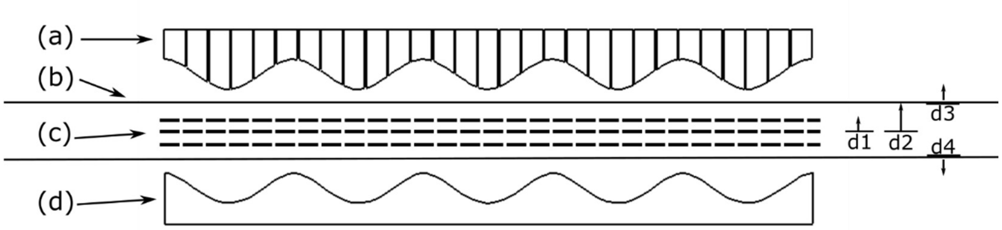

Figure 6.3: Representative Diagram (not to scale) of the simulation set up. (a) 15-segment multistep male tooling positioned d3 = 1.55 mm above the upper silicone diaphragm. (b) Silicone diaphragm. Upper and lower diaphragms are offset from centre line by d2=1mm. (c) Composite sheets. There are three layers with 0/90, +/-45, 0/90 orientations. Upper and lower sheets are offset from centreline by d1 = 0.5 mm. (d) Female tooling, positioned d4 = 0.5 mm below the bottom silicone diaphragm

The simulation includes three steps: first a gravitational acceleration of 9.81 m/s is applied to the full assembly. Secondly, a pressure of 100 pa is applied to the upper and lower surface of the diaphragm sheets and thirdly, a movement step moves the male tooling down at a fixed speed to form the part. This occurs in three ways: with one version moving all 15 segments as one to model a single step forming tool, a second version groups the segments into 5 groups of 3 to mimic the 5-step forming tool used in Chapter 3 and the final version moves each segment individually to model a 15-step forming tool.

The forming step was designed so that the tooling segments covered 10 mm in 0.02 seconds, for a speed of 500 mm/second. This compared with the speed of 8.33 mm/second (500 mm/min) in the experimental Section, or a velocity scaling of 60. The full time taken for the single step forming was 0.02 seconds. The 5 and 15 step simulations took 0.1 seconds in total as the individual forming steps were offset in time (i.e., 5 times longer than the single step forming). The full array of simulations and parameters is presented in Table 6.2.

A coulomb frictional coefficient of f_c=0.5 is applied to all interactions apart from the two surface interactions between the three composite sheets. These are given values of 0.1, 0.3 and 0.5 depending on the simulation as detailed in Table 6.2. These numbers were chosen based on a literature assessment of steady state friction in various thermoplastic composites and were intended to cover a range of outcomes from high friction of ~ 0.5 (low temperature, high sliding speed and low pressure) to low friction of ~ 0.1 [44], [82], [247]. The simulation number describes Amplitude-No. of Steps-Friction Coefficient.

Table 6.2: Details of varying parameters used in the simulations

Simulation Number	Tooling Amplitude (mm)	Number of forming steps	Interlaminar Friction Coefficient (f_c)
6mm_1_03	6	1	0.3
6mm_5_01	6	5	0.1
6mm_5_03	6	5	0.3
6mm_5_05	6	5	0.5
6mm_15_03	6	15	0.3
9mm_1_03	9	1	0.3
9mm_5_01	9	5	0.1
9mm_5_03	9	5	0.3
9mm_5_05	9	5	0.5
9mm_15_03	9	15	0.3

6.2.5 Simulation Robustness

The modelling strategy which utilised a pantographic beam and membrane mesh to simulate the composite sheet is useful as it allows for fine control over the parameters. On the other hand, it has some drawbacks which limit its usefulness. The beam elements have a very small stable time increment due to their small size and high stiffness. This slows the simulation down increasing computation costs. The stable time increment (Δt) is based on the frequency of the system, and if material damping is ignored, can be approximated as follows

$$\Delta t = \frac{L_e}{\xi} \tag{6.1}$$

where L_e = length of element, and ξ = wave speed of the material. For linear elastic materials with a Poisson's ratio of zero, wave speed can be defined as below

$$\xi = \sqrt{\frac{E}{\rho}} \tag{6.2}$$

where E = material stiffness, and ρ = material density (see Abaqus User Manual, [151]). For a given mesh dimension, the computational cost can be reduced using either velocity scaling (making the simulation faster), mass scaling (increasing the density of the part) or varying the stiffness of the material. However, all of these can impact the accuracy of the simulation [50]. The modelling uses velocity scaling of ~ 60 times to speed up the simulation. Due to the small dimensions and high stiffness required in the modelling, the beam elements in the simulation have a starting stable time increment of 1.34 $\times 10^{-7}$ seconds, which compares with the stable time increment of the silicone diaphragm of 1.11 $\times 10^{-5}$ seconds. [50]

There were also some issues with stability in the simulation. In development of the simulation, tooling with amplitudes of 12 mm were attempted, as were simulations with pressure of 100,000 Pa. The more challenging forming conditions led to failure in the simulation due to ‘excessive rotation at nodes’. These failures tended to occur at areas of high shear deformation and tensile stress suggesting instability in the numerical simulation at high deformation. Fig 6.4a shows a location of high shear deformation in the top [0/90] composite sheet in a simulation with a 12 mm amplitude tooling. Fig 6.4b shows the failing node in the middle [+/-45] composite sheet which corresponds to the location of high shear. The beam elements have been magnified in ABAQUS viewer to aid in visualisation. The node is connecting two beams with high tensile stresses and one beam with high compressive stresses. The introduction of the pantographic beams elements enables modelling of a larger number of physical phenomena. The use of the pantographic beams is still relatively novel and has not fully been explored but understanding the limitations of the simulation would be a useful future avenue for exploration.

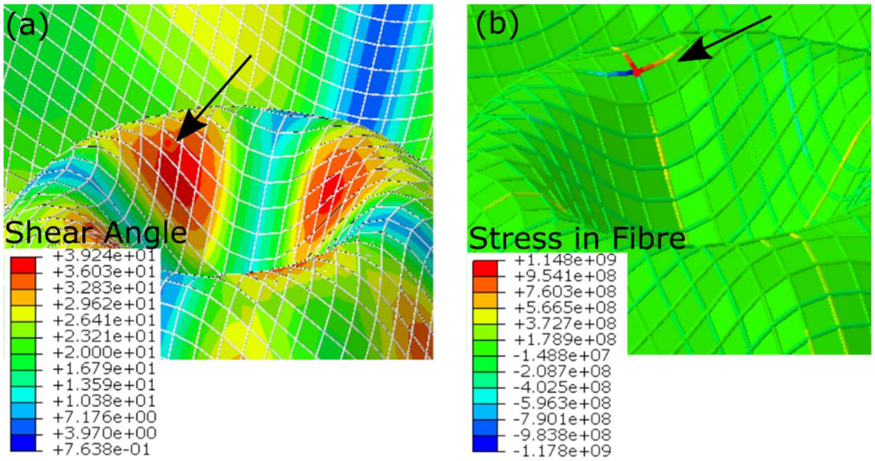

Figure 6.4. Pictures of failure during a simulation with 12 mm amplitude tooling. Arrows point at location of failing node (a) area of high shear deformation in upper [0/90] composite sheet. (b) middle [+/-45] sheet with high tensile and compressive stresses on beams connected to failing node.

6.2.6 Model Limitations

There are some limitations with the model structure which means there is some inaccuracy in representing the experiments, as outlined in Chapter 3. Firstly, the silicone diaphragm is not held by a blank holder, and the restriction is simplified to an encastre boundary condition which ignores any slippage that might occur. Furthermore, the fluid interlaminar tin is not modelled. Its impact is approximated with varied friction coefficients between the composite sheets. Modelling the flow of the interlaminar tin would be useful for future projects, but was deemed too time consuming for this study. Finally, the blank is modelled as a non-lubricated glass fibre fabric, rather than the lubricated cross-ply carbon-nylon fabric used in the experiments. The forming mechanics of the glass fabric had already been fully characterised [257]. This is a different material, and will different behaviours in some aspects such as in plane shear, as the fibres are effectively pinned at crossover points [166]. A modification is proposed in Section 6.2.7 which might address the different behaviour between woven and UD plies. The modelled blank also does not cover any effects of varying temperature that might have occurred in the real experiments, or for that matter, the thermal expansion of the silicone rubber. The pressure applied to the diaphragm surface was only 100 Pa in the simulation, compared with 100,000 Pa in the experiment. The pressure was lowered due to instabilities in the simulation leading to early failure (see Section 6.2.5). Lowering the pressure on the forming simulation makes it less representative of the real forming experiments. However, one key impact of the higher pressure in dry fabrics is to effectively increase frictional forces. Given that the simulated fabric is of dry glass fibres (i.e., not lubricated like the carbon-nylon composite used in Chapter 3), the friction forces created in the simulation are relatively high. Conversely, in lubricated composites, the total frictional forces tend not to vary much with pressure, so effective coulomb friction can, depending on contact pairings, go down as pressure increases [82]. Given the difference in frictional behaviour with pressure, lowering the pressure when modelling the glass fabric is not as disruptive to the model as it could be. Characterising these phenomena would be an appropriate next step for this forming. However, despite the different behaviour of a glass fabric [257] and a molten pre-consolidated carbon-nylon blank [166], it is believed that it is still useful to understand the forming mechanics involved in the ripple geometry, the influence of varying friction, and the influence of multi-step tooling in the forming of a common fabric type, while exploring the potential of the pantographic beam and membrane mesh method of simulating composites.

6.2.7 Alternative Multi-sheet Model

An alternative method of representing the thermoforming conditions was also trialled. The method described above uses a single sheet comprised of beam and membrane elements to represent a 4 ply [0/90/90/0] unwoven laminate. This is limited as the fibres are effectively pinned at crossover points. Therefore it was proposed to use four sheets (also with a pantographic beam and membrane element architecture) to represent the same [0/90/90/0] layup. Thus, each simulated sheet would represent a single unidirectional ply. A number of changes to the simulation were made, and these are outlined below:

- A total of 12 sheets were simulated instead of 3. With a layup of $[90/0/0/90/+45/-45]_S$.
- The primary direction beam elements retained the same material properties as previous experiments.

- The off-direction beam elements were given a nominal axial stiffness of 1 MPa to give a slight resistance to lateral fibre shift. All other properties remained the same.
- The membrane elements retain their low nominal axial stiffness from the original experiments but also retain their shear stiffness.
- Membrane thickness in each simulated sheet changed from 0.26 mm to 0.006 mm as each sheet only represents a single ply. The sheet z-positions were adjusted accordingly.
- Boundary conditions matched 6mm_5_03, with a 6mm tooling amplitude, 5 forming steps and an interlaminar friction coefficient of 0.3

Details of the parameters can be seen in Appendix A. Due to the large number of interacting elements the simulation was computationally expensive to process, so only a single simulation (to match 6mm_5_03) has been carried out. Connections issues with the University ABAQUS license limited simulation length. Simulations were terminated due to external request rather than failing to converge. The longest simulation reached approximately 72% completion after 267 hours. This compares to approximately 65 hours for the previous simulations. The results from the simulation are included in the results below however the increased computational cost suggests that this may not be a suitable simulation method going forward.

6.3 Results

A total of 10 simulations were carried out as detailed in Table 6.2. The simulations looked to vary three parameters. First, the amplitude of the ripple tool geometry (6 & 9 mm), second, the number of segmented steps in the forming process, (1, 5 & 15) and third, the interlaminar Coulomb friction coefficient (0.1, 0.3 & 0.5).

The simulated parts were primarily assessed in three ways to give a proxy for how “challenging” the forming conditions are. First, by looking at the resulting shear angle of the sheet after forming. Higher levels of shear deformation can lead to defects in the final part however are often necessary to conform to the tooling. Second, by examining the axial stress in the beam elements (beams with high tensile stress might experience tow tearing or bridging, beams with high compressive stress might experience buckling or wrinkle initiation). Finally, the axial stress in the beam is compared with the accumulated strain in the 1-fibre and 2-fibre directions of the membrane elements. This is tracked by the constitutive model in the membrane elements. These two criteria are similar, but measure slightly different physical phenomena. The strain in the fibre direction is primarily influenced by axial stresses. However, the stress in the beam elements will be a result of both axial and bending stresses in the beam. In all three cases, the maximum value of the parameter in each composite ply at each time step is plotted. The maximum stress, strain, and shear all give an indication of how challenging the forming conditions are. First the impact of varying friction is considered, then the impact of varying the number of forming steps.

6.3.1 Influence of Friction

Figure 6.5 shows the pattern of shear deformation at the end of the simulation in the 6 and 9 mm amplitude parts when varying the interlaminar friction coefficient. Fig 6.5a shows simulation “6mm_5_01” and is compared to Fig 6.5b which shows simulation “6mm_5_05”. As noted earlier, the simulation numbering system describe tooling amplitude, number of steps and friction coefficient respectively. Increasing the friction coefficient had only a minor impact on the pattern of shear deformation in the plies, with both sheets exhibiting similar levels of deformation. Fig 6.5c and Fig 6.5d show the shear deformation at the completion of forming in the “9mm_5_01” and the “9mm_5_05” simulations respectively (Note the different scale). The absolute shear deformation is higher in this model however the impact of varying the friction remains low.

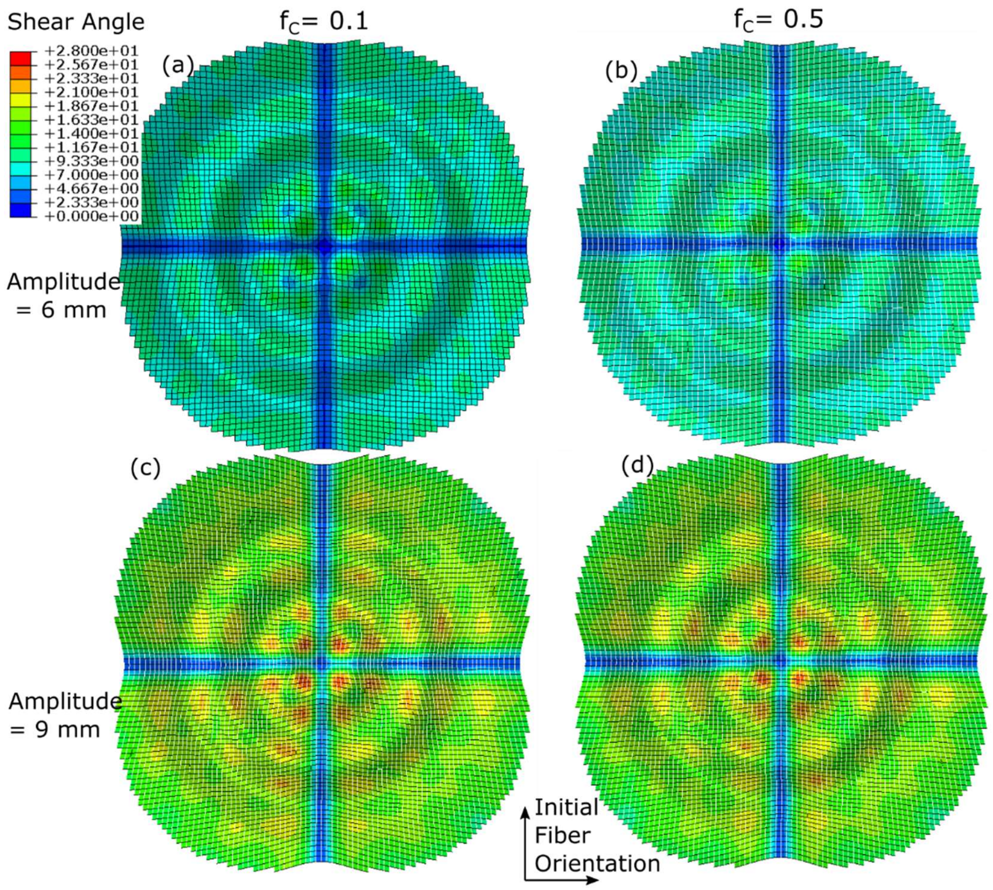

Figure 6.5 Shear angle at end of simulation in bottom ply. (a) Shear angle of 6mm_5_01 (b) Shear angle of 6mm_5_05 (c) Shear angle of 9mm_5_01, (d) Shear angle of 9mm_5_05. Initial fibre orientation of [0/90] marked on image.

Fig. 6.6 shows a comparison between the axial stress component in the beam elements of simulations with the actual formed parts. Fig. 6.6a shows the axial beam stress in the high friction simulation “6mm_5_05” (see Table 6.2), which is compared with the wrinkling occurring in the unlubricated formed part in Fig. 6.6b (See also, Fig 3.21) and the axial membrane strain in Fig. 6.6c. The highlighted red circles show similarity between compressive axial stresses in perpendicular fibres at the edge of the part, with wrinkling occurring at the edges of the formed part. The central areas experiencing high compression do not appear to match with wrinkling in the part. The lower friction simulation “6mm_5_01” in Fig. 6.6d shows lower compressive stress in the fibres, and this matches with the unwrinkled lubricated sample shown in Fig. 6.6e (see also, Fig 3.18) and compares with the strain in Fig. 6.6f. The peak tensile stresses and strains align in each simulation, both creating a cross pattern from the centre of the part. The peak tensile values occur in the centre of the part. The peak compressive stresses and strains are however rotated 45 degrees from each other, with the peak compressive stresses acting parallel to the fibre directions and the peak compressive strains occurring at a 45-degree offset.

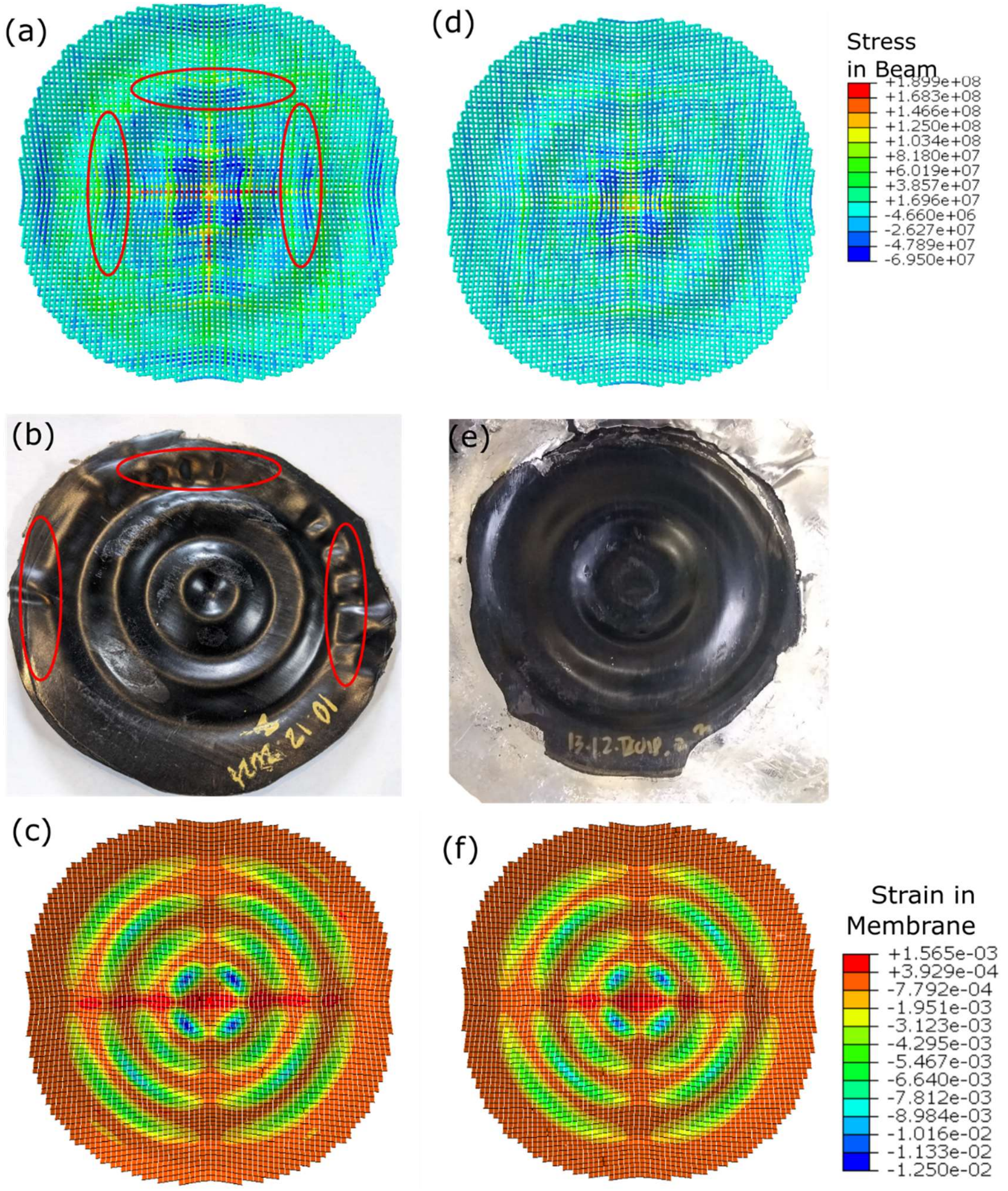

Figure 6.6: Comparison between beam stresses, formed parts and membrane strains. (a) Stresses in bottom ply of simulation “6mm_5_05” and (b) unlubricated nylon-carbon fibre part. (c) Strains in bottom ply of simulation “6mm_5_05” (d) Stresses in bottom ply of simulation “6mm_5_01” (e) nylon-carbon fibre part lubricated with interlaminar tin (f) Strains in bottom ply of simulation “6mm_5_01”. Highlighted perpendicular compressive stresses in (a) match with wrinkling (red circles) in (b). See Table 6.2 simulation details.

To further assess the overall influence of the interventions, it was desired to look at the maximum axial stresses, axial strains, and shear angles experienced over the full sheets. Therefore, the maximum shear deformation in the membrane elements, maximum axial tensile and compressive stresses in the beam elements, and maximum axial tensile and compressive strains in the membrane elements for each time stamp were extracted and plotted.

Fig 6.7a shows the maximum tensile stress in each ply (top, middle, and bottom) in both the 6 mm and 9 mm amplitude 5-step forming simulations when varying friction (f_c = 0.1, 0.3, 0.5). Fig 6.7b shows the maximum tensile strains in the membrane elements. Maximum tensile stresses and strains both occur in the top composite sheet, suggesting that fibre bridging is most likely to occur in the top sheets. Increasing friction also leads to higher peak tensile stresses in the beam elements and increasing the amplitude of the forming tool also leads to higher tensile stress. Changing f_c from 0.5 to 0.1 in the 9 mm simulation causes a drop in peak stress in the top ply of 61 % and a drop in peak strain of 66 %. As seen in Fig. 6.6, the peak tensile stresses occur in the central dip, and that pattern continues across all samples. There is good agreement between the stresses in the beams, and the strains measured in the membrane model.

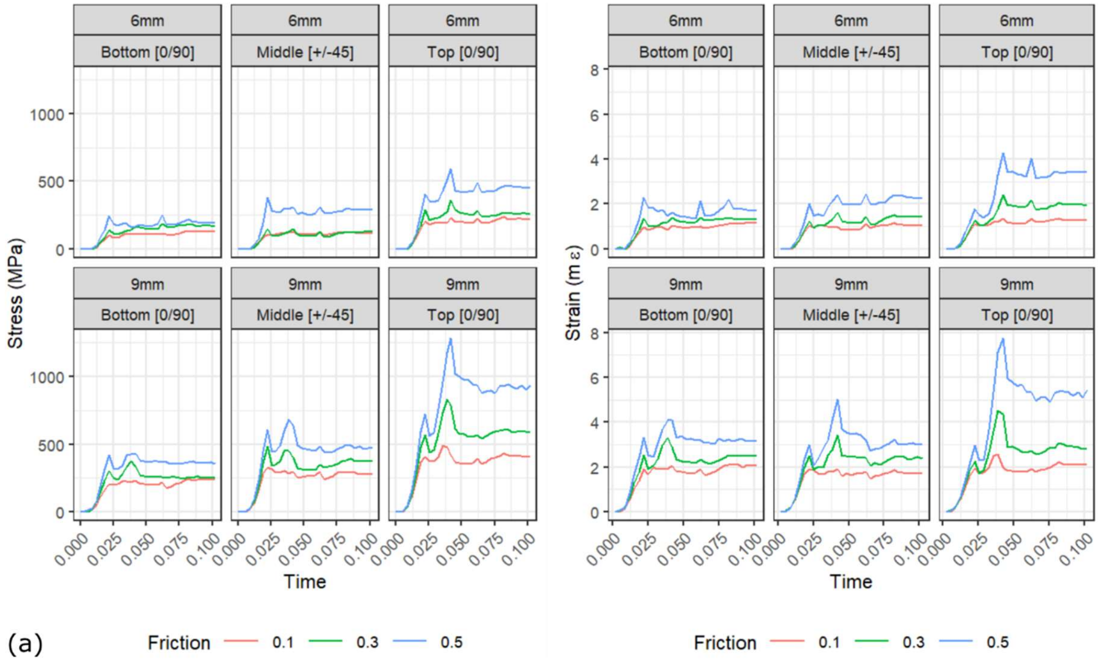

Figure 6.7: (a) Maximum tensile stress in beam elements in each ply when varying friction coefficients (b) Maximum tensile strain in membrane elements in each ply when varying friction coefficients. Number of forming steps is 5.

Figure 6.8a shows the maximum compressive stresses in the beam elements of each ply (Bottom, Middle, Top) for the 6 mm and 9 mm 5-step forming simulations, when varying friction. Fig. 6.8b shows the maximum compressive strains in the membrane elements. The influence of varying friction on axial stress is small in the top and bottom [0/90] plies. However, there is a more noticeable impact in the middle [+/-45] ply. The results for strain show similar behaviour in the 6 mm simulations, but in the 9 mm simulation, the variation in strains in the middle ply is much less than the variation in peak stresses. Overall, the compressive stresses in the beam elements have more variability than the compressive strains in the membranes. A potential reason is that the beam elements also undergo bending and torsion. This means they are more effected by out of plane forces than the membrane elements. These additional deformations may influence the measured axial stress in the beams, particularly in compression, more than in the membrane elements.

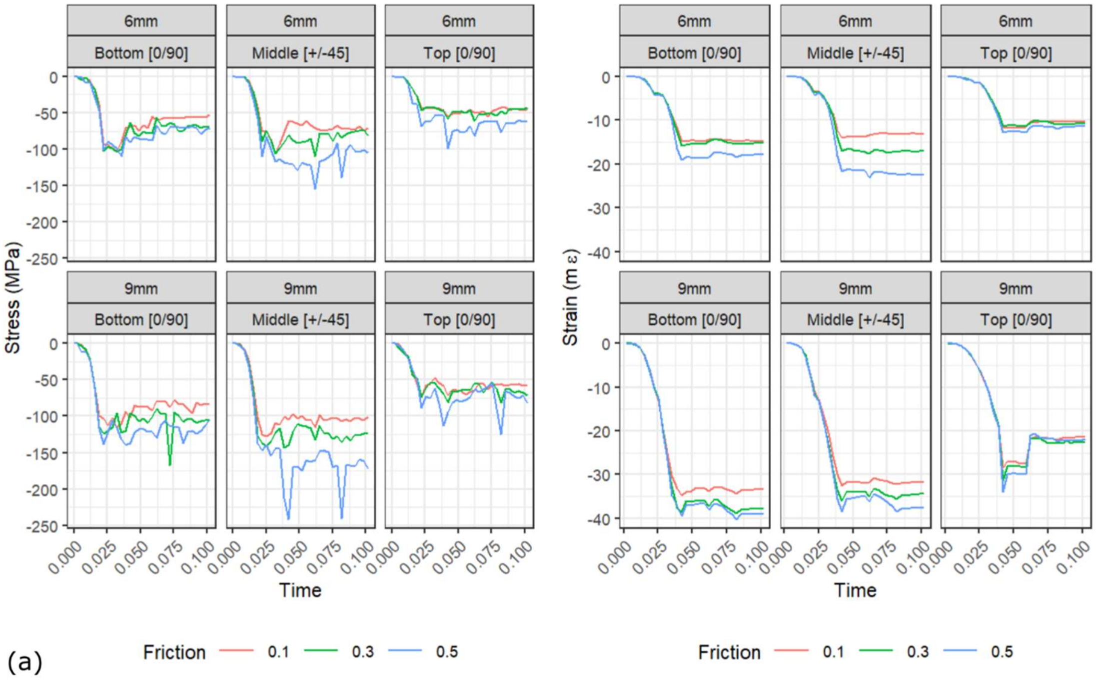

Figure 6.8: (a) Maximum compressive stress in beam elements in each ply when varying friction coefficients (b) Maximum compressive strain in membrane elements in each ply when varying friction coefficients. Number of forming steps is 5.

Fig. 6.9 shows the maximum shear angle in the membrane elements of each ply in the 6 mm and 9 mm forming studies when varying friction coefficients. This shows that varying the friction had only a small impact on the shear deformation of each sheet. There is also only a small variation between plies. The 6 mm forming simulations experience shear angles of 15.0 - 16.1 degrees, and the 9 mm simulations experience shear angles of 25.7 - 28.4 degrees.

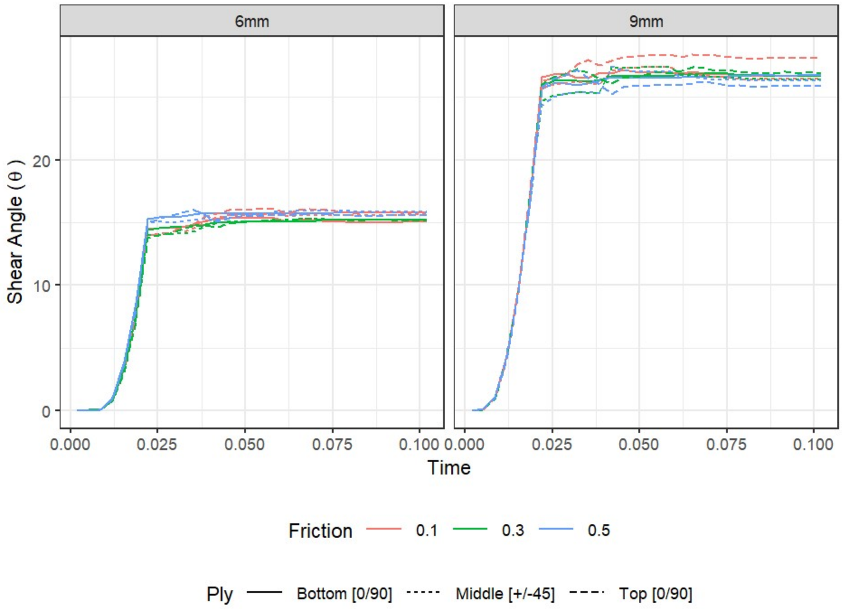

Figure 6.9: Maximum shear angle in membrane elements in each ply when varying friction coefficients. Number of forming steps is 5.

6.3.2 Influence of Number of forming steps

Simulations were also carried out to look at the influence of the number of forming steps on the difficulty of forming. These simulations used the same tool speed for all tests, which results in the 1 step simulation occurring faster than the 5 and 15 step simulations. The 15 step simulation appropriately offsets the starting time of movement in each tooling element to match the total forming time used in the 5 step specimen. Fig. 6.10a shows the variation in axial tensile stress in the beam elements, and Fig. 6.10b the maximum tensile strain in the membrane elements when varying the number of forming steps when f_c= 0.3 for both the 6 mm and 9 mm amplitudes. The single step forming results in significantly higher maximum tensile stresses which are alleviated by the 5-step forming. For example, the stress increases to over 7 times larger from ~ 184 MPa to ~ 1350 MPa in the bottom ply of the 6 mm amplitude simulation or over 10 times larger from ~ 250 MPa to ~ 2700 MPa to in the bottom ply of the 9 mm amplitude simulation. In terms of strain, there is a maximum increase of ~10 times from ~ 1.3 $m\varepsilon$ to ~ 12 $m\varepsilon$ The move from 5 to 15 steps shows minimal change in maximum stress or strain. This indicates that, for this geometry and layup, there is no additional benefit to additional segments beyond five. As there is three concentric depressions in the female tooling then three appropriately designed male tooling segments to match the three depressions may be sufficient. There is good agreement between the stress measurements in the beam and the strain measurements in the membrane elements.

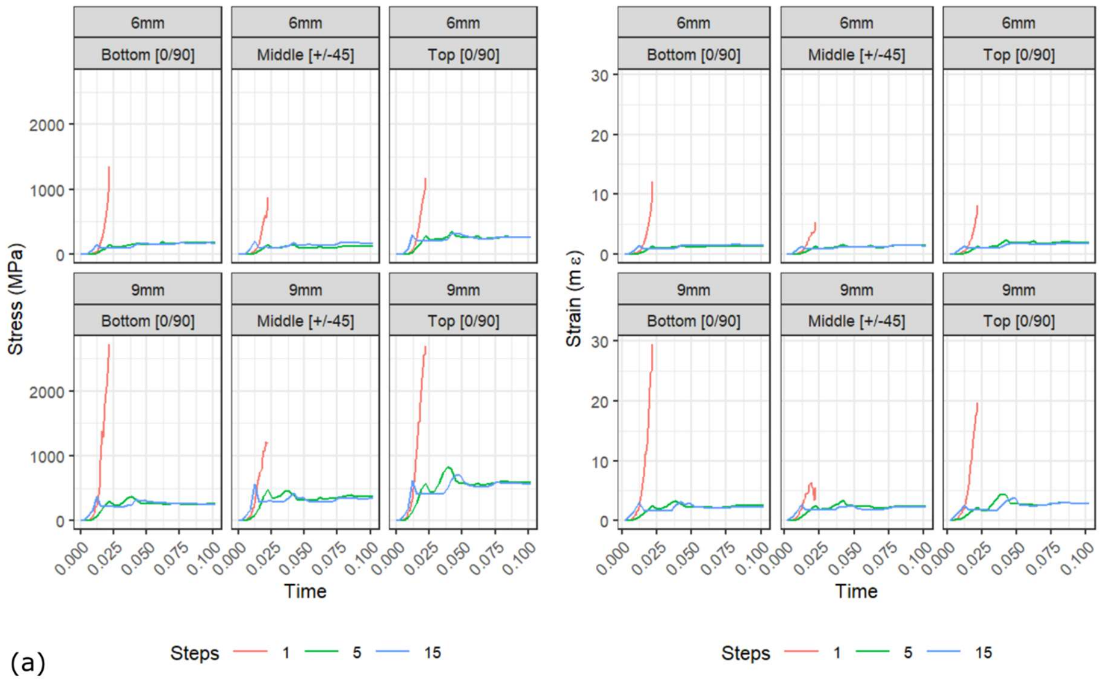

Figure 6.10: (a) Maximum tensile stress in beam elements in each ply when varying number of forming steps. (b) Maximum tensile strain in membrane elements in each ply when varying number of forming steps. f_c = 0.3.

Figure 6.11a shows the variation in axial compressive stress in each ply when varying the number of forming steps when f_c= 0.3 for both the 6 mm and 9 mm amplitudes. In the 6 mm forming, the single step tooling imparts similar compressive stresses to the multistep tooling in the top and bottom plies. However, there is a more noticeable impact in the middle ply. In the more challenging 9 mm forming, the single step has much higher maximum stresses (with the maximum stress in the middle ply being over 6 times larger in the single step forming, going from ~123 MPa to ~770 MPa). The difference between 5 and 15 steps is again minimal. Fig. 6.11b shows the maximum strain in the membrane elements over time. The maximum compressive strains appear to not significantly change when varying the number of steps, but the time taken for the strains to increase does change.

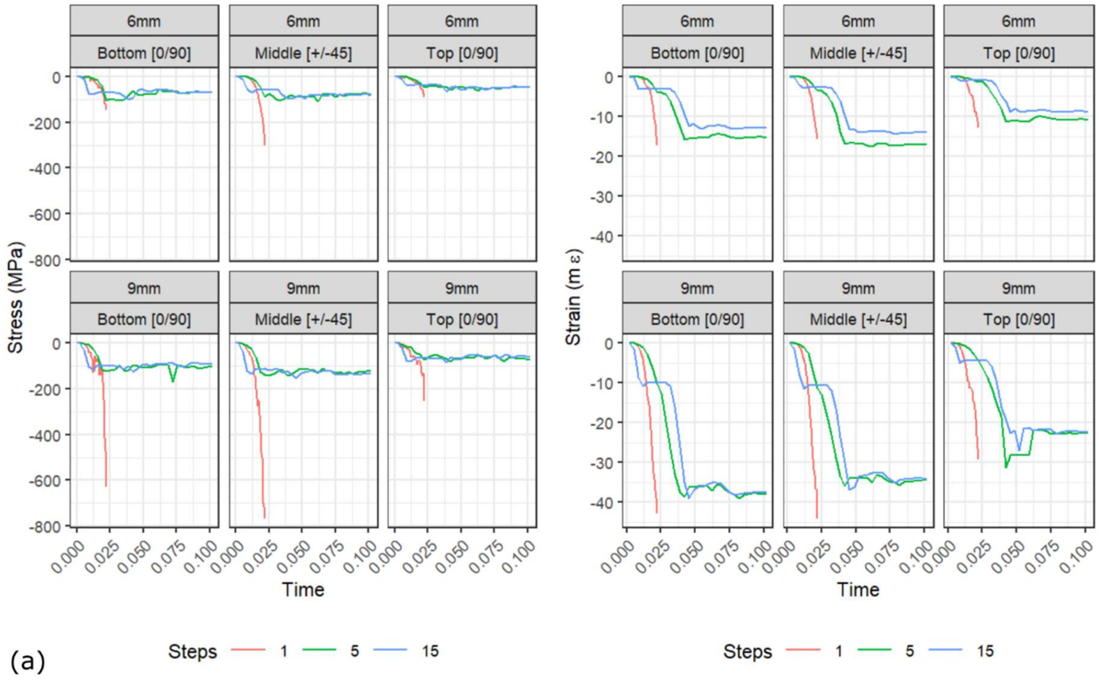

Figure 6.11: (a) Maximum compressive stress in beam elements in each ply when varying number of forming steps. (b) Maximum compressive strain in membrane elements in each ply when varying number of forming steps. f_c = 0.3.

Figure 6.12 shows the maximum shear angle in the beam elements in each ply when varying the number of forming steps (f_c=0.3). The shear angle for the 1 and 5 step simulation track each other very closely in the initial forming step for both 6 mm and 9 mm. The 15-step forming exhibits a lower maximum shear angle in the 6 mm forming, but not in the 9 mm forming. There is once again limited variation in shear angle between plies in the same simulation.

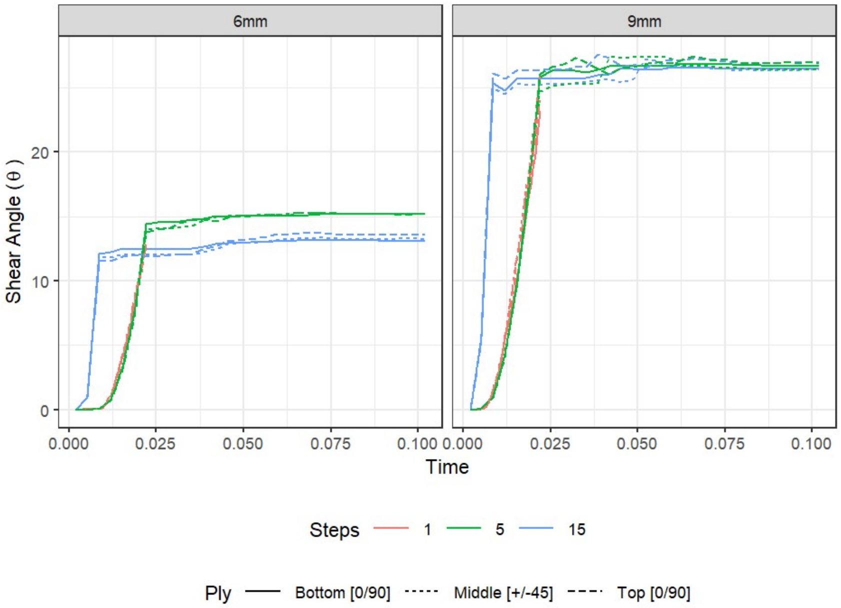

Figure 6.12: Maximum shear angle in fibres in each ply when varying number of steps. f_c = 0.3.

To check the influence of friction on the forming behaviour, it was decided to check total displacement in each ply. A line of points was selected as marked in Fig. 6.13a, with the points following the fibres direction through the centre of the formed part in the top and bottom ply, and at a 45 degree angle in the middle ply. The total displacement at each point at the end of the forming process was then plotting in Fig. 6.13b. From these numbers it can be seen that, as a result of the different fibre architecture, the middle ply experiences relative displacement compared with the top and bottom plies. This will require relative motion of the plies to resolve, and thus the frictional forces will be significant in the forming process.

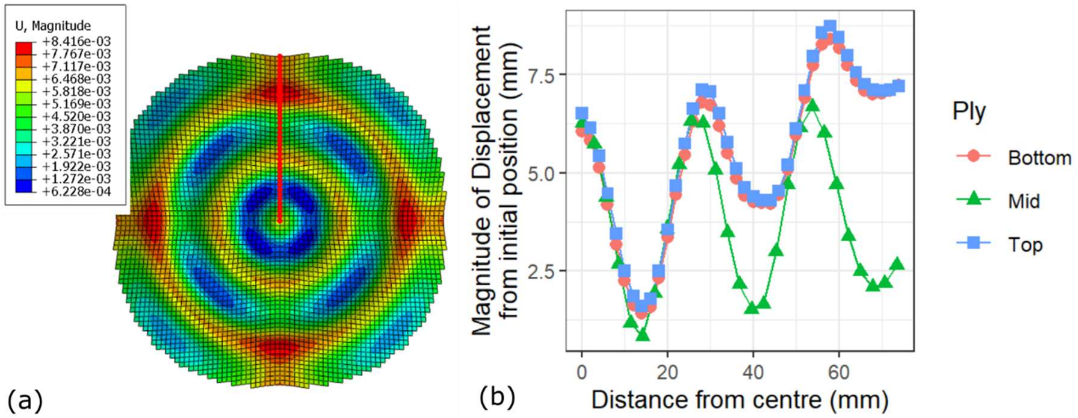

Figure 6.13: (a) Analysed line is parallel to fibre orientation in top and bottom ply (bottom ply displayed, points analysed highlighted in red), and at 45 degrees relative to fibre direction in middle ply. (b) Total displacement of points along axial line in bottom, middle and top ply. Middle ply shows different displacement magnitudes due to different fibre architecture.

6.3.3 Alternative Multi-sheet Model

As stated earlier the multi-sheet simulation was computationally expensive and as such the simulation was not completed. Fig. 6.14a shows the axial beam stresses in the mid ply of 6mm_5_03 at timestamp 0.07 seconds (to match the end point of the multi-sheet simulation) and Fig. 6.14b shows the axial beam stresses in the primary orientation of the four simulated sheets making up the [+45/-45/-45/+45] mid ply sheet in the multi-sheet simulation. To make these images, first the Warp and Weft beam elements of the middle ply were selected under Select element sets. Then under “ODB display options” menu and the “General” Submenu: “Render beam profiles” was enabled and a scale factor of 10 was applied. For Fig. 6.14b the primary beam orientation from each of the 4 sheets representing the middle [+45/-45/-45/+45] ply were highlighted, and as such lower plies are slightly obscured by upper plies. In the first scenario where the fibres are effectively pinned at crossover points, the peak tensile stresses occur in the fibres which cross through the centre of the ripple shape. However in the multi-sheet simulation where fibres have more freedom to shift laterally the peak stresses occur at the around the top of the first ripple and are more distributed around the fabric.

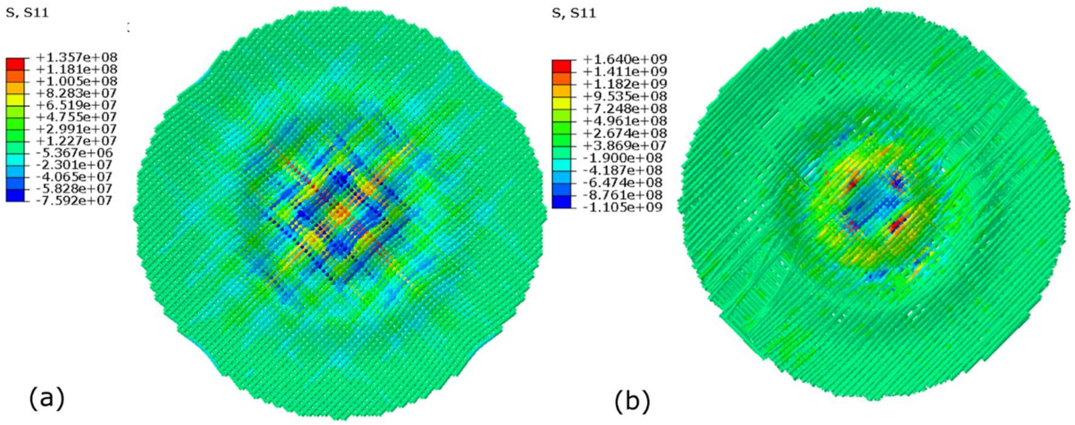

Figure 6.14: (a) S11 axial Beam stresses in mid ply of 6mm_5_03 at timestamp 0.07 (b) S11 axial beam stresses displayed in the four primary orientations of the four sheets representing the middle [+45/-45/-45/+45] ply at timestamp 0.07. Note different scales on beam stiffnesses

Fig. 6.15a shows the membrane strains in the primary orientation of a selected sheet in the middle ply of the fabric (highlighted, [+45**/-45/-**45/+45]). Fig. 6.15b shows the membrane strains in the secondary orientation of the same sheet in the middle ply. In this case the membrane strains in the secondary orientation are not representing strains in a fibre, but lateral displacement occurring between fibres. From this it can be seen that in order to accommodate the curvature of the ripples there is lateral displacement in the fibre which pass through the centre ripple. This is likely the mechanism which relieves stress in the bottom of the central ripple.

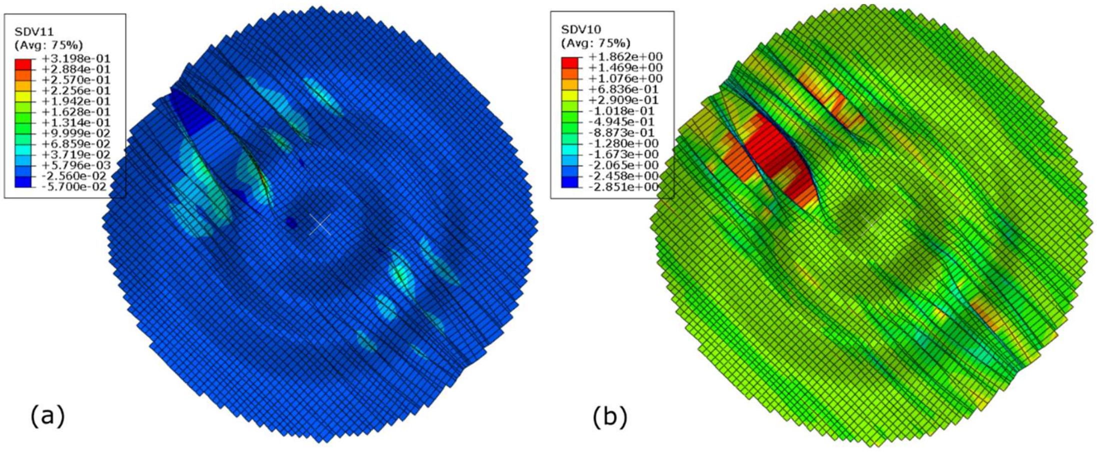

Figure 6.15: (a) Primary orientation membrane strains in selected sheet in middle ply (highlighted, [+45**/-45/-**45/+45]). (b) Secondary orientation membrane strains in selected sheet in middle ply (highlighted, [+45**/-45/-**45/+45]). Note different scales. In this case stresses primary orientation strains represent fibre strains, and strains in secondary orientation represent lateral displacement of fibres.

Fig. 6.16a shows the maximum tensile stresses in the four plies in each sheet while Fig. 6.16b shows the maximum compressive stresses in the four plies in each sheet. Similar to results in Fig. 6.7a (comparing with friction coefficient as 0.3) the peak tensile stresses occur in the top ply with the middle ply seeing the smallest tensile stresses. However, in this simulation the peak compressive stresses occur in the top ply, rather than the middle ply. The total magnitude of the experienced stresses is approximately an order of magnitude higher than in the previous simulations.

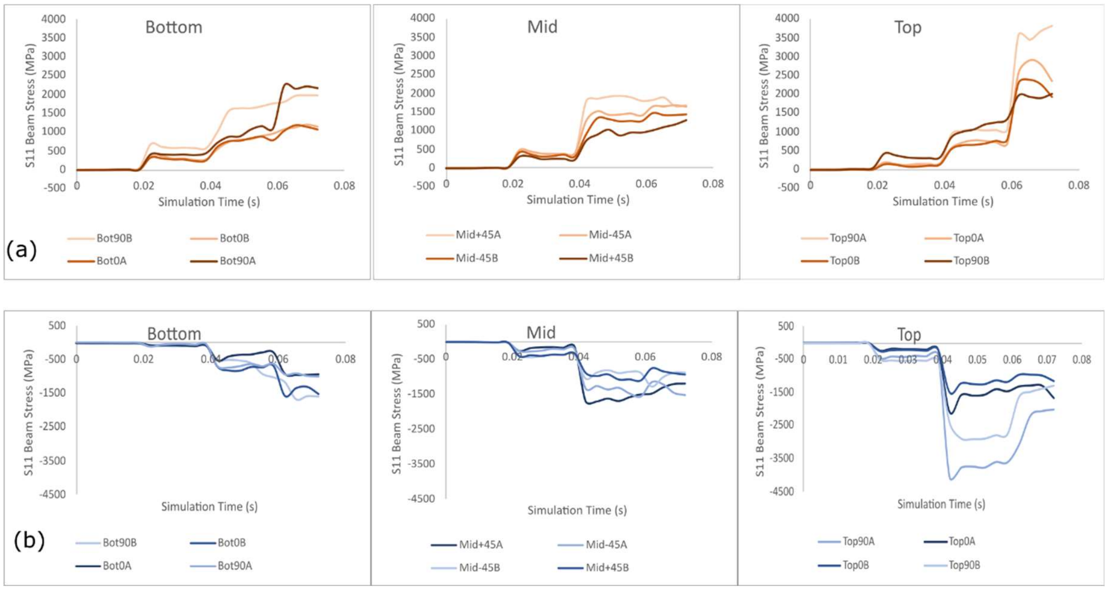

Figure 6.16. maximum beam stresses in plies in each sheet in multi-sheet simulation. In each chart light -> dark is top -> bottom of 4 ply layup. (a) Maximum tensile stresses in each of the simulated sheets in the top, bottom and middle laminates (b) Maximum compressive stresses in each of the sheets in the top bottom and middle laminates.

6.4 Discussion and Conclusions

In this Chapter, a pantographic beam and membrane mesh is used to model the multi-step diaphragm forming of three glass fabric sheets (Orientations of [0/90], [+/-45], [0/90]) into a ripple geometry. The ripple geometry consists of a sine curve, and tools with two different curve amplitudes (6 mm and 9 mm) are modelled. The number of steps in the forming tool is varied (1, 5 and 15), as are the friction coefficients between the composite sheets (f_c = 0.1, 0.3, 0.5). See Table 6.2 for details of the simulations. The method of modelling the composite sheet allows for the fibre stiffness, torsional stiffness, in plane bending stiffness, and out of plane bending stiffness, as well as the shear stiffness of the sheet to all be modelled independently. This level of control over the material properties of a composite is useful, however instabilities were experienced in the simulation when modelling more complex forming conditions (i.e., higher diaphragm pressure, or tooling with a higher amplitude, see Section 6.2.5).

The forming was assessed based on the axial stress experienced in the beam elements (both compressive and tensile), the axial strain as predicted by the non-orthogonal constitutive equation implemented in the membrane elements, as well as the shear angle. It was found that the variations in the friction coefficient had minimal impact on the shear angle for both 6 mm and 9 mm amplitudes. Single and 5-step toolings showed similar shear deformation. The 15-step forming tool lowers the maximum shear angle in the 6 mm amplitude tooling, but not in the 9 mm amplitude tooling.

More significant differences were found in the variation in tensile and compressive stresses in the fibres. Moving from single step tooling to a 5-step tool reduced the maximum tensile stress and tensile axial strain in all plies with a maximum reduction of ~90% occurring in the bottom ply of the 9 mm tooling. On the other hand, there was limited benefit from increasing the number of forming steps from 5 to 15. Increasing friction increased the peak stresses and strains measured, particularly in tensile measurements. The biggest reduction in the tensile direction was in the top ply of the 9 mm simulation (reducing stress and strain by 61 % and 66 % respectively). The compressive stresses and strains showed less influence from varying the friction, with the biggest difference coming in the mid-ply of the 6 mm simulation with 32 % and 39 % drops in compressive stresses and strains, respectively. The compressive stresses experience “spikes” which are not matched by the measured strains, and these are larger in the 9 mm simulation. The beams in compression will experience torsion and bending stresses in addition to the compression and this additional complexity may be influencing the measured results.

A multi-sheet simulation with a nominal layup of $[90/0/0/90/-45/+45]_s$, where each pantographic beam and membrane sheet represented a single UD ply, was also trialled. In this case the simulated fabric was a dry glass fabric, thus once the fibres were nominally unpinned in the simulation it led to significant lateral motion as the simulated fabric. This was primarily constrained with a nominal stiffness of 1 MPa in the off-direction of the beam elements. In a thermoplastic forming process the viscosity of the thermoplastic matrix would resist this lateral movement and appropriate modelling of this would be useful. Removing pinning at the crossover points in the fabric architecture is potentially useful in studying lateral movement of fibres in multiply UD laminates. A key drawback was the computational cost of the simulation. The primary simulations took 65-70 hours to complete on a laptop, while the multi-sheet simulation took 267 hours to reach ~70% completion. This suggests around 380 hours (~16 days) for completion. Possible improvements could be the removal of the off-direction beam elements to reduce the number of degrees of freedom in the simulation.

These results give an indication of some of the benefits of reducing interply slip and the use of multi-step forming tools. They are however, of limited use when analysing the forming of the lubricated, temperature dependent carbon fibre composites used in the rest of this thesis. The use of the pantographic beam and membrane mesh enabled modelling of a complex fabric sheet and it was also possible to compare the output parameters provided by the beam and membrane elements, with the beam elements showing spikes in value. The simulation showed the positive influence of reducing friction coefficients between plies and the positive influence of multistep forming, particularly on reducing tensile strains. The results showed limited benefits of adding additional steps beyond 5-steps when considering stresses and strains in the sheet; however, there may be benefits in terms of tin expulsion. Further avenues for exploration in this field would be to build upon prior characterisation of the carbon-nylon sheet [166] to obtain accurate temperature-dependent parameters for use in simulations to better understand the forming mechanics of the carbon-nylon layup. More challenging is to model the influence that the interlaminar tin has on the lubrication process and attempt to model the flow of tin out of the part. These characterisations were deemed too challenging to model for this project. They may, however, be useful to further inform the influence of interlaminar lubrication or multi-step tooling.

Chapter 7 Conclusions and Recommendations

7.1 Conclusions

This thesis is assesses the possibility of using a molten metal interlayer to lubricate the thermoforming of thermoplastic composite parts. Thus, a novel technique for the thermoforming of composites with an interlaminar tin sheet was developed. The interlaminar tin sheet was intended to lubricate the forming process and reduce friction coefficients. It is hoped this will allow the easier manufacture of complex geometries with a reduced risk of defects such as wrinkling. It also opens up the possibility of using the metal layers to efficiently and uniformly heat the part from the inside. To this end, several nylon-carbon composite parts (with and without a tin interlayer) were manufactured, non-destructive testing was carried out to quantify residual tin defects, mechanical testing was used to evaluate the influence of residual tin on material properties, and numerical simulation was used to assess forming mechanics of the ripple pattern with a dry glass fabric. The conclusions can be summarised as follows.

- A novel thermoforming technique is developed to form nylon-carbon composite parts with a lubricating tin interlayer. Induction heating is used to heat the tin interlayers and the carbon-nylon sheets are heated through conduction. The part is formed using a multistep tooling which creates a pressure gradient and removes the tin interlayer. The forming occurs within a silicone diaphragm to constrain the molten tin. A combination of consolidating flat sheets and forming of multi-cavity curved parts (geometry based on a cosine wave) was carried out. The possibility of in-situ induction heating via interlaminar tin layers was proven and several complications (generating heat in a moving liquid) were identified.
- These composite parts were compared with unlubricated nylon-carbon parts manufactured using a radiant heating process (which provides a

different temperature profile). While it was possible to remove the majority of the interlaminar tin from flat sheets, curved geometries proved more challenging. There was some limited evidence of reductions in wrinkling when comparing between lubricated and unlubricated samples, however there remained a high level of variability in results which precluded any numerical analysis.

- A mixture of CT scanning, X-ray scanning and microscopy was used to quantify the residual tin content using volume and projected surface area measurements. Results showed it was possible to consolidate flat carbon-nylon parts with residual tin content by volume ranging from 1.5 – 5.6% and results improved with increased user experience. However, tin contents in curved parts remained higher, with the lowest value being 8.3 % with a median of 15.2 %.
- Comparison between residual tin volume and tin surface area showed a strong correlation. It was also possible to obtain comparable results for tin surface area from both x-ray and CT. This suggests that cheaper 2-D x-rays would be an efficient way of rapidly quantifying residual tin content in the future and that the more expensive and time-consuming CT scans could be focused solely on tasks where required.
- Mechanical testing focusing on the interlaminar shear strength was carried out to assess the impact of interlaminar tin on final part quality. The remnant tin caused a reduction in yield strength and flexural stiffness, but with process refinements, it was possible to obtain similar ultimate interlaminar shear strength. A weak negative correlation between tin content and mechanical properties is seen, but variation between manufactured samples dominates suggesting further process refinement is required. Unfortunately due to the choice of the ISO standard with a thicker loading plunger than the ASTM standard, the test samples experienced compression between loading bars which prevented accurate assessment of the ductile behaviour seen in many of the samples containing residual tin.
- Numerical simulation of a composite sheet using a pantographic beam and membrane mesh was used to evaluate the influence of multistep forming in a dry glass fabric. Results suggest that the benefits of shifting the

number of forming steps from 5 to 15 steps are small, and that the biggest benefit of the 5-step forming is in lower tensile stress in the sheet (associated with lower fibre breakage, which was not seen in our multistep experiments).

7.2 Future avenues for exploration

This was a preliminary exploration of the idea and limited time was available with an induction heater to develop and refine the manufacturing process. As such, there are several future avenues for further research. Some key opportunities are listed below:

- Optimisation of the thermoforming process with the intention of consistently reducing interlaminar tin content below 1 %. Suggestions include
    - Automation and control of the induction heating process to reduce variability in the process
    - Identifying non-conductive materials with a higher temperature resistance for the female tooling. Potential candidates include higher temperature composites such as PEEK, or 3D printed ceramics (though they are currently very expensive).
    - Adjusting the tooling to account for the benefits seen from thicker silicone rubber diaphragms. The thicker rubber appeared to smooth over pressure discontinuities and made heating of the part easier. However, the additional thickness of the rubber was not accounted for in the tooling design and will have led to reduced pressure at the peaks and troughs of the curved geometry.
    - Explore the influence of parameters such as forming speed, interlayer thickness and temperature on the eventual tin quantity, material properties and wrinkling of the part.
- Further mechanical testing to assess the material properties in tension and compression, as well as further study on stiffness, ductility and crack propagation. Attempts to identify the influence of residual tin location would on final properties would also be useful, but challenging to design. If there is success in improving tin removal this becomes less crucial.

- Development of safe methods to characterise the frictional behaviour of a lubricating metal interlayer such as a pull through or pull-out test. However, the requirements of elevated temperature operation and the necessity of constraining the molten tin make this operation difficult. Possible surrogates with similar fluid viscosity at the relevant could be identified to mimic the setup.
- Exploration of the feasibility of recycling composite parts with metallic defects. The inclusion of defects will make the recycling of the components more challenging. Given the large energy costs of manufacture, and environmental cost of landfill, cost effective methods of recycling are highly desirable.
- Further development of numerical simulation to better understand the thermoforming process. In particular,
    - Produce models representative of the carbon-nylon composite sheets using prior materials characterisation and including temperature dependent properties
    - Modelling the induction heating process to allow for better control over the temperature of the part during forming.
    - Attempting to model the squeeze flow of a low viscosity molten metal interlayer as it is removed from the composite part.

The overall results suggest that the use of multi-step tooling is a fruitful avenue for reducing tensile stress and fibre breakage in the forming of multi-cavity parts. One drawback is the high capital costs incurred in tooling and heating infrastructure which would restrict it’s use to high volume manufacturing. Looking to the interlaminar tin, the inclusion of small volumes of residual tin may have only a small negative impact on the quality of manufactured components. On the other hand, further development is required to remove the interlayer when forming curved parts. Long term success of the process will depend upon proving it’s use in reducing wrinkling when forming complex parts, the ability to obtain low levels of interlaminar tin even with complex geometries and reassurance that any residual tin does not have deleterious effects on the final material properties.

Appendix A

This Appendix outlines the parameters in the numerical simulations in chapter 6.

First the parameters of the beam elements will be covered Detailed derivation of the equations can be found in two papers by Harrison et al. [50], [116]. Table A.1 shows the required input parameters for a dry glass fabric (AllScot Plain Glass Fabric – ECK12) which were obtained via a mixture of uniaxial bias extension tests (reported in Harrison et al. [258]) and cantilever bend testing undertaken internally by another student at Glasgow University in accordance with Harrison et al. [50]. The relevant parameters

- Fibre stiffness
    - Estimated to provide less than 1% fibre strain during tests
- The normalised line stiffness in the two fibre directions (Tensile stiffness of sheet multiplied by sheet thickness)
    - Obtained via manufacturer and measurement of sheet thickness
- The normalised out of plane bending modulus per unit width in each fiber direction,
    - Obtained through cantilever bending tests carried out by other Glasgow University student as outlined in Harrison [116].
- The normalised in plane bending modulus per unit width for each fibre direction
    - Obtained via Unixial Bias Extension tests as outlined in Harrison et al. [257].
- The areal density of the fabric.
    - Obtained from Manufacturer

Also required are some initial parameters related to the ABAQUS mesh, namely the initial membrane thickness and Beam Length. The Warp orientations are indicated with a 1-subscript, and the weft orientations with a 2-subscript.

Table A.1 Input parameters for beam and membrane elements. Obtained from internal testing undertook on AllScot Glass fabric by other student following methods outlined in [50], [116]

Parameter Description	Symbol	Value	Unit
Fibre Stiffness	E_B	6.5	Gpa
Line Stiffness -1	γ_1	1.30	MN/m
Line Stiffness -2	γ_2	1.30	MN/m
In Plane Flexural Modulus per unit length- 1	α_1	0.002478	N m^2/m
In Plane Flexural Modulus per unit length – 2	α_1	0.002478	N m^2/m
Out of Plane Flexural Modulus per unit length – 1	β_1	0.001239	N m^2/m
Out of Plane Flexural Modulus per unit length - 2	β_1	0.000771	N m^2/m
Areal Density of fabric	ρ_{areal}	0.3	kg/m^2
Length of Beam Element	l_B	2	mm
Membrane Thickness	t_m	0.26	mm

Table A.2 and Table A.3 show the parameters used in the Beam elements in the Abaqus simulation in the warp and weft directions respectively. For these simulations, the calculations for Warp and Weft are the same, The beam cross-sectional area (A) is calculated via the beam thickness (t_{B1}) and widths (w_{B1}). The beam thickness and width can be found as follows:

$$t_{B1} = \sqrt{\frac{12\,\beta_1}{\gamma_1}} \tag{A.1}$$

$$w_{B1} = \sqrt{\frac{12\,\alpha_1}{\gamma_1}} \tag{A.2}$$

This is repeated for both warp and weft (or 1 and 2) orientations. From there the Beam Area can be calculated:

$$A = t_{B1}\, w_{B1} \tag{A.3}$$

The Moments of Inertia can be calculated via Euler-Bernoulli slender beam theory as follows

$$I_{11} = \frac{t_1\, w_1^3}{12} \tag{A.4}$$

$$I_{22} = \frac{t_1^3\, w_1}{12} \tag{A.5}$$

The torsional constant is approximated by the following equation:

$$J = \beta_t\, a\, b^3 \tag{A.6}$$

Where a is the length of the long side, b is the length of the short side, and β_t is a parameter based on the ratio of the length of the long side to the length of the short side and can be obtained from Fenster et al. [259]. The direction cosines are the ABAQUS defaults for a beam In space. The Youngs modulus is calculated via the following

$$E_{B1} = \frac{\gamma_1^2 W\, l_B}{12\,(W+l_B) w_{B1}\sqrt{\alpha_1\beta_1}} \tag{A.7}$$

The shear modulus (G) is calculated as

$$G = \frac{E_{B1}}{2(1+\nu)} \tag{A.8}$$

Where ν (poissons ratio) is 0 for the beam elements. Transverse shear stiffness (K) is then calculated from the following equation defined in the ABAQUS user manual [151]:

$$K = k * G * A \tag{A.9}$$

Where k is a shear factor, which is defined in the ABAQUS manual as 0.85 for a rectangular beam element [151]. Damping was determined via trial and error during the simulation process.

Table A.2 Model Parameters for Beam elements in Warp Direction of composite sheet. Parameters 1-9 are under *Beam General Section. Parameters 10 under *Transverse Shear Stiffness and Parameter 11 is under *Damping, for details refer to ABAQUS documentation [151].

No.	Parameter Description	Symbol	Value	Unit
1	Area	A	1.62×10^{-8}	m^2
2	Moment of inertia for bending about the 1-axis	I_{11}	3.08×10^{-17}	m^4
3	Moment of inertia for bending about the 2-axis	I_{22}	1.54×10^{-17}	m^4
4	Torsional Constant	J	3.49×10^{-17}	m^4
5	First direction cosine of the first beam section axis	-	0	-
6	Second direction cosine of the first beam section axis	-	0	-
7	Third direction cosine of the first beam section axis	-	-1	-
8	Young's modulus 1-axis	E	1.57×10^{11}	Pa
9	Shear modulus 1-axis	G	7.82×10^{10}	Pa
10	Transverse Shear Stiffness - Homogenous	K	1076	Pa
11	Damping, Alpha	-	30	s^{-1}

Table A.3 Model Parameters for Beam elements in Weft Direction of composite sheet. Parameters 1-9 are under *Beam General Section. Parameters 10 under *Transverse Shear Stiffness and Parameter 11 is under *Damping, for details refer to ABAQUS documentation [151].

No.	Parameter Description	Symbol	Value	Unit
1	Area	A	1.28×10^{-8}	m^2
2	Moment of inertia for bending about the 1-axis	I_{11}	2.43×10^{-17}	m^4
3	Moment of inertia for bending about the 2-axis	I_{22}	7.57×10^{-18}	m^4
4	Torsional Constant	J	1.97×10^{-17}	m^4
5	First direction cosine of the first beam section axis	-	0	-
6	Second direction cosine of the first beam section axis	-	0	-
7	Third direction cosine of the first beam section axis	-	-1	-
8	Young's modulus 2-axis	E	1.98×10^{11}	Pa
9	Torsional shear modulus 2-axis	G	9.92×10^{10}	Pa
10	Transverse Shear Stiffness – Homogenous	K	1076	Pa
11	Damping, Alpha	-	30	s^{-1}

The membrane elements are used to provide shear stiffness to the fabric. The membrane elements use a constitutive model (Stress power model) implemented in VUMAT. It is outlined in more detail in Harrison et al. [256] but an overview will be given here. The model takes data from picture frame tests of a fabric and relates the measured shear force per unit length vs shear angle (F_s) to in simulation stresses and strains. A polynomial curve is fitted to the measured shear force – shear angle data, and this is the only external input required for the shear portion of the model. Through derivation outlined in Harrison et al. [256] the following equations can be found which relate the principal stresses in the stress tensor (τ_{xx} and τ_{yy}) to the shear force -shear angle curve based on the shear angle θ.

$$\tau_{xx} = \frac{F_s}{h_0}\left(\frac{\sin\theta - \cos^2\theta + 1}{\sin\theta\cos\theta}\right) \quad \text{(A.10)}$$

$$\tau_{yy} = \frac{F_s}{h_0}\left(\frac{\sin\theta + \cos^2\theta - 1}{\sin\theta\cos\theta}\right) \quad \text{(A.11)}$$

These relate stresses in the simulation with the shear force vs shear angle curve F_s. These are then expressed incrementally. This allows the shear stress-strain behaviour to be updated incrementally as a function of shear angle within ABAQUS Explicit.

$$\Delta\sigma_{ij} = \sigma_{ij}(\theta + \Delta\theta) - \sigma_{ij}(\theta) \tag{A.12}$$

Table A.4 shows the input parameters in the VUMAT subroutine which is used to determine the shear properties of the mesh. Polynomial curves and corresponding angular velocities are stored in a text based format in an accessible location with in the PC. To update the stress properties within the simulation, first the angular rate is calculated and a representative shear-force shear-angle curve is chosen. From the shear rate and shear angle, the shear force can then be chosen from the stored curves. This stress increment can then by passed back into Abaqus.

The parameters for the VUMAT subroutine were selected as follows. The Youngs Modulus, shearing modulus were given low nominal values as these properties would be dominated by the beam elements. The resin modulus was also set to zero as the simulation was of a dry fabric. The vector components identify the initial orientation of the fibres and are determined from *ORIENTATION in the ABAQUS routine.

The thickness of the fabric, number of filaments and diameter of filaments was obtained from the manufacturer. The ratio for the undulation effect and the asymmetry were both set to 1 as nominal values. The length of the picture frame and fabric thickness were obtained from internal tests on AllScot Glass fabric (ECK12) which had been carried out by other students internally in line with Harrison et al. [256]. The shear curve parameters were obtained from the data produced from the picture frame tests.

Table A.4 Model parameters in VUMAT subroutine for membrane elements in composite sheet [50], [116]

No.	Parameter Description	Value	Unit
1	Youngs Modulus for fibres in Alpha Direction	0.65	Pa
2	Shearing Modulus	0	Pa
3	Youngs Modulus for fibres in Beta Direction	0.65	Pa
4	Resin Modulus	0	Pa
5	First component of Vector Alpha - start condition	0.0074	-
6	Second component of Vector Alpha - start condition	0	-
7	First component of Vector Beta - start condition	0	-
8	Second component of Vector Beta- start condition	0.0074	-
9	Fabric Thickness	0.00026	M
10	No. of Filaments in Alpha Tow	600	-
11	No. of Filaments in Beta Tow	600	-
12	Diameter of Filament in Alpha Tow	1.6 x10^{-5}	m
13	Diameter of Filament in Beta Tow	1.6 x10^{-5}	m
14	Ratio of Youngs Modulus for Undulation Effect	1	-
16	Asymmetric Factor of Bending compression Modulus	1	-
17	Length of Picture-Frame Shear Specimen	0.24	m
18	Thickness of Picture-Frame Shear Specimen	0.00026	m
19	Shear Curve Parameter 0	1.36387	-
20	Shear Curve Parameter 1	1.147	-
21	Shear Curve Parameter 2	20.9684	-
22	Shear Curve Parameter 3	7.967	-
23	Shear Curve Parameter 4	1.3634	-
24	Shear Curve Parameter 5	0.40983	-
25	Shear Curve Parameter 6	-0.0426557	-
26	Shear Curve Parameter 7	0.00174804	-
27	Shear Curve Parameter 8	-3.25326 x 10^{-05}	-
28	Shear Curve Parameter 9	2.29584 x 10^{-07}	-

References

[1] Fortune Business Insights, ‘Composites Market’, Nov. 2020.

[2] M. Effing, ‘Expert insights in Europe’s booming composites market’, *Reinforced Plastics*, vol. 62, pp. 219–223, 2018, doi: 10.1016/j.repl.2017.06.086.

[3] H. Hu, D. Cao, Z. Cao, and S. Li, ‘Experimental and numerical investigations of wrinkle effect on failure behavior of curved composite laminates’, *Compos Struct*, vol. 261, Apr. 2021, doi: 10.1016/j.compstruct.2021.113541.

[4] M. Nartey *et al.*, ‘Understanding the impact of fibre wrinkle architectures on composite laminates through tailored gaps and overlaps’, *Compos B Eng*, vol. 196, Sep. 2020, doi: 10.1016/j.compositesb.2020.108097.

[5] Lomonosov Moscow State University, ‘Decreasing the mass of aircraft with polymer composites’, Phys.org. Accessed: Aug. 10, 2022. [Online]. Available: https://phys.org/news/2017-02-decreasing-mass-aircraft-polymer-composites.html

[6] A. J. Thompson, J. P. H. Belnoue, and S. R. Hallett, ‘Modelling defect formation in textiles during the double diaphragm forming process’, *Compos B Eng*, vol. 202, Dec. 2020, doi: 10.1016/j.compositesb.2020.108357.

[7] J. L. Gorczyca, J. A. Sherwood, L. Liu, and J. Chen, ‘Modeling of friction and shear in thermostamping of composites - Part I’, *J Compos Mater*, vol. 38, no. 21, pp. 1911–1929, 2004, doi: 10.1177/0021998304048416.

[8] M. F. Culpin, ‘The viscosity of liquid indium and liquid tin’, *Proceedings of the Physical Society. Section B*, vol. 70, no. 11, pp. 1069–1078, 1957, doi: 10.1088/0370-1301/70/11/307.

[9] H. Tanaka and K. Watanabe, ‘Shear viscosity of nylon 6 melts reinforced with microfibrous calcium silicate hydrate’, *Polym Eng*

Sci, vol. 39, no. 5, pp. 817–824, May 1999, doi: 10.1002/PEN.11469.

[10] K. Vanclooster, ‘Forming of Mulitlayered Fabric Reinforced thermoplastic Composites’, University of Leuven, 2009.

[11] Europeiska kommissionen, ‘Proposal for a Regulation amending Regulation (EU) 2019/631 ... setting CO2 emission performance standards for new passenger cars and for new light commercial vehicles’. Official Journal of the European Union, 25.4.2019(L 111/13), 2021. [Online]. Available: https://eur-lex.europa.eu/legal-content/EN/TXT/PDF/?uri=CELEX:32019R0631&from=EN

[12] J. Pruez, S. Shoukry, G. Williams, and M. Shoukry, ‘Lightweight Composite Materials for Heavy Duty Vehicles’, no. August, p. 2, 2013.

[13] A. K. Pickett, *Process and mechanical modelling of engineering composites*, 1st ed. Lightning Source UK Ltd., 2018.

[14] U. K. Vaidya and K. K. Chawla, ‘Processing of fibre reinforced thermoplastic composites’, *International Materials Reviews*, vol. 53, no. 4, pp. 185–218, Jul. 2008, doi: 10.1179/174328008X325223.

[15] A. C. Long, *Design and manufacture of textile composites*. Woodhead Publishing Limited, 2005. doi: 10.1533/9781845690823.

[16] T. G. Gutowski, *Advanced composites manufacturing*. Wiley Interscience, 1997. doi: 10.1016/s0025-5408(00)00291-9.

[17] A. Nanni, ‘Fiber Reinforced Polymer Composites for Infrastructure Strengthening-From Research to Practice’, 2005.

[18] V. R. Sastri, ‘Engineering Thermoplastics: Acrylics, Polycarbonates, Polyurethanes, Polyacetals, Polyesters, and Polyamides’, *Plastics in Medical Devices*, pp. 121–173, Jan. 2010, doi: 10.1016/B978-0-8155-2027-6.10007-8.

[19] M. B. Neiman, B. M. Kovarskaya, L. I. Golubenkova, A. S. Strizhkova, I. I. Levantovskaya, and M. S. Akutin, ‘The thermal degradation of some epoxy resins’, *Journal of Polymer Science*, vol. 56, no. 164, pp. 383–389, Feb. 1962, doi: 10.1002/pol.1962.1205616408.

[20] D. Garcia and H. W. Starkweather, ‘Hydrogen Bonding in Nylon 66 and Model Compounds.’, *Journal of polymer science. Part A-2, Polymer physics*, vol. 23, no. 3, pp. 537–555, 1985, doi: 10.1002/pol.1985.180230310.

[21] Dynisco, ‘Materials and their Flow Properties’, vol. 1, no. 508. pp. 1–25, 2018. [Online]. Available: https://www.dynisco.com/userfiles/files/Materials_and_Flow_Properties.pdf

[22] N. Kiuna, C. J. Lawrence, Q. P. V. Fontana, P. D. Lee, T. Selerland, and P. D. M. Spelt, ‘A model for resin viscosity during cure in the resin transfer moulding process’, *Compos Part A Appl Sci Manuf*, vol. 33, no. 11, pp. 1497–1503, Nov. 2002, doi: 10.1016/S1359-835X(02)00177-X.

[23] M. J. Donough, Shafaq, N. A. St John, A. W. Philips, and B. Gangadhara Prusty, ‘Process modelling of In-situ consolidated thermoplastic composite by automated fibre placement – A review’, *Compos Part A Appl Sci Manuf*, vol. 163, p. 107179, Dec. 2022, doi: 10.1016/J.COMPOSITESA.2022.107179.

[24] J. Cheon, M. Lee, and M. Kim, ‘Study on the stab resistance mechanism and performance of the carbon, glass and aramid

fiber reinforced polymer and hybrid composites', *Compos Struct*, vol. 234, Feb. 2020, doi: 10.1016/j.compstruct.2019.111690.

[25] I. R. Chowdhury, N. H. Nash, A. Portela, N. P. O'Dowd, and A. J. Comer, 'Analysis of failure modes for a non-crimp basalt fiber reinforced epoxy composite under flexural and interlaminar shear loading', *Compos Struct*, vol. 245, 2020, doi: 10.1016/j.compstruct.2020.112317.

[26] R. A. M. Santos, L. Gorbatikh, and Y. Swolfs, 'Commercial self-reinforced composites: A comparative study', *Compos B Eng*, vol. 223, p. 109108, Oct. 2021, doi: 10.1016/j.compositesb.2021.109108.

[27] B. Alcock, N. O. Cabrera, N. M. Barkoula, J. Loos, and T. Peijs, 'The mechanical properties of unidirectional all-polypropylene composites', *Compos Part A Appl Sci Manuf*, vol. 37, no. 5, pp. 716–726, May 2006, doi: 10.1016/J.COMPOSITESA.2005.07.002.

[28] K. E. Perepelkin, 'CHEMISTRY AND TECHNOLOGY OF CHEMICAL FIBRES PRINCIPLES AND METHODS OF MODIFICATION OF FIBRES AND FIBRE MATERIALS.* A REVIEW', *Fibre Chemistry*, vol. 37, no. 2, pp. 37–51, 2005.

[29] E. Frank, F. Hermanutz, and M. R. Buchmeiser, 'Carbon fibers: Precursors, manufacturing, and properties', *Macromol Mater Eng*, vol. 297, no. 6, pp. 493–501, Jun. 2012, doi: 10.1002/mame.201100406.

[30] B. A. Newcomb, 'Processing, structure, and properties of carbon fibers', *Compos Part A Appl Sci Manuf*, vol. 91, pp. 262–282, Dec. 2016, doi: 10.1016/j.compositesa.2016.10.018.

[31] M. Nciri, D. Notta-Cuvier, F. Lauro, F. Chaari, Y. Maalej, and B. Zouari, 'Modelling and characterisation of dynamic behaviour of

short-fibre-reinforced composites', *Compos Struct*, vol. 160, pp. 516–528, Jan. 2017, doi: 10.1016/j.compstruct.2016.10.083.

[32] K. Yassin and M. Hojjati, 'Processing of thermoplastic matrix composites through automated fiber placement and tape laying methods: A review', *Journal of Thermoplastic Composite Materials*, vol. 31, no. 12, pp. 1676–1725, 2018, doi: 10.1177/0892705717738305.

[33] Easy Composites, 'Easy Composites'. Accessed: Aug. 17, 2022. [Online]. Available: www.easycomposites.co.uk

[34] B. Gommers, I. Verpoest, and P. Houtte, 'Analysis of knitted fabric reinforced composites: Part II. Stiffness and strength', *Compos Part A Appl Sci Manuf*, vol. 29, no. 12, pp. 1589–1601, 1998, doi: 10.1016/S1359-835X(98)00096-7.

[35] S. S. Yao, F. L. Jin, K. Y. Rhee, D. Hui, and S. J. Park, 'Recent advances in carbon-fiber-reinforced thermoplastic composites: A review', *Compos B Eng*, vol. 142, pp. 241–250, Jun. 2018, doi: 10.1016/j.compositesb.2017.12.007.

[36] I. C. Finegan, G. G. Tibbetts, D. G. Glasgow, J. M. Ting, and M. L. Lake, 'Surface treatments for improving the mechanical properties of carbon nanofiber/thermoplastic composites', *J Mater Sci*, vol. 38, no. 16, pp. 3485–3490, 2003, doi: 10.1023/A:1025109103511.

[37] F. Liu, Z. Shi, and Y. Dong, 'Improved wettability and interfacial adhesion in carbon fibre/epoxy composites via an aqueous epoxy sizing agent', *Compos Part A Appl Sci Manuf*, vol. 112, pp. 337–345, Sep. 2018, doi: 10.1016/j.compositesa.2018.06.026.

[38] L. Bhanuprakash, S. Parasuram, and S. Varghese, 'Experimental investigation on graphene oxides coated carbon fibre/epoxy hybrid composites: Mechanical and electrical properties', *Compos*

Sci Technol, vol. 179, pp. 134–144, Jul. 2019, doi: 10.1016/j.compscitech.2019.04.034.

[39] T. Bessell and J. B. Shortall, 'The crystallization and interfacial bond strength of nylon 6 at carbon and glass fibre surfaces', *J Mater Sci*, vol. 10, pp. 2035–2043.

[40] D. S. Choudhari and V. J. Kakhandki, 'Comprehensive study and analysis of mechanical properties of chopped carbon fibre reinforced nylon 66 composite materials', *Mater Today Proc*, vol. 44, pp. 4596–4601, 2020, doi: 10.1016/J.MATPR.2020.10.828.

[41] J. Bieniaś, P. Jakubczak, M. Droździel, and B. Surowska, 'Interlaminar shear strength and failure analysis of aluminium-carbon laminates with a glass fiber interlayer after moisture absorption', *Materials*, vol. 13, no. 13, pp. 1–14, 2020, doi: 10.3390/ma13132999.

[42] M. Valente, I. Rossitti, I. Biblioteca, and M. Sambucci, 'Thermoplastic Composite Materials Approach for More Circular Components : From Monomer to In Situ Polymerization , a Review', 2022.

[43] U. Breuer, M. Neitzel, V. Ketzer, and R. Reinicke, 'Deep drawing of fabric-reinforced thermoplastics: Wrinkle formation and their reduction', *Polym Compos*, vol. 17, no. 4, pp. 643–647, 1996, doi: 10.1002/pc.10655.

[44] P. Harrison, R. Gomes, and N. Curado-Correia, 'Press forming a 0/90 cross-ply advanced thermoplastic composite using the double-dome benchmark geometry', *Compos Part A Appl Sci Manuf*, vol. 54, pp. 56–69, 2013, doi: 10.1016/J.COMPOSITESA.2013.06.014.

[45] S. Chen, L. T. Harper, A. Endruweit, and N. A. Warrior, 'Optimisation of forming process for highly drapeable fabrics',

ICCM International Conferences on Composite Materials, vol. 2015-July, 2015, Accessed: May 30, 2022. [Online]. Available: http://www.nottingham.ac.uk/~eazlth

[46] F. Abbassi, I. Elfaleh, S. Mistou, A. Zghal, M. Fazzini, and T. Djilali, ‘Experimental and numerical investigations of a thermoplastic composite (carbon/PPS) thermoforming’, *Struct Control Health Monit*, vol. 18, no. 7, pp. 769–780, Nov. 2011, doi: 10.1002/STC.491.

[47] O. Atalay and F. Ozturk, ‘Effects of gripper location and blank geometry on the thermoforming of a carbon-fiber woven-fabric/polyphenylene sulfide composite sheet’:, *Journal of Thermoplastic Composite Materials*, vol. 2022, no. 0, p. 089270572210898, Apr. 2022, doi: 10.1177/08927057221089830.

[48] S. Chen *et al.*, ‘Double diaphragm forming simulation for complex composite structures’, *Compos Part A Appl Sci Manuf*, vol. 95, pp. 346–358, Apr. 2017, doi: 10.1016/j.compositesa.2017.01.017.

[49] A. C. Long, C. E. Wilks, and C. D. Rudd, ‘Experimental characterisation of the consolidation of a commingled glass/polypropylene composite’, *Compos Sci Technol*, vol. 61, no. 11, pp. 1591–1603, 2001, doi: 10.1016/S0266-3538(01)00059-8.

[50] P. Harrison, M. F. Alvarez, and D. Anderson, ‘Towards comprehensive characterisation and modelling of the forming and wrinkling mechanics of engineering fabrics’, *Int J Solids Struct*, vol. 154, pp. 2–18, Dec. 2018, doi: 10.1016/j.ijsolstr.2016.11.008.

[51] F. Härtel and P. Harrison, ‘Evaluation of normalisation methods for uniaxial bias extension tests on engineering fabrics’, *Compos Part A Appl Sci Manuf*, vol. 67, pp. 61–69, 2014, doi: 10.1016/j.compositesa.2014.08.011.

[52] J. Skelton and W. D. Freeston, ‘Mechanics of Elastic Performance of Textile Materials: Part XIX: The Shear Behavior of Fabrics Under Biaxial Loads’, *Textile Research Journal*, vol. 41, no. 11, pp. 871–880, 1971, doi: 10.1177/004051757104101101.

[53] G. Hivet, S. Allaoui, D. Soulat, A. Wendling, and S. Chatel, ‘ANALYSIS OF WOVEN REINFORCEMENT PREFORMING USING AN EXPERIMENTAL APPROACH’.

[54] U. Breuer, M. Neitzel, V. Ketzer, and R. Reinicke, ‘Deep drawing of fabric-reinforced thermoplastics: Wrinkle formation and their reduction’, *Polym Compos*, vol. 17, no. 4, pp. 643–647, 1996, doi: 10.1002/PC.10655.

[55] P. Harrison, M. J. Clifford, A. C. Long, and C. D. Rudd, ‘Constitutive modelling of impregnated continuous fibre reinforced composites micromechanical approach’, *Plastics, Rubber and Composites*, vol. 31, no. 2, pp. 76–86, 2002, doi: 10.1179/146580102225001409.

[56] G. B. McGuinness, R. A. Canavan, T. A. Nestor, and C. M. O Bradaigh, ‘Picture-frame intraply shearing test for sheet-forming of composite materials’, *American Society of Mechanical Engineers, Materials Division (Publication) MD*, vol. 69–2, pp. 1107–1118, 1995.

[57] P. Boisse, N. Hamila, E. Guzman-Maldonado, A. Madeo, G. Hivet, and F. dell’Isola, ‘The bias-extension test for the analysis of in-plane shear properties of textile composite reinforcements and prepregs: a review’, *International Journal of Material Forming*, vol. 10, no. 4, pp. 473–492, Aug. 2017, doi: 10.1007/s12289-016-1294-7.

[58] P. Harrison and P. Potluri, ‘Shear tension coupling in Biaxial Bias Extension tests’, *ICCM International Conferences on Composite Materials*, 2009.

[59] J. Cao *et al.*, ‘Characterization of mechanical behavior of woven fabrics: Experimental methods and benchmark results’, *Compos Part A Appl Sci Manuf*, vol. 39, no. 6, pp. 1037–1053, 2008, doi: 10.1016/j.compositesa.2008.02.016.

[60] I. Taha and S. Ebeid, ‘Comparison of picture frame and Bias-Extension tests for the characterization of shear behaviour in natural fibre woven fabrics’, *Fibers and Polymers*, Jan. 2013, Accessed: Feb. 07, 2024. [Online]. Available: https://www.academia.edu/31018842/Comparison_of_picture_frame_and_Bias_Extension_tests_for_the_characterization_of_shear_behaviour_in_natural_fibre_woven_fabrics

[61] P. Boisse, N. Hamila, E. Guzman-Maldonado, A. Madeo, G. Hivet, and F. dell’Isola, ‘The bias-extension test for the analysis of in-plane shear properties of textile composite reinforcements and prepregs: a review’, *International Journal of Material Forming*, vol. 10, no. 4, pp. 473–492, Aug. 2017, doi: 10.1007/S12289-016-1294-7/FIGURES/11.

[62] P. Harrison, R. Gomes, and N. Curado-Correia, ‘Press forming a 0/90 cross-ply advanced thermoplastic composite using the double-dome benchmark geometry’, *Compos Part A Appl Sci Manuf*, vol. 54, pp. 56–69, 2013, doi: 10.1016/j.compositesa.2013.06.014.

[63] P. Harrison, M. J. Clifford, A. C. Long, and C. D. Rudd, ‘A constituent-based predictive approach to modelling the rheology of viscous textile composites’, *Compos Part A Appl Sci Manuf*, vol. 35, no. 7–8, pp. 915–931, 2004, doi: 10.1016/j.compositesa.2004.01.005.

[64] H. Hu, D. Cao, Z. Cao, and S. Li, ‘Experimental and numerical investigations of wrinkle effect on failure behavior of curved composite laminates’, *Compos Struct*, vol. 261, Apr. 2021, doi: 10.1016/j.compstruct.2021.113541.

[65] L. D. Bloom, J. Wang, and K. D. Potter, ‘Damage progression and defect sensitivity: An experimental study of representative wrinkles in tension’, *Compos B Eng*, vol. 45, no. 1, pp. 449–458, Feb. 2013, doi: 10.1016/j.compositesb.2012.05.021.

[66] K. Potter, B. Khan, M. Wisnom, T. Bell, and J. Stevens, ‘Variability, fibre waviness and misalignment in the determination of the properties of composite materials and structures’, *Compos Part A Appl Sci Manuf*, vol. 39, no. 9, pp. 1343–1354, 2008, doi: 10.1016/j.compositesa.2008.04.016.

[67] J. Amirbayat and J. W. S. Hearle, ‘The anatomy of buckling of textile fabrics: Drape and conformability’, *Journal of the Textile Institute*, vol. 80, no. 1, pp. 51–70, 1989, doi: 10.1080/00405008908659185.

[68] J. J. Bender, S. R. Hallett, and E. Lindgaard, ‘Investigation of the effect of wrinkle features on wind turbine blade sub-structure strength’, *Compos Struct*, vol. 218, pp. 39–49, 2019, doi: 10.1016/j.compstruct.2019.03.026.

[69] T. G. Clapp and H. Peng, ‘Buckling of Woven Fabrics: Part III: Experimental Validation of Theoretical Models’, *Textile Research Journal*, vol. 60, no. 11, pp. 641–645, 1990, doi: 10.1177/004051759006001103.

[70] L. Liu, J. Chen, J. L. Gorczyca, and J. A. Sherwood, ‘Modeling of friction and shear in thermostamping of composites - Part II’, *J Compos Mater*, vol. 38, no. 21, pp. 1931–1947, 2004, doi: 10.1177/0021998304048417.

[71] R. H. W. ten Thije, R. Akkerman, L. van der Meer, and M. P. Ubbink, ‘Tool-ply friction in thermoplastic composite forming’, *International Journal of Material Forming*, vol. 1, no. SUPPL. 1, pp. 953–956, 2008, doi: 10.1007/s12289-008-0215-9.

[72] R. H. W. ten Thije, R. Akkerman, M. Ubbink, and L. van der Meer, ‘A lubrication approach to friction in thermoplastic composites forming processes’, *Compos Part A Appl Sci Manuf*, vol. 42, no. 8, pp. 950–960, Aug. 2011, doi: 10.1016/j.compositesa.2011.03.023.

[73] B. Cornelissen, U. Sachs, B. Rietman, and R. Akkerman, ‘Dry friction characterisation of carbon fibre tow and satin weave fabric for composite applications’, *Compos Part A Appl Sci Manuf*, vol. 56, pp. 127–135, 2014, doi: 10.1016/J.COMPOSITESA.2013.10.006.

[74] D. M. Mulvihill, O. Smerdova, and M. P. F. Sutcliffe, ‘Friction of carbon fibre tows’, *Compos Part A Appl Sci Manuf*, vol. 93, pp. 185–198, Feb. 2017, doi: 10.1016/J.COMPOSITESA.2016.08.034.

[75] D. M. Mulvihill and M. P. F. Sutcliffe, ‘Effect of tool surface topography on friction with carbon fibre tows for composite fabric forming’, *Compos Part A Appl Sci Manuf*, vol. 93, pp. 199–206, Feb. 2017, doi: 10.1016/J.COMPOSITESA.2016.10.017.

[76] E. I. Avgoulas *et al.*, ‘Frictional behaviour of non-crimp fabrics (NCFs) in contact with a forming tool’, *Tribol Int*, vol. 121, pp. 71–77, May 2018, doi: 10.1016/J.TRIBOINT.2018.01.026.

[77] O. Smerdova and M. P. F. Sutcliffe, ‘Multiscale tool-fabric contact observation and analysis for composite fabric forming’, *Compos Part A Appl Sci Manuf*, vol. 73, pp. 116–124, 2015, doi: 10.1016/J.COMPOSITESA.2015.03.009.

[78] J. R. O. Ramalho and R. F. Bento, ‘Healing of subacute tympanic membrane perforations in chinchillas treated with epidermal growth factor and pentoxifylline’, *Otology and Neurotology*, vol. 27, no. 5. Book of Standards, pp. 720–727, 2006. doi: 10.1097/01.mao.0000226316.04940.f9.

[79] A. M. Murtagh, J. J. Lennon, and P. J. Mallon, ‘Surface friction effects related to pressforming of continuous fibre thermoplastic composites’, *Composites Manufacturing*, vol. 6, no. 3–4, pp. 169–175, 1995, doi: 10.1016/0956-7143(95)95008-M.

[80] P. Harrison, H. Lin, M. Ubbink, R. Akkerman, K. van de Haar, and A. C. Long, ‘Characterising and modelling tool-ply friction of viscous textile composites’, *ICCM International Conferences on Composite Materials*, 2007.

[81] A. M. Murtagh, M. R. Monaghan, and P. J. Mallon, ‘Investigation of the interply slip process in continuous fibre thermoplastic composites’, in *9th International Conference on Composite Materials (ICCM-9)*, 1993, pp. 311–318.

[82] P. Harrison, R. H. W. ten Thije, R. Akkerman, and A. C. Long, ‘Characterising and modelling tool-ply friction of viscous textile composites’, *World Journal of Engineering*, vol. 7, no. 1, pp. 5–22, 2010.

[83] C. A. Gunawardana *et al.*, ‘Understanding the role of magnesium stearate in lowering punch sticking propensity of drugs during compression’, *Int J Pharm*, vol. 640, p. 123016, Jun. 2023, doi: 10.1016/J.IJPHARM.2023.123016.

[84] E. S. Lower, ‘Magnesium stearate: A review of its uses in paints, plastics, adhesives and related industries’.

[85] F. Yu, S. Chen, G. D. Lawrence, N. A. Warrior, and L. T. Harper, ‘A global-to-local sub modelling approach to investigate the effect of lubrication during double diaphragm forming of multi-ply biaxial non-crimp fabric preforms’, *Compos B Eng*, vol. 254, p. 110590, Apr. 2023, doi: 10.1016/J.COMPOSITESB.2023.110590.

[86] F. Yu, S. Chen, L. T. Harper, and N. A. Warrior, ‘Investigation into the effects of inter-ply sliding during double diaphragm

forming for multi-layered biaxial non-crimp fabrics', *Compos Part A Appl Sci Manuf*, vol. 150, p. 106611, Nov. 2021, doi: 10.1016/J.COMPOSITESA.2021.106611.

[87] Z. F. Yuan, K. Mukai, K. Takagi, M. Ohtaka, W. L. Huang, and Q. S. Liu, 'Surface Tension and Its Temperature Coefficient of Molten Tin Determined with the Sessile Drop Method at Different Oxygen Partial Pressures', *J Colloid Interface Sci*, vol. 254, no. 2, pp. 338–345, Oct. 2002, doi: 10.1006/JCIS.2002.8589.

[88] R. K. Okine, 'Analysis of Forming Parts from Advanced Thermoplastic Composite Sheet Materials', 1989. doi: 10.1177/089270578900200104.

[89] D. Tatsuno, T. Yoneyama, K. Kawamoto, and M. Okamoto, 'Hot press forming of thermoplastic CFRP sheets', *Procedia Manuf*, vol. 15, pp. 1730–1737, 2018, doi: 10.1016/j.promfg.2018.07.254.

[90] C. M. O'Brádaigh, R. B. Pipes, and P. J. Mallon, 'Issues in diaphragm forming of continuous fiber reinforced thermoplastic composites', *Polym Compos*, vol. 12, no. 4, pp. 246–256, 1991, doi: 10.1002/pc.750120406.

[91] S. Delaloye and M. Niedermeier, 'Optimization of the diaphragm forming process for continuous fibre-reinforced advanced thermoplastic composites', *Composites Manufacturing*, vol. 6, no. 3–4, pp. 135–144, 1995, doi: 10.1016/0956-7143(95)95004-I.

[92] J. Krebs, K. Friedrich, and D. Bhattacharyya, 'A direct comparison of matched-die versus diaphragm forming', *Compos Part A Appl Sci Manuf*, vol. 29, no. 1–2, pp. 183–188, 1998, doi: 10.1016/S1359-835X(97)82706-6.

[93] J. Nowacki, J. Fujiwara, P. Mitschang, and M. Neitzel, 'Deep Drawing of Fabric Reinforced Thermoplastics: Maximum Drawing

Depth and Mechanism of Wrinkle Formation', *Polymers and Polymer Composites*, vol. 6, no. 4, pp. 215–222, 1998.

[94] O. Rozant, P. E. Bourban, and J. A. E. Månson, 'Drapability of dry textile fabrics for stampable thermoplastic preforms', *Compos Part A Appl Sci Manuf*, vol. 31, no. 11, pp. 1167–1177, 2000, doi: 10.1016/S1359-835X(00)00100-7.

[95] A. G. Prodromou and J. Chen, 'On the relationship between shear angle and wrinkling of textile composite preforms', *Compos Part A Appl Sci Manuf*, vol. 28, no. 5, pp. 491–503, 1997, doi: 10.1016/S1359-835X(96)00150-9.

[96] F. Nosrat Nezami, T. Gereke, and C. Cherif, 'Analyses of interaction mechanisms during forming of multilayer carbon woven fabrics for composite applications', *Compos Part A Appl Sci Manuf*, vol. 84, pp. 406–416, May 2016, doi: 10.1016/j.compositesa.2016.02.023.

[97] H. Lin, A. Long, M. Clifford, J. Wang, and P. Harrison, 'Predictive FE modelling of prepreg forming to determine optimum processing conditions', *AIP Conf Proc*, vol. 907, pp. 1092–1097, 2007, doi: 10.1063/1.2729660.

[98] F. Nosrat Nezami, T. Gereke, and C. Cherif, 'Active forming manipulation of composite reinforcements for the suppression of forming defects', *Compos Part A Appl Sci Manuf*, vol. 99, pp. 94–101, 2017, doi: 10.1016/j.compositesa.2017.04.011.

[99] S. Chen *et al.*, 'Double diaphragm forming simulation for complex composite structures', *Compos Part A Appl Sci Manuf*, vol. 95, pp. 346–358, Apr. 2017, doi: 10.1016/j.compositesa.2017.01.017.

[100] M. Hou, 'Stamp forming of fabric-reinforced thermoplastic composites', *Polym Compos*, vol. 17, no. 4, pp. 596–603, 1996, doi: 10.1002/pc.10649.

[101] S. G. Hancock and K. D. Potter, ‘Inverse drape modelling - An investigation of the set of shapes that can be formed from continuous aligned woven fibre reinforcements’, *Compos Part A Appl Sci Manuf*, vol. 36, no. 7, pp. 947–953, 2005, doi: 10.1016/j.compositesa.2004.12.001.

[102] J. Sjölander, P. Hallander, and M. Åkermo, ‘Forming induced wrinkling of composite laminates: A numerical study on wrinkling mechanisms’, *Compos Part A Appl Sci Manuf*, vol. 81, pp. 41–51, 2016, doi: 10.1016/j.compositesa.2015.10.012.

[103] J. Huang, P. Boisse, N. Hamila, and Y. Zhu, ‘Simulation of Wrinkling during Bending of Composite Reinforcement Laminates’, *Materials 2020, Vol. 13, Page 2374*, vol. 13, no. 10, p. 2374, May 2020, doi: 10.3390/MA13102374.

[104] Z. Xiao, A. Ackermann, and P. Harrison, ‘Manual 2-dimensional Fabric Steering, for the Manufacture of Variable Stiffness Panels’, in *23rd International Conference on Material Forming (ESAFORM 2020)*, 2020. doi: 10.1016/j.promfg.2020.04.111.

[105] P. Hallander, J. Sjölander, and M. Åkermo, ‘Forming induced wrinkling of composite laminates with mixed ply material properties; an experimental study’, *Compos Part A Appl Sci Manuf*, vol. 78, pp. 234–245, Nov. 2015, doi: 10.1016/j.compositesa.2015.08.025.

[106] G. B. McGuinness and C. M. ÓBrádaigh, ‘Effect of preform shape on buckling of quasi-isotropic thermoplastic composite laminates during sheet forming’, *Composites Manufacturing*, vol. 6, no. 3–4, pp. 269–280, 1995, doi: 10.1016/0956-7143(95)95020-Y.

[107] K. Vanclooster, S. V. Lomov, and I. Verpoest, ‘On the formability of multi-layered fabric composites’, *ICCM International Conferences on Composite Materials*, 2009.

[108] C. Mack and H. M. Taylor, ‘39—The fitting of woven cloth to surfaces’, *Journal of the Textile Institute Transactions*, vol. 47, no. 9, pp. T477–T488, 1956, doi: 10.1080/19447027.1956.10750433.

[109] F. L. Heisey and K. D. Haller, ‘Fitting woven fabric to surfaces in three dimensions’, *Journal of the Textile Institute*, vol. 79, no. 2, pp. 250–263, 1988, doi: 10.1080/00405008808659140.

[110] W. Qi, *The third wave*, 1st ed., no. FEBRUARY. William Morrow, 2004. doi: 10.4324/9781315107776-3.

[111] A. C. Long, B. J. Souter, F. Robitaille, and C. D. Rudd, ‘Effects of fibre architecture on deformation during preform manufacture’, *Advanced Composites Letters*, vol. 8, no. 6, pp. 333–344, Jan. 1999, doi: 10.1177/096369359900800608.

[112] A. C. Long, J. Wiggers, and P. Harrison, ‘Modelling the effects of blank-holder pressure and material variability on forming of textile preforms’, in *Proceedings of the 8th international ESAFORM conference on materials forming*, Cluj-Napoca, Romania, 2004, pp. 1–4. Accessed: Apr. 30, 2022. [Online]. Available: http://citeseerx.ist.psu.edu/viewdoc/download?doi=10.1.1.715.7435&rep=rep1&type=pdf

[113] S. G. Hancock and K. D. Potter, ‘The use of kinematic drape modelling to inform the hand lay-up of complex composite components using woven reinforcements’, *Compos Part A Appl Sci Manuf*, vol. 37, no. 3, pp. 413–422, Mar. 2006, doi: 10.1016/j.compositesa.2005.05.044.

[114] W. R. Yu, M. Zampaloni, F. Pourboghrat, K. Chung, and T. J. Kang, ‘Analysis of flexible bending behavior of woven preform using non-orthogonal constitutive equation’, *Compos Part A Appl*

Sci Manuf, vol. 36, no. 6, pp. 839–850, Jun. 2005, doi: 10.1016/j.compositesa.2004.10.026.

[115] W. R. Yu, P. Harrison, and A. Long, ‘Finite element forming simulation for non-crimp fabrics using a non-orthogonal constitutive equation’, *Compos Part A Appl Sci Manuf*, vol. 36, no. 8, pp. 1079–1093, Aug. 2005, doi: 10.1016/j.compositesa.2005.01.007.

[116] P. Harrison, ‘Modelling the forming mechanics of engineering fabrics using a mutually constrained pantographic beam and membrane mesh’, *Compos Part A Appl Sci Manuf*, vol. 81, pp. 145–157, Feb. 2016, doi: 10.1016/j.compositesa.2015.11.005.

[117] P. Boisse, J. Colmars, N. Hamila, N. Naouar, and Q. Steer, ‘Bending and wrinkling of composite fiber preforms and prepregs. A review and new developments in the draping simulations’, *Compos B Eng*, vol. 141, pp. 234–249, May 2018, doi: 10.1016/j.compositesb.2017.12.061.

[118] F. Dell’isola and D. Steigmann, ‘A Two-Dimensional Gradient-Elasticity Theory for Woven Fabrics’, *J Elast*, vol. 118, pp. 113–125, 2015, doi: 10.1007/s10659-014-9478-1.

[119] M. Ferretti, A. Madeo, F. dell’Isola, and P. Boisse, ‘Modeling the onset of shear boundary layers in fibrous composite reinforcements by second-gradient theory’, *Zeitschrift fur Angewandte Mathematik und Physik*, vol. 65, no. 3, pp. 587–612, 2014, doi: 10.1007/s00033-013-0347-8.

[120] R. H. W. ten Thije and R. Akkerman, ‘Finite element simulations of laminated composites forming processes’, *International Journal of Material Forming*, vol. 3, no. SUPPL. 1, pp. 715–718, 2010, doi: 10.1007/s12289-010-0870-5.

[121] L. Wang, P. Xu, X. Peng, K. Zhao, and R. Wei, ‘Characterization of inter-ply slipping behaviors in hot diaphragm preforming: Experiments and modelling’, *Compos Part A Appl Sci Manuf*, vol. 121, pp. 28–35, Jun. 2019, doi: 10.1016/j.compositesa.2019.03.012.

[122] J. Sjölander, P. Hallander, and M. Åkermo, ‘Forming induced wrinkling of composite laminates: A numerical study on wrinkling mechanisms’, *Compos Part A Appl Sci Manuf*, vol. 81, pp. 41–51, Feb. 2016, doi: 10.1016/J.COMPOSITESA.2015.10.012.

[123] F. Yu, S. Chen, L. T. Harper, and N. A. Warrior, ‘Double diaphragm forming simulation using a global-to-local modelling strategy for detailed defect detection in large structures’, *Compos Part A Appl Sci Manuf*, vol. 147, Aug. 2021, doi: 10.1016/j.compositesa.2021.106457.

[124] M. G. Han and S. H. Chang, ‘Draping simulation of carbon/epoxy plain weave fabrics with non-orthogonal constitutive model and material behavior analysis of the cured structure’, *Compos Part A Appl Sci Manuf*, vol. 110, pp. 172–182, Jul. 2018, doi: 10.1016/j.compositesa.2018.04.022.

[125] D. Abliz, Y. Duan, L. Steuernagel, L. Xie, D. Li, and G. Ziegmann, ‘Curing methods for advanced polymer composites -A review’, *Polymers and Polymer Composites*, vol. 21, no. 6, pp. 341–348, 2013, doi: 10.1177/096739111302100602.

[126] K. Xie, Y. He, J. Cai, and W. Hu, ‘Thermal conductivity of Nylon 46, Nylon 66 and Nylon 610 characterized by Flash DSC measurement’, *Thermochim Acta*, vol. 683, p. 178445, Jan. 2020, doi: 10.1016/J.TCA.2019.178445.

[127] R. S. Graves, T. G. Kollie, D. L. McElroy, and K. E. Gilchrist, ‘The thermal conductivity of AISI 304L stainless steel’, *Int J*

Thermophys, vol. 12, no. 2, pp. 409–415, Mar. 1991, doi: 10.1007/BF00500761/METRICS.

[128] J. Tierney and J. W. Gillespie, ‘Modeling of In Situ Strength Development for the Thermoplastic Composite Tow Placement Process’, doi: 10.1177/0021998306060162.

[129] F. Y. C. Boey and C. Y. Yue, ‘Interfacial strength of a microwave-cured epoxy-glass composite’, *J Mater Sci Lett*, vol. 10, no. 22, pp. 1333–1334, 1991, doi: 10.1007/BF00722652.

[130] C. Nightingale and R. J. Day, ‘Flexural and interlaminar shear strength properties of carbon fibre/epoxy composites cured thermally and with microwave radiation’, *Compos Part A Appl Sci Manuf*, vol. 33, no. 7, pp. 1021–1030, Jul. 2002, doi: 10.1016/S1359-835X(02)00031-3.

[131] Y. Li, L. Cheng, and J. Zhou, ‘Curing multidirectional carbon fiber reinforced polymer composites with indirect microwave heating’, *International Journal of Advanced Manufacturing Technology*, vol. 97, no. 1–4, pp. 1137–1147, Jul. 2018, doi: 10.1007/S00170-018-1974-1/METRICS.

[132] I. F. Villegas and H. E. N. Bersee, ‘Ultrasonic welding of advanced thermoplastic composites: An investigation on energy-directing surfaces’, *Advances in Polymer Technology*, vol. 29, no. 2, pp. 112–121, Jun. 2010, doi: 10.1002/ADV.20178.

[133] C. Joseph and C. Viney, ‘Electrical resistance curing of carbon-fibre/epoxy composites’, *Compos Sci Technol*, vol. 60, no. 2, pp. 315–319, Feb. 2000, doi: 10.1016/S0266-3538(99)00112-8.

[134] H. Kim, S. Yarlagadda, J. W. Gillespie, N. B. Shevchenko, and B. K. Fink, ‘A study on the induction heating of carbon fiber reinforced thermoplastic composites’, *Advanced Composite*

Materials, vol. 11, no. 1, pp. 71–80, 2002, doi: 10.1163/156855102753613309.

[135] L. Moser, P. Mitschang, and A. K. Schlarb, ‘Induction welding of thermoplastic polymer composites using robotic techniques’, *SAMPE Journal*, vol. 44, no. 5, pp. 43–48, Sep. 2008.

[136] T. Bayerl, M. Duhovic, P. Mitschang, and D. Bhattacharyya, ‘The heating of polymer composites by electromagnetic induction - A review’, *Compos Part A Appl Sci Manuf*, vol. 57, no. 2014, pp. 27–40, 2014, doi: 10.1016/j.compositesa.2013.10.024.

[137] A. Guichard and J. Feigenblum, ‘Induction heating for high speed RTM process’, *JEC Composites Magazine*, vol. 44, no. 31, pp. 40–43, 2007.

[138] I. F. Villegas, L. Moser, A. Yousefpour, P. Mitschang, and H. E. N. Bersee, ‘Process and performance evaluation of ultrasonic, induction and resistance welding of advanced thermoplastic composites’, *Journal of Thermoplastic Composite Materials*, vol. 26, no. 8, pp. 1007–1024, Sep. 2013, doi: 10.1177/0892705712456031/ASSET/IMAGES/LARGE/10.1177_0892705712456031-FIG10.JPEG.

[139] N. Zimmermann and P. H. Wang, ‘A review of failure modes and fracture analysis of aircraft composite materials’, *Eng Fail Anal*, vol. 115, 2020, doi: 10.1016/j.engfailanal.2020.104692.

[140] S. W. Tsai and E. M. wu, ‘A General Theory of Strength for Anisotropic Materials’, *J Compos Mater*, vol. 5, no. 1, pp. 58–80, 1971, doi: 10.1177/002199837100500106.

[141] C. T. Sun and J. Tao, ‘Prediction of failure envelopes and stress/strain behaviour of composite laminates’, *Compos Sci Technol*, vol. 58, no. 7, pp. 1125–1136, Jul. 1998, doi: 10.1016/S0266-3538(97)00013-4.

[142] A. Puck and H. M. Deuschle, ‘Progress in the Puck Failure Theory for Fibre Reinforced Composites : Analytical solutions for 3D-stress’, *Compos Sci Technol*, vol. 62, no. 3, pp. 371–378, 2002, Accessed: May 03, 2022. [Online]. Available: www.alfredpuck.de

[143] M. R. Wisnom, T. Reynolds, and N. Gwilliam, ‘Reduction in interlaminar shear strength by discrete and distributed voids’, *Compos Sci Technol*, vol. 56, no. 1, pp. 93–101, 1996, doi: 10.1016/0266-3538(95)00128-X.

[144] H. Y. Zhu, D. H. Li, D. X. Zhang, B. C. Wu, and Y. Y. Chen, ‘Influence of voids on interlaminar shear strength of carbon/epoxy fabric laminates’, *Transactions of Nonferrous Metals Society of China (English Edition)*, vol. 19, no. SUPPL. 2, Sep. 2009, doi: 10.1016/S1003-6326(10)60091-X.

[145] P. Zhang, X. Hu, S. Yang, and W. Yao, ‘Modelling progressive failure in multi-phase materials using a phase field method’, *Eng Fract Mech*, vol. 209, pp. 105–124, Mar. 2019, doi: 10.1016/J.ENGFRACMECH.2019.01.021.

[146] L. Zhang, H. Xie, and J. Feng, ‘Mesoscale modeling and failure mechanism of concrete considering pore structures and actual aggregate shapes’, *Constr Build Mater*, vol. 353, p. 129133, Oct. 2022, doi: 10.1016/J.CONBUILDMAT.2022.129133.

[147] C. M. López, I. Carol, and A. Aguado, ‘Meso-structural study of concrete fracture using interface elements. I: Numerical model and tensile behavior’, *Materials and Structures/Materiaux et Constructions*, vol. 41, no. 3, pp. 583–599, Apr. 2008, doi: 10.1617/S11527-007-9314-1/FIGURES/20.

[148] C. Sandino, P. Kroliczek, D. D. McErlain, and S. K. Boyd, ‘Predicting the permeability of trabecular bone by micro-computed tomography and finite element modeling’, *J Biomech*,

vol. 47, no. 12, pp. 3129–3134, Sep. 2014, doi: 10.1016/J.JBIOMECH.2014.06.024.

[149] MatWeb, ‘Tin, Sn’, MatWeb. Accessed: Feb. 25, 2022. [Online]. Available: https://www.matweb.com/search/datasheet.aspx?matguid=64d7cf04332e428dbca9f755f4624a6c

[150] Tencate, ‘TenCate Cetex® TC910 Nylon 6’, TenCate Advanced Composites. Accessed: Feb. 14, 2022. [Online]. Available: https://www.toraytac.com/product-explorer/products/r2Vf/Toray-Cetex-TC910

[151] Abaqus, ‘Abaqus User Manual’, 2017. Accessed: Sep. 06, 2022. [Online]. Available: https://abaqus-docs.mit.edu/2017/English/SIMACAEEXCRefMap/simaexc-c-docproc.htm

[152] A. A. Griffith, ‘VI. The phenomena of rupture and flow in solids’, *Philosophical Transactions of the Royal Society of London. Series A, Containing Papers of a Mathematical or Physical Character*, vol. 221, pp. 163–198, 1921.

[153] B. R. K. Blackman, H. Hadavinia, A. J. Kinloch, and J. G. Williams, ‘The use of a cohesive zone model to study the fracture of fibre composites and adhesively-bonded joints’, *Int J Fract*, vol. 119, no. 1, pp. 25–46, Jan. 2003, doi: 10.1023/A:1023998013255/METRICS.

[154] T. P. Fries and T. Belytschko, ‘The extended/generalized finite element method: An overview of the method and its applications’, *Int J Numer Methods Eng*, vol. 84, no. 3, pp. 253–304, Oct. 2010, doi: 10.1002/NME.2914.

[155] P. M. A. Areias and T. Belytschko, ‘Analysis of three-dimensional crack initiation and propagation using the extended finite

element method', *Int J Numer Methods Eng*, vol. 63, no. 5, pp. 760–788, Jun. 2005, doi: 10.1002/NME.1305.

[156] T. P. Fries and T. Belytschko, 'The extended/generalized finite element method: An overview of the method and its applications', *Int J Numer Methods Eng*, vol. 84, no. 3, pp. 253–304, Oct. 2010, doi: 10.1002/NME.2914.

[157] E. Pakdel, S. Kashi, R. Varley, and X. Wang, 'Recent progress in recycling carbon fibre reinforced composites and dry carbon fibre wastes', *Resour Conserv Recycl*, vol. 166, Mar. 2021, doi: 10.1016/J.RESCONREC.2020.105340.

[158] Y. Yang, R. Boom, B. Irion, D. J. van Heerden, P. Kuiper, and H. de Wit, 'Recycling of composite materials', *Chemical Engineering and Processing: Process Intensification*, vol. 51, pp. 53–68, Jan. 2012, doi: 10.1016/J.CEP.2011.09.007.

[159] J. Palmer, O. R. Ghita, L. Savage, and K. E. Evans, 'Successful closed-loop recycling of thermoset composites', *Composites Part A*, vol. 40, pp. 490–498, doi: 10.1016/j.compositesa.2009.02.002.

[160] R. Bernatas, S. Dagreou, A. Despax-Ferreres, and A. Barasinski, 'Recycling of fiber reinforced composites with a focus on thermoplastic composites', *Clean Eng Technol*, vol. 5, Dec. 2021, doi: 10.1016/J.CLET.2021.100272.

[161] G. Oliveux, L. O. Dandy, and G. A. Leeke, 'Current status of recycling of fibre reinforced polymers: Review of technologies, reuse and resulting properties', *Prog Mater Sci*, vol. 72, pp. 61–99, Jul. 2015, doi: 10.1016/J.PMATSCI.2015.01.004.

[162] S. R. Naqvi, H. M. Prabhakara, E. A. Bramer, W. Dierkes, R. Akkerman, and G. Brem, 'A critical review on recycling of end-of-life carbon fibre/glass fibre reinforced composites waste using

pyrolysis towards a circular economy', 2018, doi: 10.1016/j.resconrec.2018.04.013.

[163] S. J. Pickering, 'Recycling technologies for thermoset composite materials-current status', doi: 10.1016/j.compositesa.2005.05.030.

[164] S. B. Lyon, 'Corrosion of tin and its alloys', in *Shreir's Corrosion*, Elsevier, 2010, pp. 2068–2077. doi: 10.1016/B978-044452787-5.00099-8.

[165] K. Vanclooster, S. v. Lomov, and I. Verpoest, 'Investigation of interply shear in composite forming', *International Journal of Material Forming*, vol. 1, no. SUPPL. 1, pp. 957–960, 2008, doi: 10.1007/s12289-008-0216-8.

[166] P. Harrison, M. F. Alvarez, N. Correia, P. Mimoso, C. Cristovão, and R. Gomes, 'Characterising the forming mechanics of preconsolidated nylon-carbon composite', in *ECCM 2018 - 18th European Conference on Composite Materials*, 2019, pp. 24–28.

[167] S. F. Shuler and S. G. Advani, 'Transverse squeeze flow of concentrated aligned fibers in viscous fluids', *J Nonnewton Fluid Mech*, vol. 65, no. 1, pp. 47–74, Jul. 1996, doi: 10.1016/0377-0257(96)01440-1.

[168] Silex Silicones, 'Technical data sheet- Silicone Rubber Sheeting High Temperature Solid', *Siliex Silicones Ltd*, no. January. Silex Silicones Ltd, 2019. [Online]. Available: https://silex.co.uk/wp-content/uploads/2021/07/SILEX-High-Temp-Sheets-final.pdf

[169] Advent Materials, 'Advent Materials- Tin Sheet'. Accessed: Aug. 23, 2022. [Online]. Available: https://www.advent-rm.com/en-GB/Products/Pure-Metals/Tin/Form/Sheet

[170] Gelest, 'Gelest Tin Powder'. Accessed: Aug. 23, 2022. [Online]. Available: https://www.gelest.com/product/SNT7910/

[171] Alfa Aesar, ‘Alfa Aesar Tin Shot’. Accessed: Aug. 23, 2022. [Online]. Available: https://www.alfa.com/en/catalog/010377/

[172] G. Leftheriotis and P. Yianoulis, ‘Glazings and Coatings’, *Comprehensive Renewable Energy*, pp. 313–355, Jan. 2012, doi: 10.1016/B978-0-08-087872-0.00310-3.

[173] A. Basyir, R. Kurnia, C. Firdharini, D. Aryanto, W. B. Widayatno, and A. S. Wismogroho, ‘Investigation of Effect of Various Hot Gas Atomisation and Melting Pot Temperatures on Tin Alloy Powder Product’, *Sains Malays*, vol. 51, no. 9, pp. 3027–3041, Sep. 2022, doi: 10.17576/JSM-2022-5109-23.

[174] A.-P. Xian and G.-L. Gong, ‘Oxidation Behavior of Molten Tin Doped with Phosphorus’, doi: 10.1007/s11664-007-0288-0.

[175] Induction Coil Solutions, ‘Induction Coil Solutions’. Accessed: Aug. 25, 2022. [Online]. Available: https://www.inductioncoilsolutions.co.uk/

[176] P. Harrison *et al.*, ‘Induction melt thermoforming of advanced multi-axial thermoplastic composite laminates’, *J Manuf Process*, vol. 60, pp. 673–683, Dec. 2020, doi: 10.1016/j.jmapro.2020.10.026.

[177] D. Nardi and J. Sinke, ‘Design analysis for thermoforming of thermoplastic composites: prediction and machine learning-based optimization’, *Composites Part C: Open Access*, vol. 5, p. 100126, Jul. 2021, doi: 10.1016/J.JCOMC.2021.100126.

[178] K. Liu, B. Zhang, X. Xu, and J. Ye, ‘Experimental characterization and analysis of fiber orientations in hemispherical thermostamping for unidirectional thermoplastic composites’, doi: 10.1007/s12289-018-1410-y.

[179] R. J. Meredith, *Conduction and Induction Heating*, vol. 5, no. 2. London: Peregrinus, 1991. doi: 10.1049/pe:19910014.

[180] R. Hiptmair, £ J Ostrowski, and Ý. R. Quast, ‘Modelling and Simulation of Induction Heating’, 2000.

[181] Ceia Power, ‘Ceia Power’. Accessed: Aug. 25, 2022. [Online]. Available: https://www.ceia-power.com/

[182] D. Cai, A. Neyer, R. Kuckuk, and H. M. Heise, ‘Raman, mid-infrared, near-infrared and ultraviolet-visible spectroscopy of PDMS silicone rubber for characterization of polymer optical waveguide materials’, *J Mol Struct*, vol. 976, no. 1–3, pp. 274–281, Jul. 2010, doi: 10.1016/J.MOLSTRUC.2010.03.054.

[183] J. R. Howell, M. P. Mengüç, K. Daun, and R. Siegel, *Thermal Radiation Heat Transfer*. CRC Press, 2020. doi: 10.1201/9780429327308.

[184] C. Murphy, ‘Radiant Heating With Infrared’. Watlow, p. 39, 1999. [Online]. Available: www.watlow.com/downloads/en/training/STL-RADM-89.pdf

[185] Watlow, ‘Radiant Heating with Infrared’.

[186] Silex, ‘Silex’. Accessed: Aug. 25, 2022. [Online]. Available: https://silex.co.uk/

[187] I. Hanhan, R. Agyei, X. Xiao, and M. D. Sangid, ‘Comparing non-destructive 3D X-ray computed tomography with destructive optical microscopy for microstructural characterization of fiber reinforced composites’, *Compos Sci Technol*, vol. 184, Nov. 2019, doi: 10.1016/J.COMPSCITECH.2019.107843.

[188] S. Gholizadeh, ‘A review of non-destructive testing methods of composite materials’, in *Procedia Structural Integrity*, Elsevier B.V., Jan. 2016, pp. 50–57. doi: 10.1016/j.prostr.2016.02.008.

[189] D. Wildenschild and A. P. Sheppard, ‘X-ray imaging and analysis techniques for quantifying pore-scale structure and processes in

subsurface porous medium systems', *Adv Water Resour*, vol. 51, pp. 217–246, 2013, doi: 10.1016/j.advwatres.2012.07.018.

[190] J. Hsieh, *Computed Tomography: Principles, Design, Artifacts, and Recent Advances*, 3rd ed. SPIE, 2015. doi: 10.1117/3.2197756.

[191] J. H. Hubbell and S. M. Seltzer, 'NIST: X-Ray Mass Attenuation Coefficients', *Physical Reference Data*, pp. 1–112, 1996, doi: https://dx.doi.org/10.18434/T4D01F.

[192] C. v. More, R. R. Bhosale, and P. P. Pawar, 'Detection of new polymer materials as gamma-ray-shielding materials', *Radiation Effects and Defects in Solids*, vol. 172, no. 5–6, pp. 469–484, 2017, doi: 10.1080/10420150.2017.1336765.

[193] M. J. Yaffe and J. A. Rowlands, 'X-ray detectors for digital radiography', *Phys Med Biol*, vol. 42, no. 1, pp. 1–39, 1997, doi: 10.1088/0031-9155/42/1/001.

[194] S. N. Kane, A. Mishra, and A. K. Dutta, 'Preface: International Conference on Recent Trends in Physics (ICRTP 2016)', *J Phys Conf Ser*, vol. 755, no. 1, 2016, doi: 10.1088/1742-6596/755/1/011001.

[195] I. Jandejsek *et al.*, 'X-ray inspection of composite materials for aircraft structures using detectors of Medipix type', *Journal of Instrumentation*, vol. 9, no. 5, 2014, doi: 10.1088/1748-0221/9/05/C05062.

[196] V. Cnudde and M. N. Boone, 'High-resolution X-ray computed tomography in geosciences: A review of the current technology and applications', *Earth Sci Rev*, vol. 123, pp. 1–17, 2013, doi: 10.1016/j.earscirev.2013.04.003.

[197] S. C. Garcea, Y. Wang, and P. J. Withers, 'X-ray computed tomography of polymer composites', *Composites Science and*

Technology, vol. 156. Elsevier Ltd, pp. 305–319, Mar. 01, 2018. doi: 10.1016/j.compscitech.2017.10.023.

[198] C. C. Tsao and H. Hocheng, 'Computerized tomography and C-Scan for measuring delamination in the drilling of composite materials using various drills', *Int J Mach Tools Manuf*, vol. 45, no. 11, pp. 1282–1287, Sep. 2005, doi: 10.1016/j.ijmachtools.2005.01.009.

[199] Y. Nikishkov, L. Airoldi, and A. Makeev, 'Measurement of voids in composites by X-ray Computed Tomography', *Compos Sci Technol*, vol. 89, pp. 89–97, Dec. 2013, doi: 10.1016/j.compscitech.2013.09.019.

[200] A. A. Hassen, H. Taheri, and U. K. Vaidya, 'Non-destructive investigation of thermoplastic reinforced composites', *Compos B Eng*, vol. 97, pp. 244–254, Jul. 2016, doi: 10.1016/j.compositesb.2016.05.006.

[201] B. Yu, R. S. Bradley, C. Soutis, and P. J. Withers, 'A comparison of different approaches for imaging cracks in composites by X-ray microtomography', in *Philosophical Transactions of the Royal Society A: Mathematical, Physical and Engineering Sciences*, Royal Society of London, Jul. 2016. doi: 10.1098/rsta.2016.0037.

[202] J. F. Barrett and N. Keat, 'Artifacts in CT: Recognition and avoidance', *Radiographics*, vol. 24, no. 6, pp. 1679–1691, 2004, doi: 10.1148/rg.246045065.

[203] N. Otsu, 'Threshold Selection Method From Gray-Level Histograms.', *IEEE Trans Syst Man Cybern*, vol. SMC-9, no. 1, pp. 62–66, 1979, doi: 10.1109/tsmc.1979.4310076.

[204] T. W. Ridler and S. Calvard, 'Picture Thresholding Using an Iterative Slection Method.', *IEEE Trans Syst Man Cybern*, vol.

SMC-8, no. 8, pp. 630–632, 1978, doi: 10.1109/tsmc.1978.4310039.

[205] J. N. Kapur, P. K. Sahoo, and A. K. C. Wong, ‘A new method for gray-level picture thresholding using the entropy of the histogram.’, *Comput Vis Graph Image Process*, vol. 29, no. 3, pp. 273–285, 1985, doi: 10.1016/0734-189X(85)90125-2.

[206] N. M. Zaitoun and M. J. Aqel, ‘Survey on Image Segmentation Techniques’, *Procedia Comput Sci*, vol. 65, pp. 797–806, 2015, doi: 10.1016/j.procs.2015.09.027.

[207] P. Sahoo, C. Wilkins, and J. Yeager, ‘Threshold selection using Renyi’s entropy’, *Pattern Recognit*, vol. 30, no. 1, pp. 71–84, 1997, doi: 10.1016/S0031-3203(96)00065-9.

[208] J. W. Shirley, ‘An Early Experimental Determination of Snell’s Law’, *Am J Phys*, vol. 19, no. 9, pp. 507–508, 1951, doi: 10.1119/1.1933068.

[209] P. Taylor, A. I. Lvovsky, and A. I. Lvovsky, *Encyclopedia of Optical Engineering Fresnel Equations Fresnel Equations*, no. August. 2013. doi: 10.1081/E-EOE-120047133.

[210] B. L. Henke, E. M. Gullikson, and J. C. Davis, ‘X-ray interactions: Photoabsorption, scattering, transmission, and reflection at E = 50-30, 000 eV, Z = 1-92’, *Atomic Data and Nuclear Data Tables*, vol. 54, no. 2. pp. 181–342, 1993. doi: 10.1006/adnd.1993.1013.

[211] Periodic Table, ‘Periodic Table Data’. Accessed: Aug. 26, 2022. [Online]. Available: https://periodictable.com/index.html

[212] RGPBALLS, ‘NYLON® 6/NYLON® 6.6 (PA 6/PA 6.6) BALLS’. Accessed: Aug. 26, 2022. [Online]. Available: https://www.rgpballs.com/en/nylon-6-nylon-6-6-pa-6-pa-6-6-balls/

[213] TenCate, ‘TenCate Cetex TC1200 datasheet’, Company Website. Accessed: Nov. 22, 2021. [Online]. Available: https://www.toraytac.com/media/694245aa-3765-43b4-a2cd-8cf76e4aeec5/lmhIVg/TAC/Documents/Data_sheets/Thermoplastic/UD tapes, prepregs and laminates/Toray-Cetex-TC910_PA6_PDS.pdf

[214] S. Choudhury, H. Khan, Q. N. Begum, and M. Sanaullah, ‘Sensitometric Characteristics of Industrial X-Ray Films ® Sensitometric Characteristics of Industrial X-Ray Films’, Accessed: Aug. 26, 2022. [Online]. Available: https://www.researchgate.net/publication/281899367

[215] S. J. Marshall, S. C. Bayne, R. Baier, A. P. Tomsia, and G. W. Marshall, ‘A review of adhesion science’, *Dental Materials*, vol. 26, no. 2, pp. e11–e16, Feb. 2010, doi: 10.1016/j.dental.2009.11.157.

[216] T. El-Ashram, ‘Structure and properties of rapidly solidified pure tin’, *Radiation Effects and Defects in Solids*, vol. 161, no. 3, pp. 193–197, 2006, doi: 10.1080/10420150500485192.

[217] INTERNATIONAL STANDARD, ‘EN ISO 14130 : Fiber-reinforced plastic composites Determination of interlaminar shear strength’, *International Standard*, no. 1108, 1997.

[218] Y. He and A. Makeev, ‘Nonlinear shear behavior and interlaminar shear strength of unidirectional polymer matrix composites: A numerical study’, *Int J Solids Struct*, vol. 51, no. 6, pp. 1263–1273, 2014, doi: 10.1016/j.ijsolstr.2013.12.014.

[219] C. Materials *et al.*, ‘Effects of Fiber Surface-Treatment and Sizing on the Dynamic Mechanical and Interfacial Properties of Carbon / Nylon 6 Composites’, *Compos Sci Technol*, vol. 88, no. 1, pp. 9–34, 2010, [Online]. Available: https://doi.org/10.1016/j.polymertesting.2018.04.038%0Ahttp://

dx.doi.org/10.1016/j.ijsolstr.2013.12.014%0Ahttp://dx.doi.org/10.1016/j.compositesa.2016.04.028

[220] L. Yao, Y. Lu, Z. Li, S. Li, B. Wu, and C. Yang, 'Effect of surface post-oxidation of epoxy-sized carbon fibre on interlaminar shear strength of the polyamide 66 composites', *Compos Interfaces*, vol. 28, no. 8, pp. 749–770, 2021, doi: 10.1080/09276440.2020.1802166.

[221] J. W. Yi *et al.*, 'Effect of phenoxy-based coating resin for reinforcing pitch carbon fibers on the interlaminar shear strength of PA6 composites', *Compos Part A Appl Sci Manuf*, vol. 87, pp. 212–219, 2016, doi: 10.1016/j.compositesa.2016.04.028.

[222] M. A. Caminero, J. M. Chacón, I. García-Moreno, and J. M. Reverte, 'Interlaminar bonding performance of 3D printed continuous fibre reinforced thermoplastic composites using fused deposition modelling', *Polym Test*, vol. 68, no. March, pp. 415–423, 2018, doi: 10.1016/j.polymertesting.2018.04.038.

[223] D. Yavas, Z. Zhang, Q. Liu, and D. Wu, 'Interlaminar shear behavior of continuous and short carbon fiber reinforced polymer composites fabricated by additive manufacturing', *Compos B Eng*, vol. 204, p. 108460, Jan. 2021, doi: 10.1016/j.compositesb.2020.108460.

[224] P. Jakubczak, J. Bienias, and B. Surowska, 'Interlaminar shear strength of fibre metal laminates after thermal cycles', *Compos Struct*, vol. 206, pp. 876–887, Dec. 2018, doi: 10.1016/j.compstruct.2018.09.001.

[225] C. Bellini, V. di Cocco, and L. Sorrentino, 'Interlaminar shear strength study on CFRP/Al hybrid laminates with different properties', *Frattura ed Integrita Strutturale*, vol. 14, no. 51, pp. 442–448, 2020, doi: 10.3221/IGF-ESIS.51.32.

[226] C. Bellini, V. di Cocco, F. Iacoviello, and L. Sorrentino, ‘Influence of structural characteristics on the interlaminar shear strength of CFRP/Al fibre metal laminates’, in *Procedia Structural Integrity*, Elsevier B.V., Jan. 2019, pp. 373–378. doi: 10.1016/j.prostr.2019.08.177.

[227] F. Dong, S. J. Meschter, and J. Cho, ‘Improved adhesion of polyurethane-based coatings to tin surface’, *Journal of Materials Science: Materials in Electronics*, vol. 30, no. 8, pp. 7268–7279, 2019, doi: 10.1007/s10854-019-01040-6.

[228] P. Harrison *et al.*, ‘Induction melt thermoforming of advanced multi-axial thermoplastic composite laminates’, *J Manuf Process*, vol. 60, no. October, pp. 673–683, 2020, doi: 10.1016/j.jmapro.2020.10.026.

[229] N. Lona Batista, K. Anagnostopoulos, E. Cocchieri Botelho, and H. Kim, ‘Influence of crystallinity on interlaminar fracture toughness and impact properties of polyphenylene sulfide/carbon fiber laminates’, *Eng Fail Anal*, vol. 119, no. September 2020, p. 104976, 2021, doi: 10.1016/j.engfailanal.2020.104976.

[230] H. Chen, S. Li, J. Wang, and A. Ding, ‘A focused review on the thermo-stamping process and simulation progresses of continuous fibre reinforced thermoplastic composites’, *Compos B Eng*, vol. 224, no. May, p. 109196, 2021, doi: 10.1016/j.compositesb.2021.109196.

[231] I. Taketa, G. Kalinka, L. Gorbatikh, S. v. Lomov, and I. Verpoest, ‘Influence of cooling rate on the properties of carbon fiber unidirectional composites with polypropylene, polyamide 6, and polyphenylene sulfide matrices’, *Advanced Composite Materials*, vol. 29, no. 1, pp. 101–113, 2020, doi: 10.1080/09243046.2019.1651083.

[232] A. International and files indexed by mero, ‘Standard Test Method for Short-Beam Strength of Polymer Matrix Composite Materials and Their Laminates 1’, 2000.

[233] A. Makeev, Y. He, and H. Schreier, ‘Short-beam shear method for assessment of stress-strain curves for fibre-reinforced polymer matrix composite materials’, *Strain*, vol. 49, no. 5, pp. 440–450, 2013, doi: 10.1111/str.12050.

[234] R. Palazzetti and A. Zucchelli, ‘Electrospun nanofibers as reinforcement for composite laminates materials – A review’, *Compos Struct*, vol. 182, pp. 711–727, Dec. 2017, doi: 10.1016/j.compstruct.2017.09.021.

[235] Y. Ou, C. González, and J. J. Vilatela, ‘Understanding interlaminar toughening of unidirectional CFRP laminates with carbon nanotube veils’, *Compos B Eng*, vol. 201, no. August, 2020, doi: 10.1016/j.compositesb.2020.108372.

[236] B. Beylergil, M. Tanoğlu, and E. Aktaş, ‘Effect of polyamide-6,6 (PA 66) nonwoven veils on the mechanical performance of carbon fiber/epoxy composites’, *Compos Struct*, vol. 194, pp. 21–35, Jun. 2018, doi: 10.1016/j.compstruct.2018.03.097.

[237] T. Brugo *et al.*, ‘Study on Mode I fatigue behaviour of Nylon 6,6 nanoreinforced CFRP laminates’, *Compos Struct*, vol. 164, pp. 51–57, Mar. 2017, doi: 10.1016/j.compstruct.2016.12.070.

[238] Y. Ou, C. González, and J. J. Vilatela, ‘Interlaminar toughening in structural carbon fiber/epoxy composites interleaved with carbon nanotube veils’, *Compos Part A Appl Sci Manuf*, vol. 124, p. 105477, Sep. 2019, doi: 10.1016/j.compositesa.2019.105477.

[239] S. W. Hsiao and N. Kikuchi, ‘Numerical analysis and optimal design of composite thermoforming process’, *Comput Methods*

Appl Mech Eng, vol. 177, no. 1–2, pp. 1–34, Jul. 1999, doi: 10.1016/S0045-7825(98)00273-4.

[240] E. J. Barbero, *Finite element analysis of composite materials using Abaqus*, 1st ed. 2013.

[241] S. B. Sharma and M. P. F. Sutcliffe, 'A simplified finite element model for draping of woven material', *Compos Part A Appl Sci Manuf*, vol. 35, no. 6, pp. 637–643, Jun. 2004, doi: 10.1016/j.compositesa.2004.02.013.

[242] A. A. Skordos, C. Monroy Aceves, and M. P. F. Sutcliffe, 'A simplified rate dependent model of forming and wrinkling of pre-impregnated woven composites', *Compos Part A Appl Sci Manuf*, vol. 38, no. 5, pp. 1318–1330, May 2007, doi: 10.1016/j.compositesa.2006.11.005.

[243] C. M. O'Bradaigh and R. Byron Pipes, 'Finite element analysis of composite sheet-forming process', *Composites Manufacturing*, vol. 2, no. 3–4, pp. 161–170, Jan. 1991, doi: 10.1016/0956-7143(91)90135-4.

[244] X. Peng, Z. Guo, T. Du, and W. R. Yu, 'A simple anisotropic hyperelastic constitutive model for textile fabrics with application to forming simulation', *Compos B Eng*, vol. 52, pp. 275–281, Sep. 2013, doi: 10.1016/j.compositesb.2013.04.014.

[245] P. Boisse, M. Borr, K. Buet, and A. Cherouat, 'Finite element simulations of textile composite forming including the biaxial fabric behaviour', *Compos B Eng*, vol. 28, no. 4, pp. 453–464, Jan. 1997, doi: 10.1016/S1359-8368(96)00067-4.

[246] W. R. Yu, M. Zampaloni, F. Pourboghrat, K. Chung, and T. J. Kang, 'Analysis of flexible bending behavior of woven preform using non-orthogonal constitutive equation', *Compos Part A Appl*

Sci Manuf, vol. 36, no. 6, pp. 839–850, Jun. 2005, doi: 10.1016/J.COMPOSITESA.2004.10.026.

[247] U. Sachs *et al.*, ‘Characterization of the dynamic friction of woven fabrics: Experimental methods and benchmark results’, *Compos Part A Appl Sci Manuf*, vol. 67, pp. 289–298, 2014, doi: 10.1016/J.COMPOSITESA.2014.08.026.

[248] A. Cherouat and H. Bourouchaki, ‘Numerical Tools for Composite Woven Fabric Preforming’, *Advances in Materials Science and Engineering*, vol. 2013, 2013, doi: 10.1155/2013/709495.

[249] H. Lin, J. Wang, A. C. Long, M. J. Clifford, and P. Harrison, ‘Predictive modelling for optimization of textile composite forming’, *Compos Sci Technol*, vol. 67, no. 15–16, pp. 3242–3252, Dec. 2007, doi: 10.1016/j.compscitech.2007.03.040.

[250] A. Cherouat and J. Louis Billoët, ‘Mechanical and numerical modelling of composite manufacturing processes deep-drawing and laying-up of thin pre-impregnated woven fabrics’, *J Mater Process Technol*, vol. 118, pp. 460–471, 2001.

[251] S. Gatouillat, A. Bareggi, E. Vidal-Sallé, and P. Boisse, ‘Meso modelling for composite preform shaping - Simulation of the loss of cohesion of the woven fibre network’, *Compos Part A Appl Sci Manuf*, vol. 54, pp. 135–144, 2013, doi: 10.1016/j.compositesa.2013.07.010.

[252] W. R. Yu, F. Pourboghrat, K. Chung, M. Zampaloni, and T. J. Kang, ‘Non-orthogonal constitutive equation for woven fabric reinforced thermoplastic composites’, *Compos Part A Appl Sci Manuf*, vol. 33, no. 8, pp. 1095–1105, 2002, doi: 10.1016/S1359-835X(02)00053-2.

[253] P. Boisse, J. Huang, and E. Guzman-Maldonado, ‘Analysis and modeling of wrinkling in composite forming’, *Journal of Composites Science*, vol. 5, no. 3, 2021, doi: 10.3390/jcs5030081.

[254] F. Yu, S. Chen, J. V. Viisainen, M. P. F. Sutcliffe, L. T. Harper, and N. A. Warrior, ‘A macroscale finite element approach for simulating the bending behaviour of biaxial fabrics’, *Compos Sci Technol*, vol. 191, p. 108078, May 2020, doi: 10.1016/J.COMPSCITECH.2020.108078.

[255] F. Abdiwi *et al.*, ‘Characterising and modelling variability of tow orientation in engineering fabrics and textile composites’, *Compos Sci Technol*, vol. 72, no. 9, pp. 1034–1041, May 2012, doi: 10.1016/J.COMPSCITECH.2012.03.017.

[256] P. Harrison, W. R. Yu, and A. C. Long, ‘Rate dependent modelling of the forming behaviour of viscous textile composites’, *Compos Part A Appl Sci Manuf*, vol. 42, no. 11, pp. 1719–1726, Nov. 2011, doi: 10.1016/j.compositesa.2011.07.026.

[257] P. Harrison, F. Abdiwi, Z. Guo, P. Potluri, and W. R. Yu, ‘Characterising the shear-tension coupling and wrinkling behaviour of woven engineering fabrics’, *Compos Part A Appl Sci Manuf*, vol. 43, no. 6, pp. 903–914, 2012, doi: 10.1016/j.compositesa.2012.01.024.

[258] P. Harrison, F. Abdiwi, Z. Guo, P. Potluri, and W. R. Yu, ‘Characterising the shear-tension coupling and wrinkling behaviour of woven engineering fabrics’, *Compos Part A Appl Sci Manuf*, vol. 43, no. 6, pp. 903–914, Jun. 2012, doi: 10.1016/j.compositesa.2012.01.024.

[259] S. K. Fenster and A. C. Ugural, *Advanced Strength and Applied Elasticity*. Elsevier Publishing Company, 1975.